

Techniques for Characterizing and Enhancing the Performance of Long-Range Wireless Sensor Networks

Thomas Ameloot

Doctoral dissertation submitted to obtain the academic degree of
Doctor of Electrical Engineering

Supervisors

Prof. Hendrik Rogier, PhD - Prof. Patrick Van Torre, PhD

Department of Information Technology
Faculty of Engineering and Architecture, Ghent University

June 2021



Techniques for Characterizing and Enhancing the Performance of Long-Range Wireless Sensor Networks

Thomas Ameloot

Doctoral dissertation submitted to obtain the academic degree of
Doctor of Electrical Engineering

Supervisors

Prof. Hendrik Rogier, PhD - Prof. Patrick Van Torre, PhD

Department of Information Technology
Faculty of Engineering and Architecture, Ghent University

June 2021

ISBN 978-94-6355-502-9

NUR 959

Wettelijk depot: D/2021/10.500/50

Members of the Examination Board

Chair

Prof. Filip De Turck, PhD, Ghent University

Other members entitled to vote

Prof. Slawomir Ambroziak, PhD, Politechnika Gdańska, Poland

Prof. Sam Lemey, PhD, Ghent University

Prof. Marc Moeneclaey, PhD, Ghent University

Prof. Claude Oestges, PhD, Université catholique de Louvain

Supervisors

Prof. Hendrik Rogier, PhD, Ghent University

Prof. Patrick Van Torre, PhD, Ghent University

Dankwoord

Toen mij de vraag gesteld werd of een doctoraat niets voor mij zou zijn was mijn eerste reactie: “Hahaha, no way, daarmee gaan ze mij niet liggen hebben”. Een week later stond ik echter in de foyer van het UFO-gebouw te bevestigen dat “ik dat best wel interessant zou vinden”. Van waar die totale ommekeer? Gezond verstand zal er wel iets mee te maken hebben, al was het zeker niet de enige factor. Maar was dat wel een goed idee? Een doctoraat over draadloze communicatie en antennes... En ik die net alle antenne-gerelateerde keuzevakken links had laten liggen... Het antwoord: jazeker. Exact vier jaar later kijk ik terug op een periode van enorme groei. Ik ben oprecht trots op het boek dat nu voor u ligt en blij dat ik nu toch al wel iets weet te vertellen over draadloze communicatie. Maar, wie zijn queeste volbrengt mag niet vergeten welke weg hij heeft afgelegd. En al zeker niet zonder wie dat nooit gelukt zou zijn.

Ik ben in de eerste plaats mijn beide promotoren enorm dankbaar. Patrick, de uitmuntende kwaliteit van jouw lessen en je geëngageerde begeleiding van studenten waren de doorslaggevende factoren om dit doctoraat aan te durven. Zonder enige twijfel. Mijn vertrouwen was de voorbije vier jaar ook volledig op haar plaats. Jouw diepgaand inzicht gaf zuurstof aan elk onderzoeksidee en je toegankelijkheid en openheid maakten het mogelijk om elke hindernis te overwinnen. Bedankt voor de waardevolle leermomenten, wie had ooit gedacht dat propagatiemetingen en druiven zo veel met elkaar gemeen konden hebben... Hendrik, bedankt voor het vertrouwen en de vrijheid die ik kreeg in mijn werk. Jouw waardevolle feedback en academisch inzicht hebben dit doctoraat naar een ander niveau getild!

Ten derde wil ik ook graag Prof. Marc Moeneclay bedanken voor zijn buitengewoon verrijkende bijdrage aan het derde deel van mijn doctoraatsonderzoek. Marc, ik kan niet ontkennen dat ik bij bepaalde van uw vragen of bedenkingen een kleine inhoudelijke angstreactie moest onderdrukken, maar ben dan ook enorm dankbaar voor de diepgaande inzichten die deze vraagstellingen mij hebben opgeleverd. Ook collega Peter Guns wens ik te bedanken voor zijn excellente technische bijstand bij het plaatsen van onze meetopstellingen en zijn oprechte interesse in het werk dat in dit boek wordt gepresenteerd. Daarnaast wil ik ook alle andere collega's en faculteiten die instemden met het plaatsen van een LoRa-node bij hen thuis of op hun bureau nog eens uitdrukkelijk bedanken, net als de collega's bij de volkssterrenwacht Armand Pien, die de meteorologische data in deze doctoraats-thesis aanleverden. Mijn dank gaat ook uit naar Matthias de Schepper. Matthias, je bent van onschatbare waarde voor alle jonge elektronica-ingenieurs aan onze universiteit, bedankt voor de fijne samenwerking. Verder wil ik ook Martine, Davinia en Bernadette bedanken voor hun superkrachten op administratief vlak. Als volbloed administrofoob weet ik deze als geen ander te waarderen. Ten slotte ver-

dient ook Sabrina een trofee ter grootte van het iGent-gebouw voor haar moed en doorzettingsvermogen bij het leefbaar houden van onze betonnen jungle.

Ik merkte eerder al op dat ik de voorbije vier jaar een enorme groei heb ervaren. Deze groei is in grote mate te danken aan mijn dichtste collega's. *"If you are the smartest one in the room, you're in the wrong room."* Wel, beste bewoners van de 210.006, ik was zeer zeker in de juiste kamer. Mijn *street maths* konden niet tippen aan jullie stevig ontwikkelde wiskundige spierballen, mijn puzzel skills smelten als sneeuw voor de zon wanneer ze worden vergeleken met die van jullie! (Mijn gebrek aan waardevolle puzzelbijdrages was niet te wijten aan een gebrek aan interesse.) Simon, de eeuwige despoot, de schoenen die je als bureauchef achterliet waren veel te groot voor mijn kleine voeten. Bedankt voor de fantastische tijd! Ik koester mijn *employee-of-the-month* badge alsof hij van goud is. Arne, de vederlichte manier waarop jij elke dag de bureau binnen kuierde om vervolgens onderzoek neer te poten dat zelfs de grootste academicus tot een buiging dwingt was een ware inspiratie. Martijn, jouw eerste woorden tot mij waren *"we are not friends, we are friendly colleagues"*. Sta mij toe om dit unilateraal en voor eeuwig te ontcrachten. Altijd paraat om te kletsen over podcasts, provider van de beste boeken/muziek/film-tips, de menselijke incarnatie van hulpvaardigheid... Mijn waardering voor jou is gigantisch! Michiel, master of boardgames, bedankt om mij onder te dompelen in deze prachtige kant van de nerdwereld. Ik kijk met een gelukkig gevoel terug naar al die gezellige boardgame-avonden. *Duygu, a million thanks for bringing common sense and kindness into our office. You are a diamond in the midst of mortal men.* Gert-Jan, bedankt voor je geniale humor. Ik begrijp niets van basketbal of American football, maar als het nog maar half zo plezant is als jij het doet lijken kan ik niet anders dan hopen om toch eens een Super Bowl te zien, begeleid van jouw expert commentary. *Hossein, thank you for all of the colourful moments in my early PhD days.* Pieter, jouw werk is echt the stuff of legends. Ik vind het ongelooflijk cool om een echte quantum-researcher te kennen. Bedankt ook voor de prachtige planten in onze bureau. Elke dag een beetje meer Amazonewoud, I love it! Dries, ik ben vol van verwondering voor jouw ongelooflijke intellect. Bedankt voor de rust die je brengt in onze soms chaotische omgeving. Arno, vroeger was ik de persoon die met belachelijk veel onderzoeksmateriaal elk hoekje van onze bureau inpalmde, maar tot mijn grote plezier heb je me compleet van de troon gestoten. Keep it going!

Maar, ook in andere bureauruimtes werken helden dag en nacht aan een betere toekomst. Olivier, ik ben trots op onze bijdrages aan de West-Vlaamse verovering van de enclave genaamd "Gent". Bedankt voor je tips en onze interessante gesprekken. Dries, je openheid en enthousiasme zullen mij voor altijd bij blijven. Quinten en Thomas, ik moet het toegeven: ik ben stiekem schijtbang van de Sons of Maxwell. Belachelijk veel respect voor al jullie successen! *Kamil, I truly and strongly believe that if everyone in this world was just 1% more like you, there would be no troubles left in the world. You are one of the most kind and helpful people that I have ever met.* Nick, de gesprekken met jou zijn ongelooflijk deugdzaam. Of ze nu over technologie of lekker eten gaan, het is altijd in orde! Laura, ik wacht nog

altijd met heel veel ongeduld op de dag waarop we samen met Martijn mijn Trivial Pursuit - Harry Potter editie kunnen uittesten. *Igor, your lunch skills are legendary, thank you for bringing so much joy to our group.* Seppe, bedankt voor de chille thesisbegeleidingsmomentjes, we hebben dat goed gedaan!

Yet, as we had to find out the hard way, you don't even need an office for living the PhD life. Alessandro, Dennis, Joryan, Emile, Jelle, Nicolas and Reinier, I very sincerely regret not being able to get to know you as I should have over the past sixteen months. Not in my worst nightmares could I have dreamed that "this entire virus thing" would have such an enormous impact on our lives. I deeply hope, with all my heart, that you will be able to experience what it is really like to pursue a PhD in the electromagnetics group, legendary office experience included. Nowadays, many theses contain a so-called "corona-preamble", and rightly so, as a multitude of research projects were deeply impacted by the international health crisis that has left few unperturbed. I, however, am only willing to refer to the troubling times that our society has gone through by means of a Tolkien quote: "The world is indeed full of peril, and in it there are many dark places; but still there is much that is fair, and though in all lands love is now mingled with grief, it grows perhaps the greater."

Mijn diepste dankbaarheid gaat uit naar mijn familie. Het mag in het "verre" Gent zo goed of kwaad gaan als het maar wil, ik weet dat er thuis altijd liefdevolle zielen klaar staan om mijn mislukkingen te helpen dragen en de successen met mij te vieren. Het is fantastisch om zo trots te kunnen zijn op al wie voor mij kwam (tot generaties aan voorouders terug), en het is nog mooier om te zien dat ook wie na mij komt al zo goed weet waar het in het leven echt om draait. Elise, jouw onaflatende steun is één van mijn meest kostbare bezittingen. Bedankt voor alle leuke treinritten van en naar Gent, en voor alle zottigheden die toch altijd weer de dag weten te kleuren! Pieter, je ben een crème van een man, met het hart helemaal op de juiste plaats. Bedankt voor al jouw hulp in de wondere wereld der leraren. Lieve kleine Myrthe, bedankt om zo veel geluk te brengen in onze familie. Eén glimlach van jou doet de wolken verdwijnen! Nele, bedankt voor al je wijze raad en de altijd fantastisch georganiseerde reizen en weekendjes. Niemand heeft een grotere bijdrage geleverd aan mijn ontwikkeling dan jij. Glenn, je bent van onschatbare waarde voor onze familie. Jouw diepmenselijke inzicht en ijzersterke ondernemingsskills zijn een ware inspiratie! Oliver, je bent mijn beste vriend op aarde. Elke dag opnieuw weet je ons allemaal te verrassen en ons gelukkig te maken. Ik ben de meest trotse peter die er bestaat! Peter, bedankt om mij zo veel coole dingen te leren. Zonder jou had ik nooit zo goed leren mountainbiken, kon ik waarschijnlijk nog geen bocht pakken op een snowboard en was ik sowieso nooit op mijn benen geraakt op een surfplank. Ik heb altijd heel sterk naar je opgekeken, bedankt om mij te tonen dat zelfs de sky geen limiet is! Ellie, je bent het mooiste en liefste wezen op deze planeet en alle andere. Bedankt voor al je enthousiasme en je onophoudelijke liefde. Papa, in het woord eigenwijs zit het woord wijs, maar gelukkig ook een gezonde dosis humor. Bedankt om zo veel voor ons allemaal te doen en ons zo veel kansen te geven. Bedankt om je respect voor de natuur en je grote liefde voor sport met de papepel mee te geven. Ik koester elke stap uit

elke bergwandeling die we ooit gedaan hebben. Gelukkig zijn de bergschoenen nog lang niet versleten en liggen er nog zo veel bergen achter de horizon om te (her)ontdekken! Mama, de manier waarop jij ons zo veel blijft geven is onnavolgbaar. De onvoorwaardelijke liefde en steun die jij aan ons allemaal (van generatie op generatie) hebt doorgegeven is onze grootste troef! Over troef gesproken, bedankt om van mij een waardige teamgenoot te maken bij het manillen, om zo'n grote fan te zijn van mijn muzikale avonturen, om telkens opnieuw tot een gat in de nacht tijd te maken voor een goeie babbel over het leven... Ik zou gemakkelijk een boek kunnen schrijven dat tien keer zo dik is als wat nu voor je ligt als ik alles op papier zou zetten dat hier thuis hoort! Bedankt!

Aangezien een beetje romantiek elk boek beter maakt wil ik nog één persoon in het bijzonder bedanken. Liefste Julie, geen enkel natuurfenomeen is unieker dan wat jij bij mij veroorzaakt. Jij doet mij zweven, en accelereert mijn hart moeiteloos tot relativistische snelheden. In jouw buurt loopt de tijd sneller dan waar ook in het universum. Tot je in mijn ogen kijkt. Dan staat ze stil en verliest ze haar betekenis. Bedankt voor alle tijdloze momenten, dat er nog veel mogen komen!

Diksmuide, juni 2021
Thomas Ameloot

There is nothing like looking, if you want to find something. You certainly usually find something, if you look, but it is not always quite the something you were after.

J.R.R. TOLKIEN

Contents

Samenvatting	xi
Summary	xv
List of Abbreviations	xix
List of Symbols	xxiii
List of Publications	xxv
1 Introduction	3
1.1 Context	3
1.2 Challenges	4
1.3 State-of-the-Art	6
1.4 Own Contributions	17
1.5 Outline	18
Part I: Physical-Layer Performance of LoRa Networks in Different Propagation Environments	29
2 A Compact LoRa IoT Sensor Node with Extended Dynamic Range for Channel Measurements	31
2.1 Introduction	32
2.2 Hardware Design	33
2.3 Hardware Verification Setups	39
2.4 Measurement Results and Analysis	42
2.5 Conclusion	48
3 Variable Link Performance due to Weather Effects in a Long-Range, Low-Power LoRa Sensor Network	51
3.1 Introduction	52
3.2 Measurement Setup	54
3.3 Measurement Results and Analysis	60
3.4 Discussion	75
3.5 Conclusion	76

Part II: Body-Centric LoRa Networks Based on System-Integrated Textile SIW Antennas	85
4 Wearable 868 MHz LoRa Wireless Sensor Node on a Substrate-Integrated-Waveguide Antenna Platform	87
4.1 Introduction	88
4.2 Hardware Design	89
4.3 Radiation Characteristics	90
4.4 Outdoor Body-to-Body Range Test	92
4.5 Conclusion	95
5 Indoor Body-to-Body LoRa Link Characterization	99
5.1 Introduction	100
5.2 Materials and Methods	100
5.3 Measurement Results and Analysis	103
5.4 Conclusion	111
6 Experimental Parameter Optimization for Adaptive LoRa Modulation in Body-Centric Applications	115
6.1 Introduction	116
6.2 Proposed System	117
6.3 Measurement Setup	119
6.4 Measurement Results and Analysis	120
6.5 Conclusion	125
7 LoRa Base-Station-to-Body Communication with SIMO Front-to-Back Diversity	129
7.1 Introduction	130
7.2 Materials and Methods	132
7.3 Measurement Results and Analysis	136
7.4 Conclusion	144
Part III:LoRa Modulation and Detection with Software Defined Radio	149
8 LoRa Signal Synchronization and Detection at Extremely Low Signal-to-Noise Ratios	151
8.1 Introduction	152
8.2 Modulation and Detection	155
8.3 Packet Structure	159
8.4 Receiving Algorithm	160
8.5 Simulated SDR Performance	172
8.6 Comparison to Commercial Hardware	175
8.7 Conclusion	177

9	Characterizing the Impact of Doppler Effects on Body-Centric LoRa Links with SDR	185
9.1	Introduction	186
9.2	SDR-based LoRa Modulation	187
9.3	Doppler Effects Simulation and Analysis	190
9.4	Discussion	203
9.5	Conclusion	204
10	Conclusions	209
10.1	Overview	209
10.2	General Conclusions	211
10.3	Future Work	211

Samenvatting

Het wekt geen controverse om te stellen dat communicatie één van de pijlers van de beschaving is. Of ze nu wordt aangewend om de locatie van een nest wilde wolven te delen, of om te leren hoe je die perfecte moelleux bakt, communicatie is en blijft cruciaal voor het succes en voortbestaan van onze soort. Beschouw de impact van doorbraken in de communicatietechnologie op onze maatschappij. Doorheen de menselijke geschiedenis hebben deze vooruitgangen niets minder dan revoluties ontketend. De uitvinding van het schrift stelde antieke beschavingen in staat om hun kennis en wijsheid te delen met latere generaties. De boekdrukkunst wordt algemeen erkend als de vonk die de donkere middeleeuwen deed omslaan in de renaissance. En, zoals al wie haar geboorte heeft meegemaakt kan bevestigen heeft het internet onze wereld voorgoed veranderd. Men zou zich de vraag kunnen stellen waarom het zo belangrijk is om in een oogwenk toegang te krijgen tot zo veel informatie. Sommigen zouden misschien zeggen dat het belachelijk overbodig is dat te kunnen. Maar, sta even stil bij hoeveel beslissingen er op een doorsnee dag genomen worden. In elke situatie geldt dat het nemen van goeie beslissingen afhangt van de toegang tot de juiste informatie. Net daarom is het zeer nuttig om zo veel mogelijk informatie te verzamelen en deze zo breed mogelijk uit te wisselen. Bij deze uitwisseling is technologie van groot belang. We mogen niet ontkennen dat veel wetenschappelijke ontdekkingen fundamenteel zijn geweest voor ons technologisch succes. Desondanks is het duidelijk dat de meest recente vorderingen in de communicatietechnologie mogelijk zijn gemaakt door innovaties in de elektronica. Naarmate elektronische schakelingen kleiner en efficiënter worden dienen zich immers steeds weer nieuwe mogelijkheden aan. De afgelopen jaren hebben we daardoor steeds meer apparaten op het internet kunnen aansluiten, waardoor het *Internet of Things* (IoT) of - vrij vertaald - het “internet der dingen” is ontstaan.

Veel van deze “dingen” bevatten sensoren die omgevingsparameters zoals temperatuur, vochtigheid, druk en luminescentie kunnen controleren. Andere sensoren kunnen statusinformatie over een bepaald systeem verzamelen, zoals versnellingsgegevens of stroomverbruik. Weer andere sensoren kunnen zich richten op het verzamelen van biomedische informatie zoals de hartslag of bloeddruk van een persoon. In feite hebben de capaciteiten van elektronische en elektromechanische sensoren die van de mens al lang overtroffen. Door deze sensoren op het internet aan te sluiten kunnen we de informatie die ze verzamelen ook op een ongekende schaal delen. Door onderling verbonden draadloze sensoren over grote gebieden te verspreiden, ontstaan draadloze langeafstandssensornetwerken (WSN's). Deze kunnen worden ingezet voor een breed gamma aan toepassingen die mogelijk diepgaand inzicht opleveren in zeer complexe systemen. De technologieën die dit

soort sensornetwerken mogelijk maken moeten hiervoor wel een aantal uitdagingen overwinnen. Om hun volledige potentieel waar te maken is het van cruciaal belang dat de gedistribueerde sensoren (1) betrouwbare communicatie over lange afstand mogelijk maken en (2) zeer weinig energie verbruiken. Daarom worden deze soort sensornetwerken ook wel aangeduid als *low-power wide-area networks* (LPWAN's). Het lage stroomverbruik zorgt ervoor dat een netwerknode in staat is om gedurende lange tijd autonoom te blijven werken. Vandaag de dag kunnen nodes dit jaren aan een stuk zonder enige vorm van onderhoud.

Om ervoor te zorgen dat deze netwerknodes voldoende draadloze prestaties bieden en toch in hoge mate autonoom blijven, bestaan er een aantal strategieën. Deze hebben in de eerste plaats te maken met de werkfrequentie van het sensornetwerk en de specifiek toegepaste communicatietechnologie die over het algemeen een compromis moet maken tussen vermogenverbruik, communicatiebereik en datasnelheid. LPWAN's werken vaak in sub-GHz-frequentiebanden omdat lagere frequenties minder invloed ondervinden van golfdemping en in vergelijking met hogere frequenties betere gebouwpenetratie vertonen. In het sub-GHz-spectrum zijn de ISM-banden (industrial scientific and medical) het populairst omdat deze vrij kunnen worden gebruikt zolang de relevante vermogensvoorschriften en bedrijfscycli in acht worden genomen. Er bestaan verschillende technologieën die sub-GHz LPWAN-communicatie mogelijk maken. De populairste daarvan zijn LoRa en SigFox. Waar SigFox-radio's weliswaar iets minder stroom verbruiken dan LoRa-radio's biedt LoRa-technologie wel hogere datasnelheden aan. Er zijn nog een aantal andere verschillen tussen beide. LoRa-radio's maken bijvoorbeeld gebruik van een implementatie van *chirp spread spectrum* (CSS) modulatie, terwijl SigFox gebruik maakt van (varianties van) *binary phase shift keying* (BPSK). Dit proefschrift richt zich vooral op de fysieke laag van LoRa-netwerken omdat deze technologie gebaseerd is op een open standaard. Dat houdt in dat gebruikers verbindingen kunnen opzetten zonder een abonnement nodig te hebben, iets wat voor SigFox doorgaans niet het geval is.

Het doel van dit proefschrift is tweeledig: het evalueren van de prestaties van de LoRa modulatietechniek in verschillende omgevingen, en op basis van de hieruit verkregen inzichten, het verbeteren van deze prestaties door het toepassen van een verscheidenheid aan innovatieve communicatiemethodes. Dit wordt uitgevoerd in drie verschillende toepassingsomgevingen. Eerst worden conventionele draadloze sensornetwerken beschouwd. Deze zijn opgebouwd uit wijd verspreide knooppunten met een laag energieverbruik. Vervolgens wordt LoRa-modulatie gebruikt voor draadloze communicatie in de buurt van het menselijk lichaam. Ten slotte wordt *software defined radio* (SDR) technologie gebruikt om de prestaties van LoRa-ontvangers te verbeteren en de impact van Doppler-verschuivingen op LoRa-modulatie te beoordelen. Hieronder wordt de inhoud van elk hoofdstuk in dit proefschrift geschetst en worden relevante conclusies samengevat.

Om de prestaties van LoRa in langeafstandssensornetwerken te analyseren werd kanaalkarakteriseringshardware ontwikkeld met een groter dynamisch bereik voor het uitvoeren van signaal-ruisverhoudingsmetingen (SNR). Dergelijke hardware werd in de literatuur nog niet gepresenteerd en biedt dankzij haar grote dynamisch bereik unieke kansen om de performantie van LoRa in een verscheidenheid aan toepassingen in kaart te brengen. Het ontwerp en de kalibratie van deze hardware wordt gepresenteerd in Hoofdstuk 2 van dit werk. Dit hoofdstuk bevat ook een aantal verificatiemetingen die zowel binnenin gebouwen als daarbuiten werden uitgevoerd. In beide meetcampagnes werden unieke verbindingskarakteristieken waargenomen. Meer specifiek werd in de binnencampagne degradatie van de verbindingen waargenomen wanneer mensen aanwezig waren in het gebouw waarin de draadloze verbindingen waren opgesteld. In de buitenopstelling werden verminderde antenneprestaties waargenomen die het transmissiebudget aanzienlijk verminderden na perioden van regenval. De hardware die in Hoofdstuk 2 wordt voorgesteld werd ook ingezet in een onderzoeksgericht sensornetwerk in en rond de stad Gent (België). Dit netwerk bestaat uit meerdere langeafstandsverbindingen in voorstedelijke omgevingen en een aantal kortere verbindingen in een meer stedelijke setting. Door de prestaties van de verbindingen in dit netwerk gedurende meer dan een jaar op te volgen is een grondige analyse van de netwerkperformantie mogelijk. Deze analyse is opgenomen in Hoofdstuk 3 van dit proefschrift. Door de bekomen resultaten te vergelijken met seizoensgebonden weersveranderingen wordt een significante correlatie tussen de intensiteit van beide waargenomen. Hoofdstuk 3 bevat ook een bespreking van de mechanismen die dit verband kunnen veroorzaken.

Het tweede deel van dit proefschrift omvat onderzoek naar de prestaties van draadloze LoRa-netwerken in en rond het menselijk lichaam. Hoofdstuk 4 beschrijft de ontwikkeling van draagbare LoRa-nodes, gebaseerd op de hardware die in Hoofdstuk 2 is beschreven. Deze zijn voorzien van op maat gemaakte textielantennes op basis van substraat-gentegreerde golfgeleidertechnologie (SIW), en bevatten ook kleine batterijen om volledig draadloze werking mogelijk te maken. Een geïntegreerde oplossing als deze is in de literatuur uniek. In Hoofdstuk 4 worden ook de stralingseigenschappen van de draagbare nodes geanalyseerd en vergeleken met die van de antennes zelf. Verder wordt er ook een bereikstest gedocumenteerd. Deze test demonstreert een communicatiebereik van enkele honderden meters wanneer deze nodes op het lichaam van twee testpersonen gedragen worden. In Hoofdstuk 5 worden de prestaties van deze zogenaamde *body-to-body* verbindingen in een moderne kantooromgeving geanalyseerd. De invloed van zware betonnen structuren op de kwaliteit van de draadloze verbindingen wordt in kaart gebracht. Tevens worden de schaduweffecten van het menselijk lichaam geanalyseerd. Tenslotte wordt de verbindingskwaliteit beoordeeld in een betonnen trappenhall. In de hoofdstukken 6 en 7 wordt de communicatie tussen één of meerdere op het lichaam gedragen nodes en een basisstation gekarakteriseerd. Meer specifiek worden in Hoofdstuk 6 richtlijnen gegeven voor het dynamisch optimaliseren van de LoRa spreidingsfactor, om zowel de dekkingsgraad als de da-

tasnelheid in deze soort verbindingen te maximaliseren. Hoofdstuk 7 toont aan hoe de kwaliteit van de verbinding aanzienlijk kan worden verbeterd door het toepassen van diversiteit. Door de ontvangen vermogensniveaus en pakketontvangstratio's (PRR's) voor een enkele ontvanger te vergelijken met die van een zogenaamde *selection combiner* en een theoretische *maximum ratio combiner*, worden SNR-prestatieverbeteringen tot 5.5 dB gedemonstreerd. Bovendien wordt in dit hoofdstuk de invloed van Doppler-spreiding op de draadloze verbinding beoordeeld door de meetcampagne te herhalen bij hogere snelheden met behulp van een gemotoriseerd longboard. Hierbij werden echter geen significante prestatieverschillen waargenomen, wat lijkt te bevestigen dat LoRa-modulatie inderdaad goed bestand is tegen Doppler-effecten en meerpadspropagatie.

In Hoofdstuk 8 wordt een nieuw LoRa-ontvangsalgoritme gepresenteerd dat aanzienlijke prestatieverbeteringen optekent ten opzichte van de huidige commerciële LoRa-radios. Dit wordt bereikt door een aantal geavanceerde verwerkingsstappen toe te passen in elk van de fases uitgevoerd voor het ontvangen van LoRa-pakketten. Meerdere algoritmevarianten worden vergeleken op basis van hun rekenkost en hun prestaties op vlak van bitfouten. Bij de implementatie van deze algoritmevarianten op een SDR-platform wordt een gemiddelde prestatieverhoging van 4.7 dB in SNR waargenomen ten opzichte van de meest gebruikte LoRa-radio, de Semtech SX1276. De invloed van Doppler-verschuivingen op LoRa-modulatie wordt in Hoofdstuk 9 opnieuw bekeken. Meer specifiek worden met behulp van de LoRa-implementatie uit het vorige hoofdstuk statische en dynamische Doppler-verschuivingen gesimuleerd en wordt de invloed van deze verschuivingen op de prestaties van de symbooldetector bepaald. Hoofdstuk 9 bevestigt dat Doppler-effecten voor de meeste LoRa-gerelateerde toepassingen zeer weinig invloed zullen hebben op de kwaliteit van de verbinding. In extremere omgevingen, zoals bij satelliet-communicatie in een lage baan rond de Aarde (LEO), kunnen de verbindingprestaties wel worden beïnvloed door Doppler-verschuivingen, vooral wanneer hogere spreidingsfactoren gebruikt worden.

In dit proefschrift wordt bevestigd dat LoRa-modulatie een zeer robuuste technologie is voor goedkope langeafstandssensornetwerken. Er wordt echter ook aangetoond dat de prestaties aanzienlijk kunnen worden verbeterd door geavanceerde communicatiemethoden en -technieken toe te passen. Toekomstig werk kan voortbouwen op de innovaties die in dit proefschrift worden gepresenteerd om de prestaties van de fysieke laag van de LoRa modulatietechniek verder te verbeteren. Daarnaast kunnen de inzichten die in dit werk werden vergaard ook gebruikt worden om alternatieve CSS-oplossingen te ontwikkelen voor laag-vermogen langeafstandssensornetwerkcommunicatie. Deze oplossingen kunnen leiden tot verschillende compromissen tussen energieverbruik en linkprestaties.

Summary

It is safe to say that communication is one of the pillars of civilization. Whether it is employed for sharing information on a nest of particularly fierce wolves or for teaching you how to bake that perfect moelleux, communication remains key in the survival and prosperity of our species. Consider the impact of communication technology breakthroughs on our society. Across all of human history, advances in these technologies have truly enabled revolutions. The invention of writing enabled ancient civilizations to carry over their wisdom and insight to later generations. The printing press is widely acknowledged to have ended the Dark Ages. And, as anyone who has witnessed its birth can confirm, the internet has changed our world for good. One might wonder why being able to access so much information in the blink of an eye is so important. Some might even say that it is preposterously unnecessary. However, consider how many decisions are made every day. In all situations, good decisions depend on access to the right information. Hence, it is very beneficial to gather and share information as widely as possible. In this exchange, technology is instrumental. Whereas many scientific discoveries have been fundamental to our success, it is clear that most of the recent advancements in communication technology have been enabled by innovations in the field of electronics. In fact, as electronic circuits become smaller and more efficient, new opportunities endlessly keep presenting themselves. In recent years, this has enabled us to connect more and more devices to the internet, thereby creating the Internet of Things (IoT).

A lot of these “things” contain sensors which can monitor environmental parameters such as temperature, humidity, pressure and luminescence. Other sensors may gather system state information such as acceleration data or metrics on power consumption. Still others may focus on gathering biomedical information such as the heart rate or blood pressure of a person. In fact, the capabilities of sensors have long surpassed those of humans. Connecting these sensors to the internet enables us to share the information that they gather on an unprecedented scale. By distributing interconnected wireless sensors over large areas, long-range wireless sensor networks (WSNs) are created. These can be deployed for an almost infinite range of applications, potentially yielding deep insight into very complex systems. However, the technologies that enable these types of sensor networks need to overcome a number of challenges. In order for them to reach their full potential, it is key that the distributed sensor nodes (1) facilitate long distance communication while (2) consuming very little power. Hence, these types of WSNs are also labeled as low-power wide-area networks (LPWANs). Low power consumption ensures that a node is able to remain autonomous for long stretches of time. In current WSNs, nodes may operate for multiple years on end without maintenance.

In order for these nodes to achieve sufficient wireless performance while remaining highly autonomous, a number of strategies exist. These are primarily related to the operating frequency employed by the WSN and the applied communication technology, which generally features a trade-off between power consumption and data rate. LPWANs often operate in sub-GHz frequency bands as lower frequencies are less impacted by wave attenuation and exhibit better building penetration behaviour when compared to higher frequencies. In the sub-GHz spectrum, industrial scientific and medical (ISM) bands are the most popular as these can be used freely, as long as the relevant power regulations and duty cycles are obeyed. Several technologies exist that facilitate sub-GHz LPWAN communication. The most popular of these are LoRa and SigFox. While SigFox radios do consume a little less power than LoRa radios, LoRa technology offers higher data rates. A number of additional differences exist. For example, LoRa radios employ an implementation of chirp spread spectrum (CSS) modulation, while SigFox uses (variations of) binary phase shift keying (BPSK). This dissertation focuses on the physical layer of LoRa networks as this technology is based on an open standard, which allows users to set up links without needing a subscription.

The goal of this dissertation is two-fold: to assess the performance of LoRa modulation in different environments, and based on the insights gained from this, to enhance this performance by applying a variety of innovative communication methods. This is performed in three types of application environments. First, conventional wireless sensor networks are considered, with low-power nodes being distributed across a large area. Next, LoRa modulation is employed for body-centric wireless communication. And finally, software defined radio (SDR) technology is employed to enhance the capabilities of LoRa receivers and assess the impact of Doppler shifts on LoRa modulation. Below, the contents of each chapter in this dissertation are outlined and relevant conclusions are summarized.

To analyze the performance of LoRa in long-range WSNs, custom channel characterization hardware was developed with an extended dynamic range for performing signal-to-noise ratio (SNR) measurements. Such hardware has not been presented before and yields unique opportunities for assessing the performance of LoRa in a multitude of applications environments. The design and calibration of this hardware is presented in Chapter 2 of this work. This chapter also features indoor and outdoor hardware verification measurements. In both measurement campaigns, unique link characteristics were observed. More specifically, in the indoor campaign, link deteriorations were observed when people were present inside the building where the links were deployed. In the outdoor setup, reduced antenna performance was seen to significantly reduce the link budget after episodes of rainfall. The hardware presented in Chapter 2 was also deployed in a research-oriented sensor network in and around the city of Ghent, Belgium. This network features multiple long-distance links in suburban environments and a number of shorter links in a more urban setting. The measurements gathered from this network by monitoring link performance for over one year are analyzed thoroughly in Chapter 3. By comparing these results to seasonal weather variations, significant

correlation between the intensity of both is observed. Chapter 3 also features a discussion of the mechanisms that may cause this relation.

The second part of this dissertation presents research on the performance of LoRa in body-centric wireless networks. Chapter 4 presents the development of wearable LoRa nodes, based on the hardware presented in Chapter 2. These feature custom textile substrate-integrated-waveguide (SIW) antennas and low-profile batteries to enable fully wireless operation. In literature, an integrated solution such as this one is unique. In Chapter 4, the radiation characteristics of these wearable nodes are analyzed and compared to those of the standalone antennas. Additionally, an outdoor range test is documented, demonstrating a body-to-body communication range of several hundreds of meters. Chapter 5 presents body-to-body link performance in a modern office environment. The impact of heavy concrete structures on the quality of the wireless links is analyzed and body shadowing effects are considered. Finally, link performance is assessed inside a concrete stairwell. In Chapters 6 and 7, body-to-base-station communication is analyzed. More specifically, Chapter 6 presents guidelines on performing dynamic spreading factor optimization to maximize both coverage and data rate in these types of LoRa links. Chapter 7 demonstrates how link quality can be improved significantly by applying receiver diversity. By comparing the received power levels and packet reception ratios (PRRs) observed for a single receiver to the results obtained from a selection combiner and a theoretical maximum ratio combiner, SNR performance improvements up to 5.5 dB are demonstrated. Additionally, in this chapter, the impact of Doppler spread on the wireless link is assessed by repeating the measurement campaign at much higher speeds with a motorized longboard. However, no significant performance differences are observed, which confirms that LoRa modulation is indeed reasonably resistant to Doppler and multipath effects.

Chapter 8 presents a novel LoRa receive algorithm, which shows significant performance improvements in comparison to current commercial LoRa transceivers. This is achieved by applying a number of advanced processing steps in each of the stages conducted for receiving LoRa packets. Multiple algorithm variations are compared based on bit error rate (BER) performance and computational cost. When implementing these algorithm variations on SDR, an average SNR performance increase of 4.7 dB is observed with respect to the most commonly used LoRa radio, the Semtech SX1276. The impact of Doppler shifts on LoRa modulation are revisited in Chapter 9. More specifically, by employing the LoRa implementation from the previous chapter, static and dynamic Doppler shifts are simulated and the impact of these shifts on the performance of the symbol detector and on simulated receivers are determined. Chapter 9 generally confirms that for most LoRa applications, Doppler effects are expected to have very little impact on link quality. However, in more demanding environments, such as low Earth orbit (LEO) satellite-to-body communication, link performance is expected to be impacted by Doppler shifts, especially when using higher spreading factors.

In this dissertation, LoRa modulation is shown to be a very robust technology for low-cost long-range WSN deployments. However, it is also demonstrated that its

performance can be enhanced significantly by applying advanced communication methods and techniques. Potential future work may elaborate on the innovations presented in this dissertation to further improve LoRa physical-layer performance or employ the insights gathered in this work to construct alternative CSS solutions for low-power long-range sensor network communication which may result in different trade-offs between power consumption and link performance.

List of Abbreviations

5G	Fifth generation of mobile communication technologies
ADC	Analog-to-digital converter
AS-CO	Advanced Synchronization with Computed Optimum
AS-EO	Advanced Synchronization with Estimated Optimum
ATT	Attenuation
AWGN	Additive white Gaussian noise
BCWN	Body-centric wireless network
BER	Bit error rate
BPSK	Binary phase shift keying
BW	Bandwidth
CDF	Cumulative density function
CFO	Carrier frequency offset
CR	Code rate
CRC	Cyclic redundancy check
CSI	Channel state information
CSS	Chirp spread spectrum
DAB	Digital audio broadcasting
DAC	Digital-to-analog converter
DBPSK	Differential BPSK
DFT	Discrete Fourier transform
DS	Direct Synchronization
DSSS	Direct-sequence spread spectrum
DSP	Digital signal processor
DUT	Device under test
EIRP	Effective isotropic radiated power
EPS	Expanded polystyrene
ETSI	European Telecommunications Standard Institute
F/B	Front-to-back
FEC	Forward error correction
FFC	Flat flexible cable
FFT	Fast Fourier transfer
FM	Frequency modulation
FPC	Flat printed circuit cable
FPGA	Field-programmable gate array
FSK	Frequency shift keying
GFSK	Gaussian FSK
I	In-phase
I/O	Input/output
I ² C	Inter-Integrated Circuit

IC	Integrated circuit
IF	Intermediate frequency
IMU	Inertial measurement unit
IoT	Internet of Things
ISM	Industrial, scientific and medical
LEO	Low-Earth orbit
LiPo	Lithium polymer
LNA	Low-noise amplifier
LO	Local oscillator
LoS	Line-of-sight
LPC	Lost packet counter
LPWAN	Low-power wide-area network
LTE-M	Long Term Evolution-Machine Type Communication
MIMO	Multiple-input multiple-output
MRC	Maximum ratio combiner/combining
MSD	Mode of Successive Detection
NB-IoT	Narrowband-IoT
NLoS	Non-line-of-sight
OFDM	Orthogonal frequency division multiplexing
PCB	Printed circuit board
PL	Path loss
PRR	Packet reception ratio
PVC	Polyvinyl chloride
Q	Quadrature
QLoS	Quasi-line-of-sight
QoS	Quality of service
R&S	Rohde & Schwartz
RF	Radio frequency
RTC	Real-time clock
RX	Receiver
SC	Selection combiner/combining
SDR	Software defined radio
SER	Symbol error rate
SF	Spreading factor
SFD	Start-of-frame delimiter
SIMO	Single-input multiple-output
SIR	Signal-to-interference ratio
SISO	Single-input single-output
SIW	Substrate-integrated-waveguide
SMA	SubMiniature version A
SMBus	System Management Bus
SNR	Signal-to-noise ratio
SPI	Serial Peripheral Interface
SWD	Sync word
TEMP	Ambient temperature

TR	Technical report
TX	Transmitter
UART	Universal Asynchronous Receiver-Transmitter
VDD	Positive supply voltage
VGA	Variable gain amplifier
WSN	Wireless sensor network

List of Symbols

α	Slope of a chirp
$\Delta\alpha$	Slope offset
$\Delta\alpha_{\max}$	Maximum slope offset
a	Symbol value
\tilde{a}	Detected symbol
Δa	Relative acceleration
A	Attenuation
\mathbf{A}	Matrix A
$A_{\delta\tilde{n},\delta\tilde{f}}$	Element in \mathbf{A}
B	Frequency swing
c	Speed of light
d	Distance
d_0	Reference distance (usually 1 m)
ϵ_f	Frequency error
ϵ_n	Timing error
ϵ_r	Relative permittivity
\mathbf{F}	Symbol strength
E_s	Symbol energy
f	Instantaneous frequency
$\delta\tilde{f}$	Very small frequency offset
Δf	Exact frequency offset
$\tilde{\Delta f}$	Estimate for the frequency offset
Δf_{\max}	Maximum frequency offset
\mathcal{F}	Discrete Fourier transform
F	Operating frequency
F_a	Variable frequency term related to the symbol value a
\mathcal{H}	Custom operator (see Chapter 8)
H	Filter window
j	Imaginary unit
k	Delay step
K	Oversampling factor
L	Path loss (in Part II)
L	Total amount of symbols (in Part III)
$L_{=}$	Amount of equal symbols
μ	Mean value
$\bar{\mu}$	Average of multiple mean values
m	DFT bin number
M	Size of the symbol alphabet

n	Refractive index (in Introduction)
n	Path loss exponent (in Part II)
n	Sample index (in Part III)
n_1	First sample of the packet
\tilde{n}_1	Estimate for n_1
η_1	Actual start of the packet (in samples)
$\delta\tilde{n}$	Very small timing offset
Δn	Time shift (in samples)
$\Delta\tilde{n}$	Timing correction term
N	Refractivity index (in Introduction)
N	Symbol length (in samples) (in Part III)
ϕ	Instantaneous phase
P	Power
\bar{P}	Average power
P_x	Power at receiver x
q	Delay step / trial detection
\tilde{q}	Delay step that provoked signal presence detection
r	Received symbol / signal
r_1	Radius of the first Fresnel zone
σ	Standard deviation
$\bar{\sigma}$	Average of multiple standard deviations
s	LoRa signal
\bar{s}	Down-chirp
s_{up}	Up-chirp
s_{down}	Down-chirp
S	Signal-to-noise ratio
τ	Integration variable for time
τ_a	Time instant of the LoRa symbol frequency reset
t	Time
t_1	Packet starting time
T_s	Symbol duration
v_{RX}	Speed of the receiver
Δv	Relative velocity
W	Weather parameter
X_m	DFT output bins

List of Publications

Articles in international journals

- T. Ameloot, P. Van Torre, and H. Rogier, “A Compact Low-Power LoRa IoT Sensor Node with Extended Dynamic Range for Channel Measurements”, *MDPI Sensors*, vol. 18, no. 7, p. 2137, 2018.
- T. Ameloot, P. Van Torre, and H. Rogier, “Variable Link Performance Due to Weather Effects in a Long-Range, Low-Power LoRa Sensor Network”, *MDPI Sensors*, vol. 21, no. 9, 2021.
- T. Ameloot, P. Van Torre, and H. Rogier, “LoRa Base-Station-to-Body Communication With SIMO Front-to-Back Diversity”, *IEEE Transactions on Antennas and Propagation*, vol. 69, no. 1, pp. 397–405, 2021.
- T. Ameloot, H. Rogier, M. Moeneclaey, and P. Van Torre, “LoRa Signal Synchronization and Detection at Extremely Low Signal-to-Noise Ratios”, *submitted to IEEE Internet of Things Journal*, 2021.
- T. Ameloot, M. Moeneclaey, P. Van Torre, and H. Rogier, “Characterizing the Impact of Doppler Effects on Body-Centric LoRa Links with SDR”, *accepted by MDPI Sensors*, 2021.

Articles in conference proceedings

- T. Ameloot, P. Van Torre, and H. Rogier, “LoRa Indoor Performance: an Office Environment Case Study”, in *2018 International Applied Computational Electromagnetics Society Symposium - China (ACES)*, Beijing, China, 2018.
- T. Ameloot, P. Van Torre, and H. Rogier, “Periodic LoRa Signal Fluctuations in Urban and Suburban Environments”, in *2019 13th European Conference on Antennas and Propagation (EuCAP)*, Krakow, Poland, 2019.
- P. Van Torre, T. Ameloot, and H. Rogier, “Wearable 868 MHz LoRa Wireless Sensor Node on a Substrate-Integrated-Waveguide Antenna Platform”, in *2019 49th European Microwave Week (EUMW)*, Paris, France, 2019

- P. Van Torre, T. Ameloot, and H. Rogier, “Long-Range Body-to-Body LoRa Link at 868 MHz”, in *Proceedings of the 13th European Conference on Antennas and Propagation (EuCAP)*, Krakow; Poland, 2019.
- T. Ameloot, P. Van Torre, and H. Rogier, “Indoor Body-to-Body LoRa Link Characterization”, in *2019 9th IEEE-APS Topical Conference on Antennas and Propagation in Wireless Communications*, Granada, Spain, 2019.
- T. Ameloot, P. Van Torre, and H. Rogier, “Experimental Parameter Optimization for Adaptive LoRa Modulation in Body-Centric Applications”, in *2020 14th European Conference on Antennas and Propagation (EuCAP)*, Copenhagen, Denmark, 2020.
- T. Ameloot, P. Van Torre, and H. Rogier, “Body-Centric LoRa Networks Based on System-Integrated Textile SIW Antennas”, in *2020 XXXIIIrd General Assembly and Scientific Symposium of the International Union of Radio Science*, Rome, Italy, 2020.

**TECHNIQUES FOR CHARACTERIZING AND ENHANCING
THE PERFORMANCE OF LONG-RANGE WIRELESS SENSOR
NETWORKS**

1

Introduction

1.1 Context

Many brilliant minds might say that the key to success is a combination of forming the right strategies, learning, thinking critically, being creative... However, all of these are unconditionally dependent on gathering information from the environment through observation, sensing, listening. One could even say that every technological achievement in the history of our species has relied on sensing the world around us and using the gathered information to make informed choices on how to manipulate that environment to our advantage. Therefore, it should not be a surprise that we have developed a myriad of technologies to gather and share this information. From the spoken word, to the written one, the printed text to the messenger, the telegraph to the internet, more and more information can today be shared over wider and wider distances. Recently, this evolution has culminated in the creation of the Internet of Things (IoT), which encompasses a vast collection of networks that facilitate information sharing between machines, devices and wearables on an unprecedented scale.

The IoT has emerged from the cross-pollination between various branches of modern technology. At the heart of this widespread connectivity concept are a multitude of innovations in embedded systems and communication technologies. Examples include the miniaturization of integrated circuits (ICs), the design of highly specialized antennas and recent advances in data modulation techniques. These have enabled the construction of wireless networks consisting of compact, low-power nodes, which often feature one or more sensors that gather information about the environment. When distributed over large areas, these nodes form a wireless sensor network (WSN). In this type of network, the information gathered by each node is shared wirelessly across the nodes. When combined, these data can yield highly valuable insight into systems that used to be too complex for compre-

hension. WSNs are used for a myriad of applications. In the natural environment, sensors may be distributed to measure water levels, detect forest fires or monitor air quality. In industry, they may be used to monitor complex processes, oversee vehicle traffic or assess storage occupancy. Even in our personal lives, wireless sensors can measure anything from our living room temperature to our heartbeat. From the bottom of the ocean to the surface of another planet, wireless sensor networks have the power to gather and share information on a truly exceptional level.

As the title of this work suggests, this dissertation presents research on how to characterize and improve the performance of long-range wireless sensor networks. Advanced engineering methods are employed to achieve valuable insight into the capabilities of WSN technologies and a number of state-of-the-art techniques are applied to improve link performance achieved in modern WSN deployments. A specific application environment that is extensively featured in this dissertation is the one of body-centric communication. This type of communication takes place in networks deployed in and around the human body. It is a serious testament to the advancements made by modern-day electronics that this concept is actually feasible. In fact, if time travel were possible, one would not need to journey far back to encounter someone who would be fully in awe of the concept of a wearable. Yet, today, heart rate monitors, fitness trackers and smartwatches are simply part of modern life. However, body-centric wireless networks (BCWNs) hold much more promise than just tracking sports activities and notifying people of their next calendar appointment. When integrated in the garments of rescue workers, they can be a lifeline in challenging environments and when employed in healthcare applications, they can wirelessly communicate a wealth of vital biometric data to support a better life for the elderly or chronically ill patients.

1.2 Challenges

Wireless sensor networks unquestionably provide immense opportunities for an innumerable amount of use cases. However, there are a number of engineering challenges that need to be overcome in order to successfully set up a WSN. Sensor networks tend to be deployed over large areas. In nearly all of the examples presented above, the wireless links span distances from hundreds of meters to several kilometers. In order to cover these distances, sufficient link budget is needed. The available link budget can be increased by applying one or several of the following strategies:

- Boosting the transmit power.
- Employing more directive antennas.
- Using lower operating frequencies.
- Increasing the sensitivity and noise tolerance of the receiver.

However, each of these solutions yield their own challenges. Naturally, boosting the transmit power increases the power consumption of each network node. This is problematic as WSNs usually feature a large number of distributed nodes, which are required to operate autonomously for years on end. As these nodes are often powered by batteries, they tend to have a very low power budget. Hence, WSNs are often described as lower-power wide-area networks (LPWANs). Additionally, as determined by law, the effective isotropic radiated power (EIRP) must never exceed a certain maximum value specific to the application environment. The EIRP describes the amount of power a perfectly isotropic antenna would need to radiate to achieve the same field strength at a larger distance as caused in the main direction of a directive antenna.

Employing more directive antennas is a valid option when the positions of the nodes are known and stationary, and when the network assumes a star topology (as the gain of a directive antenna works for receiving as well as for transmitting). Yet, the base station in such a network is generally going to need an omnidirectional antenna. Furthermore, directive antennas must still obey EIRP regulations. Moreover, as the size of the wireless nodes is often an important design restriction, sub-optimal antennas are very regularly used.

Using lower operating frequencies reduces the attenuation caused by path loss in the wireless links. Additionally, lower frequencies exhibit more favorable propagation characteristics in challenging environments. For example, they show better building penetration behavior and diffract more easily around obstacles. As a result, in Europe, WSNs generally use one of three industrial, scientific and medical (ISM) bands below 1 GHz, located at 169 MHz, 434 MHz or 868 MHz. However, these sub-GHz frequency bands are shared between a lot of communicating devices. Hence, receivers have to deal with a lot of interference and noise. Moreover, due to the high occupancy of ISM-bands, severe duty cycle limitations are imposed by law, ranging from 0.1 % to 10 % depending on the specific sub-band [1]. This further reduces channel availability and greatly diminishes the data rate that can be achieved across the wireless links in these bands. Furthermore, for lower frequency bands, efficient antennas become increasingly larger, which may be a deal-breaker for certain applications.

The fourth and last option for increasing the available link budget is the most challenging, but also yields the most gain. The sensitivity and noise tolerance of receivers can be increased by employing high-performance radio frequency (RF) hardware or making use of one or more diversity techniques. However, this can also be achieved by applying more advanced data modulation techniques. For example, by encoding data and modulating the result, information can be spread out over time and across wider frequency ranges. This may alleviate temporary interference or frequency-selective fading, improving general noise tolerance. For example, when using LoRa modulation, a packet reception ratio (PRR) of 50 % can still be observed at a signal-to-noise ratio (SNR) of -22 dB, as shown in Chapter 8 of this dissertation. However, a lot of data rate is traded in to achieve this outstanding noise performance. Additionally, applying different modulation tech-

niques also reduces the compatibility between networks. In fact, a large number of standards are used in sub-GHz LPWANs, all of which are incompatible to each other. Hence, a unified IoT is only possible when adding additional data communication layers on top of these physical-layer standards. Yet, the incompatibility between WSNs is sometimes more of an advantage than a disadvantage, as certain sensor information may be sensitive. Additional encryption may be added to further increase network security and privacy.

In body-centric networks, communication is complicated further by channel variations caused by the movements of the person wearing the wireless node. Furthermore, more stringent constraints on the size and type of antennas that can be used in BCWNs yield additional engineering challenges.

Each of the challenges described above can be addressed by specialized methods and technologies. These solutions can be compared by rigorously determining their performance in specific application environments. In the next section, the current state-of-the-art in sub-GHz long-range sensor network technologies is presented. As this dissertation presents techniques for characterizing and enhancing the performance of specific technologies and solutions, literature on relevant concepts such as LoRa modulation, tropospheric propagation effects, body-centric wireless communication, diversity techniques and software defined radio (SDR) are also highlighted and elaborated upon in Section 1.3. In Section 1.4, an overview of the contributions to the state-of-the-art presented in this dissertation is provided. Finally, Section 1.5 provides a more detailed outline of this work.

1.3 State-of-the-Art

1.3.1 Current WSN Standards

As mentioned earlier, a number of standards exist that facilitate low-power, low data rate communication in wireless sensor networks. The most prominent of these are LoRa [2] and SigFox [3]. Other popular standards include Dash7 [4], Narrowband-IoT (NB-IoT) [5], Long Term Evolution-Machine Type Communication (LTE-M) [6], Ingenu [7], Wi-Fi HaLow [8] and different variations of Weightless [9]. Each of these standards provides a wide range of unique features, advantages and disadvantages. Furthermore, many of them offer different modes of operation, which significantly complicates comparative studies in the LPWAN technology landscape. Although a full in-depth comparison between all of the standards presented above is out of the scope of this text, a number of key attributes are compared below. More comprehensive comparisons and elaborations are presented in [10]–[18].

As mentioned earlier, sub-GHz frequencies offer superior propagation properties in comparison to higher frequency bands. Hence, technologies that use these frequencies are more interesting for long-range WSN applications due to the large areas that need to be covered. Most of the standards mentioned earlier support

operation in sub-GHz frequency bands. In fact, Ingenu is the only one that does not, as it is only available in the 2.45 GHz ISM-band. Yet, this standard is actively marketed to also reliably cover long distances. It should also be mentioned that some of the standards above (most notably NB-IoT and LTE-M) only operate in licensed frequency bands, which does come at a cost for the end user. The other standards usually operate in ISM-bands, with the exact frequencies depending on the specific location of the WSN deployment.

In terms of range, LoRa and SigFox have been shown to be the best performers, featuring link distances from 10 to 50 km in the average WSN deployment. Ingenu is estimated to reach distances up to 10 km [12]. Other standards allow ranges up to 5 km. However, these standards do often combine this range reduction with higher available data rates, revealing a trade-off between both.

LoRa supports bit rates between 293 bps and 50 kbps, depending on the modulation settings, with the lowest data rates corresponding to the longest communication ranges and the highest data rates corresponding to the shortest ranges. For SigFox, available data rates are noticeably lower, ranging from 10 to 1000 bps, again depending on the specific settings that are applied and the communication ranges that are desired. However, as one low-power wireless sensor node generally does not produce large amounts of data each day, the reduced data rate that is associated with these technologies is generally not problematic.

The current success of LoRa and SigFox most probably results from a combination of their excellent communication range, relatively low deployment cost and very low power usage. However, in addition, their early appearance on the LPWAN market has undeniably been very beneficial, having resulted in very high global adoption rates. Dash7, NB-IoT, LTE-M and Weightless feature different trade-offs in order to successfully compete with these industry forerunners. New standards such as Ingenu and Wi-Fi HaLow are technically promising. However, both are very young, so global adoption is still significantly lower.

Given their prevalence in industry, LoRa and SigFox are discussed in more detail. Though both standards achieve similar range performance in the same frequency band, SigFox actually only supports the 868 MHz and 900 MHz ISM-bands, whereas LoRa also features operation in the 434 MHz and 169 MHz ISM-bands. Hence, in theory, LoRa should overall support larger ranges. LoRa is based on chirp spread spectrum (CSS) modulation, whereas SigFox utilizes narrow-band binary phase shift keying (BPSK) and its differential version DBPSK [19]. In general, LoRa supports higher data rates than SigFox. However, SigFox radios do consume a little less power than LoRa radios. Another key difference between both is their accessibility. SigFox is generally only available on a subscription basis, whereas LoRa is presented as an open standard, which allows users to set up private networks on a free-to-air basis. However, it should be mentioned that despite being marketed as an open standard, no documentation is available on its encryption. Furthermore, LoRa radios are only produced by Semtech Inc., which holds the relevant patent. Additionally, though widely used to describe the full protocol stack, LoRa

actually only refers to the lower communication layers of the LoRaWAN standard. A variation on LoRaWAN, with the same LoRa physical layer, but a proprietary medium access (MAC) layer was developed by Link Labs, which goes by the name of Symphony Link [20]. Given its many advantages, LoRa modulation is employed in all of the research presented in this dissertation. Hence, next, a comprehensive overview on existing literature concerning this standard is provided.

1.3.2 The LoRa Standard

First developed by the French Cycleo SAS, LoRa technology is based on chirp spread spectrum modulation. In CSS, symbols are encoded in wideband frequency modulated pulses called chirps. Encoding symbols in this fashion results in spreading gain, which significantly increases the available link budget and noise tolerance of the receivers. CSS has previously been employed for sonar and radar applications in the maritime and aviation industries. In 2012, Cycleo was acquired by Semtech Inc. and in 2015, the LoRa Alliance was founded. In the same year, the first version of the corresponding networking protocol LoRaWAN was finalized [21]. Since then, LoRa technology has been adopted in a wide range of IoT applications. As a result, a lot of research has been conducted to characterize its performance for very diverse use cases. General overviews of LoRa modulation are presented in [22]–[29]. More in-depth, theoretical reviews that feature an analysis of the waveforms employed in LoRa communication are reported in [30]–[36]. A full description of LoRa waveforms and the frame structure employed for LoRa communication is omitted here, as it is presented in Chapter 8 of this thesis.

Owing to the widespread adoption of LoRa modulation in the field of wireless sensor networks, a lot of research is available that documents link performance in practical deployments. More specifically, measurement campaigns in long-range outdoor applications are presented in [37]–[43], whereas LoRa indoor performance has been documented in [44]–[47]. In general, most of the publications on LoRa demonstrate excellent performance. However, some do question its scalability [19], [24], [30], [48]. Hence, when too much nodes are present in the same area, performance is expected to degrade. Efforts that aim to improve link performance by selecting the appropriate transmission parameters for each link are documented in [49]–[51].

Although a significant number of publications document LoRa outdoor deployments, few of these feature long-term link performance analyses. However, a couple of studies do exist that assess the influence of temperature variations on LoRa technology [52], [53]. As this dissertation features long-term link characterization results from a practical LoRa deployment with multiple links over 10 km, it is interesting to provide an overview of propagation effects that may influence link performance in this type of long-range links. Such an overview is presented in the next subsection.

1.3.3 Long-Range Tropospheric Propagation Effects

In all wireless networks, the propagation environment has a large impact on the performance of the communication links. In WSNs, propagation mainly occurs through the troposphere. The term troposphere is used to describe the lowest part of the Earth's atmosphere, surrounding the planet from the ground up to 10 – 20 km above the terrain. In [54], the troposphere is more abstractly defined as “a natural layered air medium consisting of different gaseous, liquid, and crystal structures”. In this overview, a number of tropospheric propagation processes that could impact the performance of wireless links are described based on the structures and mechanisms by which they are caused.

Variations in path loss, shadowing and fading are generally caused by the wave phenomena of reflection, refraction, diffraction, scattering, interference, depolarization and Doppler spreading. In the troposphere, these wave phenomena can be associated to a wide range of propagation processes. Based on [54], the structures and mechanisms causing these processes are divided into the following groups:

- The presence of gas molecules and aerosols, and the influence of temperature and pressure on the gaseous structures they form.
- The temporary presence of hydrometeors or precipitation.
- Tropospheric turbulences, generated by irregular air movements of the wind randomly varying in speed and direction.
- Structures that are not considered to be part of the troposphere such as the Earth's surface and its geographical features as well as everything found on this surface (buildings, cars, vegetation...).

In the following, the most relevant processes are discussed for each of these effects. Illustrations of short and long term interference propagation mechanisms are shown in Figs. 1.2 and 1.3.

Gaseous Structures

The most important gases and aerosols found in the troposphere are oxygen, nitrogen and water vapor [55]. Influenced by both temperature and pressure, their presence can lead to propagation phenomena such as refraction, absorption and scattering.

The refraction process is caused by vertical variations in the troposphere's refractivity. The refractivity index N is related to the refractive index n through $N = (n - 1) \cdot 10^6$ [56]. The refractive index is given by $n = \sqrt{\epsilon_r}$, where ϵ_r denotes the relative permittivity of the medium. Refraction causes radio waves to curve slightly towards the ground in normal refractive conditions. However, this behaviour may change when atmospheric conditions cause the refractivity gradient

to change. This gradient is described by $\Delta N = dN/dh$, with h denoting the height in km. When this gradient is larger than 0, sub-refraction will occur. Conversely, when it is smaller than -79, super-refraction occurs. In the case of sub-refraction, radio waves curve away from the ground, effectively lowering the range of the link, whilst in the case of super-refraction, radio waves curve more towards the ground, increasing the range of the link. Moreover, when the refractivity gradient is smaller than -157, trapping or ducting can occur. In this case, the wave is curved so heavily towards the ground that it reflects back into the atmosphere [56]–[60]. An illustration of the different refractive conditions is shown in Fig. 1.1. Tropospheric ducting can strongly boost received signal levels and increase the communication range. However, this propagation mode is a short-term mechanism that only occurs for small percentages of time [59], [61], [62].

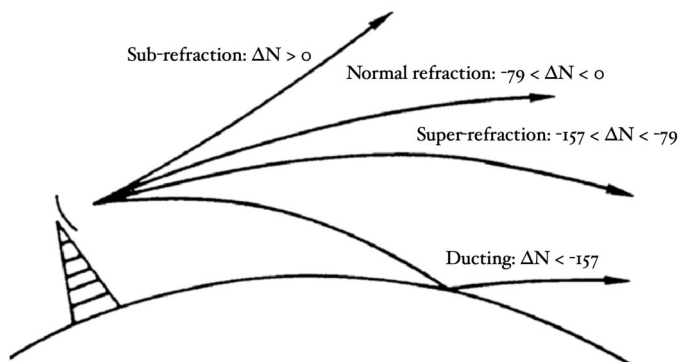


Figure 1.1: Illustration of different refractive conditions [63].

The absorption process, on the other hand, causes permanent wave attenuation which increases with the path length. Absorption can be calculated by considering the sum of the specific attenuation factors of oxygen and water vapour [57], [64]. Yet, for these particles, absorption only has a noticeable influence at frequencies above 10 GHz [64], [65]. Hence, it is not further discussed in this introduction.

Finally, scattering is the process in which energy is not absorbed, but redistributed into a wide range of different directions. Several models exist that describe this process based on the size of the scatterers. The most prevalent are Rayleigh scattering, Mie scattering and nonselective scattering [54], [66]–[68]. On a tropospheric scale, scattering can result in transhorizon propagation of radio waves when occurring in high-altitude pockets of air with a different refractivity than their surroundings [59].

Precipitation

The most common hydrometeors are rain, snow, clouds and fog. In [54], a lot of models are presented that model raindrop size distributions, rain occurrence,

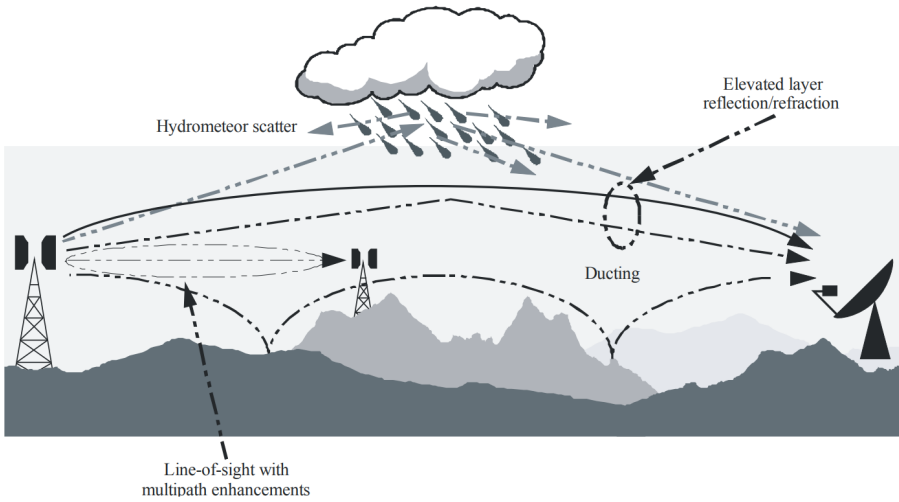


Figure 1.2: Illustration of short-term propagation mechanisms [69].

cloud occurrence and other comparable metrics. However, as the size of raindrops and water particles in clouds is very small with respect to the wavelength of sub-GHz frequencies, these can be seen as very small scatterers. Hence, they play little role in the attenuation of sub-GHz communication links. Again, these weather phenomena are described to start having an influence on wave attenuation from frequencies of 10 GHz and up [54], [70]. Additionally, hydrometeors can cause depolarization of radio waves, but as the measure of depolarization is strongly correlated with rain attenuation [71], this effect is also minimal. Based on this knowledge, precipitation seems to have little influence on propagation itself in sub-GHz networks. However, it should be mentioned that precipitation is closely related to air humidity, which does have an influence on the refractivity of air [56]. Consequently, high humidity levels (which may occur in combination with precipitation) may have a sizeable impact on the severity of the refractivity-based propagation effects discussed in the previous subsection.

Tropospheric Turbulences

Tropospheric turbulences, which are caused by spatial and temporal variations in air temperature, and wind speed and direction, are mainly responsible for two different processes: tropospheric scintillations and troposcatter.

Tropospheric scintillations occur when horizontal air layers of equal refractive indices become vertically mixed, leading to rapid variations in this refractive index over relatively small distances. This behaviour results in fast fading of the signal level received through the channel under consideration. In addition to being caused by changes in temperature and wind, tropospheric scintillations can also be caused by rain or other hydrometeors. In the first case, the scintillations are called dry, whilst in the latter case they are denoted as wet. The scintillation phenomenon is said to be strongly frequency-dependent, again being more severe for higher frequencies [54].

As was mentioned earlier, larger pockets of inhomogeneities in the refractive index of the atmosphere can cause troposcattering behaviour. In these volumes, small portions of the incoming waves are scattered back to the Earth. For wireless links spanning very large distances (often hundreds of kilometers), this troposcatter phenomenon is the only propagation mechanism that enables the reception of signals far past the radio horizon. In contrast to tropospheric ducting, the other mechanism that enables strong transhorizon propagation, troposcatter is present much more regularly. So much so that it is actually classified as a long-term interference mechanism [59], [61], [62].

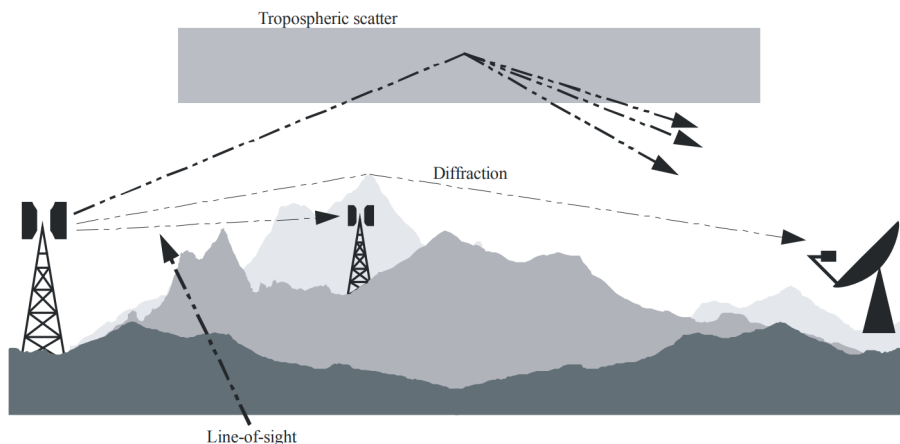


Figure 1.3: Illustration of long-term propagation mechanisms [69].

Ground Structures

Finally, there is one more propagation mechanism that can cause transhorizon propagation to occur, which is diffraction on the horizon itself. This mechanism is highly present in hilly and mountainous areas and enables wireless links to surpass large geographical features, be it at the cost of a large loss in signal level [72]. As these features are present all the time, this type of diffraction also qualifies as a long-term interference mechanism [59], [61], [62]. Shadowing by the Earth and

its geographical features are however not discussed more deeply here as it is less relevant to the specific content presented in this dissertation.

Naturally, diffraction also occurs on smaller objects and structures that obstruct the line of sight between transmitters and receivers in a communication link. Additionally, vegetation can have a significant influence on the attenuation of signals as well [73]. Eventually, all of these types of diffraction result in a fading process, the severity of which can change during occurrences of sub-refraction, super-refraction or tropospheric ducting. In these events, the ray path between the transmitting and receiving antennas may be bent in such a way that the obstacles mentioned in the above tend to block the signal even more, a phenomenon known as obstruction fading [74], [75].

Another important process in communication near ground structures is of course multipath interference caused by reflections of the waves on nearby objects and structures. Additionally, multipath can also occur in situations where direct path and atmospherically scattered signals interfere constructively and destructively in an alternating way [65].

1.3.4 Body-Centric Wireless Communication

As mentioned earlier, body-centric wireless communication is featured prominently in this dissertation. Body-centric links are employed to share data measured by sensors inside the body or gathered by electronics worn on the body. When all nodes are present in/around the same person, an on-body wireless network is formed. When wireless links connect to nodes worn by a different person, or to a base station, communication is labeled as off-body. A number of excellent overview papers have been published that provide insight in the state-of-the-art of body-centric communication [76]–[79].

Propagation in body-centric wireless links is influenced by many factors. Examples are the mobility of the user, the type of antennas employed and the overall type of propagation environment. A number of channel models have been proposed for body-centric channels in ISM-bands [80]–[82]. Deploying antennas on the human body yields a lot of challenges. For example, antenna performance is always impacted by the proximity of the wearer, as is demonstrated in [83]. Consequently, a lot of efforts have been made to develop special types of antennas for deployment in BCWNs. A large overview of wearable antennas for off-body sub-GHz links is presented in [84].

As is possible with every type of WSN, multiple network topologies can be adopted for BCWNs. As illustrated in Fig. 1.4, two variations of off-body link configurations are body-to-body and body-to-base-station links. Body-to-body links can be used to form mesh networks between moving nodes. This can be useful for several specific body-centric applications, for example those monitoring rescue workers presented in [85] and [86]. Body-to-base-station links are more likely to be found in networks with a star topology. In applications using such a topology, the base-

station will generally be used to monitor one or more separate mobile users. As shown in Fig. 1.4, a body-to-base-station link can also be used as an anchor link for one of the mesh network applications described earlier.

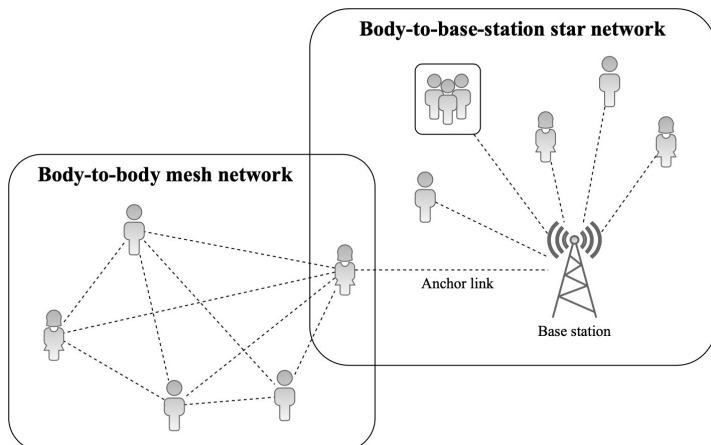


Figure 1.4: Example of a network featuring body-to-body and body-to-base-station links.

LoRa offers unique opportunities for body-centric communication, given its low power usage and excellent long-range performance. Research efforts on the application of LoRa in body-centric wireless communication are presented in [26], [87]–[91]. Additionally, assessments that determine the impact of rapid propagation channel variations on LoRa performance are also very interesting for body-centric LoRa applications. For example, as people move around in a multipath environment, Doppler spread is generated. A number of papers have been published that evaluate the impact of pure Doppler shifts on LoRa performance [17], [40], [43], [92], [93]. A possible method for improving link quality when the propagation channel is very unstable is applying diversity. A general overview of diversity techniques is presented in the next section.

1.3.5 Diversity Techniques

Diversity techniques can be employed to improve the quality and reliability of wireless communication links. When applying diversity, a single message is transmitted over two or more wireless channels with different characteristics. Upon reception, contributions from each of these channels are combined to increase the odds of successfully receiving the data. Various types of diversity exist. Time diversity, frequency diversity and spatial diversity are the most common. When employing time diversity, multiple versions of the signal are transmitted at different time instants or more time is used to send a given message. As a result, the impact of temporal channel variations can be overcome. Often, bit-interleaving and forward error correction (FEC) are applied to fully take advantage from the realized diversity gain.

Frequency diversity essentially uses multiple frequency channels or wider stretches of the frequency spectrum to transmit data. As a result, frequency-selective fading is mitigated. A lot of variations on frequency diversity exist. Examples are frequency hopping, orthogonal frequency division multiplexing (OFDM) and sub-carrier interleaving. In essence, spread spectrum modulation is also an example of frequency diversity. In fact, LoRa technically uses both time and frequency diversity to improve its reliability and noise tolerance.

For spatial diversity, multiple antennas or antenna modes are used. This is especially effective in multipath conditions, as sub-channels are increasingly uncorrelated. The most straightforward method of employing spatial diversity is varying the placement of the antennas or antenna elements. However, alternatives exist that combine various antenna characteristics such as radiation patterns, polarization characteristics and resonant modes. When spatial diversity is applied at the receiver side of the link, a single-input multiple-output (SIMO) wireless link is created. When it is also employed at the transmitter side, the system is described as multiple-input multiple-output (MIMO). Different strategies exist to combine the results from the antennas at the receiver. Notable examples are the selection combiner (SC), which selects the strongest signal, and the maximum-ratio combiner (MRC), which optimally combines the received signals.

Though also employed in previous wireless technology generations, spatial diversity is one of the cornerstones of the 5G network, where antenna arrays and beam-forming techniques are widely adopted. For off-body wireless communication, MIMO systems are presented in [94], [95]. A model for off-body communication in indoor environments specific to the 868 MHz band is presented in [96]. In body-centric LoRa applications, antenna diversity had not been applied prior to the publication of the research in Chapter 7 of this dissertation.

1.3.6 Software Defined Radio

A software defined radio (SDR) is a communication system that implements traditional radio components such as filters and (de)modulators in software instead of hardware. SDRs usually cover wide frequency ranges and facilitate very diverse applications. A block diagram of a common SDR architecture is shown in Fig. 1.5. This block diagram comprises three parts: the RF-section, the IF-section and a processing section. In the RF-section, the antenna is connected to an RF-switch which determines if the SDR is in transmit or receive mode. When the SDR is in receive mode, received signals are amplified by a low-noise amplifier (LNA) and filtered by an analog band-pass filter. Next, the resulting signal is mixed with a low frequency reference signal produced by a local oscillator (LO). The result from this step still contains the information modulated onto the carrier received by the antenna, but down-converted to a lower frequency range. It is called the intermediate frequency (IF) signal. Next, this IF signal is again filtered to prevent aliasing and amplified by a variable gain amplifier (VGA). The resulting signal is applied to an analog-to-digital converter (ADC), which samples the signal. The resulting

samples are digitally shifted to baseband and mixed with either a cosine or a sine to produce the respective I and Q signals. This is performed by a dedicated digital signal processor (DSP) or a field-programmable gate array (FPGA). The output of this receive architecture is a stream of complex samples that describes the discrete baseband signal. These complex samples can then be processed, either by the DSP, the FPGA or a computer. In software, an extensive amount of signal processing steps can be applied. Examples include packet detection, decoding, deinterleaving and many more.

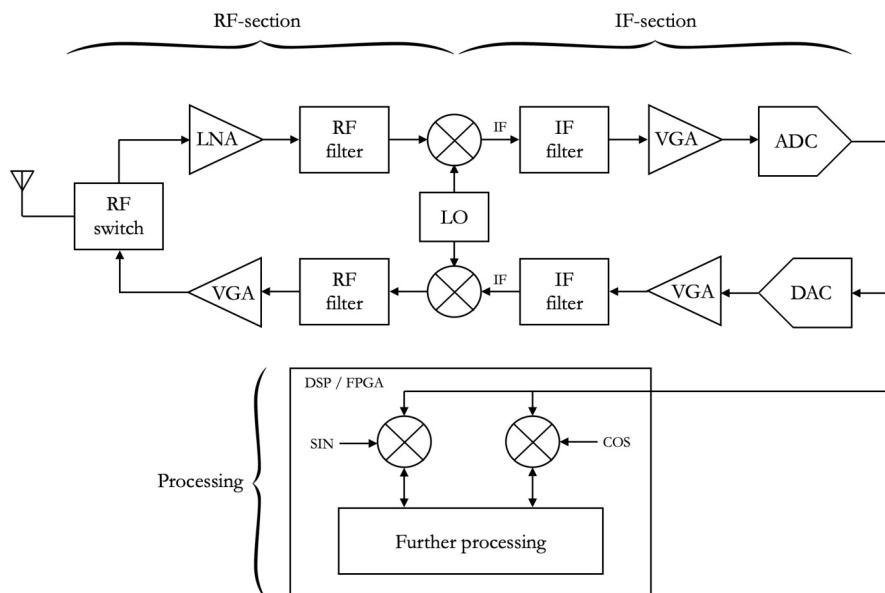


Figure 1.5: Simplified block diagram for an example SDR architecture.

When transmitting synthesized waveforms, a similar procedure is applied as for the receiver case, but in the opposite order. Data is interleaved, encoded, modulated... The resulting complex signals are divided into I and Q streams. These signals are mixed, shifted to IF and applied to a digital-to-analog converter (DAC). The synthesized waveform is amplified, filtered, mixed with an LO reference and filtered again. Finally, the signal is amplified by an RF amplifier and applied to the RF-switch connected to the antenna. Additional matching circuits may be present in the RF path.

SDRs come in various shapes and sizes. Lab-grade SDR equipment is produced by companies such as National Instruments. However, more affordable embedded SDR platforms also exist. Notable examples are HackRF One [97], RTL-SDR [98] and BladeRF [99]. In recent years, thanks to the immense performance improvements in IC technology, the capabilities of these relatively low-cost SDR platforms have increased significantly. Recently, several efforts have been made to implement

LoRa modulation on SDR platforms [33], [100]–[104]. This allows researchers to examine the capabilities of this modulation technique with much more precision and truly opens up the playing field for further innovation.

1.4 Own Contributions

This dissertation presents several contributions to LPWAN research using LoRa modulation. As specified earlier, the goal of this research is to characterize and enhance the performance of long-range WSN technologies. This is achieved in a few distinct ways.

First of all, this work documents the development of custom hardware platforms for LoRa channel characterization with extended dynamic range for channel measurements. This compact system is calibrated and tested extensively. It is also deployed in the field to monitor link performance over long stretches of time. This enables the comparison between link performance and seasonal weather conditions. This yields interesting design considerations for long-distance WSN links.

LoRa performance is also assessed in multiple body-centric wireless communication applications by integrating the aforementioned channel characterization hardware on a wearable platform, resulting in a system that reliably facilitates communication at distances up to 1.5 km. Although LoRa has previously been deployed in body-centric wireless links, this dissertation features a number of unique innovations. For example, the hardware presented here enables much finer spatial and temporal resolution for channel characterization in BCWNs. Furthermore, LoRa link characterization data are gathered to investigate design considerations for applying dynamic parameter optimization in a body-to-base-station context.

With respect to further enhancing the performance of WSN technologies, more innovations are presented. For example, this dissertation features the first research that applies receiver diversity in LoRa body-centric wireless links. When applying these methods, off-body LoRa coverage and reliability are improved significantly.

Another way of enhancing LoRa performance that is featured in this work is the application of SDR technology. Though a few SDR implementations of LoRa exist, a unique receive algorithm is presented here which features advanced signal presence detection, synchronization and symbol detection methods. When employing the most advanced version of this algorithm, SNR performance is improved by 4.5 dB in comparison to commercially available hardware. Finally, the impact of Doppler shifts on LoRa modulation is examined as well. This yields interesting results for WSN technologies, as a number of possible improvement strategies are also proposed.

1.5 Outline

This dissertation is divided in three parts, based on the different application environments featured in this work. In the first part, the physical-layer performance of LoRa networks is determined in different conventional WSN propagation environments. The second part presents a number of contributions to body-centric LoRa communication research, employing custom wearable LoRa nodes with system-integrated textile SIW antennas. In the third part of the dissertation, LoRa modulation and detection itself is considered through the application of SDR technology. Below, more details are provided on the contents of each chapter in these three parts.

Chapter 2 presents the development of the custom channel characterization hardware mentioned earlier. This hardware facilitates LoRa communication in both the 434 and 868 MHz ISM-bands. In order to enhance the performance of this system, RF attenuators are used in combination with a dynamic attenuation adjustment algorithm to extend the dynamic range for gathering SNR measurements. The result is a compact, low-power sensor node which is calibrated and tested exhaustively in both indoor and outdoor environments.

The hardware presented in Chapter 2 was deployed in a research-oriented sensor network. In this deployment, link quality is continuously monitored. By thoroughly analyzing link performance data gathered from this WSN and comparing these to meteorological observations, the impact of weather effects on the network's performance can be determined. The resulting received signal strength variations are presented and analyzed in Chapter 3.

Chapter 4 is similar to Chapter 2, as it also presents custom hardware, developed specifically for characterizing LoRa channels. In fact, in Chapter 4, the system presented in Chapter 2 is integrated onto a textile substrate-integrated-waveguide (SIW) antenna, designed for use in body-centric wireless applications. By also integrating a battery, the result is a fully autonomous wearable LoRa system. The radiation characteristics of this integrated node are compared to those of the standalone SIW antenna and body-to-body radiation patterns are presented for different test person orientations. Finally, the correct operation of this hardware is demonstrated by means of a range test.

In Chapter 5, the hardware presented in Chapter 4 is employed to perform a number of indoor body-to-body channel characterization measurement campaigns. In addition to determining the impact of body shadowing on the links, link performance is analyzed in a number of specific test person arrangements. The measurement campaigns are performed in a modern office building. Consequently, the influence of different link obstructions, such as the concrete core and floor structure of the building, is evaluated. Finally, signal strengths are monitored inside a stairwell to demonstrate how LoRa technology successfully facilitates wireless body-to-body communication in very challenging environments.

As mentioned earlier, long-range body-centric wireless communication is very challenging as channel quality is consistently impacted by an array of propagation effects. Therefore it is interesting to assess the impact of dynamically adapting LoRa modulation parameters to the actual link quality. This way, both the coverage of a LoRa base station and the data rate of the body-to-base-station wireless links can be optimized. An experimental assessment on the impact of adapting the LoRa spreading factor (SF) on link quality is presented in Chapter 6 of this thesis. Effective channel throughput is estimated based on practical measurements and guidelines are provided on how to apply dynamic parameter optimization in body-centric LoRa networks.

In Chapter 7, body-centric LoRa communication is improved further by applying receiver diversity in a body-to-base-station link configuration. By applying SIMO front-to-back diversity, it is shown that the performance impact of body shadowing and multipath on the wireless links can partly be counteracted. Additionally, the impact of Doppler spread on link performance is examined by comparing measurements gathered at different speeds along the same trajectory.

LoRa modulation and detection is approached more in depth in Chapter 8. This chapter presents a novel LoRa receive algorithm, which facilitates successful packet reception at extremely low signal-to-noise ratios. All steps of the receive algorithm are comprehensively described and advanced methods are employed to enhance signal presence detection, frame synchronization and symbol detection performance. The bit error rate (BER) performance and computational cost of different algorithm variations are examined and compared. These variations are also implemented on a real SDR platform. Finally, SNR performance is also compared to that of a commercial LoRa transceiver in a controlled environment.

In the penultimate chapter of this dissertation, the SDR implementation of LoRa developed for Chapter 8 is employed to determine the impact of Doppler shifts on the performance of LoRa symbol detectors and simulated receivers. Both static and dynamic Doppler shifts are considered and the implications of these effects for body-centric communication are evaluated. Chapter 9 also provides guidelines for mitigating the performance impact of both types of Doppler shifts.

All chapters in this dissertation feature separate introductions. Each introduction revisits the relevant context for the concepts presented in each corresponding chapter. Additionally, existing literature on these concepts is analyzed and referenced with more depth than provided in this general introduction. Naturally, each chapter is completed with its relevant conclusions. General conclusions with respect to the full range of contributions featured in this thesis are presented in the final chapter of this dissertation. Finally, Chapter 10 also discusses possible future work.

References

- [1] ETSI, *Short Range Devices (SRD) Operating in the Frequency Range 25 MHz to 1 000 MHz*, Sophia Antipolis, 2012.
- [2] LoRa Alliance, *LoRa*, <https://www.lora-alliance.org/>.
- [3] SigFox Foundation, *SigFox*, <https://www.sigfox.com/en>.
- [4] Dash7 Alliance, *Dash7*, <http://www.dash7-alliance.org/>.
- [5] GSM Association, *NarrowBand - Internet of Things (NB-IoT)*, <https://www.gsma.com/iot/narrow-band-internet-of-things-nb-iot/>.
- [6] —, *Long Term Evolution for Machines: LTE-M*, <https://www.gsma.com/iot/long-term-evolution-machine-type-communication-lte-mtc-cat-m1/>.
- [7] Ingenu Inc., *Ingenu*, <https://www.ingenu.com/>.
- [8] Wi-Fi Alliance, *Wi-Fi HaLow*, <https://www.wi-fi.org/discover-wi-fi/wi-fi-halow>.
- [9] C. Anton-Haro and M. Dohler, Eds., *Weightless Machine-to-Machine (M2M) wireless Technology using TV White Space: Developing a Standard*.
- [10] N. Baccour, A. Koubâa, L. Mottola, M. Zuniga, H. Youssef, C. Boano, and M. Alves, “Radio link quality estimation in wireless sensor networks: A survey”, English, *ACM Transactions on Sensor Networks*, vol. 8, no. 4, pp. 1–33, 2012.
- [11] K. Mikhaylov, N. Plevritakis, and J. Tervonen, “Performance Analysis and Comparison of Bluetooth Low Energy with IEEE 802.15.4 and SimpliCI”, *Journal of Sensor and Actuator Networks*, vol. 2, pp. 589–613, Sep. 2013.
- [12] C. Goursaud and J.-M. Gorce, “Dedicated networks for IoT: PHY / MAC state of the art and challenges”, *EAI Endorsed Transactions on Internet of Things*, vol. 1, p. 150 597, Oct. 2015.
- [13] G. Margelis, R. Piechocki, D. Kaleshi, and P. Thomas, “Low Throughput Networks for the IoT: Lessons Learned from Industrial Implementations”, in *2015 IEEE 2nd World Forum on Internet of Things (WF-IoT)*, 2015, pp. 181–186.
- [14] S. Kartakis, B. D. Choudhary, A. D. Gluhak, L. Lambrinos, and J. A. McCann, “Demystifying Low-Power Wide-Area Communications for City IoT Applications”, in *Proceedings of the Tenth ACM International Workshop on Wireless Network Testbeds, Experimental Evaluation, and Characterization*, ser. WiNTECH ’16, New York City, New York: Association for Computing Machinery, 2016, pp. 2–8.

- [15] M. Centenaro, L. Vangelista, A. Zanella, and M. Zorzi, “Long-Range Communications in Unlicensed Bands: the Rising Stars in the IoT and Smart City Scenarios”, *IEEE Wireless Communications*, vol. 23, no. 5, pp. 60–67, 2016.
- [16] U. Raza, P. Kulkarni, and M. Sooriyabandara, “Low Power Wide Area Networks: An Overview”, *IEEE Communications Surveys Tutorials*, vol. 19, no. 2, pp. 855–873, 2017.
- [17] U. Noreen, A. Bounceur, and L. Clavier, “A Study of LoRa Low Power and Wide Area Network Technology”, in *2017 International Conference on Advanced Technologies for Signal and Image Processing (ATSIP)*, 2017, pp. 1–6.
- [18] M. Barbiroli, F. Fuschini, G. Tartarini, and G. E. Corazza, “Smart Metering Wireless Networks at 169 MHz”, *IEEE Access*, vol. 5, pp. 8357–8368, 2017.
- [19] K. Mikhaylov, J. Petäjäjärvi, and T. Haenninen, “Analysis of Capacity and Scalability of the LoRa Low Power Wide Area Network Technology”, in *22th European Wireless Conference*, 2016, pp. 1–6.
- [20] Link Labs, *Symphony Link*, <https://www.link-labs.com/symphony>.
- [21] N. Sornin, M. Luis, T. Eirich, T. Kramp, and O. Hersent, *LoRaWAN Specification 1.0*, <https://www.lora-alliance.org/>, LoRa Alliance, 2015.
- [22] M. Aref and A. Sikora, “Free Space Range Measurements with Semtech LoRa x2122 Technology”, in *2014 2nd International Symposium on Wireless Systems within the Conferences on Intelligent Data Acquisition and Advanced Computing Systems*, 2014, pp. 19–23.
- [23] L. Vangelista, A. Zanella, and M. Zorzi, “Long-Range IoT Technologies: The Dawn of LoRa”, Sep. 2015, pp. 51–58.
- [24] M. C. Bor, U. Roedig, T. Voigt, and J. M. Alonso, “Do LoRa Low-Power Wide-Area Networks Scale?”, in *Proceedings of the 19th ACM International Conference on Modeling, Analysis and Simulation of Wireless and Mobile Systems*, Malta, Malta, 2016, pp. 59–67.
- [25] A. Augustin, J. Yi, T. Clausen, and W. M. Townsley, “A Study of LoRa: Long Range & Low Power Networks for the Internet of Things”, *Sensors*, vol. 16, no. 9, 2016.
- [26] J. Petäjäjärvi, K. Mikhaylov, M. Hmlinen, and J. Iinatti, “Evaluation of LoRa LPWAN Technology for Remote Health and Wellbeing Monitoring”, in *2016 10th International Symposium on Medical Information and Communication Technology (ISMICT)*, 2016.
- [27] T. Petric, M. Goessens, L. Nuaymi, L. Toutain, and A. Pelov, “Measurements, Performance and Analysis of LoRa FABIAN, a Real-World Implementation of LPWAN”, in *2016 IEEE 27th Annual International Symposium on Personal, Indoor, and Mobile Radio Communications (PIMRC)*, 2016, pp. 1–7.

- [28] F. Adelantado, X. Vilajosana, P. Tuset-Peiro, B. Martinez, J. Melia-Segui, and T. Watteyne, “Understanding the Limits of LoRaWAN”, *IEEE Communications Magazine*, vol. 55, no. 9, pp. 34–40, 2017.
- [29] G. Ferré, “Collision and Packet Loss Analysis in a LoRaWAN Network”, in *2017 25th European Signal Processing Conference (EUSIPCO)*, 2017, pp. 2586–2590.
- [30] B. Reynders, W. Meert, and S. Pollin, “Range and Coexistence Analysis of Long Range Unlicensed Communication”, in *2016 23rd International Conference on Telecommunications (ICT)*, 2016, pp. 1–6.
- [31] L. Vangelista, “Frequency Shift Chirp Modulation: The LoRa Modulation”, *IEEE Signal Processing Letters*, vol. 24, no. 12, pp. 1818–1821, 2017.
- [32] T. Elshabrawy and J. Robert, “Closed-Form Approximation of LoRa Modulation BER Performance”, *IEEE Communications Letters*, vol. 22, no. 9, pp. 1778–1781, 2018.
- [33] T. Elshabrawy, P. Edward, M. Ashour, and J. Robert, “On the Different Mathematical Realizations for the Digital Synthesis of LoRa-Based Modulation”, in *European Wireless 2019; 25th European Wireless Conference*, 2019, pp. 1–6.
- [34] M. Chiani and A. Elzanaty, “On the LoRa Modulation for IoT: Waveform Properties and Spectral Analysis”, *IEEE Internet of Things Journal*, vol. 6, no. 5, pp. 8463–8470, 2019.
- [35] T. Elshabrawy and J. Robert, “Evaluation of the BER Performance of LoRa Communication using BICM Decoding”, in *2019 IEEE 9th International Conference on Consumer Electronics (ICCE-Berlin)*, 2019, pp. 162–167.
- [36] G. Ferré and A. Giremus, “LoRa Physical Layer Principle and Performance Analysis”, in *2018 25th IEEE International Conference on Electronics, Circuits and Systems (ICECS)*, 2018, pp. 65–68.
- [37] J. Petäjäjärvi, K. Mikhaylov, A. Roivainen, T. Hanninen, and M. Pettissalo, “On the Coverage of LPWANs: Range Evaluation and Channel Attenuation Model for LoRa Technology”, in *2015 14th International Conference on ITS Telecommunications (ITST)*, 2015, pp. 55–59.
- [38] M. Cattani, C. A. Boano, and K. Römer, “An Experimental Evaluation of the Reliability of LoRa Long-Range Low-Power Wireless Communication”, *Journal of Sensor and Actuator Networks*, vol. 6, no. 2, 2017.
- [39] O. Iova, A. L. Murphy, G. P. Picco, L. Ghio, D. Molteni, F. Ossi, and F. Cagnacci, “LoRa from the City to the Mountains: Exploration of Hardware and Environmental Factors”, in *Proceedings of the 2017 International Conference on Embedded Wireless Systems and Networks*, Uppsala, Sweden: Junction Publishing, 2017, pp. 317–322.

- [40] J. Petäjäjärvi, K. Mikhaylov, M. Pettissalo, J. Janhunen, and J. Iinatti, “Performance of a Low-Power Wide-Area Network Based on LoRa Technology: Doppler Robustness, Scalability, and Coverage”, *International Journal of Distributed Sensor Networks*, vol. 13, no. 3, 2017.
- [41] J. Gaelens, P. Van Torre, J. Verhaevert, and H. Rogier, “LoRa Mobile-To-Base-Station Channel Characterization in the Antarctic”, *Sensors*, vol. 17, no. 8, 2017.
- [42] H. Linka, M. Rademacher, K. Jonas, and O. Aliu, “Path Loss Models for Low-Power Wide-Area Networks: Experimental Results using LoRa”, May 2018.
- [43] J. C. Liando, A. Gamage, A. W. Tengourtius, and M. Li, “Known and Unknown Facts of LoRa: Experiences from a Large-Scale Measurement Study”, *ACM Trans. Sen. Netw.*, vol. 15, no. 2, 16:1–16:35, 2019.
- [44] L. Gregora, L. Vojtech, and M. Neruda, “Indoor Signal Propagation of LoRa Technology”, in *2016 17th International Conference on Mechatronics - Mechatronika (ME)*, 2016, pp. 1–4.
- [45] P. Neumann, J. Montavont, and T. Nol, “Indoor Deployment of Low-Power Wide Area Networks (LPWAN): A LoRaWAN Case Study”, in *2016 IEEE 12th International Conference on Wireless and Mobile Computing, Networking and Communications (WiMob)*, 2016, pp. 1–8.
- [46] L. H. Trinh, V. X. Bui, F. Ferrero, T. Q. K. Nguyen, and M. H. Le, “Signal Propagation of LoRa Technology Using for Smart Building Applications”, in *2017 IEEE Conference on Antenna Measurements Applications (CAMA)*, 2017, pp. 381–384.
- [47] J. Haxhibeqiri, A. Karaağaç, F. Van den Abeele, W. Joseph, I. Moerman, and J. Hoebeke, “LoRa Indoor Coverage and Performance in an Industrial Environment: Case Study”, Limassol, Cyprus, 2017, pp. 1–8.
- [48] O. Georgiou and U. Raza, “Low Power Wide Area Network Analysis: Can LoRa Scale?”, *IEEE Wireless Communications Letters*, vol. 6, no. 2, pp. 162–165, 2017.
- [49] M. Bor and U. Roedig, “LoRa Transmission Parameter Selection”, in *2017 13th International Conference on Distributed Computing in Sensor Systems (DCOSS)*, 2017, pp. 27–34.
- [50] V. Hauser and T. Hgr, “Proposal of Adaptive Data Rate Algorithm for LoRaWAN-Based Infrastructure”, in *2017 IEEE 5th International Conference on Future Internet of Things and Cloud (FiCloud)*, 2017, pp. 85–90.
- [51] J. Lim and Y. Han, “Spreading Factor Allocation for Massive Connectivity in LoRa Systems”, *IEEE Communications Letters*, vol. 22, no. 4, pp. 800–803, 2018.

- [52] C. A. Boano, M. Cattani, and K. Römer, “Impact of Temperature Variations on the Reliability of LoRa - An Experimental Evaluation”, in *Proceedings of the 7th International Conference on Sensor Networks - Volume 1*, SciTePress, 2018, pp. 39–50.
- [53] N. Souza Bezerra, C. hlund, S. Saguna, and V. A. de Sousa, “Temperature Impact in LoRaWANA Case Study in Northern Sweden”, *Sensors*, vol. 19, no. 20, 2019.
- [54] N. Blaustein and C. Christodoulou, “Radio Propagation and Adaptive Antennas for Wireless Communication Links: Terrestrial, Atmospheric and Ionospheric”, in John Wiley & Sons, 2007, ch. 6, pp. 175–235.
- [55] ITU-R, *Recommendation ITU-R P835-6: Reference Standard Atmospheres*, Geneva, 2017.
- [56] —, *Recommendation ITU-R P453-13: The Radio Refractive Index: its Formula and Refractivity Data*, Geneva, 2017.
- [57] —, *Recommendation ITU-R P530-17: Propagation Data and Prediction Methods Required for the Design of Terrestrial Line-of-Sight Systems*, Geneva, 2017.
- [58] —, *Recommendation ITU-R P834-9: Effects of Tropospheric Refraction on Radiowave Propagation*, Geneva, 2017.
- [59] S. Gunashekar, “An Investigation of the Propagation of 2 GHz Radio Waves over Sea Paths”, Ph.D. dissertation, University of Leicester, Oct. 2006.
- [60] N. Mufti, “Investigation into the Effects of the Troposphere on VHF and UHF Radio Propagation and Interference between Co-Frequency Fixed Links”, Ph.D. dissertation, University of Leicester, Oct. 2011.
- [61] ITU-R, *Recommendation ITU-R P452-16: Prediction Procedure for the Evaluation of Interference Between Stations on the Surface of the Earth at Frequencies Above About 0.1 GHz*, Geneva, 2015.
- [62] L. Barclay, Ed., *Propagation of Radiowaves*, 3rd ed. London, United Kingdom: The Institution of Engineering and Technology, 2013.
- [63] A. Kulesa, A. Barrios, J. Claverie, S. Garrett, T. Haack, J. Hacker, H. Hansen, K. Horgan, Y. Hurtaud, C. Lemon, R. Marshall, J. McGregor, M. McMillan, C. Periard, V. Pourret, J. Price, L. Rogers, C. Short, M. Veasey, and V. Wiss, “The Tropical Air-Sea Propagation Study (TAPS)”, *Bulletin of the American Meteorological Society*, vol. 98, Jul. 2016.
- [64] ITU-R, *Recommendation ITU-R P676-11: Attenuation by Atmospheric Gases*, Geneva, 2016.
- [65] O. Sasaki and T. Akiyama, “Studies on Radio Duct Occurrence and Properties”, *IEEE Transactions on Antennas and Propagation*, vol. AP-30, no. 5, pp. 853–858, Sep. 1982.
- [66] D. Deirmendjian, *Electromagnetic Scattering on Spherical Polydispersions*. New York: American Elsevier, 1969.

- [67] H. Nussenzveig and W. Wiscombe, “Efficiency Factors in Mie Scattering”, *Phys. Rev. Lett.*, vol. 45, pp. 1490–1494, 1980.
- [68] W. Zhang, “Scattering of Radiowaves by Melting Layer of Precipitation in Backward and Forward Directions”, *IEEE Transactions on Antennas and Propagation*, vol. 42, pp. 347–356, 1994.
- [69] ITU-R, *Recommendation ITU-R P452-15: Prediction Procedure for the Evaluation of Interference between Stations on the Surface of the Earth at Frequencies above about 0.1 GHz*, Geneva, 2013.
- [70] W. L. Flock, *Propagation Effects on Satellite Systems at Frequencies Below 10 GHz*. NASA Reference Publication 1108, 1983.
- [71] S. Saunders, *Antennas and Propagation for Wireless Communication Systems*. New York: John Wiley & Sons, 1999.
- [72] ITU-R, *Recommendation ITU-R P526-14: Propagation by Diffraction*, Geneva, 2018.
- [73] —, *Recommendation ITU-R P833-9: Attenuation in Vegetation*, Geneva, 2016.
- [74] M. O. Asiyó and T. J. O. Afullo, “Tropospheric Propagation Mechanisms Influencing Multipath Fading Based on Local Measurements”, in *Proceedings of Southern Africa Telecommunication Networks and Applications Conference*, George, South Africa, 2012.
- [75] A. Vigants, “Microwave Radio Obstruction Fading”, *The Bell System Technical Journal*, vol. 60, no. 6, pp. 785–801, 1981.
- [76] H. Cao, V. Leung, C. Chow, and H. Chan, “Enabling Technologies for Wireless Body Area Networks: A Survey and Outlook”, *IEEE Communications Magazine*, vol. 47, no. 12, pp. 84–93, 2009.
- [77] A. Pantelopoulos and N. G. Bourbakis, “A Survey on Wearable Sensor-Based Systems for Health Monitoring and Prognosis”, *IEEE Transactions on Systems, Man, and Cybernetics, Part C (Applications and Reviews)*, vol. 40, no. 1, pp. 1–12, 2010.
- [78] M. Chen, S. Gonzalez, A. Vasilakos, H. Cao, and V. C. Leung, “Body Area Networks: A Survey”, *Mob. Netw. Appl.*, vol. 16, no. 2, pp. 171–193, Apr. 2011.
- [79] S. L. Cotton, “A Statistical Model for Shadowed Body-Centric Communications Channels: Theory and Validation”, *IEEE Transactions on Antennas and Propagation*, vol. 62, no. 3, pp. 1416–1424, 2014.
- [80] S. L. Cotton and W. G. Scanlon, “Characterization and Modeling of On-Body Spatial Diversity within Indoor Environments at 868 MHz”, *IEEE Transactions on Wireless Communications*, vol. 8, no. 1, pp. 176–185, 2009.

- [81] S. L. Cotton and W. G. Scanlon, "Channel Characterization for Single- and Multiple-Antenna Wearable Systems Used for Indoor Body-to-Body Communications", *IEEE Transactions on Antennas and Propagation*, vol. 57, no. 4, pp. 980–990, 2009.
- [82] R. Rosini and R. D'Errico, "Off-Body Channel Modelling at 2.45 GHz for Two Different Antennas", in *2012 6th European Conference on Antennas and Propagation (EUCAP)*, 2012, pp. 3378–3382.
- [83] E. Firrao, A. Annema, and B. Nauta, "Antenna Behaviour in the Presence of Human Body", in *The 15th ProRisc Workshop on Circuits, Systems and Signal Processing (ProRisc 2004)*, STW, Nov. 2004, pp. 487–490.
- [84] P. Nepa and H. Rogier, "Wearable Antennas for Off-Body Radio Links at VHF and UHF Bands (below 1 GHz): Challenges, State-of-the-Art and Future Trends", *IEEE Antennas and Propagation Magazine*, pp. 1–1, Oct. 2015.
- [85] P. Van Torre, L. Vallozzi, C. Hertleer, H. Rogier, M. Moeneclaey, and J. Verhaevert, "Dynamic Link Performance Analysis of a Rescue Worker's Off-Body Communication System Using Integrated Textile Antennas", *English, IET Science, Measurement & Technology*, vol. 4, pp. 41–52, 2 2010.
- [86] P. Vanverdegheem, P. Van Torre, C. Stevens, J. Knockaert, and H. Rogier, "Synchronous Wearable Wireless Body Sensor Network Composed of Autonomous Textile Nodes", *Sensors*, vol. 14, no. 10, pp. 18 583–18 610, 2014.
- [87] J. Petäjajarvi, K. Mikhaylov, R. Yasmin, M. Hämäläinen, and J. Iinatti, "Evaluation of LoRa LPWAN Technology for Indoor Remote Health and Wellbeing Monitoring", *International Journal of Wireless Information Networks*, vol. 24, no. 2, pp. 153–165, 2017.
- [88] P. A. Catherwood, S. McComb, M. Little, and J. A. D. McLaughlin, "Channel Characterisation for Wearable LoRaWAN Monitors", in *Loughborough Antennas Propagation Conference (LAPC 2017)*, 2017, pp. 1–4.
- [89] F. Wu, T. Wu, and M. Yuce, "An Internet-of-Things (IoT) Network System for Connected Safety and Health Monitoring Applications", *Sensors*, vol. 19, no. 1, p. 21, 2018.
- [90] F. Wu, J. Redout, and M. R. Yuce, "WE-Safe: A Self-Powered Wearable IoT Sensor Network for Safety Applications Based on LoRa", *IEEE Access*, vol. 6, pp. 40 846–40 853, 2018.
- [91] M. Shahidul Islam, M. T. Islam, A. F. Almutairi, G. K. Beng, N. Misran, and N. Amin, "Monitoring of the Human Body Signal through the Internet of Things (IoT) Based LoRa Wireless Network System", *Applied Sciences*, vol. 9, no. 9, p. 1884, 2019.
- [92] D. Patel and M. Won, "Experimental Study on Low Power Wide Area Networks (LPWAN) for Mobile Internet of Things", in *2017 IEEE 85th Vehicular Technology Conference (VTC Spring)*, 2017, pp. 1–5.

- [93] A. A. Doroshkin, A. M. Zadorozhny, O. N. Kus, V. Y. Prokopyev, and Y. M. Prokopyev, “Experimental Study of LoRa Modulation Immunity to Doppler Effect in CubeSat Radio Communications”, *IEEE Access*, vol. 7, pp. 75 721–75 731, 2019.
- [94] P. Van Torre, L. Vallozzi, C. Hertleer, H. Rogier, M. Moeneclaey, and J. Verhaevert, “Indoor Off-Body Wireless MIMO Communication with Dual Polarized Textile Antennas”, *IEEE Transactions on Antennas and Propagation*, vol. 59, no. 2, pp. 631–642, 2011.
- [95] P. Van Torre, L. Vallozzi, L. Jacobs, H. Rogier, M. Moeneclaey, and J. Verhaevert, “Characterization of Measured Indoor Off-Body MIMO Channels with Correlated Fading, Correlated Shadowing and Constant Path Loss”, *IEEE Transactions on Wireless Communications*, vol. 11, no. 2, pp. 712–721, 2012.
- [96] S. Cotton and W. Scanlon, “Spatial Diversity and Correlation for Off-Body Communications in Indoor Environments at 868 MHz”, Apr. 2007, pp. 372–376.
- [97] Great Scott Gadgets, *HackRF One*, <https://greatscottgadgets.com/hackrf/>.
- [98] RTL-SDR, *RTL-SDR*, <https://www.rtl-sdr.com/>.
- [99] Nuand, *BladeRF*, <https://www.nuand.com/>.
- [100] B. Sikken, *Decoding LoRa*, <https://revspace.nl/DecodingLora>.
- [101] J. Blum, *LoRa SDR Project*, <https://github.com/myriadrf/LoRa-SDR>.
- [102] RTL-SDRangelove, *Github Project Page*, <https://github.com/hexameron/rtl-sdrangelove>.
- [103] P. Robyns., P. Quax., W. Lamotte., and W. Thenaers., “A Multi-Channel Software Decoder for the LoRa Modulation Scheme”, in *Proceedings of the 3rd International Conference on Internet of Things, Big Data and Security - Volume 1*, SciTePress, 2018, pp. 41–51.
- [104] P. Edward, A. Muhammad, S. Elzeiny, M. Ashour, T. Elshabrawy, and J. Robert, “Enhancing the Capture Capabilities of LoRa Receivers”, in *2019 International Conference on Smart Applications, Communications and Networking (SmartNets)*, 2019, pp. 1–6.

PART I

Physical-Layer Performance of
LoRa Networks in Different
Propagation Environments

2

A Compact Low-Power LoRa IoT Sensor Node with Extended Dynamic Range for Channel Measurements

Based on "A Compact LoRa IoT Sensor Node with Extended Dynamic Range for Channel Measurements" by Thomas Ameloot, Patrick Van Torre and Hendrik Rogier, as published in *MDPI Sensors*, vol. 18, no. 7, pp. 2137.



As sub-GHz wireless Internet of Things (IoT) sensor networks set the stage for long-range, low-data-rate communication, wireless technologies such as LoRa and SigFox receive a lot of attention. They aim to offer a reliable means of communication for an extensive amount of monitoring and management applications. Recently, several studies have been conducted on their performance, but none of these feature a high dynamic range in terms of channel measurements. In this chapter an autonomous, low-power, LoRa-compatible wireless sensor node is presented. The main uses for this node are situated in LoRa channel characterization and link performance analysis. By applying stepped attenuators controlled by a dynamic attenuation adjustment algorithm, this node provides a dynamic range that is significantly larger than what is provided by commercially available LoRa modules. The node was calibrated in order to obtain accurate measurements of the received signal power in dBm. In this chapter, both the hardware design as well as some verification measurements are discussed, unveiling various LoRa-related research applications and opportunities.

2.1 Introduction

Wireless sensor networks (WSNs) are at the heart of the ever-developing Internet of Things (IoT). They have received a great deal of attention across a diverse range of research areas such as environmental monitoring, disaster surveillance, smart buildings, smart grids, healthcare, agricultural control, predictive maintenance, transport and asset tracking [1]–[4]. Seeing WSN deployment over larger and larger areas, it becomes evident to consider the use of sub-GHz frequency bands for communication in these long-range networks, given the superior propagation characteristics when compared to higher frequency bands. Conveniently, the reduction of the available bandwidth at lower frequencies does not degrade performance since communication links in WSNs are typically very low data-rate connections anyway.

Multiple standards for low data-rate sub-GHz communication have been proposed, the most prominent of which are LoRa, SigFox and Dash7 [1], [5]–[8]. As Dash7 is promoted to be a medium-range technology [7], for long-range networks, the scope has shifted towards LoRa and SigFox. The adjustable data rate of the LoRa standard, combined with its slightly higher level of global coverage [5], [6] makes for a very promising technology both for applications in WSNs and other long-range, low data-rate connections. LoRa is based on a chirp spread spectrum (CSS) modulation technology. To encode information, this technology uses wideband frequency modulated pulses called chirps to achieve spreading gain, which results in the successful reception of packets at extremely low signal-to-noise ratio (SNR) levels. The LoRa modulation technique was described in a rigorous way in [9]. Additionally, the expected performance of LoRa has been discussed in a decent number of other publications [8], [10]–[13], all of these praising the potential of LoRa modulation, but some also warning for reduced performance as the number of end-devices grow [8], [12], [13].

To explore the capabilities of LoRa modulation, a suitable radio platform is needed. A commercial LoRa platform frequently used in literature is the SX127X family from Semtech Corp [8], [14]–[18]. Unfortunately, as most commercially available LoRa modules are tailored towards industry applications, they often lack dedicated measurement functions required for research applications. On the other end of the spectrum, lab-grade software radios do offer a lot of functionality, but in addition to being very expensive, they can also be very bulky for certain types of research. In fact, in any type of studies involving mobility or areas that are difficult to reach, both the size and power dependency of research equipment can seriously impede the possible research applications. The middle ground can be found by integrating a commercially available LoRa module into a system with more capabilities to create a compact, low-power wireless sensor node.

In this chapter, such a node is proposed, designed and tested. For LoRa compatibility, a commercially available LoRa transceiver module [19] is used. This module facilitates LoRa communication in both the 434 MHz and 868 MHz industrial, scientific and medical (ISM) radio bands. The LoRa module also offers channel

measurement functions, such as SNR estimation, but due to the fact that LoRa is a proprietary technology, research determining the physical performance of this technology is primarily bound to the capabilities of the most sensitive transceiver available, in this case: the SX1276. In the sensor node proposed in this chapter, this is partly circumvented by using stepped attenuators to considerably increase the dynamic range of the measurement node. The transceiver module is also certified to the LoRaWAN 1.0 specification, enabling the use of this node within the existing LoRaWAN network infrastructure [19].

This chapter is structured as follows. In Section 2.2, the hardware design and calibration of the wireless sensor node are described in detail. To verify the correct operation of the node, several experiments were carried out in and around the city of Ghent, Belgium. The setup for these measurements is described in Section 2.3 and the results of these measurements are discussed in Section 2.4. Finally, in Section 2.5, a conclusion to this chapter is presented.

2.2 Hardware Design

To give a full overview of the hardware design, a block diagram of the node is presented in Figure 2.1. The largest blocks in this diagram depict an 8-bit, low-power microcontroller (Silicon Labs C8051F342) and a commercial LoRa module (Microchip Technology Inc. RN2483), which is built around a Semtech SX1276 LoRa transceiver. These components provide the core functionality of the microcontroller section and the radio frequency (RF) section, respectively.

2.2.1 Microcontroller Section

The C8051F342 is a general purpose microcontroller featuring a high-speed 8-bit core, 64 kB of flash memory, two timers, a USB function controller and multiple popular bus interfaces such as System Management Bus (SMBus), Inter-Integrated Circuit (I²C), Universal Asynchronous Receiver-Transmitter (UART) and Enhanced Serial Peripheral Interface (SPI). Most of these interfaces can be routed through any of the available input/output (I/O) ports using the on-chip I/O configurator, yielding a versatile, yet compact, low-cost and low-power control center for the wireless sensor node. The microcontroller can be programmed and debugged through the integrated two-wire debug interface using a Silicon Labs USB Debug Adapter.

2.2.2 RF-Section

Among other things, the LoRa transceiver module is equipped with a LoRaWAN protocol stack, a 434 MHz and 868 MHz LoRa radio and a command processor providing the user with an easy-to-use ASCII-over-UART command interface. According to the transceiver's documentation, the module can theoretically achieve

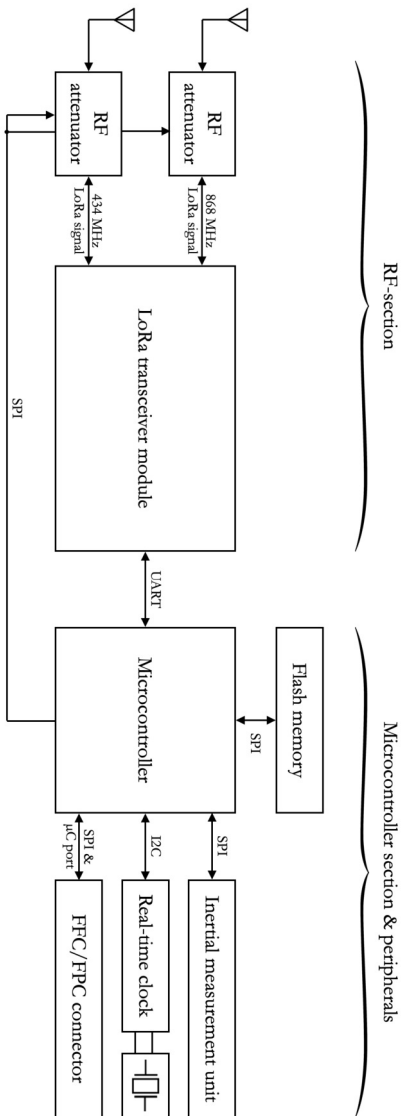


Figure 2.1: Block diagram of the wireless sensor node.

receiver sensitivities down to -146 dBm by selecting the appropriate spreading factor (SF) and bandwidth (BW) of the LoRa modulation scheme [5]. Complemented by the integrated 14 dB power amplifier, very high link budgets can be obtained. The available documentation defines the receiver sensitivity as the received power level at which the packet error rate equals 1%. In addition to LoRa modulation, the transceiver module also features Frequency shift keying (FSK) and Gaussian frequency shift keying (GFSK) modulation [5].

With regard to channel characterization and link performance, the RN2483 module can provide the user with the SNR of the last received packet. Unfortunately, no metrics on the measurement scheme used for this are given in the transceiver's documentation. Therefore a calibration procedure was carried out in an anechoic chamber, linking the measured SNR value to the received power, thus establishing a baseline for SNR measurements.

The calibration method outlined in Figure 2.2 is performed in three phases. In the first phase, the LoRa transmitter (TX) is connected directly to a Rohde and Schwartz FSV40 spectrum analyser, to accurately measure the transmitted power. Second, the TX is placed in the anechoic chamber and is connected via low-leakage coaxial transmission lines and a high-precision stepped attenuator to the spectrum analyzer in the shielded control room. In this step, the losses induced by the coaxial cables are measured to be calibrated away. The setup with the TX in the anechoic chamber and the RX in the shielded control room is necessary to provide enough isolation for the third measurement phase, where the attenuation has to be increased to over 150 dB in order to reach the detection limit of the LoRa RX.

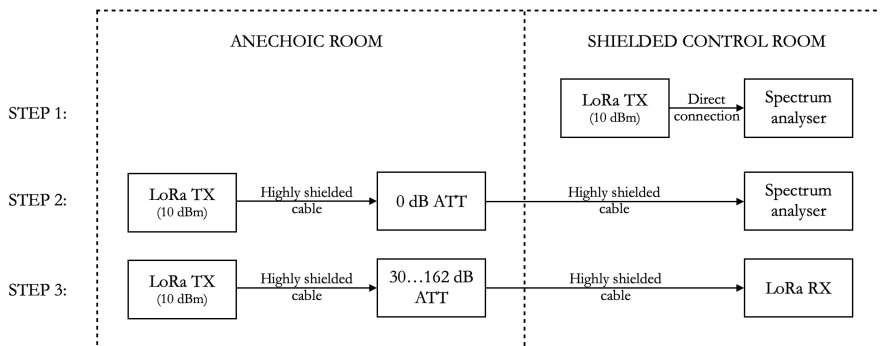


Figure 2.2: Calibration setup.

In this third phase, using the stepped attenuator, the attenuation is adjusted from 50 dB to 162 dB, which is the maximum setting. For every data point in the calibration, ten SNR measurements were performed and averaged. This procedure was performed for both the 434 MHz and 868 MHz frequency bands. The results of the calibration measurements are shown in Figure 2.3.

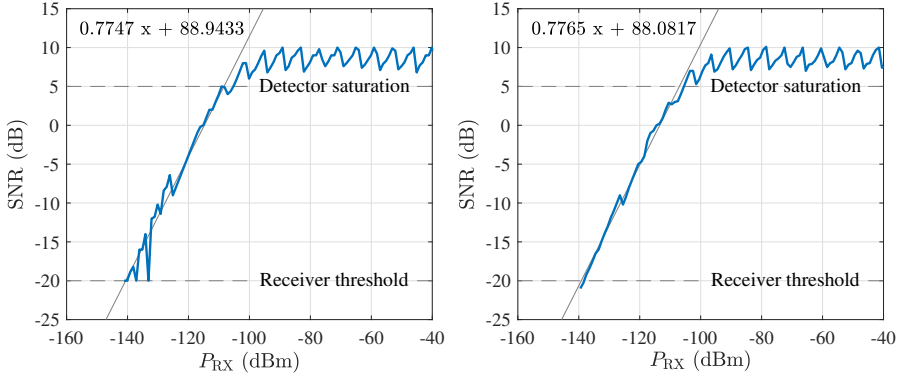


Figure 2.3: SNR measurement calibration for 434 MHz (left) and 868 MHz (right).

The calibration data show that using its default settings (SF = 12 and BW = 125 kHz), the transceiver achieves a receiver sensitivity of -140 dBm, which corresponds to an SNR of -20 dB. This sensitivity is slightly better than the value of -136 dBm specified by the manufacturer for the default parameters. Note that for measured SNR values greater than 5, the detector is seen to saturate and behave in a highly non-linear fashion. In the linear region, first-order regression models are fitted to the calibration data, yielding the following formula to calculate the received power ($P_{RX,dBm}$) based on the measured SNR ($S_{meas,dB}$):

$$P_{RX,dBm} = \frac{S_{meas,dB} - 88.51}{0.7756} \quad (2.1)$$

Because of the strong similarity of the models for both frequency bands (their difference is lower than the measurement resolution), it is concluded that this relation is valid for both bands. Furthermore, the coefficients found for these models are very similar to those of the model presented for 868 MHz in [20].

As can be seen in Figure 2.3, only a relatively small SNR detection range is actually available. To resolve this issue, the RF-section also features two stepped attenuators. These attenuators serve to increase the range of the signal level measurement by dynamically attenuating signals that are too strong. The measured received power is described by

$$P_{RX,dBm} = P_{ant,dBm} - A_{dB} \quad (2.2)$$

with $A_{dB} \geq 0$ denoting the applied attenuation in dB and $P_{ant,dBm}$ equal to the received power at a well-matched antenna, neglecting the minimal losses of the short transmission lines. This equation is rewritten to find the received power at the antenna:

$$P_{ant,dBm} = P_{RX,dBm} + A_{dB}. \quad (2.3)$$

Attenuation levels can vary between 0 dB and 31.5 dB and can be changed in 0.5 dB steps. The applied attenuation adjustment algorithm is visualized in the flowchart depicted in Figure 2.4. In short, this algorithm either increases the attenuation by 1 dB when the SNRs of the received packets approach the saturation level of the detector - which is approximately equal to 5 dB, so a threshold of 3 dB is chosen - or lowers the attenuation by 1 dB when three subsequent packets are no longer received. The amount of lost packets needed to cause a decrease in attenuation was chosen at three because a lower value may cause the system to react to sudden changes in SNR caused by momentaneous interference issues while a higher value may cause the system to lose too much packets before adapting to a real change in propagation conditions. The step size was chosen at 1 dB because using the full 0.5 dB resolution of the attenuators would cause the amount of time needed for the algorithm to settle to the appropriate settings to be too high given that the amount of packets that can be sent per minute is subject to quite severe duty cycle regulations (ranging from 0.1 % to 10 % depending on the specific sub-band [21]). On the other hand, using an even larger step size would result in a more sizable loss of resolution, which is also undesirable.

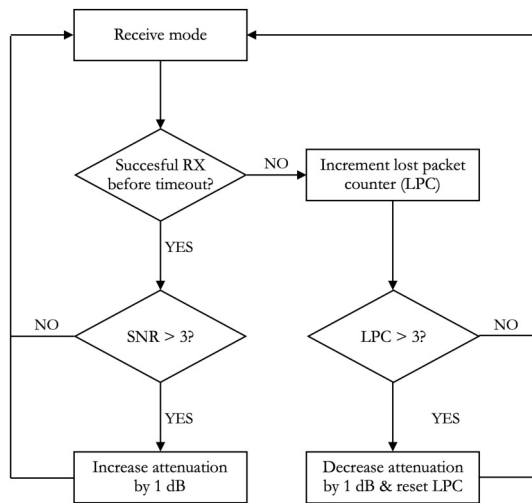


Figure 2.4: Flowchart of the attenuation adjustment algorithm.

Given that the LoRa module has a linear SNR measurement range corresponding to a signal level range of 32 dB, a simple calculation reveals that the use of attenuators at the receiver's side of the link increases the node's theoretical dynamic range for signal measurements to 63.5 dB. Furthermore, by using the attenuators of the transmitter as well, this dynamic range can be shifted over an additional 31.5 dB. However, since this affects the transmitted signal power, receivers located further away from the transmitter could experience an increase in packet loss when this strategy is used. Consequently, care should be taken when shifting the dynamic

range when multiple receivers are used. In addition to received power measurements, more straightforward link statistics such as packet loss can be gathered by using the general purpose microcontroller described earlier.

2.2.3 Peripherals

To diversify the potential applications of the wireless node, some peripherals are added to the microcontroller section of the design. First, a 32 Mbit flash memory IC is added to significantly enhance storage space on the node, thus allowing prolonged measurement campaigns to take place. Second, an inertial measurement unit (IMU) is integrated into the system. This sensor encompasses a 3D accelerometer, a 3D gyroscope and a 3D magnetometer, adding applications such as indoor navigation and motion monitoring to the list of possible use cases. Both the flash memory and the IMU can be accessed by means of the microcontroller's SPI interface. The third addition to the node is a real-time clock (RTC) with its own separate 32.768 kHz quartz crystal for keeping time, which is exploited to set timestamps and to wake up the system out of low-power mode using interrupts. Especially this last feature may considerably reduce the total energy consumption of the node, which is very beneficial when using a battery as power source. The microcontroller can communicate with the RTC using its I²C interface and offers a dedicated connection for interrupts. Finally, through a flat flexible cable (FFC) and flat printed circuit cable (FPC) connector, a full 8-lead microcontroller I/O port, the SPI bus and a 3.3 V power line are made available to a potential peripheral sensor or sensor array that can be placed on a different printed circuit board (PCB).

2.2.4 Power

By all means, the node should not only communicate in a wireless fashion, it should also be powered by an independent power source. Being designed with multiple research applications in mind, the proposed system can be powered by any battery producing a voltage in between 3.3 V and 12 V. To further expand the amount of possible power sources, a micro-USB connector is provided as well, facilitating the use of commercial USB battery packs. The power drawn by the node roughly ranges from 4 mA when in standby mode to 40 mA when sending or receiving LoRa packets. To prevent the RTC from resetting when the battery is changed, a 0.22 F supercapacitor is added, giving the user more time to attach the new battery.

2.2.5 PCB Implementation

Naturally, a compact PCB design is paramount to obtain a significant size reduction when implementing custom hardware instead of using a development board or software radio. To this end, a lot of consideration went into a compact 4-layered

PCB layout for this sensor node. The final result is depicted in Figure 2.5 and measures 70 mm by 32 mm.



Figure 2.5: Compact PCB implementation of the wireless sensor node (70 mm x 32 mm).

2.3 Hardware Verification Setups

Both indoor and outdoor tests were performed to assess the system’s performance. In the following subsections, the setups used for these verification measurements will be discussed in detail.

2.3.1 Outdoor Measurement Setup

To perform the outdoor measurements presented in this chapter, nodes were placed at three locations in the city of Ghent, Belgium. The exact locations of these sites are marked on Figure 2.6, which also shows the (sub)urban propagation environment in between the sites. In each of the outdoor experiments, small packets of data were sent from the transmitter location in the center of the city of Ghent to be received by two receivers located near the south of the city.

Transmitter

The transmitter (TX) was equipped with two copper ground plane monopole antennas, featuring five 15 cm or 7.5 cm elements, for the 434 MHz and 868 MHz versions respectively. For its power supply, the node relied on a heavy-duty battery providing multiple weeks of autonomy. The transmitter node, the antennas and the battery were placed in a waterproof enclosure. As seen in Figure 2.7, this enclosure was attached to two horizontal iron bars on the outside of a window approximately 20 m above the ground at the south side of a university building, slightly higher than the surrounding houses. To comply with the 1% duty cycle legal restrictions regarding the use of the 434 MHz and 868 MHz ISM-bands, only one packet was transmitted every minute, alternating between both bands. This packet contains just a 2-byte unsigned integer describing the packet number. A single packet number was, however, used once in each of the two ISM-bands mentioned earlier. Hence, the packet counter increases once every two minutes. The packets were sent at a bitrate of 293 bps and a spreading factor (SF) of 12 was used for the LoRa modulation.

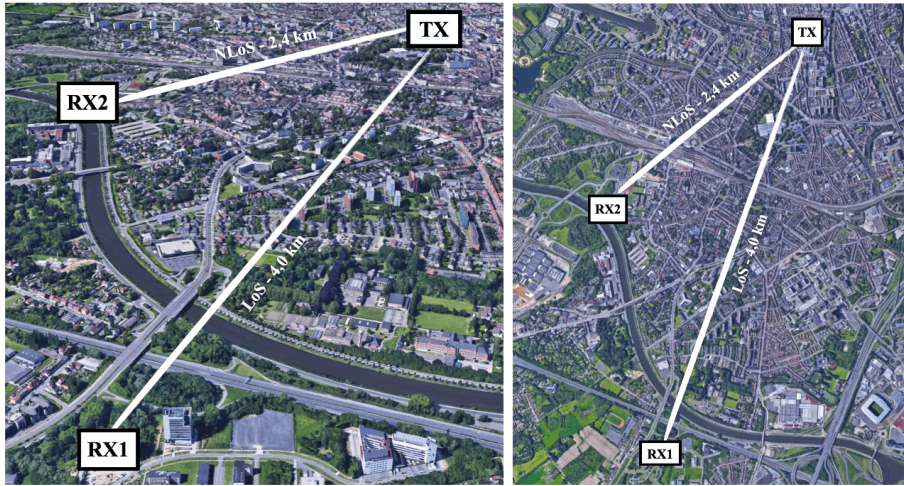


Figure 2.6: 3D and satellite views of the outdoor node locations. Map Data: Google, Landsat/Copernicus.



Figure 2.7: Location of the transmitter at the Armand Pien observatory.

Receivers

The first receiver (RX1) was placed in an office environment at the eleventh floor of a modern building located at the edge of the city of Ghent. The distance from this building to the transmitter is approximately 4.0 km. The line-of-sight (LoS) path includes several urban features such as densely packed houses, a sizable park, a large conference center, a university campus, large apartment buildings, a canal and multiple large roads. The receiver was placed indoors, allowing it to be powered by a power supply. It was connected to similar monopole antennas as used at the transmit side. Yet, the 868 MHz antenna was attached to the outside of the building in order to avoid the signal attenuation by the building's highly insulating windows, which block the 868 MHz signals in such a way that they could

not be received indoors. Interestingly, 434 MHz signals propagate through these windows considerably better. A second receiver (RX2) was placed indoors, on the fourth floor of a building located closer to the transmitter. For this receiver, the distance to the transmitter equals 2.4 km. However, the path to this transmitter is non-line-of-sight (NLoS) and includes densely packed houses, a large railway station and a university campus. The hardware setup is equal to the one used for the other receiver (RX1). All of the receivers discussed in this chapter store both the received packet numbers as well as the SNR measurements and attenuation settings corresponding to these packets in their flash memory.

2.3.2 Indoor Measurement Setup

In a second test phase, indoor measurements were performed using a setup in the same building where receiver RX1 was located during the outdoor measurements. Nodes were deployed in three rooms located on two similarly structured floors - the ninth and the eleventh - of the office tower. As seen in Figure 2.8, the floors of this building all feature a thick concrete core with multiple elevator shafts and stairwells, surrounded by a large number of office spaces.

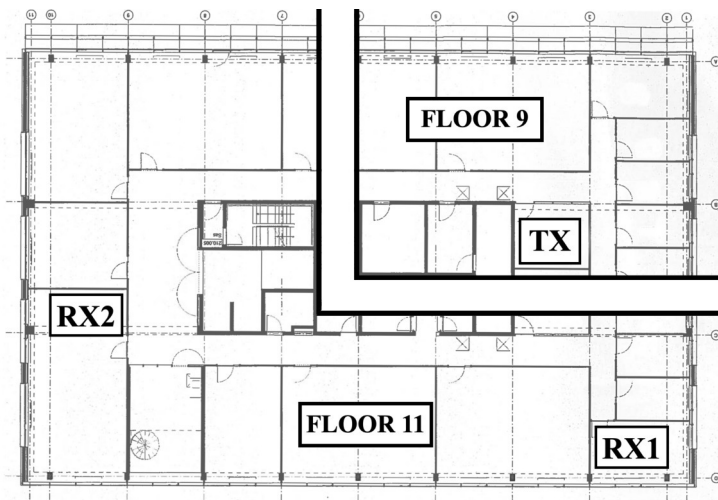


Figure 2.8: Indoor node locations.

Transmitter

The transmitter (TX) was placed in a small meeting room on the ninth floor, adjacent to the concrete core of the building. Again, two ground plane monopole antennas were used. However, this time, the transmitted data packets also included a timestamp and readings of the transmitter's supply voltage and the ambient temperature.

Receivers

Two receivers were placed in offices on the eleventh floor. The first receiver (RX1) was placed in an office on the same side of the building as the transmitter. Another receiver (RX2) was placed in an office located at the other side of the building. To reach this receiver, radio waves have to propagate through or around the core of the building.

2.4 Measurement Results and Analysis

According to the measurement setups described in section 2.3, multiple sets of test data were gathered. In the following sections, the most interesting data are discussed in detail.

2.4.1 Outdoor Received Power Measurements

Received Power Measurements at RX1

For a time period of seven days, outdoor measurements were performed according to the measurement setup outlined in Section 2.3.1. The measurement data recorded by RX1 are presented in the upper half of Figure 2.9. The data in this part of the graph are filtered by a moving-average window with a size of 30 samples, which corresponds to one hour of gathered measurements, thereby eliminating sudden interference peaks and revealing possible underlying trends. The raw received power levels are observed to fluctuate with standard deviations of 1.29 dB at 434 MHz and 2.09 dB at 868 MHz. According to free space propagation theory, one would expect the average 434 MHz signal to be 6 dB stronger than the average 868 MHz signal. This behavior is not present here, due to the different placement of the antennas (the 434 MHz antenna being placed indoors and the 868 MHz antenna being placed outdoors, as discussed in Section 2.3.1). Additionally, based on the received packet numbers, the packet loss was determined. For this test, this loss adds up to 0.61% for the 434 MHz band and 6.11% for the 868 MHz band. The packet loss in the latter band is higher because of collisions with packets from other transmitters. A more detailed analysis indeed revealed a much higher occupation of the 868 MHz band, when compared to the 434 MHz band.

To investigate the cause of the sizable drop in received power of the 868 MHz signal on day 6, temperature and rainfall data was provided by the Armand Pien weather observatory. These data are presented in the lower half of Figure 2.9. On day 6, a sizable peak in rainfall was observed which coincides directly with the signal level dip. A slightly lower amount of rainfall was observed on the first day of measurement (day 0), resulting in a smaller, but still measurable drop in signal level on that day. These signal dips are however not present in the 434 MHz data, which were measured with an indoor antenna. Hence, an explanation for this feature is most probably to be found in the antenna placement. With the 868 MHz

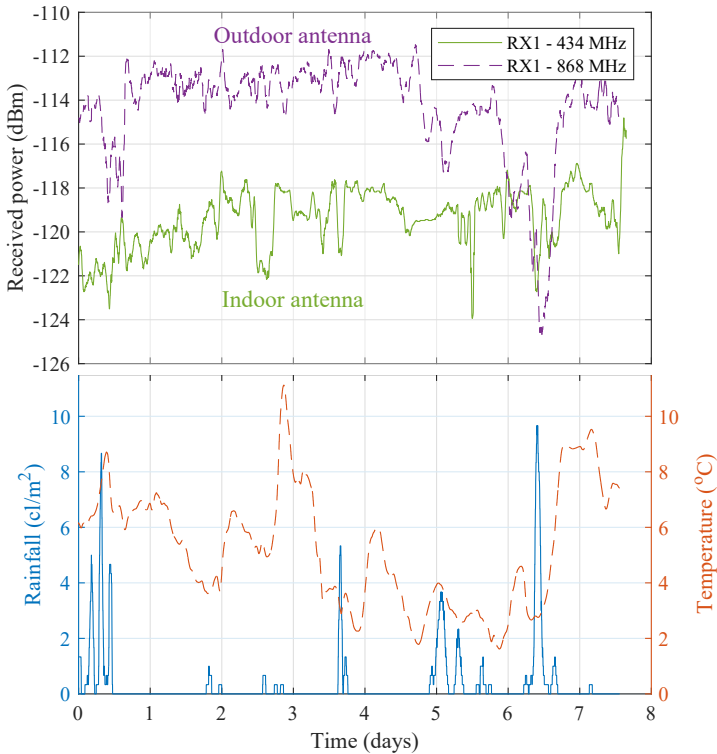


Figure 2.9: 7 days of outdoor received power measurements gathered at RX1 compared to temperature (orange curve) and rainfall (blue curve) data.

antenna being placed outdoors, the water on this antenna is expected to have changed its behavior in such a way that a mismatch occurred, causing the drop in received signal energy. Consequently, for outdoor operation, more weatherproof antennas should be selected. The temperature on the other hand did not influence the measured data in any discernible way as temperature fluctuations were too limited to have a significant impact on the receiver noise. Finally, it has to be noted that because of the relatively low power levels that were received, this receiver's attenuators remained at 0 dB during this experiment.

Received Power Measurements at RX2

To verify the correct operation of these attenuators and the dynamic attenuation adjustment algorithm that controls them, similar measurements were performed by receiver RX2. As this receiver was located closer to the transmitter, in a building with older, conventional - not highly insulating - glass windows, it was expected that the attenuation settings would be altered immediately after receiving the first

packets and would continue to change until the detector was no longer saturated. Figure 2.10 shows the actual startup behavior of the node, which indeed corresponds to this expected behavior. The slope in the graph corresponds to an increase in attenuation of 30 dB/h, which is equal to 1 dB every two minutes. This can of course be explained by legal restrictions only allowing the transmitter to send one packet every two minutes in each band. The slow response was deliberately conserved because we do not want the system to overreact to sudden changes caused by temporary effects such as potential interference. It should also be noted that the attenuation settings are only altered when receiving packets with the right ID tag, originating from our own transmitter. Consequently, potential strong signals from unknown LoRa sources do not influence the attenuation settings.

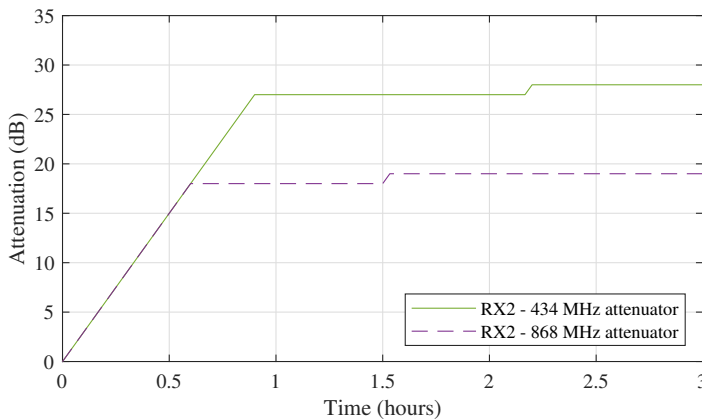


Figure 2.10: Attenuator startup behavior at outdoor receiver RX2. The slow response is a result of legal restrictions, but also prevents the system from reacting to sudden, temporary effects.

The received power measurements gathered during this ten-day test are presented in Figure 2.11. Again, an averaging window of one hour is used. With standard deviations of 0.61 dB for the raw 434 MHz data and 0.64 dB for the raw 868 MHz data, these measurements show a lot less fluctuation than the ones gathered by receiver RX1. This could be attributed to the smaller distance to the transmitter and the resulting larger signal-to-interference ratio (SIR). In further contrast to the data presented in Section 2.4.1, this time, the theoretically expected signal power difference of 6 dB between the 434 MHz band and the 868 MHz band is clearly visible. Finally, the packet loss for this second test is also calculated, adding up to a mere 1.17% for the 434 MHz band and 1.6% for the 868 MHz band. This second packet loss value is a lot smaller than the packet loss measured for the 868 MHz band at RX1 thanks to the lower height of RX2 and the smaller number of nearby LoRa sources at RX2.

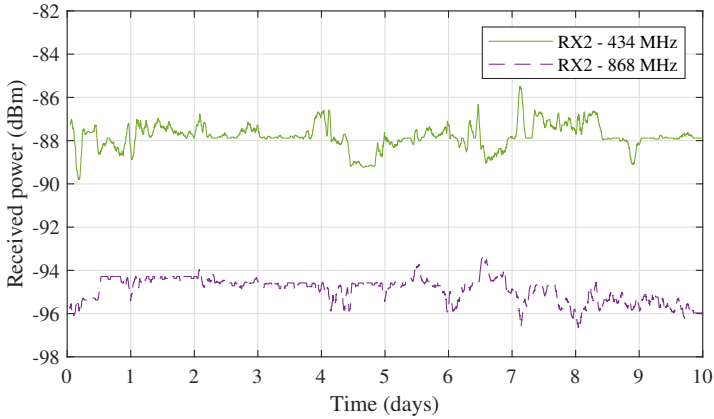


Figure 2.11: Ten days of outdoor received power measurements gathered at RX2.

2.4.2 Indoor Signal Level Measurements

Finally, the indoor setup described in Section 2.3.2 was considered to gather a third set of signal measurements. These data are presented in Figure 2.12. They document half a month of indoor LoRa channel measurements performed in the first half of April 2018. The first observation we make on this graph is that the average received powers of the 434 MHz signals ($\mu_{434, \text{RX1}} = -70.9$ dBm and $\mu_{434, \text{RX2}} = -88.2$ dBm) are considerably larger than those of the corresponding 868 MHz signals ($\mu_{868, \text{RX1}} = -91.7$ dBm and $\mu_{868, \text{RX2}} = -116.0$ dBm). Hence, it can be concluded that using the 434 MHz ISM-band is indeed a much better option for indoor LoRa communication than using the 868 MHz ISM-band.

Considering the signal fluctuations, a clear distinction can be made between data gathered when the building was empty and data gathered when it wasn't. During weekend days, the received signals are much more stable than on week days. Furthermore, these fluctuations mostly disappear by the end of the work day to reappear the next morning. This indicates that the presence of people has a clear and measurable influence on the stability of the LoRa channel. To properly describe this behavior, the mean values and standard deviations of the received powers are calculated for intervals of 8 hours during the day (9 a.m. - 5 p.m.) and during the night (9 p.m. - 5 a.m.). To clarify this, a subset of these descriptive statistics can be found in Table 2.1, describing the second week of indoor measurements at RX1. Now, the average mean values ($\bar{\mu}$) of the subsets of signal data that describe the channel performance when there are people in the building (by day, on working days) and those subsets of data that describe the channel performance when people are not around (at night and in the weekends) are calculated for both bands and both receivers. Moreover, the average standard deviations ($\bar{\sigma}$) of the received powers are calculated for the same subsets (DAY vs. NIGHT, RX1 vs. RX2 and 434 vs. 868). These values can be found in Table 2.2.

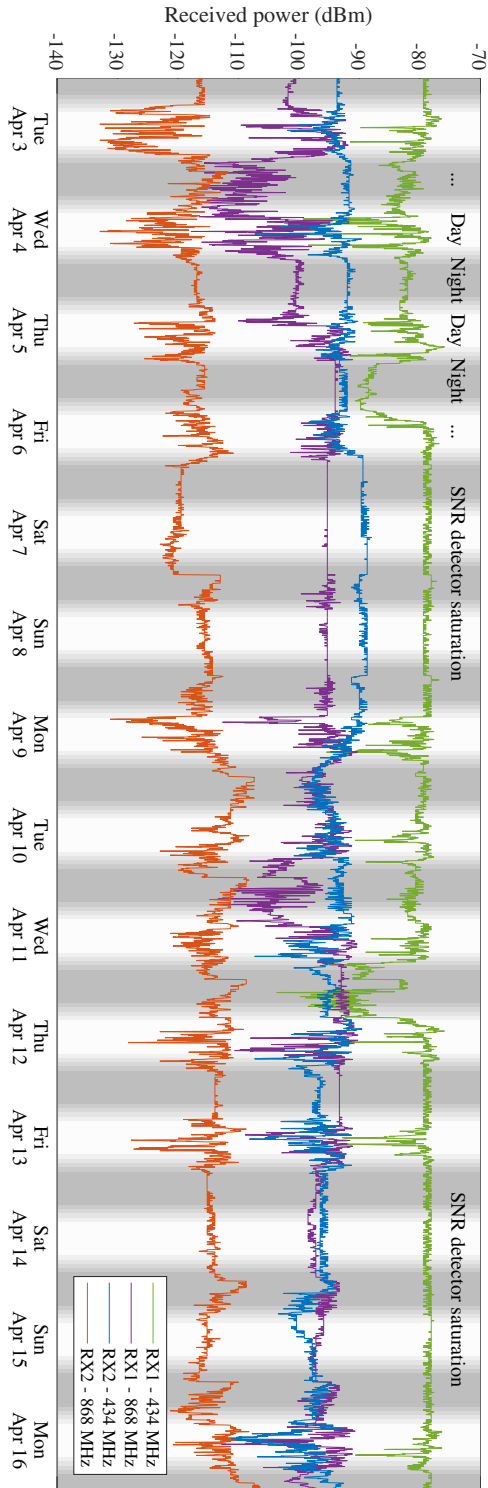


Figure 2.12: Fourteen days of indoor received power measurements.

Although there is no significant change in mean received signal power, for both receivers RX1 and RX2 and both ISM-bands, there is a clear difference between the standard deviations of the power levels measured when people are around and when they are not. This confirms the claim stated earlier that the channel is less stable when people are present in the building. Signal levels remained well above the detection limit of the LoRa unit configured with the default parameters for the 434 MHz band for both receivers, whereas this was not the case for receiver RX2 in the 868 MHz band.

	434 MHz				868 MHz			
	DAY		NIGHT		DAY		NIGHT	
	μ	σ	μ	σ	μ	σ	μ	σ
Mon 9 April	-72.4	4.0	-70.3	0.8	-89.5	4.1	-91.3	1.9
Tue 10 April	-70.9	2.3	-71.9	1.2	-88.9	2.8	-96.6	4.4
Wed 11 April	-71.1	2.4	-79.8	5.3	-88.7	4.0	-86.9	0.7
Thu 12 April	-70.1	2.7	-69.8	0.6	-89.3	5.2	-87.0	0.1
Fri 13 April	-71.9	3.4	-69.5	0.6	-89.2	4.1	-90.7	0.6
Sat 14 April	-69.7	0.6	-69.4	0.6	-91.3	0.6	-88.8	1.4
Sun 15 April	-69.2	0.5	-69.4	0.6	-90.7	0.8	-89.2	1.6

All μ values expressed in dBm and σ values expressed in dB.

Table 2.1: Statistics describing the second week of indoor power measurements gathered at RX1. (DAY: 9 a.m. - 5 p.m. & NIGHT: 9 p.m. - 5 a.m.).

	434 MHz				868 MHz			
	DAY		NIGHT		DAY		NIGHT	
	$\bar{\mu}$	$\bar{\sigma}$	$\bar{\mu}$	$\bar{\sigma}$	$\bar{\mu}$	$\bar{\sigma}$	$\bar{\mu}$	$\bar{\sigma}$
RX1	-71.1	3.00	-70.8	0.82	-90.8	4.30	-92.5	1.09
RX2	-88.8	2.75	-87.5	0.77	-116.5	4.05	-115.4	1.35

All μ values expressed in dBm and σ values expressed in dB.

Table 2.2: Average values of the descriptive statistics describing subsets of indoor power measurements. (DAY: 9 a.m. - 5 p.m. & NIGHT: 9 p.m. - 5 a.m.).

As a side note to Figure 2.12, it should be mentioned that due to the small distance between the transmitter and RX1, the detector of RX1 is often saturated when measuring the SNR of packets received in the 434 MHz band. Nevertheless, during week days, this detector comes out of saturation, which further establishes the influence of the presence of people on the quality of the LoRa link. This saturation behavior could be mitigated by signaling this back to the transmitter using bidirectional LoRa-communication. This way, the transmitter could also increase its attenuation settings. Naturally, as was discussed in Section 2.2.2, this may increase the packet loss of other receivers, illustrating the trade-off between receiving more low-power packets and detecting higher received power values.

2.5 Conclusion

An autonomous LoRa-compatible wireless sensor node for the IoT was designed, fabricated, calibrated and tested. This node is not only unique in its ability to perform channel characterization in both the 434 MHz and 868 MHz ISM-bands, it can also accurately measure received power levels over a large dynamic range. A feat which is possible thanks to the stepped attenuators implemented in this design and the calibration of the unit performed in the lab.

Several design choices (such as the addition of a real-time clock with a dedicated interrupt line and a supercapacitor buffering the supply voltage) were made to increase the autonomy of the node, enabling prolonged measurement campaigns to take place. Moreover, both the incorporation of various other peripheral components and the fact that this custom hardware is significantly smaller than a development board or software radio show that this system qualifies for a very broad range of LoRa research applications.

The correct operation of the node was successfully validated by performing both indoor and outdoor test measurements. In these measurement campaigns, the expected superiority of the 434 MHz band for long-range communication links was repeatedly confirmed. Moreover, with measured received power values ranging from -140 dBm to -70 dBm, the need for and usefulness of an enhanced dynamic range for channel measurements was clearly illustrated.

The outdoor tests have also provided insight into the difference in link quality between the 434 MHz and 868 MHz LoRa channels. With an additional distance of 1.6 km to the transmitter, the standard deviation of the SNR of the packets received by receiver RX1 exhibited an increase of 1.29 dB for the 434 MHz band and 3.98 dB for the 868 MHz band when compared to the SNR of the packets received by RX2. When comparing rainfall and temperature data to the signals measured outdoors, a correlation was found between a sudden drop in signal and an episode of rainfall. This indicated that the behavior of the antenna, which was placed outside of the building, had changed substantially due to the water present on it. No correlation was found between the outdoor temperature fluctuation and the measured signal levels.

Indoor measurements indicated that the presence of people in a building also has a measurable influence on the quality of a LoRa link in that building. When considering the 434 MHz band, the average standard deviations of the received powers measured by day differ from those measured by night or in the weekend by approximately 2 dB for both indoor receivers. For the 868 MHz band, these differences amount to approximately 3 dB for both receivers.

In conclusion, the system successfully recorded several propagation characteristics in both the 434 MHz and 868 MHz ISM-bands over a wider dynamic range than achievable with off-the-shelf LoRa units.

References

- [1] U. Raza, P. Kulkarni, and M. Sooriyabandara, “Low Power Wide Area Networks: An Overview”, *IEEE Communications Surveys Tutorials*, vol. 19, no. 2, pp. 855–873, 2017.
- [2] R. Almeida, R. Oliveira, M. Lus, C. Senna, and S. Sargento, “A Multi-Technology Communication Platform for Urban Mobile Sensing”, *Sensors*, vol. 18, no. 4, 2018.
- [3] M. Cerchecci, F. Luti, A. Mecocci, S. Parrino, G. Peruzzi, and A. Pozzebon, “A Low Power IoT Sensor Node Architecture for Waste Management Within Smart Cities Context”, *Sensors*, vol. 18, no. 4, 2018.
- [4] A. Lozano, J. Caridad, J. F. De Paz, G. Villarrubia Gonzalez, and J. Bajo, “Smart Waste Collection System with Low Consumption LoRaWAN Nodes and Route Optimization”, *Sensors*, vol. 18, no. 5, 2018.
- [5] LoRa Alliance, *LoRa*, <https://www.lora-alliance.org/>.
- [6] SigFox Foundation, *SigFox*, <https://www.sigfox.com/en>.
- [7] Dash7 Alliance, *Dash7*, <http://www.dash7-alliance.org/>.
- [8] A. Augustin, J. Yi, T. Clausen, and W. M. Townsley, “A Study of LoRa: Long Range & Low Power Networks for the Internet of Things”, *Sensors*, vol. 16, no. 9, 2016.
- [9] L. Vangelista, “Frequency Shift Chirp Modulation: The LoRa Modulation”, *IEEE Signal Processing Letters*, vol. 24, no. 12, pp. 1818–1821, 2017.
- [10] U. Noreen, A. Bounceur, and L. Clavier, “A Study of LoRa Low Power and Wide Area Network Technology”, in *2017 International Conference on Advanced Technologies for Signal and Image Processing (ATSIP)*, 2017, pp. 1–6.
- [11] J. Haxhibeqiri, F. Van den Abeele, I. Moerman, and J. Hoebeke, “LoRa Scalability: A Simulation Model Based on Interference Measurements”, *Sensors*, vol. 17, no. 6, 2017.
- [12] O. Georgiou and U. Raza, “Low Power Wide Area Network Analysis: Can LoRa Scale?”, *IEEE Wireless Communications Letters*, vol. 6, no. 2, pp. 162–165, 2017.
- [13] K. Mikhaylov, J. Petäjajarvi, and T. Haenninen, “Analysis of Capacity and Scalability of the LoRa Low Power Wide Area Network Technology”, in *22th European Wireless Conference*, 2016, pp. 1–6.

- [14] M. Aref and A. Sikora, “Free Space Range Measurements with Semtech LoRa x2122 Technology”, in *2014 2nd International Symposium on Wireless Systems within the Conferences on Intelligent Data Acquisition and Advanced Computing Systems*, 2014, pp. 19–23.
- [15] O. Iova, A. L. Murphy, G. P. Picco, L. Ghio, D. Molteni, F. Ossi, and F. Cagnacci, “LoRa from the City to the Mountains: Exploration of Hardware and Environmental Factors”, in *Proceedings of the 2017 International Conference on Embedded Wireless Systems and Networks*, Uppsala, Sweden: Junction Publishing, 2017, pp. 317–322.
- [16] T. Petric, M. Goessens, L. Nuaymi, L. Toutain, and A. Pelov, “Measurements, Performance and Analysis of LoRa FABIAN, a Real-World Implementation of LPWAN”, in *2016 IEEE 27th Annual International Symposium on Personal, Indoor, and Mobile Radio Communications (PIMRC)*, 2016, pp. 1–7.
- [17] M. Cattani, C. A. Boano, and K. Römer, “An Experimental Evaluation of the Reliability of LoRa Long-Range Low-Power Wireless Communication”, *Journal of Sensor and Actuator Networks*, vol. 6, no. 2, 2017.
- [18] J. Petäjäjärvi, K. Mikhaylov, M. Pettissalo, J. Janhunen, and J. Iinatti, “Performance of a Low-Power Wide-Area Network Based on LoRa Technology: Doppler Robustness, Scalability, and Coverage”, *International Journal of Distributed Sensor Networks*, vol. 13, no. 3, 2017.
- [19] Microchip Technology Inc., *RN2483 Low-Power Long Range LoRa[®]*, www.microchip.com.
- [20] J. Gaelens, P. Van Torre, J. Verhaever, and H. Rogier, “LoRa Mobile-To-Base-Station Channel Characterization in the Antarctic”, *Sensors*, vol. 17, no. 8, 2017.
- [21] ETSI, *Short Range Devices (SRD) Operating in the Frequency Range 25 MHz to 1 000 MHz*, Sophia Antipolis, 2012.

3

Variable Link Performance due to Weather Effects in a Long-Range, Low-Power LoRa Sensor Network

Based on "Variable Link Performance due to Weather Effects in a Long-Range, Low-Power LoRa Sensor Network" by Thomas Ameloot, Patrick van Torre and Hendrik Rogier, as published in *MDPI Sensors*, vol. 21, no. 9, pp. 3128.



When aiming for the wider deployment of low-power sensor networks, the use of sub-GHz frequency bands shows a lot of promise in terms of robustness and minimal power consumption. Yet, when deploying such sensor networks over larger areas, the link quality can be impacted by a host of factors. Therefore, this chapter demonstrates the performance of several links in a real-world, research-oriented sensor network deployed in a (sub)urban environment. Several link characteristics are presented and analyzed, exposing frequent signal deterioration and, rarer, signal strength enhancement along certain long-distance wireless links. A connection is made between received power levels and seasonal weather changes and events. The irregular link performance presented in this thesis is found to be genuinely disruptive when pushing sensor networks to their limits in terms of range and power use. This chapter aims to give an indication of the severity of these effects in order to enable the design of truly reliable sensor networks.

3.1 Introduction

Since many Internet of Things (IoT) applications rely on the deployment of low-power wireless sensor networks (WSNs) over rather large areas, research on sub-GHz wireless communication technologies has seen a steady rise in popularity. Modern low-power, wide-area network (LPWAN) technologies such as Narrow-Band IoT (NB-IoT) [1], Long Term Evolution-Machine Type Communication (LTE-M) [2], Dash7 [3], SigFox [4] and, in particular, LoRa [5] receive a lot of attention, as they trade in data rate for communication range, link reliability and power efficiency. Therefore, they could soon become ubiquitous in the low data-rate sensor networks, part of the fifth generation of mobile communication technologies (5G).

LoRa technology has been assessed in a relatively large number of publications. First of all, general descriptions of operational aspects of LoRa technology are presented in [6]–[9]. More in-depth, theoretical reviews of LoRa modulation are found in [10], [11]. The physical-layer performance of LoRa is discussed for indoor environments in [12]–[18]. Outdoor measurement campaigns are presented in [19]–[25]. When pushing the boundaries of LPWAN technologies such as LoRa by deploying outdoor sensor networks with relatively large inter-nodal distances, large-scale propagation effects and mechanisms such as obstruction fading, tropospheric scattering and tropospheric ducting may become increasingly important as these may have a sizeable impact on the quality and reliability of wireless links [26]. Given that both tropospheric scattering and tropospheric ducting could vastly increase the communication range for a single wireless link [27], [28], inter-cell interference may turn out to be just one of those hurdles when scaling up modern LPWAN technologies. In case of LoRa, [6], [7], [29], [30] have actually warned for reduced performance when the number of end-devices grows. Furthermore, adverse weather conditions are known to impact outdoor antenna performance and electronic circuit reliability. In general, it is important to identify the challenges these effects pose to engineers when designing sensor networks spanning large distances. However, to this date, the amount of literature on the impact of large-scale propagation phenomena and weather effects in LoRa networks is limited.

3.1.1 Related Work

For LoRa technology, research indicates that temperature variations can have a significant impact on the wireless links [31], [32]. [31] describes different experiments where large packet loss is recorded when the node temperature is very high. A small hysteresis is observed in moments when the receiver is warming up or cooling down. Similarly, in [32], the authors present an experimental evaluation of the reliability of LoRa receivers in the presence of temperature variations. Lab measurements are performed and design guidelines are provided to alleviate these temperature effects.

Recently, a number of long-term measurement campaigns that monitor link quality over time have been published. In [33], received signal levels are presented for outdoor sensors deployed in the north of Sweden. It is observed that noise power is reduced when temperatures are low, which leads to better signal-to-noise ratios (SNRs). The authors of [33] also demonstrate that snowfall has a detrimental impact on link quality, especially when large distances are covered. [34] presents an analysis of LoRa propagation characteristics in different land and water environments. Different antenna heights, node distances and, where applicable, tidal water levels are considered. Similarly, [35] presents received power levels from a 8.33 km link over water in different weather conditions. Measurements were gathered over a period of 70 days.

In a multitude of other publications, LoRa networks are employed to communicate sensor data describing the ambient temperatures, relative humidity levels or other meteorological parameters [36]–[38]. However, none of these papers compare the measured parameters to the performance of the network. Conversely, a large number of papers have been published that discuss temperature and/or humidity effects in WSNs in general, but which do not employ LoRa technology [39]–[47].

3.1.2 Contributions

This chapter aims to contribute to existing LoRa network monitoring research by analyzing the prevalence and severity of link fluctuations in LPWANs through the analysis of channel monitoring data gathered from an actual LoRa network over a timespan of multiple months. This WSN was established by deploying six custom-built wireless nodes, specifically designed for LoRa channel characterization, at various locations in and around the city of Ghent, Belgium. The chapter is structured as follows. First, in Section 3.2, the wireless sensor network setup used to gather the data presented in this work is described. Subsequently, in Section 3.3, the gathered experimental data are presented, revealing large signal deteriorations measured daily along the longest links in the network. In Sections 3.3.2, 3.3.3, 3.3.4 and 3.3.5, an evidence-based approach is adopted to describe and identify the nature of these fluctuations. Additionally, some potential consequences of these effects with respect to LPWANs are highlighted. Finally, in Section 3.5, a conclusion to this chapter is presented.

3.2 Measurement Setup

In order to examine the performance of IoT sensor networks, measurement data were gathered from an actual LoRa network in the city of Ghent, Belgium. This network was established using custom LoRa nodes, developed specifically for channel characterization purposes and thoroughly described in [17]. In this section, a very brief outline of the characteristics and functions of this hardware is given, together with the deployment details of the network and the measurement methodology adopted to gather the data.

3.2.1 Hardware

In short, the custom LoRa transceiver system used in this research is built around a low-power, 8-bit microprocessor and a dual-frequency LoRa transceiver module, facilitating communication in both the 434 MHz and 868 MHz ISM-bands. It also includes some peripheral hardware such as a real-time clock (RTC), an inertial measurement sensor unit (IMU) and a 32 Mbit flash memory IC to locally store measurement data. Additionally, attenuators are used to significantly increase the dynamic range for SNR measurements. Using these off-the-shelf components, this hardware is much more comparable to what one would expect to find in actual LoRa applications, yielding more realistic system performance results. Furthermore, this hardware is a lot smaller, cheaper and more energy-efficient than channel-sounding equipment, enabling deployment at locations where it would not be feasible to install such bulky and expensive lab equipment. Fig. 2.5 shows a compact (72 mm x 30 mm) PCB-implementation of this custom LoRa transceiver.

In most receiver locations, the transceiver system shown in Fig. 2.5 was paired with a copper end-fed half-wavelength dipole, impedance-matched via a quarter-wave stub [48], [49]. For each LoRa transceiver, two of these antennas were manually fabricated, the first one intended for use in the 434 MHz band and the second one intended for use in the 868 MHz band. The radiating part of these antennas measures 29.5 cm for the 434 MHz versions and 13.5 cm for the 868 MHz versions. The impedance-matching structures respectively measure 21.5 cm and 10.5 cm. For each of the deployed antennas, the correct operation was verified in the lab. H-plane radiation patterns are omnidirectional with a gain of 2.2 dBi. For nodes to be deployed outdoors, waterproof polyvinyl chloride (PVC) enclosures were produced that fit both the 434 MHz and 868 MHz antennas along with the LoRa hardware and a large-capacity battery. A deployment of one of these setups can be seen in Fig. 3.1. Owing to the low power consumption of the LoRa node, such a basic outdoor setup can operate autonomously for multiple months on end.



Figure 3.1: Outdoor setup of one of the LoRa nodes.

3.2.2 Node Deployment

When gathering the measurements presented in this work, the LoRa nodes were configured to form a broadcast network, as this enables time-synchronization between the nodes. The transmitter (TX), which is shown in Fig. 3.1, was placed at a height of approximately 55 m, on the roof of a modern 12-story office building in the south of the city of Ghent. The locations of the receiving nodes are shown in Fig. 3.2. This figure also includes descriptions of the different types of obstructions in the longest link paths. These obstructions mostly consist of buildings or trees as the area surrounding the city of Ghent is largely flat. Hence, there are no large geographical features such as hills or mountains which significantly obstruct the link paths. Each of the receiver locations is considered in more detail below.

RX1

The first receiver was deployed on the second floor of a university building, located at 2.1 km from the transmitter. The propagation path between TX and RX1 is mostly urban, as it encompasses multiple large, low-rise buildings and some larger road infrastructure. Although the RX1 receiving node was deployed indoors, this path can be labeled line-of-sight (LoS) as the only obstructions between the transmitting and receiving antennas were the glass window in front of the two receive antennas and the PVC enclosure covering the two transmit antennas, which had very little influence on the performance of these antennas.



Figure 3.3: LoRa network node locations in and around the city of Ghent, Belgium. Map Data: Google, Landsat/Copernicus.

RX2

A second receiver was deployed on the fifth floor of another university building, located at 4.0 km from the transmitter. The path from TX to RX2 includes the very same features as the path to RX1, in addition to several high-rise apartment buildings, located closer to RX2. As a consequence, the path between TX and RX2 is non-line-of-sight (NLoS), although the receive node was again located close to a window. This implies that, for this receiver, the reception of LoRa packets depends on signal diffraction, reflection and potential transmission through these structures.

RX3

As for the TX-RX2 link, the path between TX and RX3 is NLoS due to the surrounding buildings. Yet, RX3 is a fully urban receiver location, located in the heart of the city of Ghent, also at 4.0 km from the transmitter. However, in this environment, the buildings are a lot lower than the apartment towers surrounding RX2. Additionally, this receiver was deployed at a lower height than the one at RX2, more specifically on the third floor of a laboratory building. It is important to note that the direct path between TX and RX3 is also obstructed by a large medieval abbey. Consequently, its very thick stone walls may have a measurable influence on the average power received at this location.

RX4

The fourth receiver was installed in the attic of a house in a suburban satellite town located to the northwest of the city. At a distance of 10.6 km to the transmitter, this link is significantly longer than the previous ones. Nevertheless, as the direct path to this link is mostly unobstructed by buildings and as there are no large geographical features in the surrounding area, an acceptable signal level can still be expected. Although no large obstacles are present, this path does contain a lot of vegetation and some residential areas. As the trees (western European broad-leaves trees: 10 to 15 m tall) are generally higher than the houses (two or three floor levels: 6 to 10 m high) in this suburban area, these are considered to be the most important features affecting the wireless link. Yet, since trees are not really solid structures, the radio link is classified near-line-of-sight (which is denoted here as nLoS). Eventually, to increase the link budget and, hence, the packet reception ratio (PRR), two Yagi-Uda antennas were used at RX4. These antennas, aligned with the transmitter, exhibit gains of 9 dBi and 13 dBi at 434 MHz and 868 MHz, respectively.

RX5

Similar to the fourth receiver, the fifth receiver was also deployed in the attic of a house. However, this house is located further away from the transmitter, to the east of the city of Ghent, where the environment is more rural. Although this 13.9 km radio link between TX and RX5 is mostly rural, closer to the transmitter, there are some office buildings and a large football stadium, both of which may obstruct the direct propagation path, making the categorisation as NLoS the most accurate for this link. Similar to the receiver at RX4, two Yagi-Uda antennas were used to increase the PRR.

TX monitor

A receiver was also placed in a technical room, on the same roof as the transmitter. This receiver was used to monitor the stability of the transmitter's power output.

3.2.3 Link Models

It is interesting to assess the expected performance of each link presented above. To this end, the Okumura-Hata propagation model [50] was employed to estimate the power levels that would be received by the remote nodes as a function of the distance between each receiver and the transmitter. These power levels are shown in Fig. 3.3 for node heights of 1, 3, 8 and 15 meters.

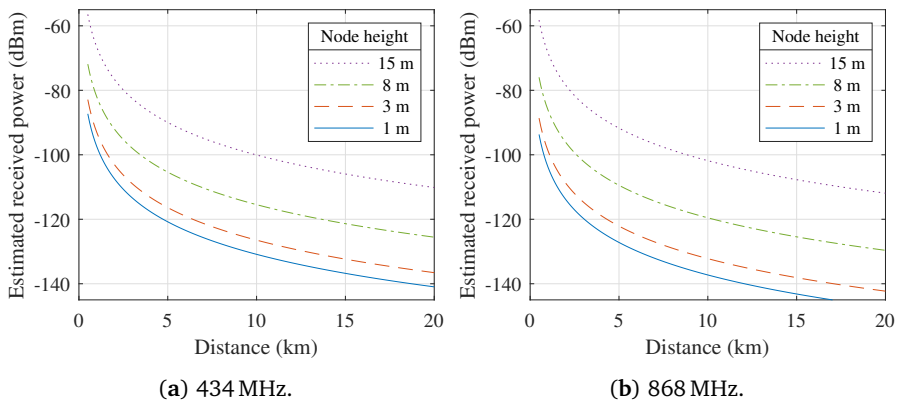


Figure 3.3: Estimated power received by a remote node at different heights, based on the Okumura-Hata model [50]. (Transmit power = 10 dBm, transmitter height = 55 m.)

Yet, it is important to note that in practical IoT deployments, remote nodes are often placed in a suboptimal position for communication with the base station. In fact, whereas in other types of applications, the antenna might be deployed on a mast to achieve a reliable connection, WSN nodes are usually installed much closer to link obstructions, as is also apparent from the node placements described in Section 3.2.2. Furthermore, given the long distances covered in the network, the first Fresnel zone is often populated with a large amount of scatterers and obstacles. As an illustration, the maximum radius r_1 of the first Fresnel zone is calculated for each link by applying the following expression:

$$r_1 = 8.656 \sqrt{\frac{d}{f}}, \quad (3.1)$$

where d denotes the distance to the transmitter (in meters) and f indicates the operating frequency (in Hz) [50]. As shown in Table 3.1, all of the links to RX2, RX3, RX4 and RX5 have their first Fresnel zone intersecting with the ground. Hence, with the exception of the links to RX1, all links have a significant amount of obstacles in their first Fresnel zone.

Table 3.1: Maximum radius (in meters) of the first Fresnel zone for each link path.

	434 MHz	868 MHz
RX1	19.0	13.5
RX2	26.3	18.6
RX3	26.3	18.6
RX4	42.8	30.3
RX5	49.0	34.6

All values expressed in meters.

3.2.4 Measurement Methodology

As can also be seen in Table 3.2, the 16-byte packets were broadcast that include a transmitter identifier string, a unique packet number and a timestamp as well as some information on the transmitter's operational status, such as its power supply level (VDD) and the ambient temperature (TEMP).

TX ID	TIMESTAMP	PACKET N°	VDD	TEMP
4 bytes	6 bytes	2 bytes	2 bytes	2 bytes

Table 3.2: Packet structure. TX ID: transmitter identifier string, VDD: supply voltage, TEMP: ambient temperature.

Although the 434MHz and 868MHz bands used in the network described above are ISM-bands, there is a maximum duty cycle imposed by law to avoid users occupying the channel for too long, ranging from 0.1 % to 10 % depending on the specific sub-band [51]. To comply with these legal duty cycle limitations, one packet was transmitted every minute, alternating between both bands. Hence, per day, 720 packets were transmitted in each of the bands. A full overview of the LoRa modulation and the general network settings are described in Table 3.3. A LoRa spreading factor of 12 is chosen as the most remote nodes in the network can only be reliably reached by using this setting, which is the highest configurable spreading factor, corresponding to the highest sensitivity. The bandwidth and code rate both assume their default values.

PARAMETER	VALUE
LoRa spreading factor (SF)	12
LoRa bandwidth (BW)	125 kHz
LoRa coding rate (CR)	4/5
Bit rate	293 bps
Packet length	16 bytes
Packet rate	1 packet / 2 min

Table 3.3: LoRa modulation and general network settings.

3.3 Measurement Results and Analysis

Based on the measurement setup described in the previous Section, various measurement campaigns were performed. The general performance of the network is discussed first. Then, the most interesting features in the data gathered from this network are investigated and thoroughly analyzed.

3.3.1 General Results

Fig. 3.4 shows the average powers received by nodes RX1, RX2, RX3 and RX4, over a period of about two weeks in May 2018. The plotted curves clearly illustrate the different node behaviours found in the network. They were obtained by filtering the raw data using a one-hour moving average window to eliminate sudden interference peaks and reveal the underlying trends. While not always explicitly mentioned, this strategy was applied to all time-domain representations of received power level data presented in this work. The links to the first two receivers (RX1 and RX2) were found to be very stable. This is also reflected in Table 3.4, which shows the average received power levels (μ) and the standard deviations (σ) of these data. Additionally, the packet reception ratios (PRRs) for these links, which are also listed in Table 3.4, are very high.

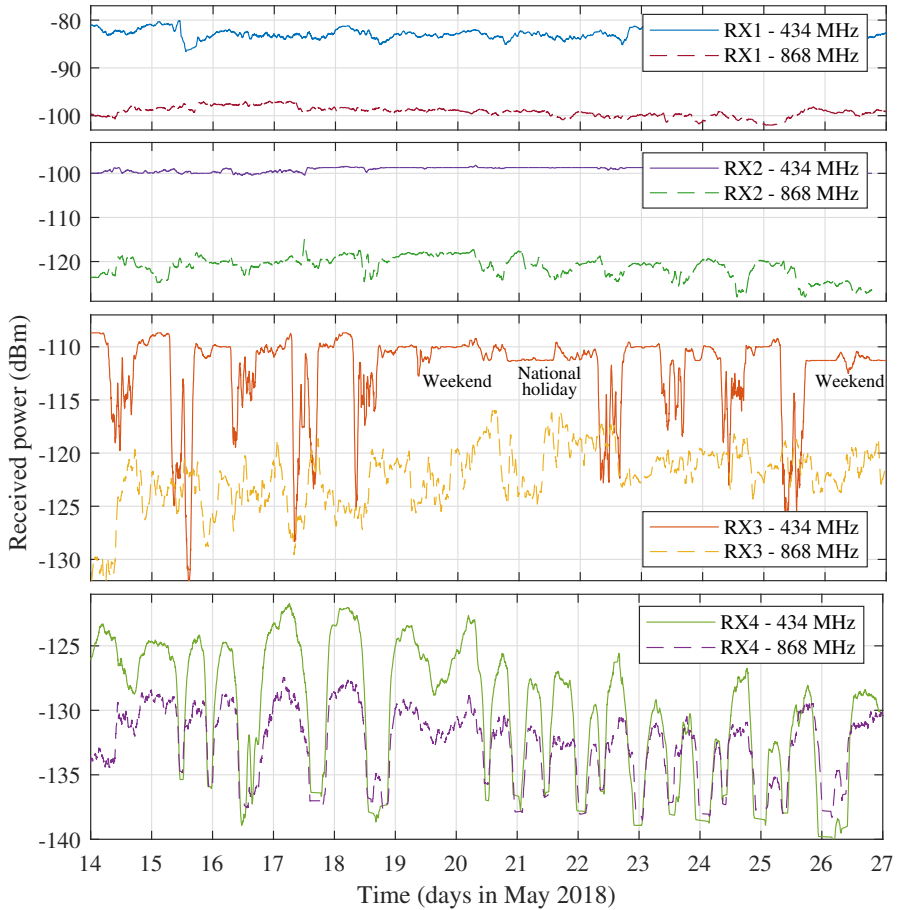


Figure 3.4: Selection of the general measurement results showing some of the most interesting features found in the datasets.

	434 MHz			868 MHz		
	μ (dBm)	σ (dB)	PRR (%)	μ (dBm)	σ (dB)	PRR (%)
RX1	-82.6	1.5	100	-99.2	1.7	96.0
RX2	-99.5	1.9	99.1	-121.3	2.1	97.0
RX3	-112.3	5.0	98.6	-123.0	4.6	97.6
RX4	-128.7	5.1	82.0	-131.4	3.3	86.3
RX5	Not yet active.					

Table 3.4: Descriptive statistics on the general performance of the LoRa network links (as registered in May 2018).

Fig. 3.4 and Table 3.4 also show that the standard deviation of the power measurements performed on the 434 MHz link to RX3 is significantly higher than the standard deviations measured for the 434 MHz links to RX1 and RX2. When looking at the time domain behaviour of this metric, it appears that the link is very unstable during working hours and fairly stable at night and in the weekends. In fact, the unstable periods correspond directly to those times during which the buildings surrounding RX3 (some low-rise offices and a very popular student restaurant) were full of people. This behaviour is very similar to the indoor link effects described in [17] and [52]. In these papers, significant signal degradation was observed on days when people were present inside the test building. In [17], these fluctuations are attributed to human body absorption. Remarkably, this is the first time that these effects are observed in an outdoor LoRa link. Although it appears that the 868 MHz link to RX3 is less impacted by this specific phenomenon, it can be observed that the measured signal levels fluctuate significantly more than along the other 868 MHz links.

The most interesting links are those to RX4. Due to the longer propagation distance, a lot more fluctuation is observed on these links. In fact, the most eye-catching features are the large signal drops occurring once or twice each day. They are also reflected in the standard deviation and PRR data in Table 3.4. This unusual behaviour will be investigated thoroughly in the next subsections. The link to RX5 was not active when the measurements presented in Fig. 3.4 were gathered, but as will be shown in the next subsections, the node at RX5 detected similar signal fluctuations as registered by the node at RX4. As the power levels received by the nodes located closer to the transmitter show less fluctuations than those received by the long-distance nodes, these link variations are not significant enough for further statistical analysis.

3.3.2 Daily Signal Fluctuations on Long-Distance Links: General

To enable a more rigorous characterization of the large signal fluctuations found in the data gathered from the long-distance links to RX4, additional measurement campaigns were performed during the entire year that followed, employing the nodes at RX4 and RX5. This has resulted in a very large dataset, describing the performance of these long-distance links over a large variety of weather conditions. As a full time-domain representation of these data would be very impractical due to the large size of this dataset, only a selection of received power levels — more specifically those gathered in the month of July 2018 — are shown in Fig. 3.5. This time period was specifically chosen because of the very stable weather experienced in Belgium during those days. In fact, from July 13 to July 27, a heatwave was registered in the country, providing a sizable stretch of days during which the potential influences of day-to-day variations of the weather conditions on these fluctuations were limited. In addition to this heatwave, hardly any rainfall was recorded for weeks on end during this period.

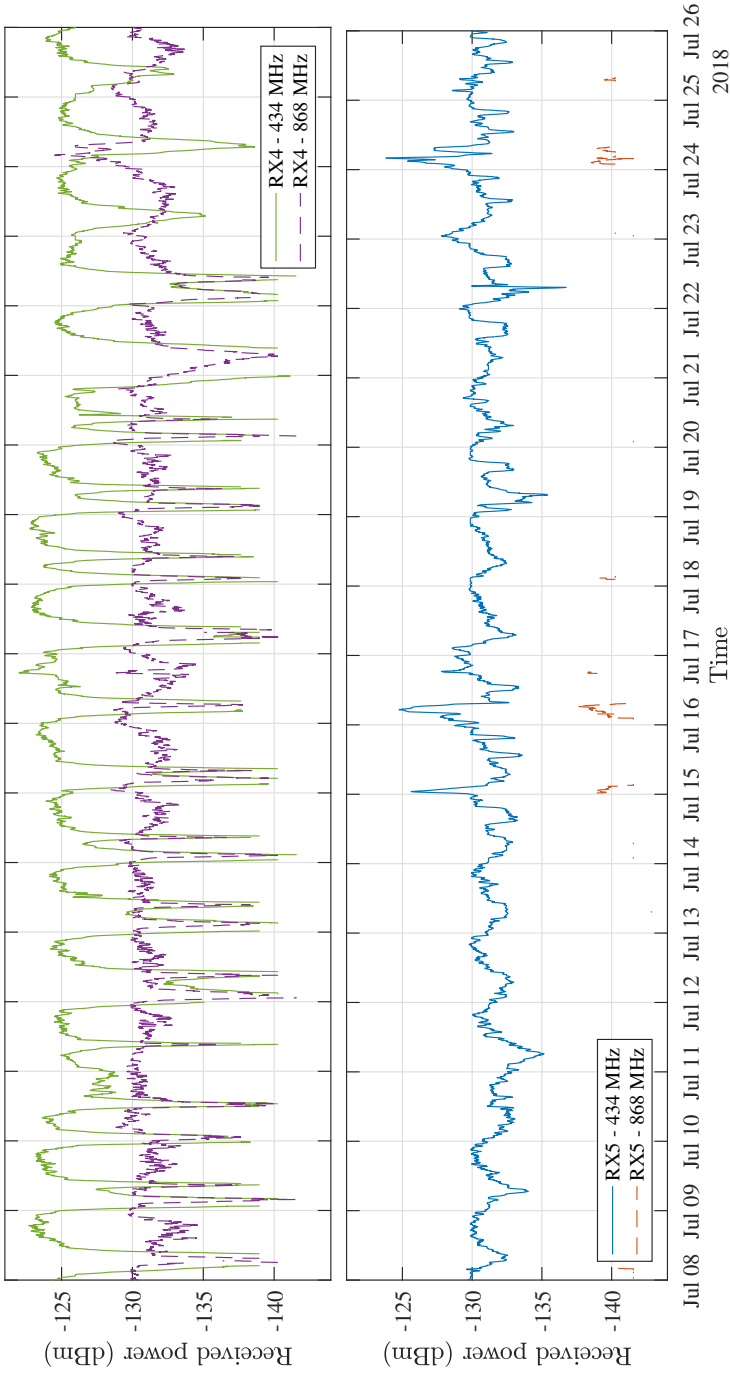


Figure 3.6: Selection of link monitoring data gathered at RX4 and RX5 during a heatwave in July 2018.

Fig. 3.5 shows that the signal level fluctuations are very severe for the links to RX4, regularly lowering the signal level by over 15 dB for the 434 MHz link and by about 10 dB for the 868 MHz link. During these drops, the PRR practically reduces to zero, so the power loss could actually be even higher. For the 434 MHz links to RX5, the deteriorations are a lot less severe, as seen in these data's standard deviation and PRR metrics that are presented in Table 3.5. Due to the large distance to the transmitter, the 868 MHz link to RX5 has a very low PRR, so little can be said about possible fluctuations in this link. Likewise, the standard deviation on the SNR and power levels of the received packets is very low because of the proximity to the receiver sensitivity level, which causes many packets to be lost. Based on the calibration data for the SNR measurements presented in [17], the background noise level is estimated at -114 dBm in both of the employed ISM bands. The influence of the signal degradations is also apparent in Fig. 3.6, which shows the received signal level distributions obtained by performing piecewise polynomial interpolation on the histograms that describe the distribution of the received power levels presented in Fig. 3.5. These distributions are reasonably symmetric in general, but the ones describing the RX4 data do have distinct irregular left sided tails, which are clearly caused by the signal deteriorations.

	434 MHz			868 MHz		
	μ (dBm)	σ (dB)	PRR (%)	μ (dBm)	σ (dB)	PRR (%)
RX4	-127.1	3.6	85.0	-131.2	2.1	92.6
RX5	-131.0	1.43	99.7	-139.4	1.1	1.2

Table 3.5: Descriptive statistics on the performance of the links to RX4 and RX5 during a heatwave in July 2019.

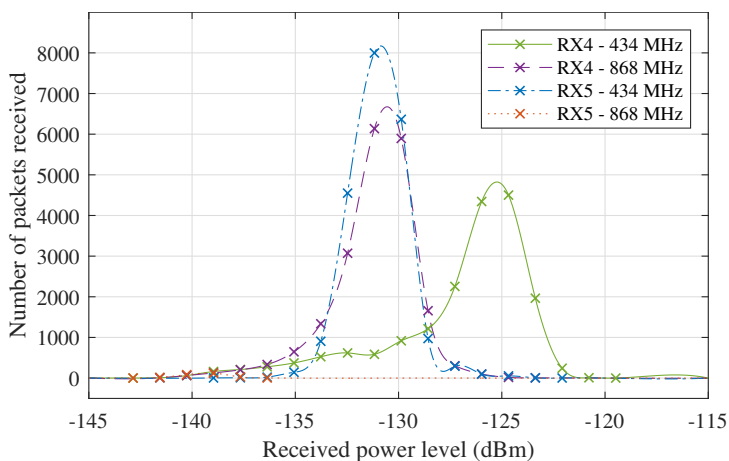


Figure 3.6: Received signal level distributions for the RX4 and RX5 data presented in Fig. 3.5.

Although it is not possible to pinpoint the cause for these fluctuations upon this first observation, it is interesting to see that they occur in the two long-range links, while they are not observed in the data gathered by the nodes located closer to the transmitter or in the data gathered by the TX power monitor. Given that these degradations are indeed observed in both bands by both the RX4 and RX5 receivers and that they occur at different times every day, it can be ruled out that they would be caused by interference. The gradual recession and reappearance of the signal levels — with a time-constant larger than the window size of the moving-average filter used here — further supports this claim. In the long-distance links, the influence of interference is further reduced by the filtering that occurs in the LoRa receiver’s front-end, and by the application of the highly directional Yagi-Uda antennas, which are pointed towards the transmitter. Yet, to rigorously determine the source of the fluctuations shown in Fig. 3.5, the data obtained using RX4 and RX5 will be analyzed more deeply in the following subsections based on the correlation between the links (Section 3.3.3), the periodicity of the fluctuations (Section 3.3.4) and the influence of the weather on these occurrences (Section 3.3.5). Because of the low PRR registered using the 868 MHz link to RX5, this link will be omitted in these analyses.

3.3.3 Daily Signal Fluctuations: Correlation

First, it is interesting to look at the general correlation levels between the long-distance links under study. To this end, normalized correlation coefficients are calculated for all relevant data gathered using these three links (being those portions of the full dataset when both RX4 and RX5 were active). As shown in Table 3.6, they indicate a relatively weak positive correlation between the 434 MHz and 868 MHz data gathered at RX4. More peculiar is the slightly stronger, but negative correlation between the links to RX4 and the 434 MHz link to RX5. Despite their lower values, all of these coefficients are statistically significant with p-values smaller than 0.1 % when a statistical t-test is considered.

		RX4		RX5
		434 MHz	868 MHz	434 MHz
RX4	434 MHz	1	0.2045	-0.2308
	868 MHz	0.2045	1	-0.2788
RX5	434 MHz	-0.2308	-0.2788	1

Table 3.6: Normalized correlation coefficients between power levels received over the long-distance links.

It is interesting to examine how these correlation levels change over time. To this end, the longest uninterrupted measurement campaign that took place at RX4 and RX5 is considered now. This link characterization effort was carried out between October 18, 2018 and May 5, 2019. Descriptive statistics on the subsets of data gathered in this period are shown in Table 3.7.

	434 MHz			868 MHz		
	μ (dBm)	σ (dB)	PRR (%)	μ (dBm)	σ (dB)	PRR (%)
RX4	-123.4	4.4	93.0	-129.0	3.1	93.6
RX5	-136.6	3.23	62.1	N/A	N/A	< 0.001

Table 3.7: Performance of the links to RX4 and RX5 between October 18, 2018 and May 5, 2019.

By daily sampling the correlation of both links for a time window of 14 days (which corresponds to $14 \cdot 24 \cdot 30 = 10080$ measurements points), a high-resolution representation of how the correlation behaviour changes over time can be produced. This specific window size is chosen as it reveals underlying trends, without eliminating specific link characteristics that change over the course of a few days/weeks, as the weather changes. Fig. 3.7 shows the results of this operation for all three combinations of the three links under study. This figure primarily exposes that the correlation levels vary significantly over time and that they sometimes change polarity, which explains why the correlation values are fairly low in Table 3.6.

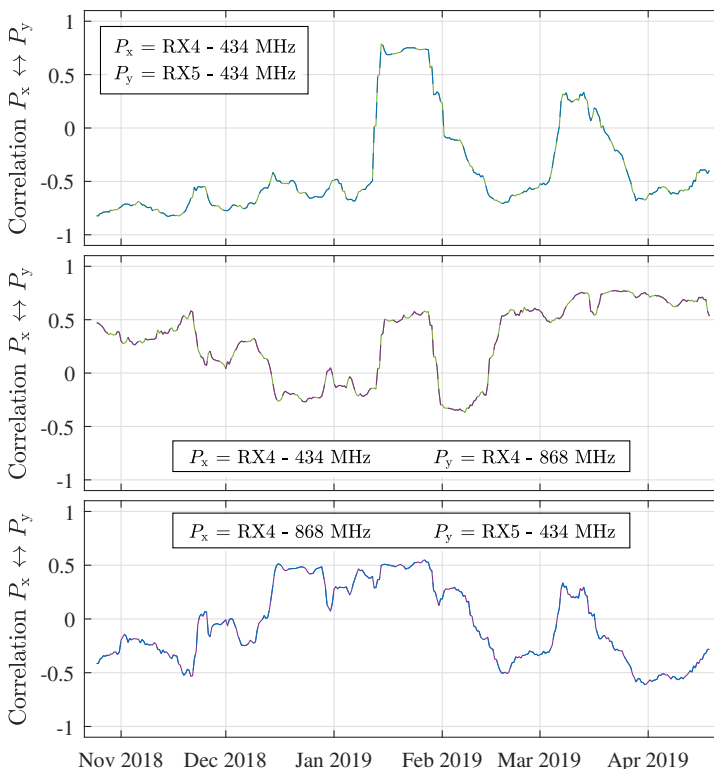


Figure 3.7: Normalized correlation between P_x and P_y over time (window = 14 days).

This behaviour is very apparent for the power levels measured in the same frequency band (434 MHz) at different receiver locations (RX4 and RX5), as shown in the top part of Fig. 3.7. In fact, short-term correlation levels as monitored over time between RX4 and RX5 are fairly high at 434 MHz. Interestingly, during the third week of January, when all three links are strongly and positively correlated with one another, several cm of snowfall were observed in Belgium. It is also observed that the correlation between both frequency bands (middle and bottom plots) tends to diminish during the rest of the winter, while near the end of autumn and throughout spring, these correlation levels are stronger, sometimes flipping between positive and negative levels. Additionally, these results hint at the influence of certain weather conditions on the presented link fluctuations. Consequently, this is investigated further in Section 3.3.5. However, first the strength of the periodicity of the link fluctuations is considered.

3.3.4 Daily Signal Fluctuations: Periodicity

To examine the periodicity of the signal fluctuations, the fast Fourier transform (FFT) was performed on the (linear) power levels gathered on the three long-distance links. To be able to compare the magnitude of certain peaks between different measurement locations, the measured power levels were first normalized by dividing them by their mean value. Hence, the periodicity is calculated as $|\text{FFT}(P_x/\overline{P_x})|$, where P_x indicates the received power levels, $\overline{P_x}$ denotes the average received power and the subscript x indicates the receiver under study. The resulting graphs can be found in Fig. 3.8. To make the result of the FFT-transformation easier to interpret, the frequency axis was inverted to show the period instead. Fig. 3.8 shows very distinct peaks on the 1 day mark, proving that the fluctuations are recurring with a period of exactly one day, at both receiver locations. For the 434 MHz data, smaller peaks can also be observed at the half-day mark.

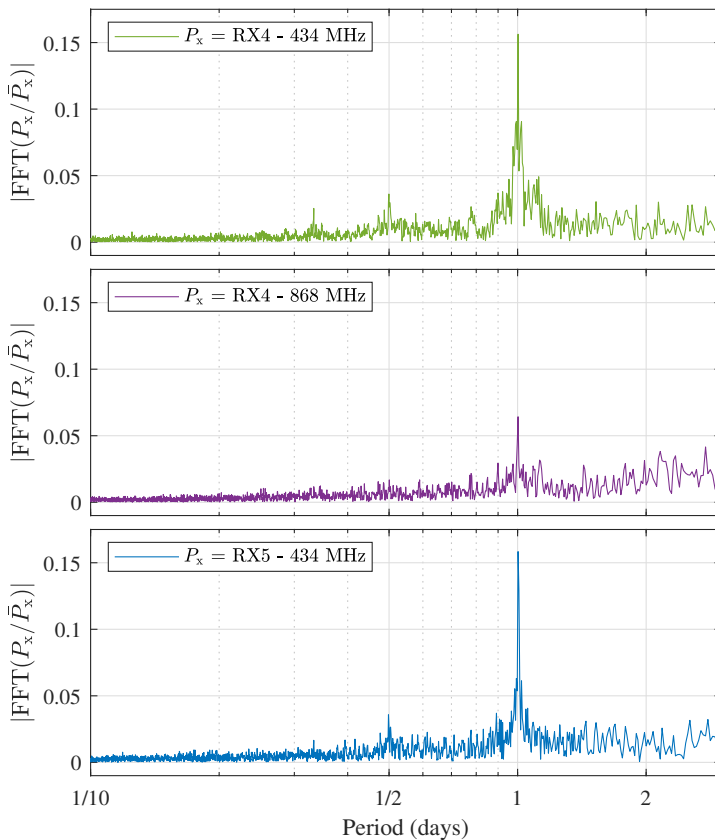


Figure 3.8: FFTs of the normalized linear power levels (P_x/\bar{P}_x) gathered by the receivers at RX4 and RX5.

Additionally, it is also interesting to see how the FFT-profiles presented in Fig. 3.8 change over time. To this end, these profiles were calculated each day with a window size of 14 days, resulting in the spectrograms shown in Fig. 3.9. Again, a very clear trend is observable in all three of these plots: a distinct amount of energy is present on the one-day mark, near the end of autumn and during most of spring, which again hints at a weather-dependency of the signal fluctuations. In addition, during some of these moments, there is also a faint ridge on the half-day mark, resulting in the smaller peaks of Fig. 3.8 that were discussed earlier. Furthermore, there are also some minor FFT-artifacts in these spectrograms, which were found to be caused by packet loss. This explains why the RX5 - 434 MHz spectrogram is the noisiest. As an extension to Fig. 3.9, the amount of energy in the FFT bin corresponding to a period of one day is also shown in Fig. 3.10. This value gives an indication of how the intensity of the signal fluctuations changes over time. As also shown in Table 3.8, there is a strong correlation between the intensity of the signal level fluctuations in all three links under study.

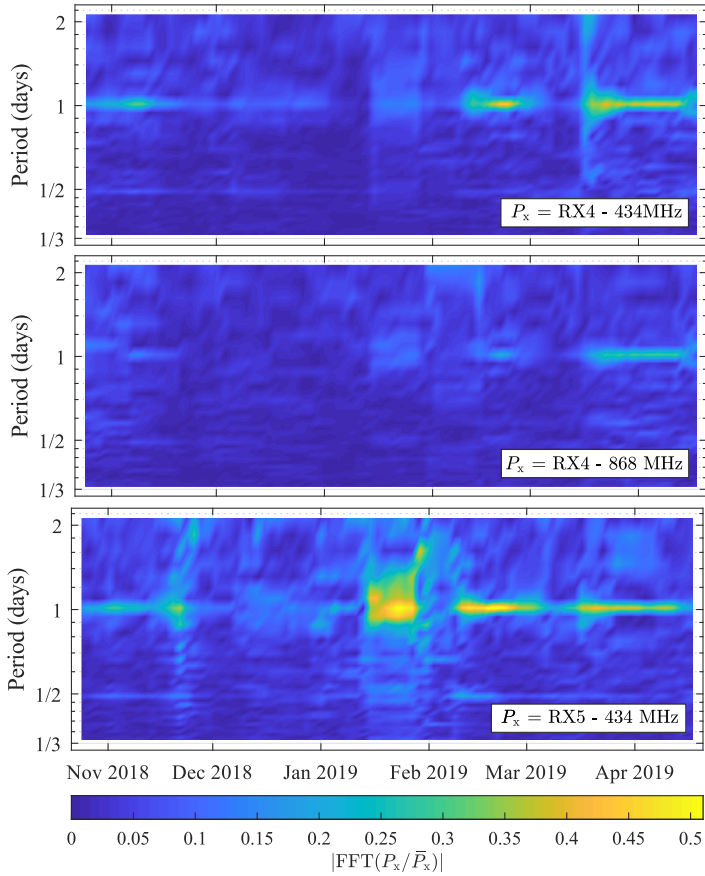


Figure 3.9: Spectrograms of the signal fluctuations observed at RX4 and RX5 (window = 14 days).

		RX4		RX5
		434 MHz	868 MHz	434 MHz
RX4	434 MHz	1	0.8907	0.6775
	868 MHz	0.8907	1	0.6258
RX5	434 MHz	0.6775	0.6258	1

Table 3.8: Normalized correlation coefficients between the periodicity of the fluctuations registered at RX4 and RX5.

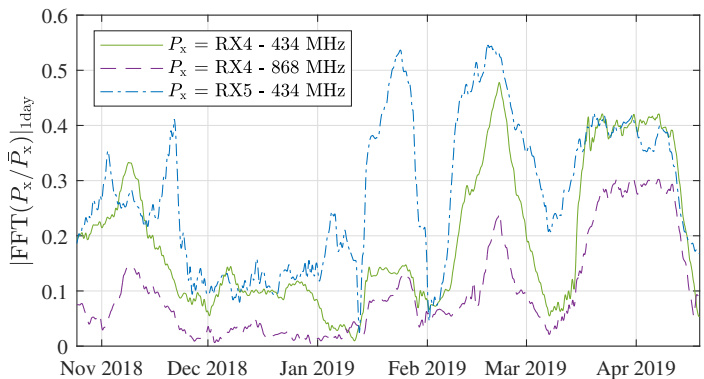


Figure 3.10: Intensity of the signal fluctuations over time, determined as the normalized energy in the FFT bins for period = 1 day in Fig. 3.9.

Complementary to Fig. 3.10, we can also assess the intensity of the fluctuations by considering the standard deviation of the links on a daily basis. For the measurement campaign described in Fig. 3.10, these standard deviations are compiled in a cumulative density function (CDF) to give an indication of the percentage of time in which certain fluctuations were observed. The result, shown in Fig. 3.11, shows that for the RX4 links, the standard deviation of these fluctuations is limited to 3 dB in 60% of the days in the measurement campaign. For the 434 MHz link to RX5, this is the case for 40% of time. Furthermore, for approximately 75% of the days, the standard deviation stayed under 6 dB at both receiver locations. Yet, more extreme variations up to 10 dB did sporadically occur.

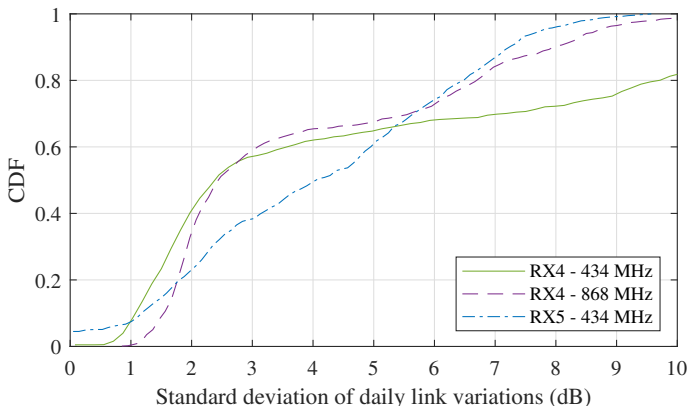


Figure 3.11: CDF of the standard deviations of the received power level fluctuations as measured daily for each link to RX4 and RX5.

3.3.5 Daily Signal Fluctuations: Influence by Weather

Throughout the entire year, many co-occurrences between weather phenomena and signal fluctuations were observed. A specific example of this is shown in Fig. 3.12. Here, the power levels gathered during 8 days in the first half of November 2018 are considered along with the relative humidity and temperature at that time, as provided by the public observatory Armand Pien of Ghent University and part of the dataset presented in [53]. Over the course of these 8 days, the weather was relatively monotonic, which manifested itself in the absence of large temperature and humidity variations on certain days. Interestingly, on November 7, 10, 11 and 12, the absence of temperature and humidity variations directly coincides with less severe drops in signal level.

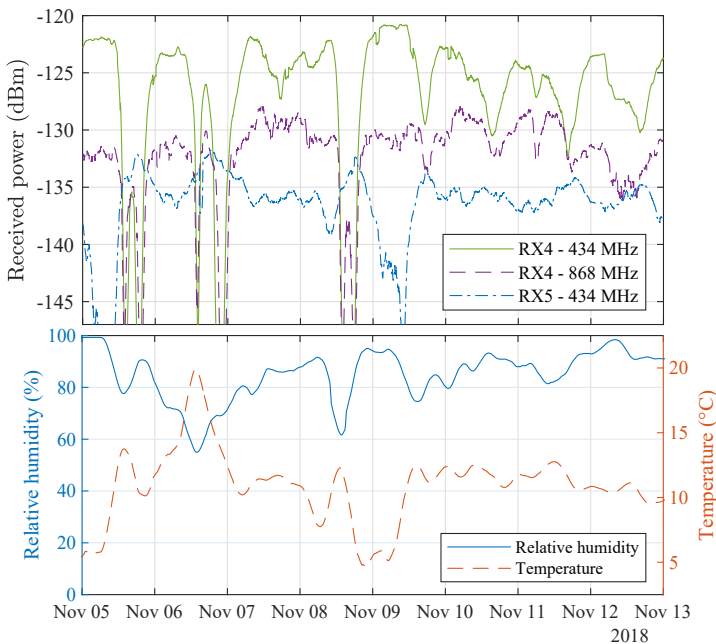


Figure 3.12: Power levels received from November 5 until November 12 2018 (top) and the ambient temperature and relative humidity during those days (bottom).

It is also interesting to zoom in on the snowfall that occurred near the end of January, as mentioned in Section 3.3.3. In all three long-distance links, this snowfall resulted in very strong periodic signal fluctuations and significant signal strength enhancements. The power levels received during these days are shown in Fig. 3.13, where they are compared to the ambient temperature and relative humidity at that time. This figure clearly demonstrates how the received power levels are distinctly dependent on the weather conditions that were observed when these data were gathered. However, as was shown in Section 3.3.3, most of the data that

were gathered are less correlated across the different receiver locations than during these three days in January. Moreover, for the majority of the measurements, an inverse correlation was found between RX4 and RX5 at 434 MHz.

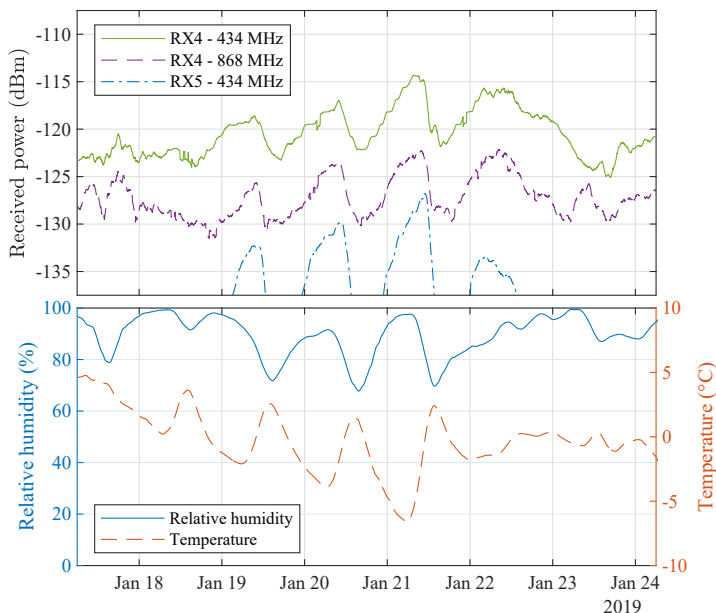


Figure 3.13: Power levels received during several days of episodic light snowfall in January 2019 (top) and the ambient temperature and relative humidity during those days (bottom).

To assess the general weather dependency of the signal fluctuations, larger sets of meteorological data need to be examined as well. In order to provide a general indication of the correlation between the ambient temperature and humidity data and the received power levels, the correlation coefficients between these measures are given in Table 3.9. First of all, these numbers show that the data gathered at RX5 is strongly correlated with the ambient temperature. Because of the very strong negative correlation between the temperature and humidity, this results in a moderately strong correlation with the relative humidity as well. Additionally, Table 3.9 shows a weaker - yet still statistically significant - correlation between the RX4 data and the weather parameters under study. Once more, there is a disparity between the signs of the correlation values.

		Temperature	Humidity
RX4	434 MHz	-0.3226	0.1259
	868 MHz	-0.3040	0.2272
RX5	434 MHz	0.6509	-0.4497

Table 3.9: Normalized correlation coefficients between the received power levels and the ambient temperature and relative humidity.

Again, a lot more can be learned from looking at how these correlation levels change over time. Therefore, the variation of these correlation levels is shown in Fig. 3.14. This figure shows the 14-day moving average correlation between the received power levels and the weather parameters under study. In order to increase the readability of the graph, an additional moving average filter with a window size of 7 days was used as well. Fig. 3.14 mainly shows that the correlation between the signal fluctuations and the weather parameters under study is the strongest for the 434 MHz links. Interestingly, the correlation between the data gathered at RX5 and the temperature is strong and positive during the entire measurement campaign except around those days when snowfall was recorded (see also Fig. 3.13), when it suddenly becomes negative. In general, the correlation behaviour between the received power levels and the relative humidity is less convincing as the relevant correlation coefficients are lower and fluctuate more over time.

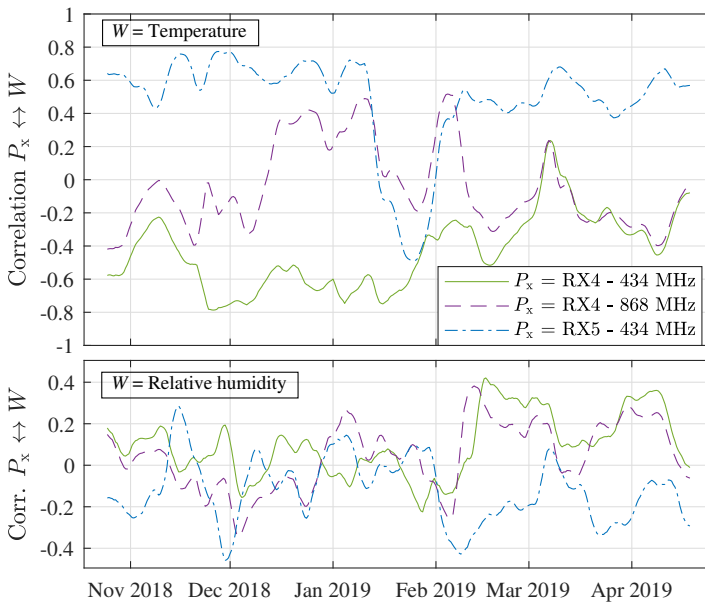


Figure 3.14: Normalized correlation coefficients between the received power levels (P_x) and ambient temperature (top) or relative humidity (bottom) over time.

As a final step in this analysis, the intensity of the temperature and humidity variations is displayed as a function of time in Fig. 3.15. This figure was made in the same way as Fig. 3.10, with the exception that the intermediate step of showing spectrograms first is skipped here. Ultimately, given the great similarity between this figure and Fig. 3.10, this is the best example of how the periodic signal fluctuations presented in this work are strongly connected to the weather. It shows that greater temperature and humidity variations directly correspond to heavier signal drops, which is also reflected in the correlation coefficients that describe this correspondence in Table 3.10.

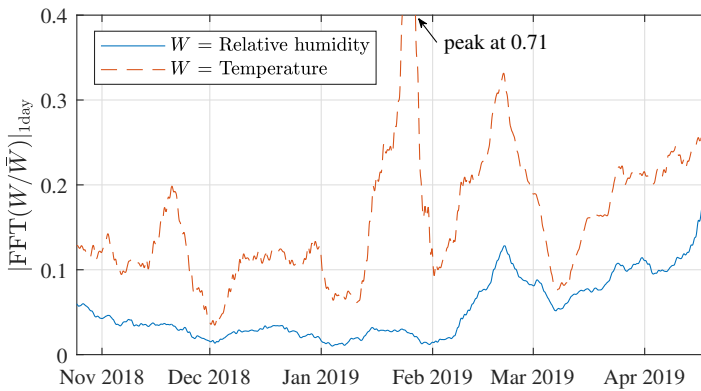


Figure 3.15: Intensity of the weather fluctuations over time, determined as the normalized energy in the FFT bins for period = 1 day, when describing the frequency content of the ambient temperature and relative humidity data.

		Temperature	Humidity
RX4	434 MHz	0.4175	0.7046
	868 MHz	0.4846	0.7220
RX5	434 MHz	0.7305	0.5019

Table 3.10: Normalized correlation coefficients between the intensity of the signal fluctuations (as shown in Fig. 3.10) and the intensity of the variations in ambient temperature and relative humidity (as shown in Fig. 3.15).

3.4 Discussion

Based on the evidence presented in Section 3.3, it is clear that the daily signal deteriorations presented in this work are at least partly caused by weather-related effects. When trying to identify potential contributions of certain weather-related tropospheric propagation effects, a few well-known large-scale effects and mechanisms can be eliminated right away. Scattering by gaseous structures in the direct link path, attenuation due to absorption by gaseous structures and attenuation due to precipitation are unlikely to be direct causes of this phenomenon as literature suggests that these mechanisms only have a noticeable influence at higher frequencies [27], [54]–[56]. Furthermore, potential contributions from tropospheric scintillations are eliminated from the data by the moving average process mentioned in Section 3.3.1. Since the receivers were all located well within the radio horizon of the transmitter (which is approximately equal to 30 km for this transmitter setup), diffraction on the earth itself is not relevant here either.

However, diffraction around static or quasi-static objects such as buildings, infrastructure and vegetation may be playing a role in this phenomenon. In fact, the weather-dependency of the signal degradations indicates that daily variations in tropospheric refractivity may contribute to the signal fluctuations; and as is mentioned in [57] and [58], these changes in refractivity can have an influence on the severity of the fading process caused by diffraction around the static and quasi-static obstructions mentioned earlier. This obstruction fading process would also explain why the signal degradations measured by RX4 and RX5 seem somewhat different, as each link is unique, having its own dominant obstructions. Additionally, as tropospheric refractivity variations may alter the various link paths in different ways, diverse multipath contributions can be expected to impact the performance of the links differently as well. Furthermore, a contribution of troposcatter cannot be ruled out as this mechanism is present in any tropospheric radio link.

In addition to causing certain propagation effects, seasonal weather effects may also have an impact on the performance and reliability of communication hardware. For example, outdoor antennas may suffer from the proximity of water or other precipitation such as snow and ice. In fact, in [17], decreased antenna performance was observed for a wireless link that employed an outdoor antenna during a period of significant rain, while the signal received by an indoor antenna remained largely unimpacted. Finally, extreme temperatures and temperature swings may impact the noise performance of RF-circuitry and power delivery circuitry in exposed IoT hardware.

In the past, effects similar to the signal deteriorations and enhancements presented in this work have been observed and documented for some very long-distance links, generally using higher-altitude antennas at both sides of the links. Most research on this topic concentrates on tropospheric ducting in over-sea paths as this is where super-refractive phenomena occur most often and are most pronounced [59]–[63]. In [64] and [65], the link was made between signal strength enhancements and the presence of anticyclones, which causes low-altitude tropospheric stratifications by

means of subsidence and advection, resulting in anomalous propagation conditions [59], [66], [67]. Furthermore, in more recent link characterization research, it was shown that snowfall has a detrimental effect on link quality [33] and that packet reception is slightly lower in summer months when compared to winter months [41].

With the advent of the IoT and 5G, new long-range, low-power technologies are being developed for which the variable link performance presented in this work and propagation effects presented elsewhere may be very relevant. Not only could these large signal deteriorations cause coverage reduction in these networks, possible increases in range may also cause interference between neighbouring networks. As a result, this may severely lower the quality of service (QoS) for those LPWAN network technologies such as LoRa for which the scalability is already being questioned [6], [7], [29], [30]. Therefore, knowledge about relevant weather-related propagation phenomena should be updated for modern day environments such as large urban, suburban and industrial areas, considering their importance in long-range sensor networks and the IoT, as well as for natural environments where IoT-based monitoring solutions can support initiatives aiming to increase the sustainability of modern society.

A distinction can be made between frequent link fluctuations, caused by variations in refractivity and diffraction around obstacles, ever changing multipath conditions, etc. and infrequent fluctuations, such as those caused by snowfall or extreme heat. Whether either of these types of fluctuations are problematic for a given network setup is to be determined by the designer, based on the characteristics of each network. For example, for sensor communication systems, a link outage may be tolerable, while it might be unacceptable when sharing time-critical information. Figs. 3.10 and 3.11 may aid the system designer in their analysis.

3.5 Conclusion

Custom low-power channel characterization hardware was used to monitor the performance of a (sub)urban LoRa network featuring 10 outdoor wireless links communicating over both the 434 MHz and 868 MHz ISM-bands. A lot of attention went to the performance of two long-distance links spanning 10.6 km and 13.9 km, on which large signal deteriorations were observed. These >15 dB signal drops were found to be correlated significantly between both frequency bands and both receiver locations. They were also found to be periodic with a period of exactly one day, additionally showing some half-day periodicity during certain weather conditions. Upon further analysis, multiple co-occurrences were observed between certain weather conditions and the shape and regularity of the signal deteriorations. The strongest evidence for this relation between the signal fluctuations and the weather is undoubtedly the strong correlation between the intensity of the weather variations and the severity of the signal fluctuations.

Mechanisms causing these signal fluctuations may be tropospheric in nature. More specifically, received power levels may vary due to daily variations in the refractivity of the troposphere, which in turn may have an influence on the fading process caused by diffraction around buildings, infrastructure and vegetation on the link path. Additionally, possible contributions of troposcatter and multipath cannot be ruled out. Finally, diminished antenna performance due to humidity or reduced hardware performance due to temperature fluctuations may also contribute to these effects. Keeping in mind the severity of the signal deteriorations described in this work, it is clear that both frequent as infrequent weather-induced link deteriorations should be taken into account when designing IoT-networks in order to increase their quality and reliability.

References

- [1] GSM Association, *NarrowBand - Internet of Things (NB-IoT)*, <https://www.gsma.com/iot/narrow-band-internet-of-things-nb-iot/>.
- [2] —, *Long Term Evolution for Machines: LTE-M*, <https://www.gsma.com/iot/long-term-evolution-machine-type-communication-lte-mtc-cat-m1/>.
- [3] Dash7 Alliance, *Dash7*, <http://www.dash7-alliance.org/>.
- [4] SigFox Foundation, *SigFox*, <https://www.sigfox.com/en>.
- [5] LoRa Alliance, *LoRa*, <https://www.lora-alliance.org/>.
- [6] A. Augustin, J. Yi, T. Clausen, and W. M. Townsley, “A Study of LoRa: Long Range & Low Power Networks for the Internet of Things”, *Sensors*, vol. 16, no. 9, 2016.
- [7] M. C. Bor, U. Roedig, T. Voigt, and J. M. Alonso, “Do LoRa Low-Power Wide-Area Networks Scale?”, in *Proceedings of the 19th ACM International Conference on Modeling, Analysis and Simulation of Wireless and Mobile Systems*, Malta, Malta, 2016, pp. 59–67.
- [8] U. Noreen, A. Bounceur, and L. Clavier, “A Study of LoRa Low Power and Wide Area Network Technology”, in *2017 International Conference on Advanced Technologies for Signal and Image Processing (ATSIP)*, 2017, pp. 1–6.
- [9] M. Centenaro, L. Vangelista, A. Zanella, and M. Zorzi, “Long-Range Communications in Unlicensed Bands: the Rising Stars in the IoT and Smart City Scenarios”, *IEEE Wireless Communications*, vol. 23, no. 5, pp. 60–67, 2016.
- [10] L. Vangelista, “Frequency Shift Chirp Modulation: The LoRa Modulation”, *IEEE Signal Processing Letters*, vol. 24, no. 12, pp. 1818–1821, 2017.
- [11] M. Chiani and A. Elzanaty, “On the LoRa Modulation for IoT: Waveform Properties and Spectral Analysis”, *IEEE Internet of Things Journal*, vol. 6, no. 5, pp. 8463–8470, 2019.
- [12] L. Gregora, L. Vojtech, and M. Neruda, “Indoor Signal Propagation of LoRa Technology”, in *2016 17th International Conference on Mechatronics - Mechatronika (ME)*, 2016, pp. 1–4.
- [13] P. Neumann, J. Montavont, and T. Nol, “Indoor Deployment of Low-Power Wide Area Networks (LPWAN): A LoRaWAN Case Study”, in *2016 IEEE 12th International Conference on Wireless and Mobile Computing, Networking and Communications (WiMob)*, 2016, pp. 1–8.

- [14] L. H. Trinh, V. X. Bui, F. Ferrero, T. Q. K. Nguyen, and M. H. Le, “Signal Propagation of LoRa Technology Using for Smart Building Applications”, in *2017 IEEE Conference on Antenna Measurements Applications (CAMA)*, 2017, pp. 381–384.
- [15] J. Haxhibeqiri, A. Karağaç, F. Van den Abeele, W. Joseph, I. Moerman, and J. Hoebeke, “LoRa Indoor Coverage and Performance in an Industrial Environment: Case Study”, Limassol, Cyprus, 2017, pp. 1–8.
- [16] J. Petäjäjärvi, K. Mikhaylov, R. Yasmin, M. Hämäläinen, and J. Iinatti, “Evaluation of LoRa LPWAN Technology for Indoor Remote Health and Wellbeing Monitoring”, *International Journal of Wireless Information Networks*, vol. 24, no. 2, pp. 153–165, 2017.
- [17] T. Ameloot, P. Van Torre, and H. Rogier, “A Compact Low-Power LoRa IoT Sensor Node with Extended Dynamic Range for Channel Measurements”, *MDPI Sensors*, vol. 18, no. 7, p. 2137, 2018.
- [18] T. Ameloot, P. Van Torre, and H. Rogier, “Indoor Body-to-Body LoRa Link Characterization”, in *2019 9th IEEE-APS Topical Conference on Antennas and Propagation in Wireless Communications*, Granada, Spain, 2019.
- [19] J. Petäjäjärvi, K. Mikhaylov, A. Roivainen, T. Hanninen, and M. Pettissalo, “On the Coverage of LPWANs: Range Evaluation and Channel Attenuation Model for LoRa Technology”, in *2015 14th International Conference on ITS Telecommunications (ITST)*, 2015, pp. 55–59.
- [20] J. Petäjäjärvi, K. Mikhaylov, M. Pettissalo, J. Janhunen, and J. Iinatti, “Performance of a Low-Power Wide-Area Network Based on LoRa Technology: Doppler Robustness, Scalability, and Coverage”, *International Journal of Distributed Sensor Networks*, vol. 13, no. 3, 2017.
- [21] O. Iova, A. L. Murphy, G. P. Picco, L. Ghio, D. Molteni, F. Ossi, and F. Cagnacci, “LoRa from the City to the Mountains: Exploration of Hardware and Environmental Factors”, in *Proceedings of the 2017 International Conference on Embedded Wireless Systems and Networks*, Uppsala, Sweden: Junction Publishing, 2017, pp. 317–322.
- [22] R. Sanchez-Iborra, J. Sanchez-Gomez, J. Ballesta-Vias, M.-D. Cano, and A. F. Skarmeta, “Performance Evaluation of LoRa Considering Scenario Conditions”, *Sensors*, vol. 18, no. 3, 2018.
- [23] J. Gaelels, P. Van Torre, J. Verhaever, and H. Rogier, “LoRa Mobile-To-Base-Station Channel Characterization in the Antarctic”, *Sensors*, vol. 17, no. 8, 2017.
- [24] T. Ameloot, P. Van Torre, and H. Rogier, “LoRa Base-Station-to-Body Communication With SIMO Front-to-Back Diversity”, *IEEE Transactions on Antennas and Propagation*, vol. 69, no. 1, pp. 397–405, 2021.
- [25] —, “Experimental Parameter Optimization for Adaptive LoRa Modulation in Body-Centric Applications”, in *2020 14th European Conference on Antennas and Propagation (EuCAP)*, Copenhagen, Denmark, 2020.

- [26] S. D. Gunashekar, D. R. Siddle, and E. M. Warrington, "Transhorizon Radiowave Propagation due to Evaporation Ducting", *Resonance*, vol. 11, no. 1, pp. 51–62, Jan. 2006.
- [27] N. Blaustein and C. Christodoulou, "Radio Propagation and Adaptive Antennas for Wireless Communication Links: Terrestrial, Atmospheric and Ionospheric", in John Wiley & Sons, 2007, ch. 6, pp. 175–235.
- [28] L. Barclay, Ed., *Propagation of Radiowaves*, 3rd ed. London, United Kingdom: The Institution of Engineering and Technology, 2013.
- [29] O. Georgiou and U. Raza, "Low Power Wide Area Network Analysis: Can LoRa Scale?", *IEEE Wireless Communications Letters*, vol. 6, no. 2, pp. 162–165, 2017.
- [30] K. Mikhaylov, J. Petäjäjärvi, and T. Haenninen, "Analysis of Capacity and Scalability of the LoRa Low Power Wide Area Network Technology", in *22th European Wireless Conference*, 2016, pp. 1–6.
- [31] M. Cattani, C. A. Boano, and K. Römer, "An Experimental Evaluation of the Reliability of LoRa Long-Range Low-Power Wireless Communication", *Journal of Sensor and Actuator Networks*, vol. 6, no. 2, 2017.
- [32] C. A. Boano, M. Cattani, and K. Römer, "Impact of Temperature Variations on the Reliability of LoRa - An Experimental Evaluation", in *Proceedings of the 7th International Conference on Sensor Networks - Volume 1*, SciTePress, 2018, pp. 39–50.
- [33] N. Souza Bezerra, C. hlund, S. Saguna, and V. A. de Sousa, "Temperature Impact in LoRaWAN Case Study in Northern Sweden", *Sensors*, vol. 19, no. 20, 2019.
- [34] J. Cecílio, P. M. Ferreira, and A. Casimiro, "Evaluation of LoRa Technology in Flooding Prevention Scenarios", *Sensors*, vol. 20, no. 14, 2020.
- [35] L. Parri, S. Parrino, G. Peruzzi, and A. Pozzebon, "Offshore LoRaWAN Networking: Transmission Performances Analysis Under Different Environmental Conditions", *IEEE Transactions on Instrumentation and Measurement*, vol. 70, pp. 1–10, 2021.
- [36] S. Wang, Y. Chen, T. Chen, C. Chang, Y. Cheng, C. Hsu, and Y. Lin, "Performance of LoRa-Based IoT Applications on Campus", in *2017 IEEE 86th Vehicular Technology Conference (VTC-Fall)*, 2017, pp. 1–6.
- [37] Y. Adityawarman and J. Matondang, "Development of Micro Weather Station Based on Long Range Radio Using Automatic Packet Reporting System Protocol", in *2018 International Conference on Information Technology Systems and Innovation (ICITSI)*, 2018, pp. 221–224.
- [38] N. H. Abd Rahman, Y. Yamada, M. H. Husni, and N. H. Abdul Aziz, "Analysis of Propagation Link for Remote Weather Monitoring System through LoRa Gateway", in *2018 2nd International Conference on Telematics and Future Generation Networks (TAFGEN)*, 2018, pp. 55–60.

- [39] R. Marfievici, A. L. Murphy, G. P. Picco, F. Ossi, and F. Cagnacci, “How environmental factors impact outdoor wireless sensor networks: A case study”, in *2013 IEEE 10th International Conference on Mobile Ad-Hoc and Sensor Systems*, 2013, pp. 565–573.
- [40] K. Bannister, G. Giorgetti, and S. Gupta, “Wireless Sensor Networking for Hot Applications: Effects of Temperature on Signal Strength, Data Collection and Localization”, in *Proceedings of the 5th Workshop on Embedded Networked Sensors (HotEmNets 08)*, Citeseer, 2008, pp. 1–5.
- [41] H. Wennerström, F. Hermans, O. Rensfelt, C. Rohner, and L. Nordén, “A Long-Term Study of Correlations between Meteorological Conditions and 802.15.4 Link Performance”, in *2013 IEEE International Conference on Sensing, Communications and Networking (SECON)*, 2013, pp. 221–229.
- [42] F. Schmidt, M. Ceriotti, N. Hauser, and K. Wehrle, “Hotbox: Testing Temperature Effects in Sensor Networks”, *arXiv preprint arXiv:1412.2257*, 2014.
- [43] —, “If You Cant Take the Heat: Temperature Effects on Low-Power Wireless Networks and How to Mitigate Them”, in *European Conference on Wireless Sensor Networks*, Springer, 2015, pp. 266–273.
- [44] C. A. Boano, J. Brown, Z. He, U. Roedig, and T. Voigt, “Low-Power Radio Communication in Industrial Outdoor Deployments: The Impact of Weather Conditions and ATEX-Compliance”, vol. 29, Sep. 2009, pp. 159–176.
- [45] C. Boano, H. Wennerström, M. Zuniga, J. Brown, C. Keppitiyagama, F. Oppermann, U. Roedig, L.-A. Norden, T. Voigt, and K. Römer, “Hot Packets: A Systematic Evaluation of the Effect of Temperature on Low Power Wireless Transceivers”, English, in *Extreme Conference on Communication*, United States: Association of Computing Machinery, 2013, pp. 7–12.
- [46] C. A. Boano, K. Römer, and N. Tsiftes, “Mitigating the Adverse Effects of Temperature on Low-Power Wireless Protocols”, in *2014 IEEE 11th International Conference on Mobile Ad Hoc and Sensor Systems*, 2014, pp. 336–344.
- [47] J. Luomala and I. Hakala, “Effects of Temperature and Humidity on Radio Signal Strength in Outdoor Wireless Sensor Networks”, in *2015 Federated Conference on Computer Science and Information Systems (FedCSIS)*, 2015, pp. 1247–1255.
- [48] B. Collins, *VHF and UHF Communication Antennas*. New York: McGraw-Hill, 1984, 27.2127.22.
- [49] J. S. Huggins, *Mast mountable antenna*, US Patent 10468743B2, 2017.
- [50] T. S. Rappaport, *Wireless Communications: Principles and Practice*. Upper Saddle River, New Jersey: Prentice Hall PTR, 1996.

- [51] ETSI, *Short Range Devices (SRD) Operating in the Frequency Range 25 MHz to 1 000 MHz*, Sophia Antipolis, 2012.
- [52] T. Ameloot, P. Van Torre, and H. Rogier, "LoRa Indoor Performance: an Office Environment Case Study", in *2018 International Applied Computational Electromagnetics Society Symposium - China (ACES)*, Beijing, China, 2018.
- [53] S. Caluwaerts, R. Hamdi, S. Top, D. Lauwaet, J. Berckmans, D. Degrauwe, H. Dejonghe, K. De Ridder, R. De Troch, F. Duchne, B. Maiheu, M. Van Ginderachter, M.-L. Verdonck, T. Vergauwen, G. Wauters, and P. Termont, "The Urban Climate of Ghent, Belgium: A Case Study Combining a High-Accuracy Monitoring Network with Numerical Simulations", *Urban Climate*, vol. 31, p. 100 565, 2020.
- [54] O. Sasaki and T. Akiyama, "Studies on Radio Duct Occurrence and Properties", *IEEE Transactions on Antennas and Propagation*, vol. AP-30, no. 5, pp. 853–858, Sep. 1982.
- [55] ITU-R, *Recommendation ITU-R P676-11: Attenuation by Atmospheric Gases*, Geneva, 2016.
- [56] W. L. Flock, *Propagation Effects on Satellite Systems at Frequencies Below 10 GHz*. NASA Reference Publication 1108, 1983.
- [57] M. O. Asiyó and T. J. O. Afullo, "Tropospheric Propagation Mechanisms Influencing Multipath Fading Based on Local Measurements", in *Proceedings of Southern Africa Telecommunication Networks and Applications Conference*, George, South Africa, 2012.
- [58] A. Vigants, "Microwave Radio Obstruction Fading", *The Bell System Technical Journal*, vol. 60, no. 6, pp. 785–801, 1981.
- [59] S. Gunashekar, "An Investigation of the Propagation of 2 GHz Radio Waves over Sea Paths", Ph.D. dissertation, University of Leicester, Oct. 2006.
- [60] N. Mufti, "Investigation into the Effects of the Troposphere on VHF and UHF Radio Propagation and Interference between Co-Frequency Fixed Links", Ph.D. dissertation, University of Leicester, Oct. 2011.
- [61] V. K. Ivanov, V. N. Shalyapin, and Y. V. Levadny, "Microwave Scattering by Tropospheric Fluctuations in an Evaporation Duct", *Radiophysics and Quantum Electronics*, vol. 52, no. 4, pp. 277–286, 2009.
- [62] S. Najib, R. Mehreen, and N. Mufti, "Modelling of the Vertical Radio Refractivity Near Arabian Sea", in *2016 IEEE-APS Topical Conference on Antennas and Propagation in Wireless Communications (APWC)*, 2016, pp. 217–220.
- [63] J. Lane, "The Radio Refractive Index Gradient over the British Isles", *Journal of Atmospheric and Terrestrial Physics*, vol. 21, no. 2, pp. 157–166, 1961.

- [64] U. Kühn and S. Ogulewicz, “Propagation Measurements at 500 MHz over Sea for Varying Meteorological Parameters”, *Proceedings of the IEE*, vol. 117, no. 5, pp. 879–886, 1970.
- [65] J. A. Lane, “Small Scale Variations of Radio Refractive Index in the Troposphere, Part 1, Relationship to Meteorological Conditions”, *Proceedings of the IEE*, vol. 115, pp. 1227–1234, 1968.
- [66] M. P. M. Hall, *Effects of the Troposphere on Radio Communication*. Institution of Electrical Engineers, 1979.
- [67] G. D. Bye, “Radio-meteorological aspects of clean-air anomalous propagation in NW Europe”, *British Telecom Technology Journal*, vol. 6, no. 3, pp. 32–45, 1988.

PART II

Body-Centric LoRa Networks
Based on System-Integrated
Textile SIW Antennas

4

Wearable 868 MHz LoRa Wireless Sensor Node on a Substrate-Integrated-Waveguide Antenna Platform

Based on "Wearable 868 MHz LoRa Wireless Sensor Node on a Substrate-Integrated-Waveguide Antenna Platform" by Patrick Van Torre, Thomas Ameloot, and Hendrik Rogier, as published in the proceedings of the *49th European Microwave Week (EUMW)*, Paris, France, 2019, pp. 496-499.

And "Long-Range Body-to-Body LoRa Link at 868 MHz" by Patrick Van Torre, Thomas Ameloot, and Hendrik Rogier, as published in the proceedings of the *13th European Conference on Antennas and Propagation (EuCAP)*, Krakow, Poland, 2019, pp. 1-5.



Nowadays, LoRa sensor networks are becoming more and more ubiquitous, owing to their impressive link budget. This link budget is also ideal for body-centric communication. However, when using wearable devices that operate in sub-GHz frequency bands, it is challenging to keep the antenna dimensions sufficiently small. By exploiting substrate-integrated-waveguide technology, a 868 MHz LoRa sensor node has successfully been integrated onto a compact textile antenna platform. This chapter documents the construction and radiation patterns of this wearable node. Additionally, an outdoor long-range performance test is presented as a proof of concept. In static conditions, a range of 1.44 km is observed.

4.1 Introduction

Recently, a number of modulation techniques have become popular for long-range wireless sensor networks operating at sub-GHz frequencies. Different technologies are used in industry, of which LoRa [1], SigFox [2] and Dash7 [3] are the most prominent. These technologies operate in industrial scientific and medical (ISM) frequency bands on a license-exempt basis and incorporate techniques to mitigate interference experienced in this heavily occupied part of the radio spectrum.

LoRa transmissions employ chirp spread spectrum (CSS) modulation, whereas Dash7 uses Gaussian frequency shift keying (GFSK). Both transmission modes allow a relatively high data rate, but LoRa combines this with a significantly larger range. The SigFox standard employs narrow-band bi-phase shift keying (BPSK) and its differential version DBPSK, respectively. A large range is possible but corresponds to a very narrow bandwidth and hence a low data rate. For body-centric wireless sensor networks, LoRa offers the combination of both a long range and an acceptable throughput. Additionally, configurable LoRa transmission parameters allow flexibility to exchange range for more data rate, if desired.

In sub-GHz ISM-bands, operation frequencies correspond to wavelengths of 35 cm or more, which leads to better propagation in indoor, as well as outdoor environments. Particularly in the presence of obstacles, these radio waves have better penetration properties and/or diffract more around obstacles, compared to signals in the widely used 2.45 GHz ISM-band, where the wavelength amounts to only 12 cm. The total number of unlicensed sub-GHz frequency bands is limited. In Europe, for example, the available ISM-bands are at 434 MHz and 868 MHz. Of these two bands, the 434 MHz band has the best propagation properties, but as the wavelength approaches 70 cm, wearable antennas for this band tend to become rather large. The 868 MHz band allows excellent solutions, combining fairly compact wearable antennas with good propagation characteristics.

Although LoRa modulation is applied in a wide range of wireless environments, only a limited number of scientific publications document its performance in body-centric applications. Recent publications about LoRa communication links document Doppler robustness, scalability and coverage in mobile operating conditions [4], [5] as well as long-range fixed links from base station to base station [6]. Channel characterization for a LoRaWAN device has been documented in [7] for a body-to-base-station link. The statistics of the propagation fit to a Nakagami distribution. However, the information in the paper is limited and, moreover, the measurements have been performed with an off-the-shelf LoRa device, not optimized for body-centric applications. To our knowledge, body-to-body communication using LoRa nodes has not been documented in literature before.

In this chapter, a fully functional wearable wireless LoRa sensor node for the 868 MHz band is presented. A substantially different approach from existing literature is adopted, proposing a fully integrated system based on a substrate-integrated-waveguide (SIW) textile antenna, which can unobtrusively be integrated into gar-

ments. The wearable LoRa node combines excellent radiation characteristics and advanced autonomy with a compact size. The LoRa system integrated into this wearable LoRa sensor node was developed recently and is presented in [8]. Its design is implemented on a compact printed circuit board (PCB) and attached to the back of the SIW antenna, which is probe-fed by the circuit board without a transmission line in between. The radiation pattern of the fully integrated wearable LoRa node is compared to the one for the standalone SIW antenna, connected via a SubMiniature version A (SMA) connector. Additionally, as a proof of concept, an outdoor body-to-body measurement campaign is presented, which demonstrates the range that can be achieved by the system. The propagation environment of this range test can be categorized as suburban and features a straight line-of-sight path, surrounded by trees and buildings. The path loss is assessed with the antennas directed towards each other and away from each other. A range of over one kilometer is demonstrated. The hardware design and radiation characteristics of the LoRa unit are presented in Sections 4.2 and 4.3. The long-range body-to-body communication test is discussed in Section 4.4. A conclusion is summarized in Section 4.5.

4.2 Hardware Design

The design of the wearable LoRa node is split in two parts. First, the LoRa hardware, also presented in [8], is briefly discussed in Section 4.2.1. Next, this hardware is integrated on a textile SIW antenna, which is documented in Section 4.2.2.

4.2.1 LoRa Hardware

As broadly discussed in [8], the sensor node circuit board features an RN2483 LoRa transceiver module by Microchip, which is configured by means of a low-power microcontroller. This board is also equipped with flash memory, a real-time clock and a sensor unit. The sensor unit includes a 3-axis accelerometer, gyroscope and magnetometer, all in one chip. Ample flash memory is available to store months of measurement results. The real-time clock is a very low power device, allowing to keep track of the time and date also with the battery disconnected, extracting power from a 0.5 F supercapacitor on the board. The hardware is fully autonomous, being powered by a low profile lithium polymer (LiPo) battery that is also integrated into the wearable system. A special feature of this design is the use of a stepped attenuator in the RF front end. This attenuator can be configured from 0 to 31.5 dB in steps of 0.5 dB and enables measurements with a larger dynamic range [8]. Embedded software, written in C, controls the operation of the system. The mode of operation depends on the nature of the measurements to be performed.

4.2.2 Textile SIW Antenna and System Integration

The textile antenna is based on an eight-mode substrate-integrated-waveguide design, extensively documented in [9]. The antenna can be assembled easily thanks to the automated manufacturing of its main components. Electro-textile materials (tightly-woven, copper-plated taffeta polyester with conductivity 3×10^5 S/m), as well as dielectrics (closed-cell expanded rubber with relative permittivity 1.495 and loss tangent 0.015) are accurately laser-cut to their appropriate sizes, including notches and cut-outs that guide the convenient assembly of the full antenna structure. The polarization of the antenna is elliptical and its radiation is directed away from the body, with the antenna pattern covering approximately a half space in front of the body, when wearing the device on the torso. The largest dimension of the antenna, its diagonal, measures 16 cm. The LoRa hardware discussed in Section 4.2.1 is integrated on the back of the antenna, which is probe-fed directly from a via in the PCB. The low-profile battery mentioned earlier is also attached to the back of the antenna. The fully integrated system is displayed in Fig. 4.1.

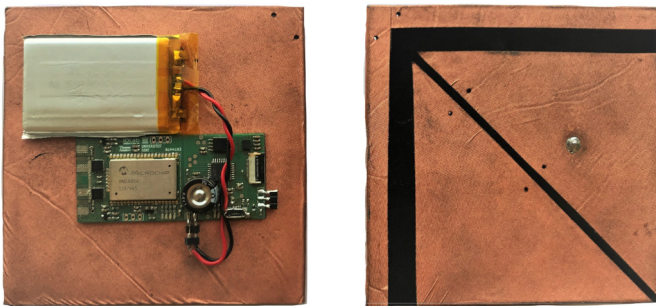


Figure 4.1: The LoRa sensor node and battery fully integrated on the wearable textile SIW antenna.

4.3 Radiation Characteristics

The radiation patterns of the wearable LoRa unit are shown as captured with a standard gain horn in vertical and horizontal polarization in Figs. 4.2a and 4.2b, respectively. The unit under test is programmed in CW mode, transmitting a continuous carrier signal at a fixed frequency. Both antennas/devices were placed in an anechoic chamber. The diagrams in Figs. 4.2a and 4.2b are plotted as effective isotropic radiated power (EIRP) and correspond to the maximum power setting of the unit, being 14 dBm. Two curves are plotted, one for the SIW antenna connected to the transceiver board via an SMA connector, and one for the fully integrated transceiver. Both patch antennas were mounted to an expanded polystyrene

(EPS) arm that rotates in the azimuth plane, which relates to the transverse/axial plane when worn on the human body.

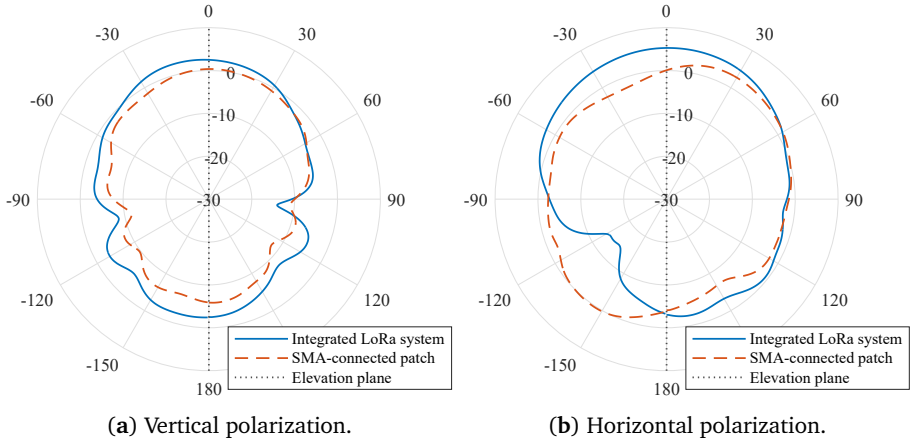


Figure 4.2: EIRP (in dBm) of the fully integrated LoRa system and the standalone patch antenna (connected via SMA) in the azimuth plane.

The radiation pattern measured with a vertically polarized standard gain horn is displayed in Fig. 4.2a, showing a directional radiation pattern which is strongest on broadside, at 0° . Hence, when worn with the ground plane towards to human body, the main lobe is directed away from the body. Interestingly, the EIRP is significantly higher for the fully integrated antenna when compared to the antenna connected via the SMA connector. Clearly some losses are avoided as a result of the direct connection of the antenna to the circuit board of the LoRa hardware. A difference in peak EIRP is also visible for the pattern measured with horizontal polarization in Fig. 4.2b. Some influence of radiation from the PCB is visible for the SMA-connected unit. As shown in Fig. 2.5, this PCB is rather long and narrow, causing the polarization of radiation from it to be predominantly horizontal. Note that the radiated power remains well below the maximum allowed EIRP. The European Telecommunications Standard Institute's (ETSI) Technical Report (TR) 103 526 [10] defines the maximum ERP (relative to a half-wave dipole) as 25 mW, which corresponds to 14 dBm. The EIRP (relative to an isotropic radiator) is 2.15 dB higher, resulting in a maximum value of 16.15 dBm.

Additionally, the radiation pattern of the node when worn on the front of the body is measured in a body-to-body context. To gather these measurements, one test person is placed stationary on one side of the anechoic room, wearing a transmitting node, while the other test person is automatically rotated over 360° on a platform, wearing a node in receive mode. Very short packets containing a 16-bit packet number are continuously sent from the transmitter to the receiver. For each received packet, the received power level is determined and saved to the on-board flash memory. The distance between the test persons is 4.3 m. This measurement

is performed three times, with the stationary person oriented over angles of 0° , 90° and 180° , described as Front, Side and Back orientations. Front means both persons are directed with the wearable nodes pointing toward each other. These measurements yield realistic practical body-to-body link performance by fully eliminating the effect of measurement equipment. Received power levels are shown in Fig. 4.3. These data are treated as far-field results as the distance between transmit and receiving antennas is more than 12λ and the size of the on-body antenna is only 16 cm along the diagonal.

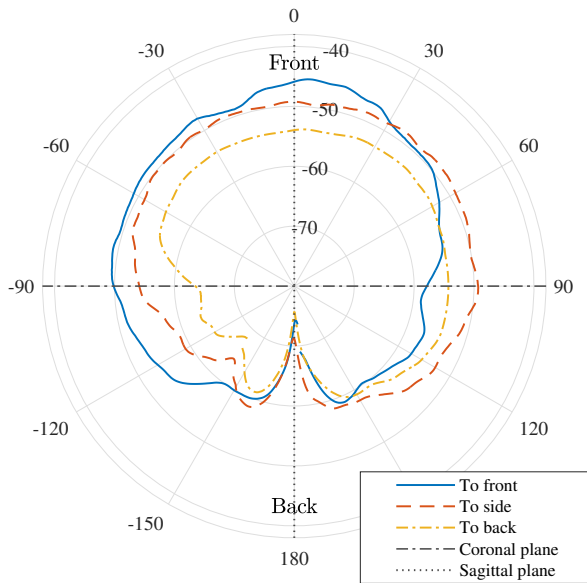


Figure 4.3: Received power levels when rotating one test person over 360° on a moving platform at 4.3 m from another test person, oriented at angles of 0° , 90° and 180° w.r.t. the first person.

4.4 Outdoor Body-to-Body Range Test

4.4.1 Measurement Setup

An outdoor long-range communication test has been performed along the water-sports track in Ghent, Belgium. As seen in Fig. 4.4, the total track is about 2.28 km long. The propagation environment is considered to be suburban, as it is situated outside of the city center but includes a number of high-rise buildings nearby. The propagation is line-of-sight (LoS).

For this measurement campaign, a transmitting node sends LoRa packets with a unique packet number, timestamp and information about the transmit power. The following LoRa parameters are employed: spreading factor (SF) = 7, bandwidth



Figure 4.4: Satellite view of the watersports track in Ghent, Belgium. Map Data: Google, Landsat/Copernicus.

(BW) = 125 kHz, code rate (CR) = 4/5, preamble length = 10 chips and cyclic redundancy check (CRC) is active. The CRC guarantees that all received packets are error free, which is important in order to obtain accurate measurement data. The data rate is 293 bps with this configuration. Each packet is transmitted at four different transmit powers, employing the transceiver's power settings combined with the stepped attenuators. Another node is configured as the receiver, logging signal-to-noise ratios (SNRs), packet numbers, power information and timestamps into local flash memory.

To obtain information about the distance covered, both test persons are using a sports tracker app on their smartphones. Positioning data from the sports trackers is obtained in steps of 50 m, along with the relevant timestamps. Linear interpolation is performed on these data, providing a pair of distances to the starting point for every second of measurement. As shown in Fig 4.4, the watersports track is perfectly straight, hence the total distance covered is determined by simple addition of the distances from the two sports trackers.

The measurement is started halfway along the watersports track with perfect LoS propagation conditions. First the persons are walking away from each other, up to a distance of 1.44 km with the antennas oriented away from each other. At the end of this path, both persons turn around and approach each other again, until they meet. Clearly, the directional radiation pattern of the wearable antennas is expected to produce a large difference when antennas are oriented away from or toward each other.

4.4.2 Results and Analysis

The resulting received power levels are displayed in Fig. 4.5, with separate curves for the test persons walking towards and away from each other. As expected, the received power is higher when the antennas are directed towards each other. Comparing the signals for equal distances along the first 100 m, the average difference is 6 dB. For these first 100 m, the direct LoS path is clearly dominant and based on linear fitting the path loss was determined in this region.

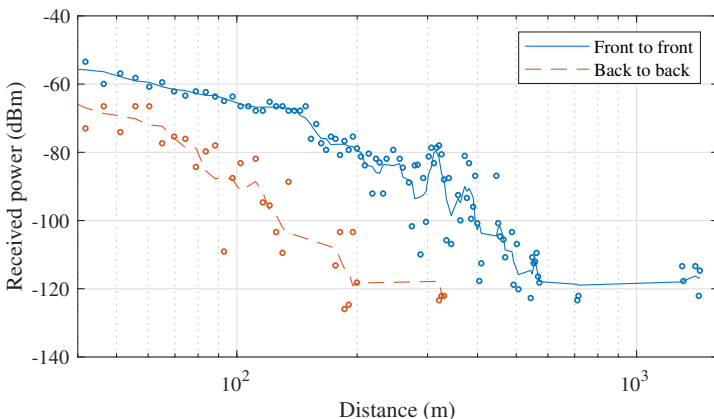


Figure 4.5: Power levels received in the outdoor body-to-body range test as a function of distance and test person orientation. Test persons are either walking towards each other (front to front) or walking away from each other (back to back). Dots show the raw measurements, whereas the lines display the moving average over the last five received packets.

When the test persons are approaching each other, the received power is approximated by means of a linear fit of P_{RX} in dBm to $\log_{10}(d)$, with d the distance in meters. The resulting equation is given by

$$P_{RX} = 11 \text{ dBm} - 52 \cdot \log_{10}(d). \quad (4.1)$$

The corresponding path loss (L) is given as

$$L(d) = L(d_0) + 10 \cdot n \cdot \log_{10}\left(\frac{d}{d_0}\right), \quad (4.2)$$

with the path loss exponent $n = 5.2$ and $d_0 = 1$ m. Similarly, with the test persons walking away from each other, the path loss exponent is found to be 3.9. According to [11], the expected path loss exponents for an urban environment are in the range 2.5 – 4.

For larger distances, in particular with the antennas pointed towards each other, the signal fluctuations become more apparent. This indicates the increasing influence of ground reflections and probably also reflections on the surrounding buildings. The range which is obtained with little packet loss is about 200 m with the antennas facing away from each other, whereas it is easily more than 500 m when the antennas are pointed towards each other. As the signals become weaker, a lot of packet loss occurs. For example, at a distance of 700 m, only two packets were received during the walk. For larger distances nothing is received while walking.

Note however, that at the end of the trajectory, at 1440 m distance, several packets are received. At the end of the path, the test persons were standing still for a while. While walking, the mobile transmissions produce Doppler spread on the already noisy signals at this distance. Hence, the LoRa transceiver is observed to decode the packets better when the channel is more stable. It is interesting to see that the specifications for the LoRa SX1276 transceiver chip [12], on which the Microchip RN2483 unit is based, mention the importance of an accurate crystal oscillator as a reference, indirectly revealing a possible sensitivity of the receiver to frequency offsets.

4.5 Conclusion

A fully autonomous textile-antenna-based wearable LoRa node was successfully designed, fabricated and tested. Different variations of the node's radiation patterns were presented, highlighting the benefits of directly integrating the LoRa system and the antenna. In an outdoor body-to-body range test, communication was reliable for a range of 500 m with the antennas pointed towards each other and over 200 m with both antennas pointing away from each other. The decoding of weak signals appears to suffer from movement during the transmission as channel fluctuation and Doppler spread are observed to compromise the link at greater distances. In static conditions, a range of 1.44 km was observed.

References

- [1] LoRa Alliance, *LoRa*, <https://www.lora-alliance.org/>.
- [2] SigFox Foundation, *SigFox*, <https://www.sigfox.com/en>.
- [3] Dash7 Alliance, *Dash7*, <http://www.dash7-alliance.org/>.
- [4] J. Petäjajarvi, K. Mikhaylov, M. Pettissalo, J. Janhunen, and J. Iinatti, “Performance of a Low-Power Wide-Area Network Based on LoRa Technology: Doppler Robustness, Scalability, and Coverage”, *International Journal of Distributed Sensor Networks*, vol. 13, no. 3, 2017.
- [5] J. Gaelens, P. Van Torre, J. Verhaever, and H. Rogier, “LoRa Mobile-To-Base-Station Channel Characterization in the Antarctic”, *Sensors*, vol. 17, no. 8, 2017.
- [6] N. Jovalekic, V. Drndarevic, E. Pietrosemoli, I. Darby, and M. Zennaro, “Experimental Study of LoRa Transmission over Seawater”, *Sensors*, vol. 18, no. 9, 2018.
- [7] P. A. Catherwood, S. McComb, M. Little, and J. A. D. McLaughlin, “Channel Characterisation for Wearable LoRaWAN Monitors”, in *Loughborough Antennas Propagation Conference (LAPC 2017)*, 2017, pp. 1–4.
- [8] T. Ameloot, P. Van Torre, and H. Rogier, “A Compact Low-Power LoRa IoT Sensor Node with Extended Dynamic Range for Channel Measurements”, *MDPI Sensors*, vol. 18, no. 7, p. 2137, 2018.
- [9] S. Agneessens, “Coupled Eighth-Mode Substrate Integrated Waveguide Antenna: Small and Wideband with High Body-Antenna Isolation”, *IEEE Access*, vol. 6, pp. 1595–1602, 2018.
- [10] ETSI, *System Reference Document (SRdoc); Technical Characteristics for Low Power Wide Area Networks Chirp Spread Spectrum (LPWAN-CSS) Operating in the UHF Spectrum below 1 GHz*, Sopia Antipolis, 2018.
- [11] J. Isabona, “Urban Area Path loss Propagation Prediction and Optimisation Using Hata Model at 800MHz”, *IOSR Journal of Applied Physics*, vol. 3, pp. 8–18, Jan. 2013.
- [12] *137 MHz to 1020 MHz Low Power Long Range Transceiver*, SX1276/77/78/79, Rev. 5, Semtech Corporation, Aug. 2016.

5

Indoor Body-to-Body LoRa Link Characterization

Based on "Indoor Body-to-Body LoRa Link Characterization" by Thomas Ameloot, Patrick Van Torre and Hendrik Rogier, as published in the proceedings of the *2019 IEEE-APS Topical Conference on Antennas and Propagation in Wireless Communications (APWC)*, Granada, Spain, 2019, p. 42-47.



This chapter examines the performance of LoRa in an indoor, body-centric IoT context. This is achieved by deploying custom-made wearable LoRa nodes, featuring a textile substrate-integrated-waveguide antenna, on the chests of test persons who walked around in a modern office environment, logging the strength of the link between them. Both the influence of the test person's bodies as well as the challenging environment, which includes large masses of reinforced concrete, are investigated. The measured channel characterization data illustrate the excellent performance achieved by combining the building penetration qualities of signals at sub-GHz frequencies and the high link budget of the LoRa modulation standard.

5.1 Introduction

As wireless sensor networks (WSNs) are being rolled out all over the world, relentlessly expanding the Internet of Things (IoT), a lot of research and development is being carried out to continuously improve the performance of low-power network technologies. At the heart of this new communication technology revolution are emerging industrial standards such as LoRa [1], SigFox [2] and NB-IoT [3]. They enable distributed sensors to operate autonomously for years on end, often communicating over sub-GHz industrial, scientific and medical (ISM) bands. Furthermore, large distances can be covered owing to the excellent propagation characteristics associated with these sub-GHz bands, enabling ever more widespread WSN deployments.

Yet, the potential applications of these technologies are far more diverse than industrial sensor network deployments. By integrating low-power sub-GHz network systems on wearable antennas, off-body communication ranges can be greatly improved, provided that a lower data rate is acceptable. The superior building penetration offered by radio wave propagation at sub-GHz frequencies is also expected to enable these body-worn systems to operate in far more demanding indoor environments than previously deemed possible.

To assess the performance of such a system, a custom-built LoRa node [4] was integrated on a wearable substrate-integrated-waveguide (SIW) antenna [5]. By transmitting very short packets with a low LoRa spreading factor, a decent repetition rate can be achieved to probe channels and characterize off-body wireless links. This chapter presents the characterization of an indoor body-to-body LoRa link, with the focus on determining building penetration behavior.

In the experiments to determine this behavior, two persons equipped with wearable LoRa nodes perform a set of walks in a modern building featuring different construction materials, including large masses of reinforced concrete. The chapter is structured as follows. In Section 5.2, the wearable LoRa system, measurement strategy and indoor environment used for these experiments are discussed. Next, the statistics of the recorded signal levels are analyzed to characterize the performance of the body-to-body LoRa link. Finally, in Section 5.4, a conclusion to this work is formulated.

5.2 Materials and Methods

5.2.1 Wearable LoRa system

To probe the indoor channel, two custom-built wearable LoRa nodes are used. These nodes consist of a compact, low-power LoRa system with extended dynamic range for performing channel measurements [4], integrated on a substrate integrated waveguide textile antenna [5]. Each node is powered using a low-profile lithium polymer (LiPo) battery, which is also integrated on the antenna. The front

and back sides of this wearable LoRa system are shown in Fig. 4.1. A more detailed description of this system is presented in [6].

5.2.2 Measurement Strategy

To gather an acceptable amount of data points, a high channel probing rate should be used to examine the highly fluctuating indoor channel between two moving nodes. To this end, a LoRa spreading factor (SF) of 7 and a bandwidth (BW) of 125 kHz are used, resulting in a packet transmission rate of 10 packets per second. Unfortunately, relying on a low spreading factor also decreases the overall sensitivity of the system and whilst a LoRa system can receive packets with powers down to -140 dBm using a SF of 12, this system rarely receives packets with a power smaller than -125 dBm. Hence, it should be noted that when a lower data-rate is acceptable, a larger range than what is presented in this work could be achieved by adjusting the LoRa modulation settings.

The dynamic range of the LoRa node is extended by continually probing the channel with different dynamic range settings (see also Chapter 2) and combining the data from all datasets. Statistical performance data of the channel under investigation are always based on the measurements gathered when using the most sensitive dynamic range settings. However, to create graphical representations of the received power and calculate average values, packets that saturated the receiver are omitted in favor of those packets that were received with a dynamic range shifted up by using the on-board RF-attenuators, as was thoroughly described in [4]. In all experiments, packets are transmitted with a transmission power of 10 dBm.

5.2.3 Indoor environment

The measurements presented in this chapter were gathered in an office environment on the top floors of a large, modern office building in Ghent, Belgium. The floors of this building are very similar and consist of a large concrete core, which is surrounded by a square hallway giving access to a large number of offices, located along the outside of the building. These offices and additionally, two meeting rooms located on the inside of the hallway, are separated by thin, plastered walls, which contrasts with the heavy concrete that makes up the rest of the core of the building. An annotated plan of one of these floors is shown in Fig. 5.1. Additionally, photo's taken at markers B and D are shown in Fig. 5.2. As LoRa has already been proven to work fairly well in indoor experiments [7]–[10], this work mainly investigates the influence of the thick floor structures and heavy concrete core of this building, features which are very commonplace in modern high-rise buildings.

In all of the experiments presented in this chapter, two male test persons with an average build each wore one LoRa node on the front of the chest. During most experiments, one of the test persons walked around the concrete core of the building with his LoRa node continually transmitting packets to the receiver which was stationary either in the hallway, at marker A, or in an office, at marker Z, on

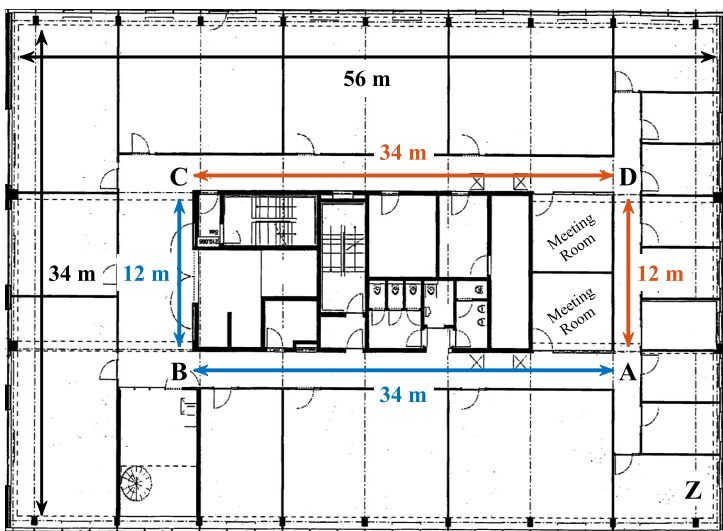


Figure 5.1: Annotated layout of the indoor office environment.

the bottom right of the building layout on Fig. 5.1. In a final experiment, the transmitter was stationary on the eleventh floor, inside the stairwell in the center of the building, while the receiver walked down the stairs until the connection was lost. At this point, the receiver turned around and climbed the stairs back up to the eleventh floor.



Figure 5.2: Photo's taken at markers B (top) and D (bottom).

5.3 Measurement Results and Analysis

5.3.1 Nodes on the same office floor

First, a series of walks were performed where both test persons remained on the same floor. As was partly mentioned in the previous section, the transmitter moved through the hallway in different directions while the receiver was either located in the hallway (A), pointing the receiving node towards the transmitter, or located inside the corner office (Z), pointing the receiver away from the hallway. Because of the great similarity between the data gathered in both of these situations, the choice was made to describe those measurements that were gathered in the latter case only by means of their averages, as described in Table 5.1. The sets of measurements corresponding to those situations when the receiver was located in the hallway are shown in Fig. 5.3. Additionally, these data are represented graphically on the floor plan of the building in Figs. 5.4 and 5.5 for those situations when the transmitter walked away from or in the direction of the receiver respectively. To reduce the contribution of small scale fading, averaging is performed by walking all of the trajectories twice and taking a moving average with a window size corresponding to 4 m.

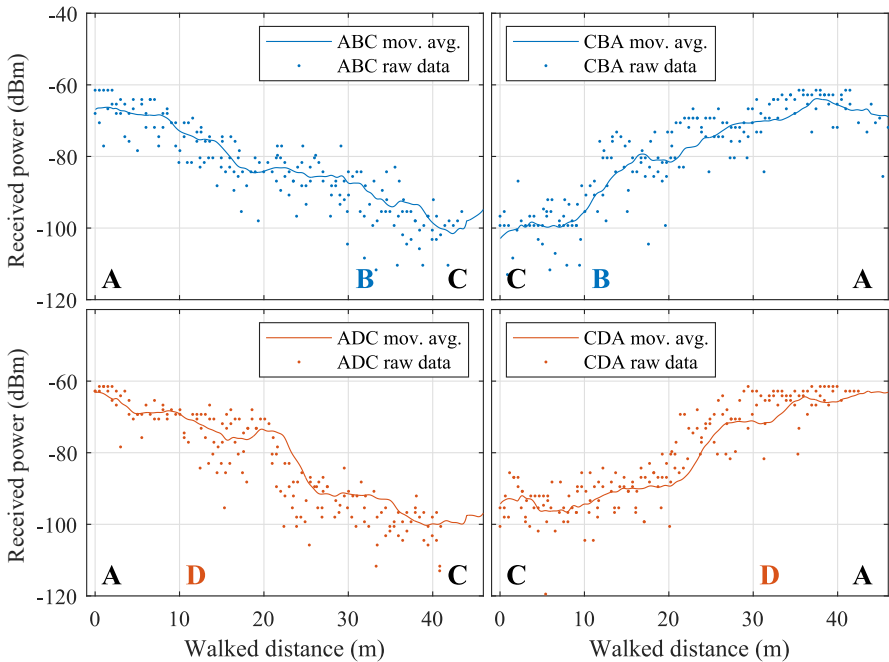


Figure 5.3: Power received by the node at marker A when the transmitter walked around the core of the building in different directions. (Mov. avg. = moving average over a window corresponding to 4 m.)

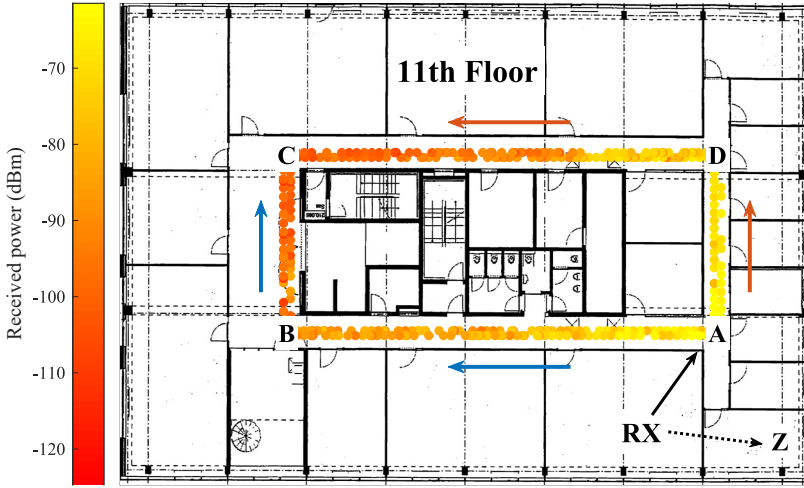


Figure 5.4: Power received when moving away from the receiver (A), with both nodes located on the same floor (ABC & ADC).

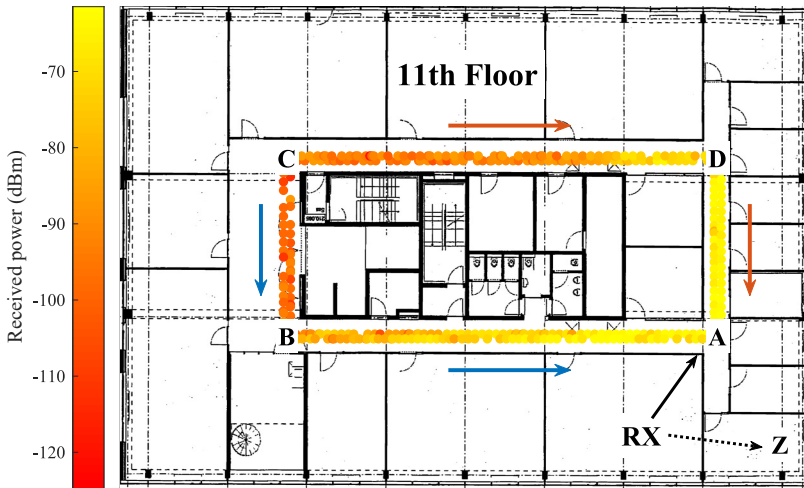


Figure 5.5: Power received when moving towards the receiver (A), with both nodes located on the same floor (CBA & CDA).

In the data presented in Fig. 5.3, the presence of the concrete core of the building is clearly visible. For example, in the CBA data, a sudden increase in signal level is registered around marker B, which is where the link between the nodes is suddenly line-of-sight (LoS) as the moving test person turns the corner towards the receiver. A corresponding drop in signal level is not present in the ABC data because these data were gathered when moving away from the transmitter. In this situation,

communication is mostly dependent on wave reflections, which are still present after turning the corner towards C. In the ADC and CDA data, similar signal level jumps are present. However, these do not occur around marker D, but at a point eight meters to the left of this marker. This corresponds to the location where the walls of the building's core are made of concrete instead of the plaster that was used to separate the meeting rooms.

		RX @ A			
		ABC	ADC	CBA	CDA
RX @ A	ABC				
	ADC	0.69			
	CBA	3.64	2.95		0.63
	CDA	3.01	2.31		

		RX @ Z			
		ABC	ADC	CBA	CDA
RX @ Z	ABC		5.49		
	ADC				
	CBA	6.38	11.86		3.51
	CDA	2.86	8.35		

		RX @ Z			
		ABC	ADC	CBA	CDA
RX @ A	ABC	8.33	13.82	1.96	5.47
	ADC	9.03	14.51	2.65	6.16
	CBA	11.97	17.46	5.60	9.11
	CDA	11.34	16.83	4.96	8.48

Table 5.1: Means of the average power differences (in dB) between the 11th floor trajectories and both receiver locations, expressed as the excess power level observed in the trajectory indicated by the row label w.r.t. the trajectory indicated by the column label.

When considering the average signal level differences between the walked trajectories (as given in Table 5.1), it can be seen that on average, the body of the walking test person combined with the radiation pattern of the antenna [6] contribute to the attenuation by 2.98 dB for those trajectories where the receiver was stationed at marker A and 7.36 dB for those situations when the receiver was standing in the corner office (Z). In the latter situations, the differences vary widely between 2.86 dB and 11.86 dB. This illustrates that the added complexity of the propagation paths, caused by the additional walls, doors and furniture between the test persons, contributes strongly to these attenuation values.

When comparing the averaged signal levels received at Z to those received at A, an average additional attenuation of 7.04 dB is observed for those trajectories where the transmitter moved towards the receiver (CBA and CDA). For the opposite trajectories (ABC and ADC), this additional attenuation is equal to 11.42 dB. Natu-

rally, these negative contributions to the link budget are caused by the walls and furniture between markers Z and A, in addition to the body of the test person wearing the receiving node (which, as mentioned before, was turned away from the hallway). Furthermore, not having a LoS component in the data gathered at Z also influences these averages. To assess the reliability of the links discussed in this section, packet reception ratios (PRRs) were also calculated, all of which exceeded 99 %.

Finally, for the LoS sections of the trajectories, path loss exponents (n) can be calculated using equation (4.2). These path loss exponents amount to $n = 1.87$ and $n = 0.79$ when approaching the receiver (at A) from B and D respectively. The former of these values is more realistic because of the higher number of samples used to obtain it. Nevertheless, both of them are very low, which is testament to the fact that propagation through an empty hallway is subject to a waveguiding effect, which lowers the path loss. Received power levels for these trajectories are shown in Fig. 5.6.

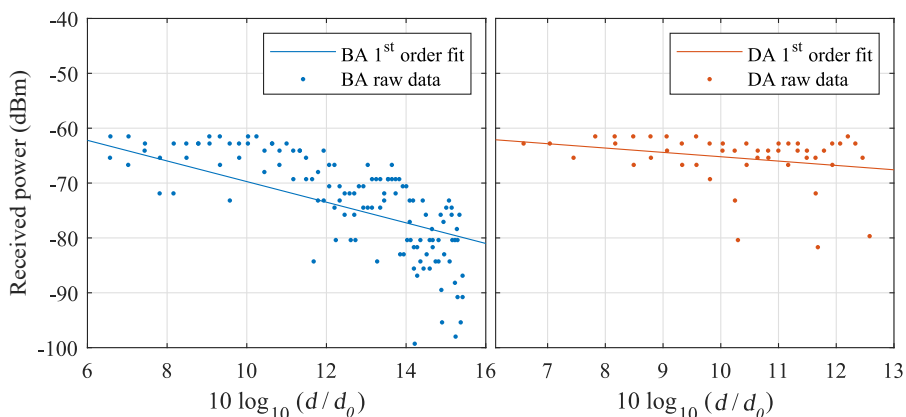


Figure 5.6: Received power levels for the LoS trajectories BA and DA.

5.3.2 Nodes on different office floors

In a second experiment, the walks presented in the previous subsection were performed again, but this time with the transmitter walking on the floor below the one where the receiver was stationed. These data are presented in the same way as those of the previous experiments in Figs. 5.7, 5.8 and 5.9 and Table 5.3.

In general, it can be seen that the link is lost a lot more frequently now, which is also reflected in the PRRs of these links, presented in Table 5.2. It is also clear that the orientation of the test persons matters more in this experiment, since there is significantly less link budget available to buffer the fluctuations caused by the movement of the test persons. This is most apparent in the average power differ-

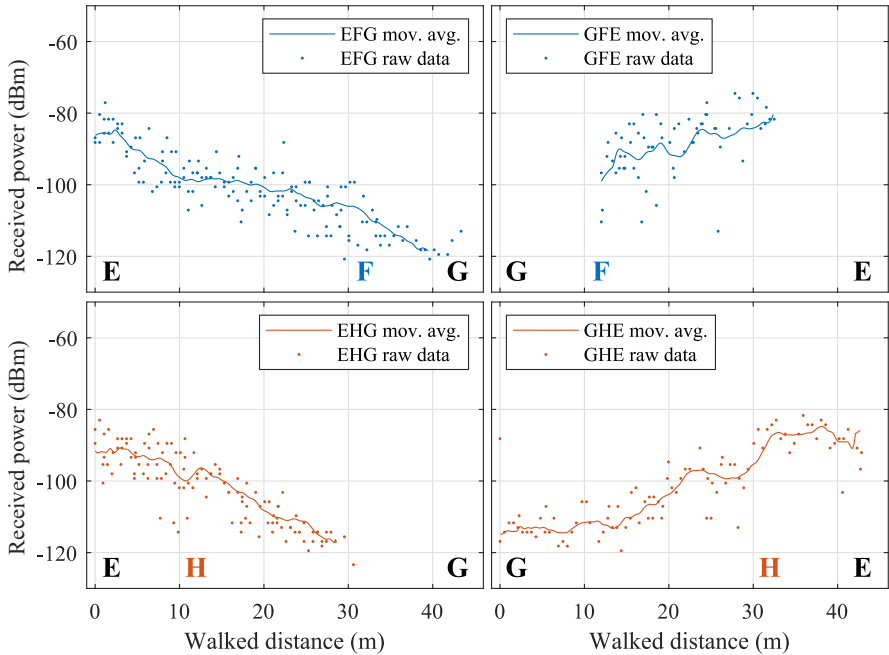


Figure 5.7: Power received by the node at marker A when the transmitter walked around the core of the building in different directions, on the floor below. (Mov. avg. = moving average over a window corresponding to 4 m.)

	PRR (%)	
	RX = A	RX = Z
EFG	88.8	58.6
EHG	69.4	34.7
GFE	41.3	40.8
GHE	67.2	54.9

Table 5.2: PRRs for links between nodes on different floors.

ences shown in Table 5.3. It should also be mentioned that the influence of the concrete core of the building is less pronounced in these data, as there is no LoS component anymore. In fact, now that all parts of the trajectories are non-line-of-sight (NLoS), the average power level differences between the data gathered when walking towards or away from the receiver are bigger (at 9.48 dB and 7.90 dB for receiver locations A and Z respectively). Nevertheless, the difference between having the receiver at A or Z is clearly smaller and this time, having it in the corner office (Z) actually ensures better reception than having it in the hallway (A). This last observation can be explained by considering the radiation patterns of the textile antennas. These roughly radiate in a hemisphere away from the front of the

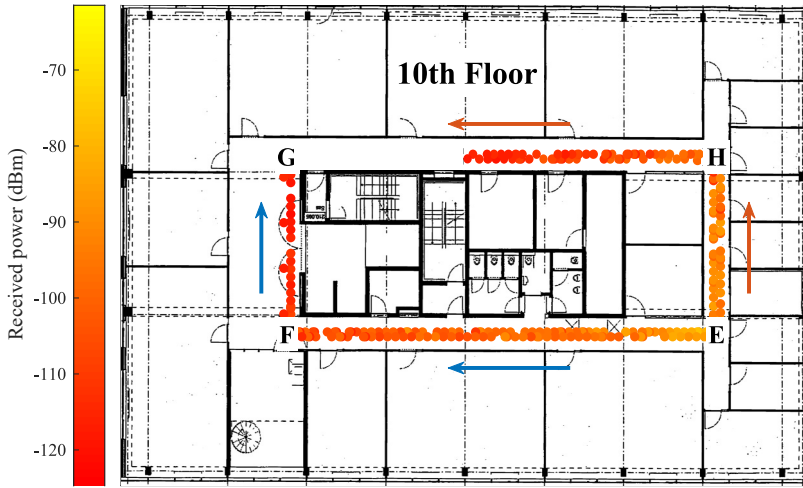


Figure 5.8: Power received when moving away from the receiver (A), with both nodes located on different floors (EFG & EHG).

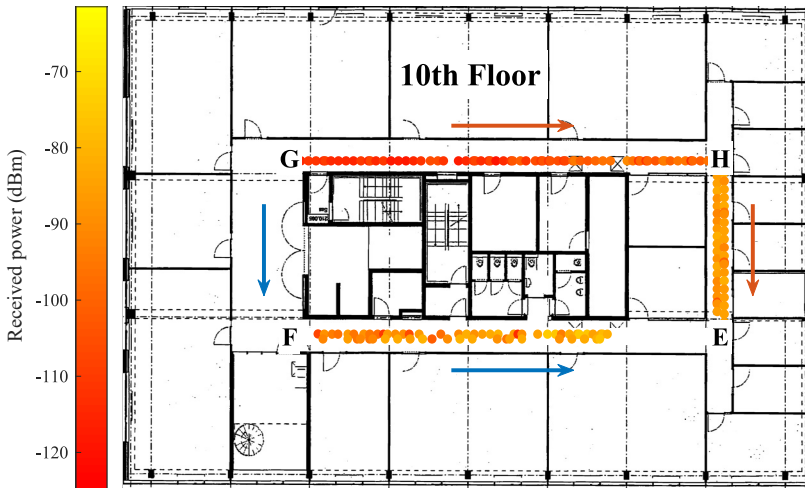


Figure 5.9: Power received when moving towards the receiver (A), with both nodes located on different floors (GFE & GHE).

test person's body, thus exhibiting less gain in directions along the coronal plane of the wearer. Consequently, when both test persons are directly below each other, a lower link budget is to be expected.

The average differences between the data gathered when the nodes were on the same floors and those gathered when they were on different floors are shown in Table 5.4. When only considering data gathered using the same walking trajec-

		RX @ A			
		EFG	EHG	GFE	GHE
RX @ A	EFG	0.20			
	EHG				
	GFE	10.59	10.90	4.38	
	GHE	8.11	8.31		

		RX @ Z			
		EFG	EHG	GFE	GHE
RX @ Z	EFG	0.60			
	EHG	0.60			
	GFE	8.04	7.44		
	GHE	8.37	7.76	0.33	

		RX @ Z			
		EFG	EHG	GFE	GHE
RX @ A	EFG	12.65	12.05	4.61	3.13
	EHG	12.34	11.74	4.30	2.93
	GFE	23.24	22.64	15.20	14.87
	GHE	18.86	18.25	10.82	11.24

Table 5.3: Means of the average power differences (in dB) between the 10th floor trajectories and both receiver locations, expressed as the excess power level observed in the trajectory indicated by the row label w.r.t. the trajectory indicated by the column label.

ries, on average, link budget reductions of 16.47 dB and 20.92 dB are observed for receiver locations A and Z respectively. These are directly caused by the structure between both floors. When considering all possible combinations of link trajectories and receiver locations, a more general impact of the floor structure on the performance of the links can be obtained. This yields an average signal level reduction of 18.09 dB when comparing any arbitrary link between nodes on the same floor to one between nodes on different floors.

5.3.3 Nodes in stairwell

To evaluate the link between two nodes inside the core of the building, one test person took place in one of the stairwells on the eleventh floor while the other one descended these stairs until the connection was lost. At this point, the second test person turned around and climbed the stairs back up again. The raw and averaged data for these trajectories are presented in Fig. 5.10. They show an average extra loss of 13.79 dB for each additional floor between the test persons. Note that the average signal level flattens out near the end of the range because packets with a power lower than the sensitivity of the receiving node are not received anymore, skewing the average data at that point. Additionally, some of the direct

		RX @ A			
		EFG	EHG	GFE	GHE
RX @ A	ABC	18.61	18.81	8.77	10.50
	ADC	19.31	19.51	10.24	11.20
	CBA	22.25	22.45	14.24	14.14
	CDA	21.62	21.82	12.09	13.51

		RX @ Z			
		EFG	EHG	GFE	GHE
RX @ Z	ABC	23.51	22.90	15.47	13.41
	ADC	18.28	17.68	10.24	7.93
	CBA	30.72	30.13	22.70	19.79
	CDA	26.44	25.84	18.40	16.28

Table 5.4: Means of the average power differences (in dB) between the 10th and 11th floor trajectories for both receiver locations, expressed as the excess power level observed in the trajectory indicated by the row label w.r.t. the trajectory indicated by the column label.

link power penetrating through the stairs is filtered out by the radiation patterns of the antennas, contributing to link fluctuations in this experiment. Consequently, the estimated average signal loss for each additional floor between the nodes is probably somewhat conservative in this last experiment. However, as both nodes are in the same stairwell, signal reflections definitely increase the average received power as well.

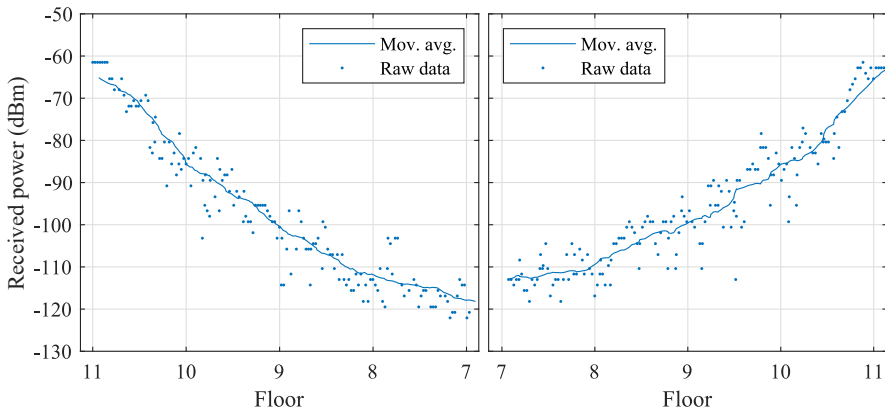


Figure 5.10: Power received by the node walking up and down the stairs between the 7th and 11th floors (Mov. avg. = moving average with a window of 30 measurements).

5.4 Conclusion

Several LoRa body-to-body link characterization efforts were performed in a modern office environment. They show that even when using a low spreading factor of 7, a near-perfect link can be established when both nodes are moving on the same floor, even when a thick concrete building core separates them. When moving across floors, packet reception ratios start to decline when using this lower spreading factor, because of the lower sensitivity of the node when using these settings. When comparing both cases, it is shown that links across two floors are subject to an additional average loss of 18.06 dB. Additionally, packet reception statistics fluctuate significantly for the different links, which illustrates how indoor propagation is strongly governed by reflections. These may sometimes balance the losses experienced by shadowing of the body of the test persons, which were found to equal 2.98 dB in line-of-sight situations, and 7.36 dB in non-line-of-sight situations. Yet, as can be expected, in other locations, these reflections may just as well degrade the link performance further, resulting in a worst-case average loss of 11.86 dB when compared to a situation without body shadowing. In general, LoRa was found to be an excellent modulation technique for low-power and low data-rate communication in challenging indoor environments, even when using a low spreading factor. Furthermore, its performance could be increased significantly by using higher spreading factors, when a very low data-rate is acceptable.

References

- [1] LoRa Alliance, *LoRa*, <https://www.lora-alliance.org/>.
- [2] SigFox Foundation, *SigFox*, <https://www.sigfox.com/en>.
- [3] GSM Association, *NarrowBand - Internet of Things (NB-IoT)*, <https://www.gsma.com/iot/narrow-band-internet-of-things-nb-iot/>.
- [4] T. Ameloot, P. Van Torre, and H. Rogier, “A Compact Low-Power LoRa IoT Sensor Node with Extended Dynamic Range for Channel Measurements”, *MDPI Sensors*, vol. 18, no. 7, p. 2137, 2018.
- [5] S. Agneessens, “Coupled Eighth-Mode Substrate Integrated Waveguide Antenna: Small and Wideband with High Body-Antenna Isolation”, *IEEE Access*, vol. 6, pp. 1595–1602, 2018.
- [6] P. Van Torre, T. Ameloot, and H. Rogier, “Wearable 868 MHz LoRa Wireless Sensor Node on a Substrate-Integrated-Waveguide Antenna Platform”, in *2019 49th European Microwave Week (EUMW)*, Paris, France, 2019.
- [7] L. Gregora, L. Vojtech, and M. Neruda, “Indoor Signal Propagation of LoRa Technology”, in *2016 17th International Conference on Mechatronics - Mechatronika (ME)*, 2016, pp. 1–4.
- [8] L. H. Trinh, V. X. Bui, F. Ferrero, T. Q. K. Nguyen, and M. H. Le, “Signal Propagation of LoRa Technology Using for Smart Building Applications”, in *2017 IEEE Conference on Antenna Measurements Applications (CAMA)*, 2017, pp. 381–384.
- [9] J. Petäjäjärvi, K. Mikhaylov, R. Yasmin, M. Hämäläinen, and J. Iinatti, “Evaluation of LoRa LPWAN Technology for Indoor Remote Health and Wellbeing Monitoring”, *International Journal of Wireless Information Networks*, vol. 24, no. 2, pp. 153–165, 2017.
- [10] J. Haxhibeqiri, A. Karaağaç, F. Van den Abeele, W. Joseph, I. Moerman, and J. Hoebeke, “LoRa Indoor Coverage and Performance in an Industrial Environment: Case Study”, Limassol, Cyprus, 2017, pp. 1–8.

6

Experimental Parameter Optimization for Adaptive LoRa Modulation in Body-Centric Applications

Based on "Experimental Parameter Optimization for Adaptive LoRa Modulation in Body-Centric Applications" by Thomas Ameloot, Patrick Van Torre and Hendrik Rogier, as published in the proceedings of the *14th European Conference on Antennas and Propagation (EuCAP)*, Copenhagen, Denmark, 2020, pp. 1-5.



The relentless expansion of the Internet of Things is fueled by constant innovations in low-power wide-area network technologies. Industry forerunners such as LoRa, SigFox and NB-IoT continuously seek to achieve larger communication ranges while consuming as little energy as possible. These efforts, in turn, facilitate vast performance increases in a wide range of related application areas, such as body-centric communication. However, as the resulting communication links need to accommodate mobile users, many nodes will regularly be communicating using suboptimal LoRa modulation parameters as these users move around. Adaptive LoRa modulation aims to solve this by optimizing these parameters in real-time, based on the location of the user and the actual performance of the wireless link. In this chapter, the optimal settings for one of the key LoRa modulation parameters, the spreading factor, are experimentally determined. The results also yield insight into more general LoRa communication aspects by analyzing packet reception and channel throughput data gathered in an urban environment.

6.1 Introduction

In recent years, sub-GHz, low-power communication technologies such as LoRa [1], SigFox [2] and NB-IoT [3] have seen a strong rise in popularity. These technologies facilitate the deployment of large sensor networks with nodes that can operate autonomously for years on end before running out of battery power. Additionally, by using sub-GHz frequencies, they can cover much larger areas than more traditional wireless network technologies such as WiFi (IEEE 802.11) and Bluetooth, when a lower data rate is acceptable. In addition to being one of the strongest contenders for market share, LoRa is very popular for research applications as well since it has been found to offer great performance [4]–[8], while also being license-free, allowing users to build their own networks on the link layer without having to pay for a subscription. For these reasons, but also by virtue of its slightly larger global coverage, its network layer counterpart LoRaWAN is actively being adopted for a wide range of Internet of Things (IoT) applications.

One application area where sensor network technologies such as LoRa are significantly changing the playing field is body-centric communication. As a result of the very low power usage associated with LoRa, this technology can be integrated onto wearable nodes without requiring an excessively large battery to power the on-board communication hardware. In previous research, LoRa has shown good promise for body-to-body and body-to-base-station sensor communication applications that do not require a high data rate [9], [10]. One of the greatest strengths of this modulation technology lies without doubt in its reconfigurability. By changing the spreading factor (SF), bandwidth (BW) and code rate (CR) of a LoRa message, the communication protocol can be configured to favor either a larger range or a higher data rate. In body-centric LoRa propagation research, gathering as much measurement points as possible is usually more important than achieving a large communication range. Consequently, lower spreading factors are favored for these applications. However, this results in a systematic underestimation of the performance that can be achieved with LoRa. To explore which data rates can really be obtained at which communication ranges, a system should be implemented that actively optimises the LoRa modulation settings used at a given node location, based on a real-time assessment of the link performance. By judiciously choosing the right settings, such an optimization scheme also optimizes the data rate, which is very valuable for mobile sensor communication systems that benefit from a (relatively) higher data rate.

Some more details and considerations concerning this proposed system are discussed in the next section. Then, in Section 6.3, the measurement strategy and setup used to determine some of the key design considerations and performance predictions for such a system are introduced. The data gathered using this setup are presented and analyzed in Section 6.4 and finally, in Section 6.5, a conclusion to this work is formulated.

6.2 Proposed System

As previously mentioned, the premise of this work is to get both sides of a body-to-base-station LoRa link to agree on a set of modulation settings that co-optimize the data rate at which they communicate and the coverage of the network they are in. As seen in Table 6.1, the LoRa receiver sensitivity specifications provided by Semtech for its most popular SX1276 LoRa radio [11] show that the largest variation in link performance results from varying the LoRa spreading factor (SF). Due to the popularity of using a bandwidth (BW) of 125 kHz and the added complexity of optimizing both bandwidth and spreading factor, a fixed BW setting of 125 kHz will be used for all of the experiments in this chapter. For similar reasons, a fixed code rate (CR) of 4/5 is selected. Additionally, it should be noted that when already using the largest spreading factor and smallest bandwidth, one last way of increasing the data rate is switching to a different modulation technology supported by the LoRa radio such as frequency shift keying (FSK). However, as this work is in the scope of characterizing the performance of LoRa links, this option will not be considered further.

		SF					
		7	8	9	10	11	12
BW	125 kHz	-123	-126	-129	-132	-133	-136
	250 kHz	-120	-123	-125	-128	-130	-133
	500 kHz	-116	-119	-122	-125	-128	-130

Table 6.1: 868 MHz LoRa receiver sensitivities (in dBm) for different bandwidth (BW) and spreading factor (SF) settings. [11]

Since LoRa transmits in public ISM-bands, a duty cycle restriction between 0.1 and 10% is imposed by law, depending on the specific sub-band [12]. This work explores the performance of LoRa in the 868 MHz band, where the strictest rules apply. This severe limitation on the time that a communication system is allowed to use the band should be taken into account when implementing an adaptive LoRa modulation scheme.

The amount of air time required to transmit a LoRa packet is inversely proportional to the useful bit rate R_b of a LoRa link, which can be calculated using [11]

$$R_b = \text{SF} \cdot \frac{\text{BW}}{2^{\text{SF}}} \cdot \text{CR}. \quad (6.1)$$

However, as can be seen in Fig. 6.1, lab measurements performed with a Rohde and Schwartz FSV40 spectrum analyzer and a commercial LoRa transceiver show that some packet sizes are more efficient than others, which is due to how information is encoded in a LoRa message. In Fig. 6.1, the air time needed to transmit a packet of a certain length with a certain spreading factor is indeed described by a stepped line instead of the smooth line that would be expected from 6.1.

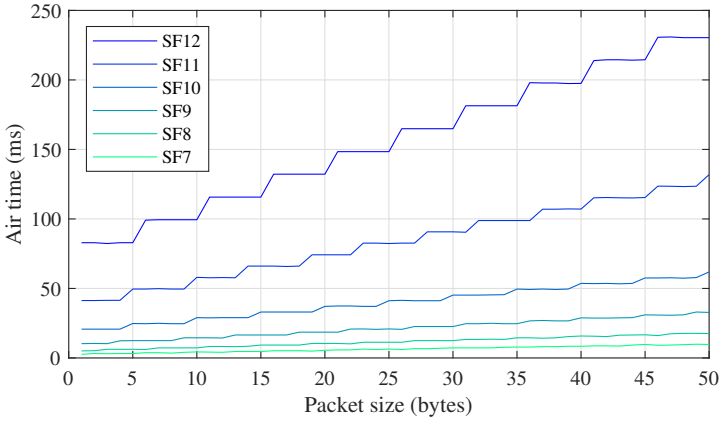


Figure 6.1: Experimentally determined air time for packets transmitted with different spreading factors (SF) and packet sizes.

Based on these air times, the maximum data rates that can be achieved for each of the spreading factor and packet size choices shown in Fig. 6.1 were evaluated. The results are shown in Fig. 6.2.

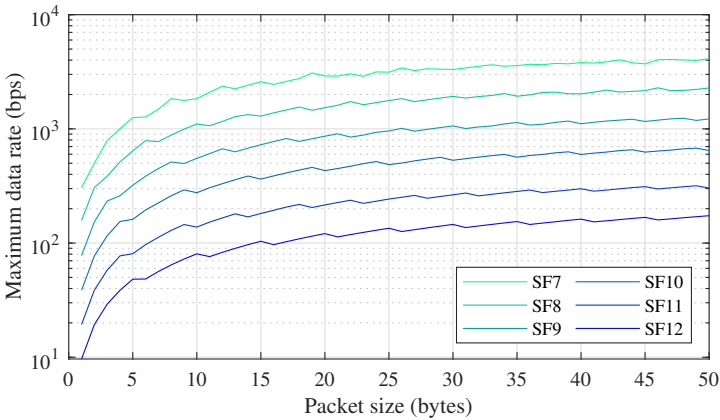


Figure 6.2: Maximum data rates for packets transmitted with different spreading factors (SF) and packet sizes, based on the air times presented in Fig. 6.1.

From Fig. 6.2, one might decide that the packet size should be chosen as large as possible to optimize the data rate. However, the packet loss probability should also be taken into account. For example, when choosing a large message payload size to reduce the impact of communication overhead, a lost packet may have a very severe impact on the achieved data rate. As the channel between mobile wireless nodes can be heavily impacted by packet loss, practical link characterization data

should be used to determine the optimal packet size. Additionally, for all current LoRa transceivers, using larger packet sizes also limits the rate at which the channel can be probed, limiting the amount of data available to perform accurate channel estimation.

Another hurdle to realize adaptive LoRa modulation lies in constructing a good algorithm to determine how and when to switch between certain modulation settings. Naturally, messages sent with different settings than those expected by the receiver will not be received and, as such, there needs to be a robust way for nodes to commonly decide on which settings to use for the next packet. Reliably agreeing on these settings could prove to be a real challenge, especially when having to comply with the duty cycle limitations currently imposed on the relevant ISM-bands.

6.3 Measurement Setup

An exploratory measurement campaign was performed to make informed choices about how to configure a wearable LoRa communication system with a dynamic data rate and coverage co-optimization scheme and how to accurately predict the performance of such a system. Therefore, a LoRa link between a base station and a test person equipped with wearable LoRa nodes was characterized. Along with descriptions of the measurement methodology and the propagation environment used for this test, a brief overview of the wearable hardware is given in the next subsections.

6.3.1 Hardware

The wireless nodes employed to characterize the body-centric LoRa link are based on the custom-built research-oriented LoRa platform described in [13]. One of these nodes serves as a base station. Therefore, it is connected to a vertically polarized omnidirectional antenna. This base station was placed on the roof of a modern office building, at a height of 57 m.

On the mobile side of the link, a test person was outfitted with two wearable LoRa nodes. To construct these nodes, the LoRa platform mentioned earlier was integrated onto a substrate-integrated-waveguide (SIW) antenna implemented in bendable textile materials. This yields a low-profile system that can be worn unobtrusively on the front and back of the torso. The test person was equipped with two nodes because the radiation patterns of each textile antenna only reliably covers a single hemisphere. Combining the results from two nodes worn on opposite sides of the body also mitigates the signal losses caused by body shadowing.

6.3.2 Measurement Strategy

The LoRa base station discussed in the previous subsection was configured to continuously transmit very short packets while constantly varying the spreading factor of the LoRa modulation. All packets are sent with a transmit power of 10 dBm. The receive nodes are synchronized with the transmitter through their internal clocks. They update their clocks every time a packet is received with a spreading factor of 12, since these packets are the most likely to be received. Upon each packet reception, the receiving nodes also measure the signal-to-noise ratio (SNR) of the LoRa message and store this value in their flash memory, along with a timestamp and packet number. This enables us to relate this value to the location of the test person, which is logged using a GPS app on the test person's smartphone.

6.3.3 Propagation Environment

As mentioned earlier, the base station (TX) was placed at a height of 57 m, on the roof of a modern office building. As seen in Figs. 6.3 and 6.4, the test person moved along a number of trajectories to the north of this building. Most notably, he traveled along both sides of the nearby canal and along the wide avenue running from the oddly shaped roundabout (marked with a *) in the north of the area to the high-tech industry park south of this canal. It is important to note that this avenue crosses the waterway and a nearby highway by means of a relatively wide bridge, providing a terrain that is slightly elevated compared to the surrounding area, whereas the roads next to the canal are slightly more recessed than most of the other terrain.

6.4 Measurement Results and Analysis

To assess the performance of the LoRa link setup described in the previous section, the SNR values were registered for all successfully received packets. The results are shown in Fig. 6.3. First, this figure shows that there are a lot of areas where the link is shadowed by obstacles in the environment. For example, the (already slightly recessed) road on the south side of the canal is almost completely shadowed by buildings and trees. Additionally, for a lot of packets that were received, a negative SNR was registered, which again shows the benefits of using a modulation technology such as LoRa for outdoor off-body applications. Furthermore, it is also apparent that certain areas very close to the base station are less well covered due to shadowing by the building. Yet, it should also be mentioned that, in contrast to the link performance in these non-line-of-sight (NLoS) areas, packet reception was a lot higher in line-of-sight (LoS) areas, such as along the avenue crossing the canal.

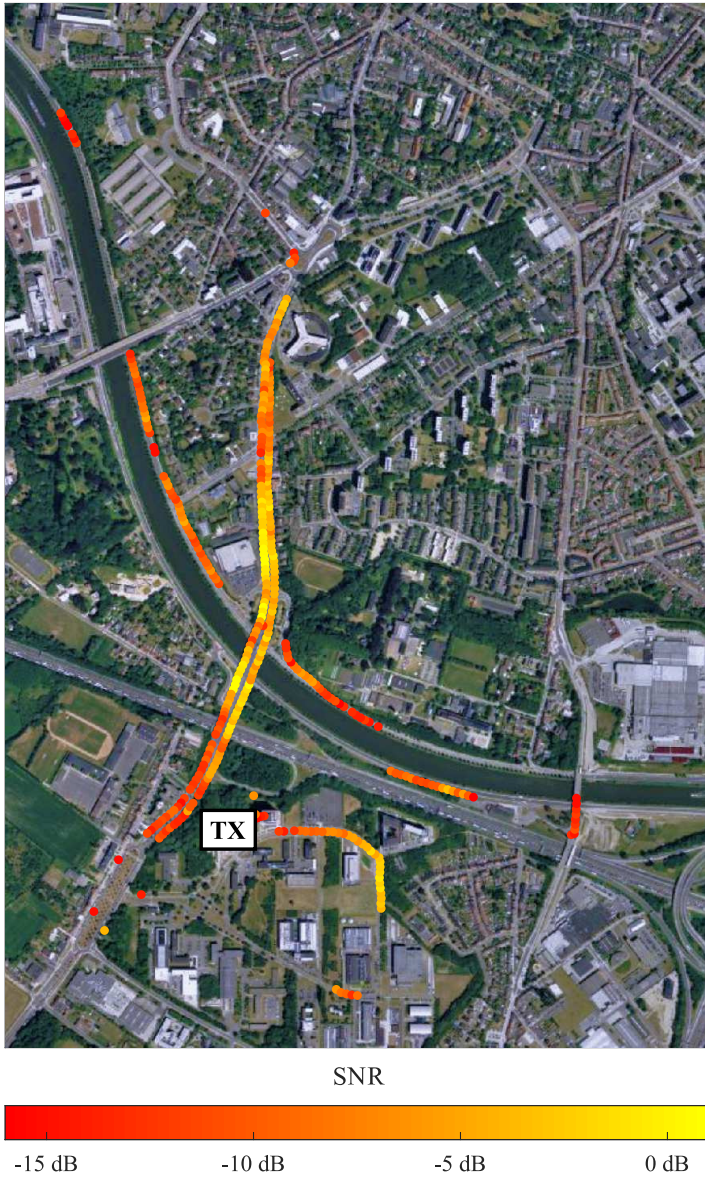


Figure 6.3: Signal-to-noise ratios measured by the wearable LoRa nodes.

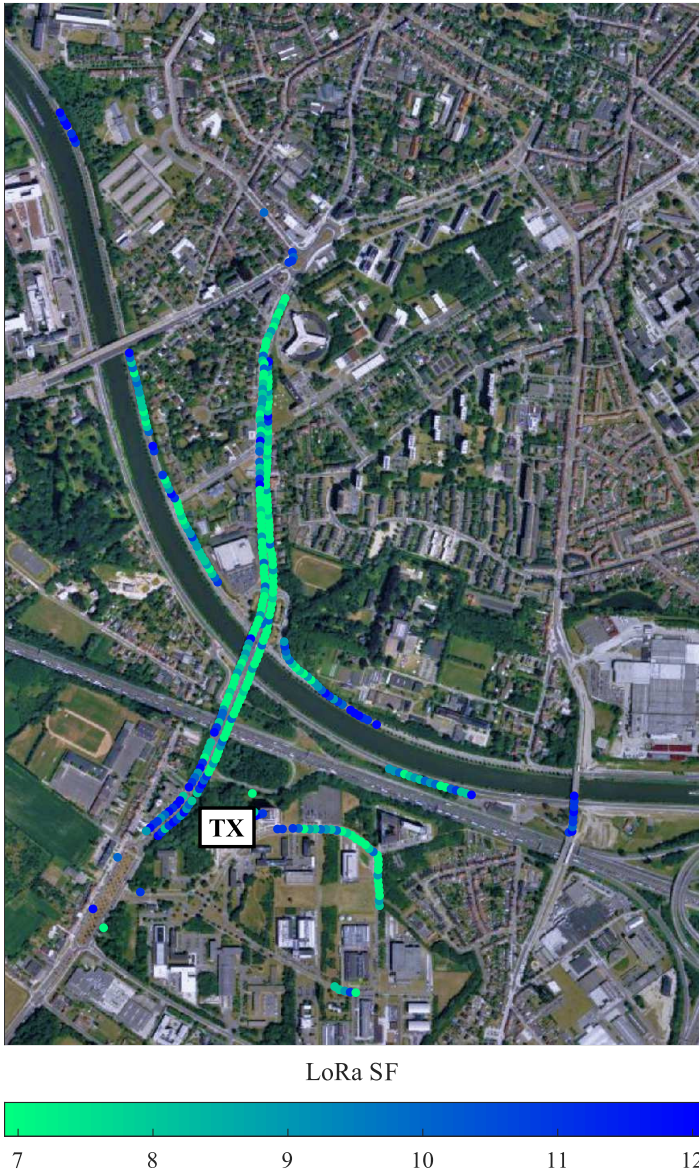


Figure 6.4: Lowest spreading factor settings that result in successful packet reception.

While the SNR is a good measure for judging the strength and reliability of these communication links, it does not really provide a lot of information on how LoRa modulation can be adapted to suit the needs of a mobile user. Therefore, Fig. 6.4 shows the lowest spreading factor that enabled the receivers to demodulate packets along the test trajectories. When comparing the coverage that is achieved

when using a spreading factor of 12 to the coverage achieved for $SF = 7$, a notable increase is seen. This implies that, depending on the speed of the mobile user and the density of scatterers in the environment, there indeed are a good number of areas where dynamically adjusting the spreading factor can yield noticeable improvements to the performance of the communication links.

Yet, identifying the best way to design a spreading factor optimization scheme requires a deeper analysis of the data presented above. As such, looking at the cumulative packet reception ratios (PRRs) for increasing SNR values, as shown in Fig. 6.5, yields a lot of insight in the performance of different SF settings. This characteristic shows how the use of higher spreading factors is beneficial to the packet reception ratio for all received power levels. It also shows how many packets will still be received for a given spreading factor when for example only those areas with the lowest SNRs are considered.

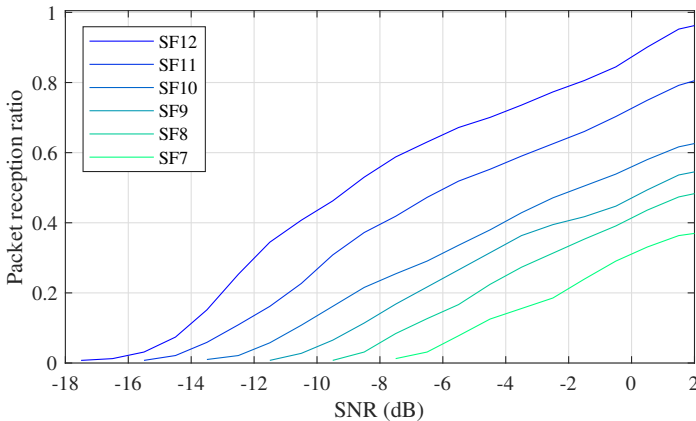


Figure 6.5: Cumulative packet reception ratios for rising SNR values in all areas that have coverage when $SF = 12$.

Ultimately, multiplying the data in Fig. 6.5 with the data rates, as presented in Fig. 6.2, yields the cumulative throughput of the LoRa channel for each of the SF settings (Fig. 6.6). In turn, these data are easily transformed into the effective throughput shown in Fig. 6.7, which gives an indication of the throughput achieved at each SNR level. This characteristic also shows which spreading factor results in the highest data rate. Therefore, the plot is a good reference for selecting the optimal spreading factor for different levels of SNR. To this end, a decision table was constructed (Table 6.2), which also includes the maximum data rate, as shown in Fig. 6.2.

Of course, when designing a spreading factor switching protocol based on these metrics, some other application parameters should be considered as well. Given the relatively small differences in performance between neighbouring spreading factors, an adaptive optimization algorithm that switches between all possible

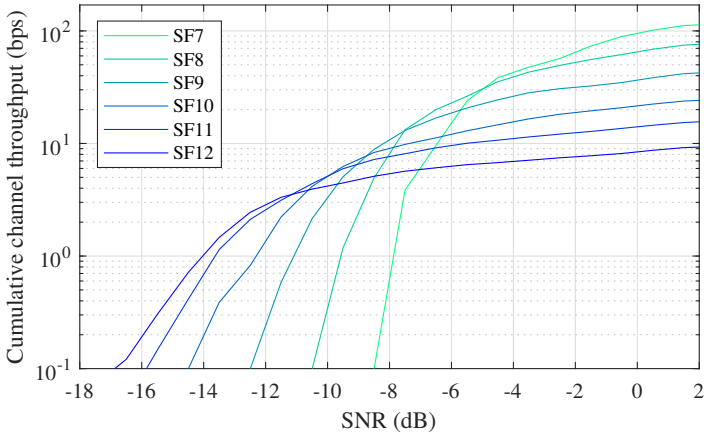


Figure 6.6: Cumulative channel throughput as a function of the SNR (for continuous bursts with packet size = 1 byte).

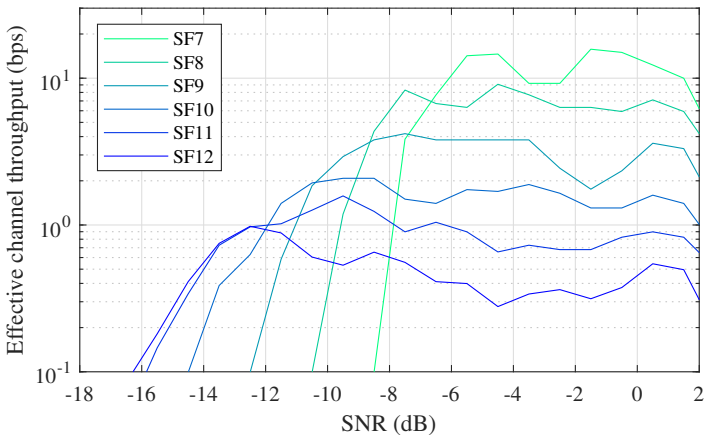


Figure 6.7: Effective channel throughput as a function of the SNR (for continuous bursts with packet size = 1 byte).

spreading factors will probably be quite inefficient. Instead, switching between two or three preset levels may significantly reduce the overhead of switching while retaining the benefits offered by adapting the spreading factor to the propagation conditions. Naturally, the most obvious choices for a system that switches between two spreading factors are SF = 7 and SF = 12. A possible third option might be SF = 9 or SF = 10, depending on the specific propagation environment.

Another factor that should be taken into account is the speed of the mobile user. Based on Fig. 6.4, it is clear that for a fast-moving receiver (such as a cyclist), the time spent in zones where only packets sent with a high spreading factor are

SNR Range	Optimal SF	Maximum data rate (bps) for packet size = 1 byte
] -7, ... [7	307
] -9, -7]	8	158
] -11, -9]	9	78
] -12, -11]	10	39
] -13, -12]	11	19
] ... , -13]	12	10

Table 6.2: Optimal spreading factor for a given SNR range and the corresponding maximum data rate, when transmitting with a packet size of one byte.

received is limited to only a few seconds. This means that the added value of switching the spreading factor during those short moments is fairly low, which even advocates against using any form of adaptive SF algorithm. In contrast, for lower (walking) speeds, the time spent in zones where only those packets with a high spreading factor are received might be a lot longer, which does justify the use of adaptive LoRa modulation.

Additionally, it should be mentioned that the limited duty cycle that is imposed on LoRa by law could be a serious hurdle for probing the channel and deciding when to change the spreading factor. Yet, for a system that only uses two or three SF options, as proposed earlier, this might not be a serious issue, since the lower amount of SF choices greatly simplifies this decision process.

A final option consists of changing the spreading factor based on positioning data and thus decide on changing certain modulation settings based on prior knowledge about the propagation environment. Ideally, in this kind of scheme, the wireless communication should be set up when channel conditions are favorable while the system should be inactive when the connection is likely to degrade.

6.5 Conclusion

Within the research framework that proposes an adaptive LoRa modulation system for use in body-centric communication networks, this chapter empirically determines how the spreading factor influences the performance of a mobile body-to-base-station LoRa link. Optimal SF switching parameters were determined (Table 6.2) based on link performance data gathered in an outdoor measurement campaign, yielding insight into how a mobile LoRa system may adapt its modulation settings to optimize the data rate while maintaining the largest possible coverage area. It was concluded that, due to the small differences in performance between neighbouring spreading factors, adaptive LoRa modulation will only be useful when implemented with a very small number of SF options. Future work includes determining a good SF switching algorithm and communication protocol to decide when to switch between different LoRa settings and to avoid losing the

connection, while respecting the duty cycle limit imposed on 868 MHz LoRa links. Despite this obvious challenge, adaptive LoRa modulation is still regarded as a viable way to improve the performance of communication links in applications that benefit from increased data rates on the one hand, but still rely on achieving the best possible coverage on the other hand.

References

- [1] LoRa Alliance, *LoRa*, <https://www.lora-alliance.org/>.
- [2] SigFox Foundation, *SigFox*, <https://www.sigfox.com/en>.
- [3] GSM Association, *NarrowBand - Internet of Things (NB-IoT)*, <https://www.gsm.a.com/iot/narrow-band-internet-of-things-nb-iot/>.
- [4] U. Noreen, A. Bounceur, and L. Clavier, "A Study of LoRa Low Power and Wide Area Network Technology", in *2017 International Conference on Advanced Technologies for Signal and Image Processing (ATSIP)*, 2017, pp. 1–6.
- [5] J. Haxhibeqiri, F. Van den Abeele, I. Moerman, and J. Hoebeke, "LoRa Scalability: A Simulation Model Based on Interference Measurements", *Sensors*, vol. 17, no. 6, 2017.
- [6] A. Augustin, J. Yi, T. Clausen, and W. M. Townsley, "A Study of LoRa: Long Range & Low Power Networks for the Internet of Things", *Sensors*, vol. 16, no. 9, 2016.
- [7] O. Georgiou and U. Raza, "Low Power Wide Area Network Analysis: Can LoRa Scale?", *IEEE Wireless Communications Letters*, vol. 6, no. 2, pp. 162–165, 2017.
- [8] K. Mikhaylov, J. Petäjajarvi, and T. Haenninen, "Analysis of Capacity and Scalability of the LoRa Low Power Wide Area Network Technology", in *22th European Wireless Conference*, 2016, pp. 1–6.
- [9] P. Van Torre, T. Ameloot, and H. Rogier, "Wearable 868 MHz LoRa Wireless Sensor Node on a Substrate-Integrated-Waveguide Antenna Platform", in *2019 49th European Microwave Week (EUMW)*, Paris, France, 2019.
- [10] P. Van Torre, T. Ameloot, and H. Rogier, "Long-Range Body-to-Body LoRa Link at 868 MHz", in *Proceedings of the 13th European Conference on Antennas and Propagation (EuCAP)*, Krakow; Poland, 2019.
- [11] *137 MHz to 1020 MHz Low Power Long Range Transceiver*, SX1276/77/78/79, Rev. 5, Semtech Corporation, Aug. 2016.
- [12] ETSI, *Short Range Devices (SRD) Operating in the Frequency Range 25 MHz to 1 000 MHz*, Sophia Antipolis, 2012.
- [13] T. Ameloot, P. Van Torre, and H. Rogier, "A Compact Low-Power LoRa IoT Sensor Node with Extended Dynamic Range for Channel Measurements", *MDPI Sensors*, vol. 18, no. 7, p. 2137, 2018.

7

LoRa Base-Station-to-Body Communication with SIMO Front-to-Back Diversity

Based on "LoRa Base-Station-to-Body Communication with SIMO Front-to-Back Diversity" by Thomas Ameloot, Patrick Van Torre and Hendrik Rogier, as published in *IEEE Transactions on Antennas and Propagation*, vol. 69, no. 1, pp. 397-405.



The LoRa standard is currently widely employed for low-power long-range wireless sensor networks at sub-GHz frequency bands. The longer wavelengths associated with sub-GHz technology provide excellent radiowave propagation characteristics, yielding much larger coverage compared to higher frequency bands. In the case of wearable sensors, the 868 MHz band can be covered by textile substrate-integrated-waveguide antennas of a convenient size. In body-centric communication systems, front-to-back diversity is an important asset to mitigate the shadowing of the antennas by the presence of the human body. This chapter describes a diversity textile-antenna-based LoRa platform with integrated transceivers. Outdoor measurement campaigns are conducted to assess the performance of the wearable LoRa nodes with front-to-back diversity in an urban radio propagation environment at walking and cycling speeds. These experiments prove that large ranges of 1.5 km can easily and reliably be achieved for off-body LoRa communication links. The results demonstrate a significant performance improvement in terms of packet loss in NLoS situations when comparing single-receiver performance to different spacial receiver diversity applications. Additionally, link budget increases up to 5.5 dB are seen, owing to the realized diversity gain.

7.1 Introduction

Wireless sensor networks are widely employed for a plethora of data links operating in the industrial, scientific and medical (ISM) bands. ISM-band systems have the advantage of operating in unlicensed parts of the spectrum, allowing private networks on a free-to-air basis. For these networks, the most widely used system is WiFi, which operates at 2.45 GHz or 5.8 GHz frequencies. These bands offer a wide bandwidth but also suffer from a limited range due to the difficult radiowave propagation conditions in indoor environments, with large attenuation caused by walls and other structures. More narrow-band systems such as IEEE 802.15.4 (physical layer for ZigBee) allow for an extension of the range, which is however still limited.

In contrast, sub-GHz frequencies provide more favorable propagation characteristics, with signal penetration through building structures with limited attenuation. In Europe, two sub-GHz ISM-bands are currently available, at 434 MHz and 868 MHz. Whereas the lowest frequency band offers the best radio propagation characteristics, suitable antennas tend to be rather large, due to the wavelength of about 70 cm. At 868 MHz, the wavelength and, hence, also the antennas are only half that size, but the propagation characteristics are still considerably better than at 2.45 GHz or higher. By employing substrate-integrated-waveguide (SIW) technology, efficient and compact wearable textile antennas have been developed for the 868 MHz band [1]–[3]. In that band, LoRa technology [4] has been proven to offer communication ranges of over 10 km in outdoor environments [5], [6]. Recently, a compact LoRa node with extended dynamic range for channel measurement purposes has been documented in [7]. The integration of this type of node on an SIW antenna results in a wearable unit for off-body LoRa communication, able to cover kilometer range links [8]. In this chapter, we investigate the performance of a novel body-worn LoRa front-to-back diversity wireless communication system, based on these recent developments.

Using LoRa for off-body communication is not a completely new concept. [9], [10] and [11] describe LoRa systems that monitor vital signs and environmental data while worn on the body. Unfortunately, these publications do not discuss the performance of the wireless links besides mentioning the available communication ranges. In contrast, [12], [13] and [14] present the deployment of an arm-mounted LoRa platform to more rigorously evaluate the feasibility of applying LoRa in a body-centric wireless communication system. In [12] and [13], the nodes are deployed in an indoor environment to assess the application of LoRa for health and wellbeing monitoring. In [14], the results from an outdoor measurement campaign are presented and analyzed to characterize the wireless channel. Similar to this chapter, [12], [13] and [14] concern base-station-to-body communication. However, there are a few decisive differences between these publications and the work presented here. All three of these earlier publications present data that were gathered over a longer time interval, whereas this chapter presents a real-time link monitoring effort during which the test person is following a fixed trajectory.

Consequently, this chapter focuses more on real-time link performance and achieves a much finer spatial resolution. Additionally, in [12], [13] and [14], commercial LoRaMote devices were used to gather data, whereas in this work, custom LoRa channel characterization hardware was deployed that dynamically implements different dynamic range settings. Moreover, by using textile materials, the SIW antennas in this system are very light and bendable. These textile antennas are deployed on the front and back of the torso of the test person, as this placement is more robust against depolarization for dynamic users [15]. Yet, the biggest advancement made in this chapter with respect to previous research is undoubtedly the application of receiver diversity and additionally, the investigation of link quality at higher speeds. In the following paragraphs, both concepts are briefly introduced.

Although a single LoRa unit is definitely able to transmit and receive data over a large range, in off-body communication systems where wearable, low-profile antennas are deployed, the communication link often suffers from shadowing by the human body [14], [16], [17]. As demonstrated extensively by many researchers for the 2.45 GHz band, front-to-back (F/B) diversity is a key asset for improving the reliability of the wireless link [18]. The performance of diversity antenna systems worn on the front and back of the torso have been documented for indoor environments at 868 MHz in [19] and [20], and at 2.45 GHz in [21], [22] and [23]. At sub-GHz frequencies, diffraction of waves around the body is more present. However, significant body shadowing still exists and additionally, the wearable antennas themselves have a directional radiation pattern, approximately covering a hemisphere around the body. Therefore, front-to-back diversity systems are expected to remain useful at sub-GHz frequency bands, enabling significantly more robust off-body communication over larger distances.

From the viewpoint of the mobile user, Doppler spread also has an important impact on the wireless link quality. Earlier research has concluded that the LoRa modulation protocol is fairly Doppler-resistant [24], [25]. Other research states that for LoRa, the 868 MHz channel is sufficiently reliable at low speeds (up to 25 km/h), but performance is seen to deteriorate for speeds upwards of 40 km/h [26]. This work compares the link quality measured at walking speeds and at an average speed of 31.1 km/h, which is considered a good approximation of the maximum speed of an average cyclist. Additionally, it is seen as a credible upper bound for the speed of alternative personal transport vehicles such as motorized steps, unicycles or skateboards. To comfortably reach higher speeds, a mobile user would need to use a different means of transport, such as a motorcycle or car. In these cases, one might no longer need to use battery-powered, body-worn nodes for data communication.

As mentioned earlier, this work investigates the performance of a body-worn LoRa front-to-back diversity communication system. The results are based on two outdoor base-station-to-body measurement campaigns at 868 MHz. In the first measurement campaign, the improvement achieved by applying F/B diversity is examined, whilst in the other measurement campaign the influence of the speed of the user on the performance of the links is investigated. The chapter is further organized as follows. In Section 7.2, the measurement infrastructure and methodology are described. The measurement results are presented and analyzed in detail in Section 7.3. Finally, a conclusion completes the chapter in Section 7.4.

7.2 Materials and Methods

7.2.1 LoRa base station

A fixed, battery-powered LoRa transmitter is placed on top of a 57 m high building in an urban environment (Fig. 7.1). The transmitter has a maximum output power of 10 dBm and is connected via a 50 Ω coaxial cable to a wire-based groundplane monopole antenna. This transmitter sends ten 1-byte packets per second, including only an incrementing packet number. The very short packet length guarantees the shortest possible airtime per transmission and allows to transmit at this fairly high repetition rate. The power output of the LoRa hardware connected to the omnidirectional base station antenna was calibrated using a Rohde & Schwartz (R&S) FSV40 spectrum analyzer.



Figure 7.1: Base station antenna (right) on top of the access ladder (middle) to the uppermost roof portion of the office building (left) located at marker A.

7.2.2 Wearable LoRa system

The body-worn LoRa system consists of two identical nodes, displayed in Fig. 4.1, worn on the front and back of the body to implement diversity. These units consist of a textile SIW antenna [1] on which a compact LoRa transceiver is integrated, along with a low-power microcontroller, 32 Mbit of flash memory and a triaxial magnetometer, accelerometer and gyroscope. The unit is also equipped with a very low-profile battery, preserving the compactness and wearability of the node. In Fig. 7.2, the normalized directivity of the standalone textile SIW antenna is compared to that of the entire system when worn on the body. Additional hardware design features and operational principles of this transceiver node are broadly discussed in [7] and [8].

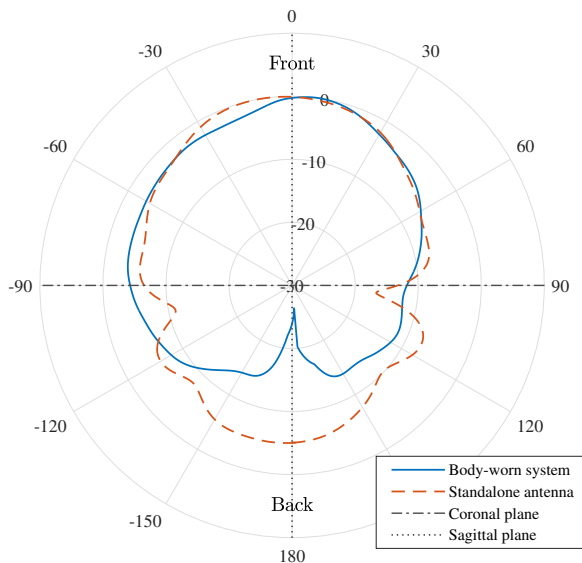


Figure 7.2: Normalized directivity (in dB) of the standalone textile SIW antenna and the fully integrated LoRa system when worn on the chest.

Fig. 7.2 primarily shows that a sizable portion of the energy radiated along the backward hemisphere of the antenna is absorbed by the wearer. With the average front-to-back (F/B) ratio of the body-worn node equaling as much as 9.57 dB, it can be concluded that body shadowing is in fact a very prominent link obstruction mechanism for the wearable system. Fig. 7.2 also shows that the directivity of the body-worn node is highly regular in front of the coronal plane. Given the large amount of small variations in the orientation and posture of the test person during the measurement campaigns, limited variations in the radiation pattern are assumed to be averaged out across a large range of angles when moving through the environment. A similar reasoning can be applied to the expected effects of the

single notch on the back side of the radiation pattern as the cumulative impact of this notch is assumed to be distributed across the (already heavily attenuated) back hemisphere of the pattern when the test person is moving. In consideration of this mechanism and the high F/B ratio presented earlier, in this chapter, the analysis is based on the separate and combined results gathered from the front and back nodes, assuming half dome radiation patterns in front of the body with some leakage around the body. As a consequence, in addition to path loss, shadowing by the environment, small-scale fading, and reflections in the environment, body-centric link parameters such as body shadowing and variations in the orientation and posture of the test person are considered to be part of the physical link under study.

Power level measurements performed by this hardware are calibrated using a three-phase calibration procedure, which is comprehensively described in [7]. The first phase of this procedure consists of calibrating the power output of a reference node when directly connected to the R&S FSV40 spectrum analyzer. Then, a high-precision stepped attenuator and a set of highly shielded coaxial cables are placed between the reference node and the spectrum analyzer. Next, this setup is calibrated for all possible attenuation settings. In the third phase, the reference node is used to inject a signal into the now calibrated stepped attenuator. Finally, the power levels measured by the device under test (DUT) can be compared to those measured in the previous phase to calibrate the receiver. To shield the DUT from any leakage from the reference node or the stepped attenuator, both components are placed in an anechoic chamber, while the DUT is installed in the shielded control room adjacent to this chamber.

7.2.3 Measurement Strategy

Due to their high system integration level, LoRa transceivers provide very few options to extract channel state information. Moreover, a very limited dynamic range in terms of signal-to-noise ratio (SNR) is typically observed as strong signals tend to easily saturate the detector [5], [7]. In [7], this is circumvented by integrating stepped attenuators onto the wireless node. Their attenuation settings are based on the signal strength of previously received packets, enabling these nodes to adapt to different transmission path lengths and propagation losses. However, given the very rapid variations of the wireless channel between a fixed base station and a mobile receiver, this kind of adaptive scheme for extending the dynamic range is not suitable for the experiments presented in this work. Consequently, a different measurement strategy was adopted.

Keeping in mind that a high channel sampling rate is desirable when a mobile user is involved, a low LoRa spreading factor (SF) of 7 was chosen, which greatly limits the airtime needed for transmitting a single data packet. Unfortunately, using a lower SF also lowers the sensitivity of the system, which has an adverse effect on the already limited dynamic range, revealing a trade-off between the channel sounding dynamic range and sampling rate. In this case, the dynamic range was re-

duced to 15 dB. However, as it has been demonstrated that attenuators can be used to shift the channel sounding dynamic range up [7], the increased packet transmission rate can be exploited to transmit packets at varying transmission powers in quick succession to probe the channel at different dynamic range settings. Varying the transmission power (P_{TX}) and transmitter attenuation settings (A_{TX}) enables the body-worn nodes to characterize the channel over a relatively large dynamic range of about 60 dB, which is composed of four 15 dB subranges according to the predefined scheme, shown in Table 7.1.

Packet nr. mod 4	0	1	2	3
P_{TX}	10 dBm	5 dBm	0 dBm	-5 dBm
A_{TX}	0 dB	10 dB	20 dB	30 dB
$P_{TX,total}$	10 dBm	-5 dBm	-20 dBm	-35 dBm
$A_{TX,10dBm}$	0 dB	15 dB	30 dB	45 dB

Table 7.1: Dynamic range settings.

This range could be extended further, to a theoretical maximum of 90 dB, by also dynamically using the attenuators at the receiver side of the link. However, more packets would need to be sent to perform a single scan of this 90 dB dynamic range. As the highest power level received during preliminary measurements rarely exceeded half of the maximum power that can be measured by the system, this extension was not implemented. When receiving a data packet, the dynamic range settings used to transmit it can be found by considering the remainder of the division of the packet number by 4.

Subtracting the transmitter attenuation A_{TX} from the corresponding transmit power P_{TX} yields the total transmission power $P_{TX,total}$ for each of the four dynamic range settings. The power that would be received when always transmitting at 10 dBm can eventually be described as the sum of the power level measured by the receiver and the virtual attenuation applied to the transmitter w.r.t. this constant transmit power of 10 dBm ($A_{TX,10dBm}$). Using this metric, the channel attenuation (A_{CH}) can be calculated as follows:

$$A_{CH} = 10 \text{ dBm} - (P_{RX,meas} + A_{TX,10dBm}) \quad (7.1)$$

in which $P_{RX,meas}$ denotes the power that was measured by the receiver. The measurement scheme presented in Table 7.1 was calibrated by setting up a link between two nodes in an anechoic room and testing all possible transmission power and attenuation settings. Due to the limited speed at which the LoRa nodes can send and receive packets, the earlier mentioned transmission rate of ten 1-byte data packets per second was achieved through extensive code and timing optimization, thus enabling a full scan of the channel at the four different dynamic range settings every 400 ms, using the aforementioned SF of 7, a code rate of 4/5 and a bandwidth of 125 kHz.

7.2.4 Outdoor trajectory

In the experiments presented in this chapter, a medium-build test person moves through a relatively open suburban/urban environment in the south of the city of Ghent, Belgium, while wearing a wireless node both at the front and back of the body. As can be seen in Fig. 7.3, the trajectory followed by this person starts at the foot of the office building on top of which the base station is located (A). He first walks around a patch of vegetation (B) to the south-west of this tower to gain access to a bridge (C) over the nearby highway, waterway and ring roads. The test person keeps moving north until a distance of 1.5 km from the base station is reached, where the link is no longer to be considered LoS (between D and E). From this point, the trajectory runs back along the same route. However, when arriving back in the vicinity of the transmitter, a detour (H-I-J) is taken, which runs around several large three- to five-story university buildings before arriving back at the starting point of the trajectory. While moving along this 5.66 km long route, received SNR values and packet numbers are continuously recorded by both the front and back nodes according to the measurement strategy presented in the previous subsection. First, the test person follows the course on foot, walking at an average speed (v_{RX}) of 6.2 km/h. Next, the same course is also traversed using a motorized longboard at an average speed of 31.1 km/h to consider the influence of the speed of the mobile receiver on the quality of the links.

7.3 Measurement Results and Analysis

The propagation environment of the trajectory presented in Section 7.2.4 is now described and characterized more thoroughly, based on the measurements gathered when walking along this route. Next, the performance gain achieved by applying spatial receiver diversity is investigated, for both selection combining (SC) and maximum ratio combining (MRC), based on the packet reception ratios and the received power level distributions. Finally, the results measured when moving at a higher speed are presented and compared to the channel characteristics when walking.

7.3.1 Channel when walking at 6.2 km/h

The signal powers measured when walking the trajectory are presented in Fig. 7.4, showing individual packets as dots and the average received signals, which are calculated by averaging the raw measurements over 9.6 seconds, as lines. Additionally, the average received power is also superimposed on the satellite picture of the trajectory shown in Fig. 7.3. Upon first observation, there seems to be a large spread of received powers over the entire trajectory. This can mainly be attributed to the movement of the receiver, which causes rapidly varying multipath conditions. In general, the trajectory can be split into paths where there is a clear LoS between the base station and the receiver (paths C-D, F-G, H-I and J-A) and

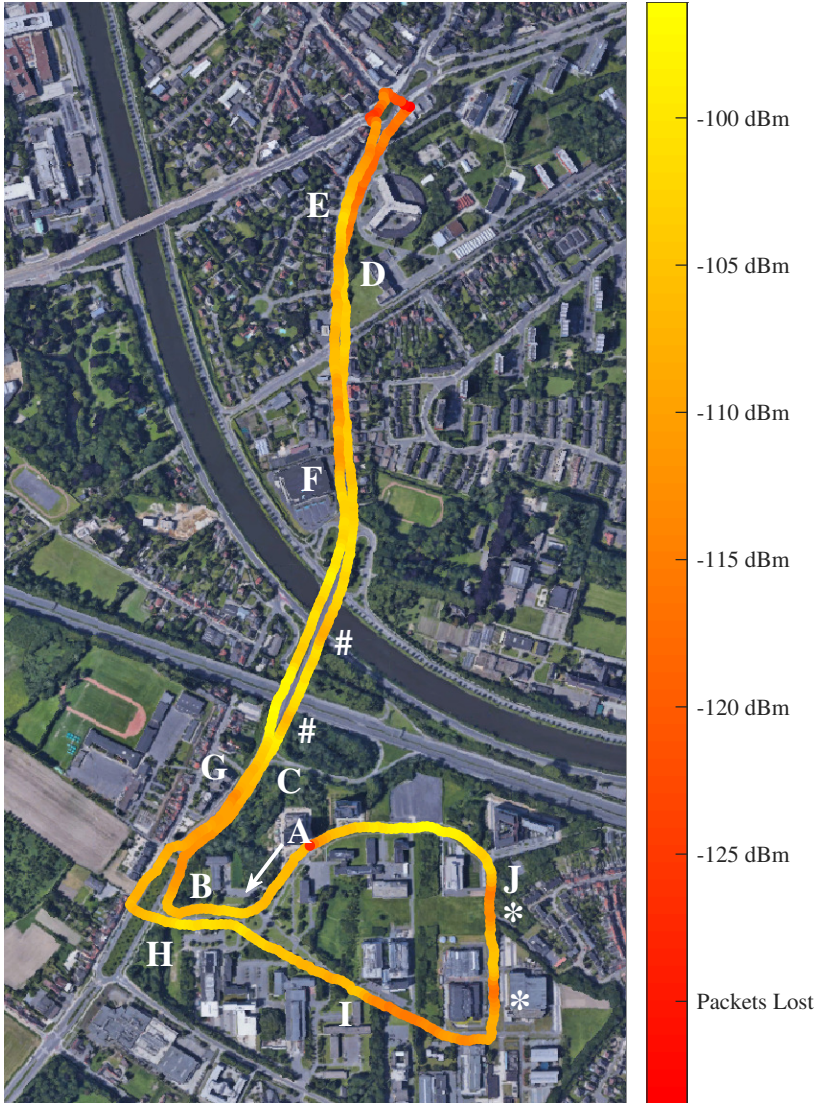


Figure 7.3: Full trajectory walked by the test person with indication of the average received signal power measured, using selection combining. ($v_{RX} = 6.2$ km/h) Map Data: Google, Landsat/Copernicus.

areas where there is no LoS (NLoS) (A-C, D-E, G-H and I-J). At the farthest end of the trajectory (D-E), a lot of buildings obstruct the link, resulting in a considerable loss of data packets. Another episode of packet loss can be identified right underneath the base station (A). This is caused by the radiation pattern of the monopole located high above this area in addition to shadowing by the office building underneath it.

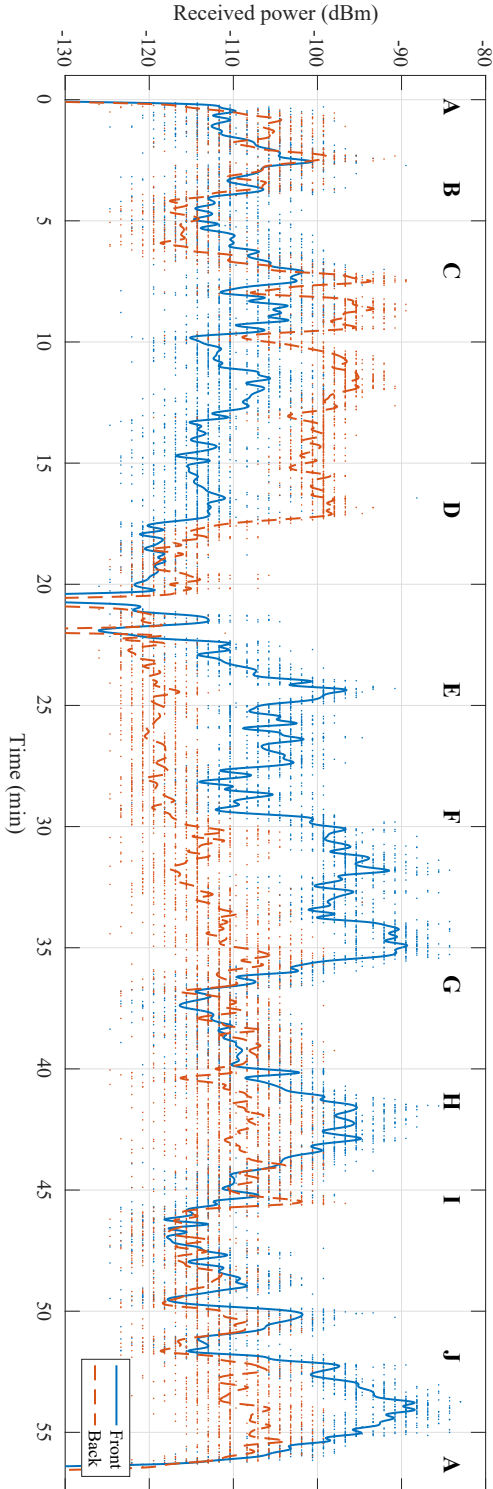


Figure 7.4: Average power levels (lines) of all packets (dots) received by both nodes with $v_{rx} = 6.2 \text{ km/h}$.

Path Loss

The path loss (PL) imposed by the propagation environment cannot be characterized for the full dataset due to the complex propagation mechanisms. However, for packets received in LoS areas, an estimation can be made. For two LoS subsets of data, gathered by the front node between markers F and G and by the back node between markers J and A, path loss characteristics are determined by fitting the data to the conventional formula in equation (4.2). The path loss exponents found for the selected subsets are $n_{FG} = 2.53$ and $n_{JA} = 2.64$. Path loss exponents are expected between 2.5 and 4 for urban environments [27].

Note that the transmitter was placed very high (57 m) and very clear LoS paths exist between the base station and the areas between markers F-G and J-A, spanning distances between 150 and 750 m.

Front-to-back diversity

When considering the data shown in Fig. 7.4, it is clear that exploiting a selection combining diversity scheme may significantly increase the average power received by the system, as the fluctuations in the envelopes of the front and back signals are quite complementary. This is especially true for the areas where there is a LoS path between one of the receivers and the base station. In these areas, relatively large signal level differences are caused by body shadowing and the directionality of the wearable antennas.

Between markers E and F, the path is not entirely LoS due to surrounding houses. Yet, the signals received by the front node are still significantly stronger than those received by the back node. This is mainly caused by a street canyon, in addition to the body shadowing and the antenna directionality mentioned earlier. As a consequence of this behaviour in absence of a true line of sight, the wireless link can be described as quasi-line-of-sight (QLoS). Based on the difference between the average signal levels measured in this situation, it can be concluded that selection combining may still solidly improve the average received power.

Also note the shadowing effect caused by the trees north of marker C (#), where the connection is otherwise LoS, and between markers I and J (*), where the connection is mostly NLoS. In these and other NLoS areas, a selection combiner would not be expected to significantly increase the average signal that is received, as the powers received by the front and back nodes are more comparable.

Packet reception ratios

The performance increase of using a selection combining F/B diversity scheme is apparent from the measured packet reception ratios (PRRs), shown in Table 7.2. For all packets sent without any form of attenuation (packet number modulo 4 = 0), the individual PRRs are reasonably high for both body-worn nodes without di-

versity, which results in a very high PRR of 98.4% after SC. Moreover, for a transmit power of -5 dBm, an even more significant diversity gain in PRR is observed.

	PRR (%)	
	$P_{TX} = 10$ dBm	$P_{TX} = -5$ dB
Front node (SISO)	92.5	54.2
Back node (SISO)	88.8	41.7
SC diversity	98.4	72.9

Table 7.2: Packet reception ratios for single-receiver and F/B receiver diversity situations, evaluated for different transmit powers. ($v_{RX} = 6.2$ km/h)

Table 7.2 also reveals a noticeable difference between the PRRs measured by the front and back nodes when considering single-input single-output (SISO) operation. This can be attributed to the asymmetry in the northern part of the trajectory, where most packet loss seems to occur. To obtain more insight into this behaviour and the corresponding PRR variations along this path, the total number of received packets is shown as a function of time in the top half of Fig. 7.5. The corresponding instantaneous PRRs, measured over a time window of 20 seconds, are shown in the bottom half of Fig. 7.5.

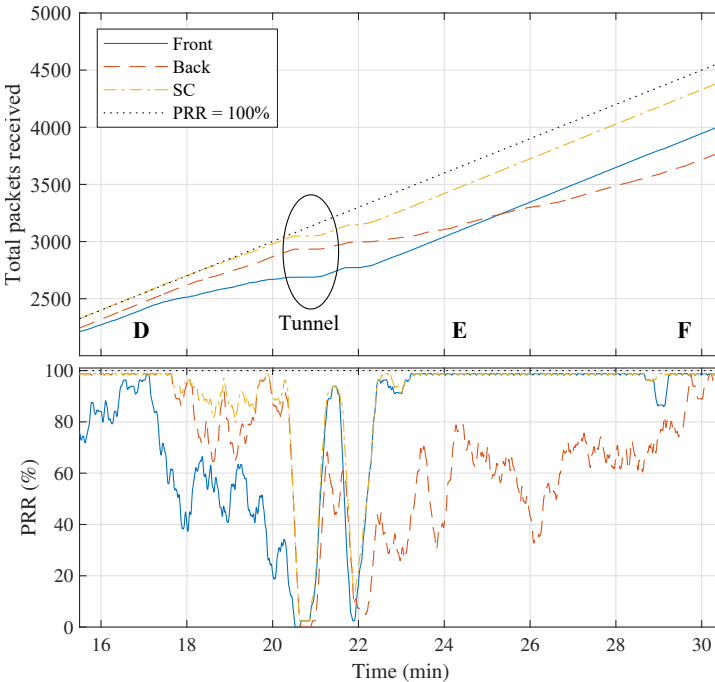


Figure 7.5: Total number of received packets (top) and local PRRs (bottom) along the path D-E-F. ($v_{RX} = 6.2$ km/h)

This figure shows that F/B diversity strongly contributes to the packet reception in NLoS situations. Only during two relatively short episodes between the twentieth and twenty-third minute of the experiment, large dips in PRR are registered for both nodes at the same time, resulting in an overall loss of the communication link. These drops in the communication link correspond to two specific parts of the trajectory where the test person first walked through a small tunnel and next crossed the road in an area severely shadowed by the surrounding buildings.

Statistics of the received power levels

Table 7.3 shows the average received signal powers together. In general, SC and MRC increase the average received power by some dB compared to the SISO channels.

	μ (dBm)	σ (dB)
Front node (SISO)	-108.7	5.9
Back node (SISO)	-111.3	5.8
SC diversity	-106.6	5.5
MRC diversity	-105.8	5.5

Table 7.3: Average signal levels and corresponding standard deviations. ($v_{RX} = 6.2$ km/h)

Next, cumulative density functions (CDFs) were generated describing the distribution of the received powers w.r.t. the number of packets that were sent. By doing so, the CDFs don't start at 0 because of the packet loss experienced in the wireless links. As a result, Fig. 7.6 shows both the improvement gained in the distribution of the received power levels as well as the improvement in packet reception. As expected, the distribution for the SC signals is essentially shifted toward higher signal levels when compared to the SISO cases. Additionally, MRC outperforms SC only by a small margin.

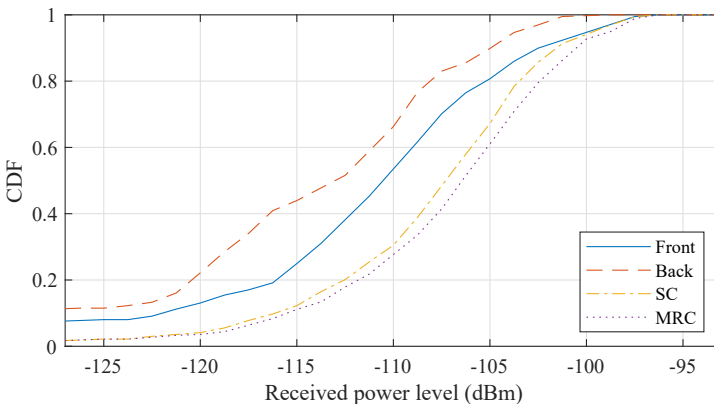


Figure 7.6: CDFs of the different links. ($v_{RX} = 6.2$ km/h)

7.3.2 Channel when moving at 31.1 km/h

Fig. 7.7 shows the average received power when completing the course with a motorized longboard at 31.1 km/h. Because of the shorter time-frame, less packets were transmitted, lowering the resolution. Generally, the data exhibit the same behaviour as those gathered at lower speed. Because of this similarity, a graphical representation such as shown in Fig. 7.3 is omitted. The LoS path loss exponent found by considering the area between F-G is equal to 2.44, which is similar to the previous channel sounding experiment. Due to the movement of the receiver, the amount of data packets was too low to calculate a reliable path loss exponent in the LoS area between markers J and A.

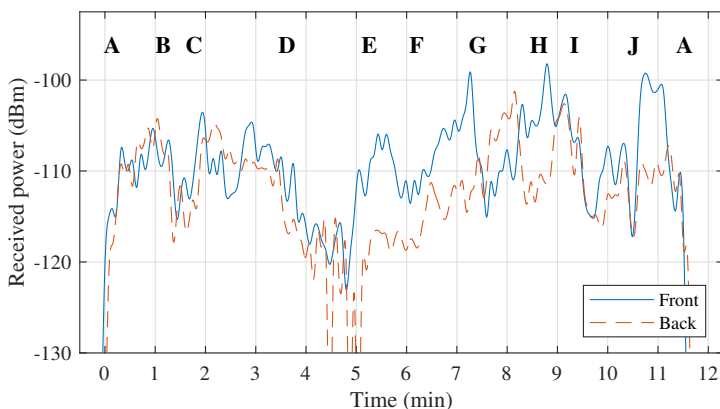


Figure 7.7: Average received power with $v_{\text{RX}} = 31.1$ km/h.

The most significant difference are the lower power levels measured when moving away from the base station between markers C and D. This is also seen in the overall PRRs, shown in Table 7.4. Overall, the PRR of the back node is 5.5 % lower than the one measured when walking. This is partly made up by the PRR measured by the front node, which is a small 1.2 % higher. The resulting SC/MRC diversity PRR is 1.4 % lower. Furthermore, the PRRs measured when considering a -5 dBm transmission power are considerably lower, showing respective losses of 8.7 %, 10.9 % and 13.3 % for front, back and SC/MRC diversity situations. This indicates that at higher speeds, Doppler effects appear to further complicate channel estimation based on packets that are received at a very low SNR.

Overall, these higher losses are consistent with the lower average signal levels, shown in Table 7.5, and the CDF data, shown in Fig. 7.8. However, the differences between these values and those measured when walking are relatively small and not statistically significant. Additionally, given the great similarity between these data and those gathered during the first measurement campaign presented in this work, this second experiment also serves as a validation for the first one.

	PRR (%)	
	$P_{TX} = 10 \text{ dBm}$	$P_{TX} = -5 \text{ dB}$
Front node (SISO)	93.7	45.5
Back node (SISO)	83.3	30.8
SC diversity	97.0	59.6

Table 7.4: Packet reception ratios at each individual node and for F/B receiver diversity situations at different transmit powers. ($v_{RX} = 31.1 \text{ km/h}$)

	μ (dBm)	σ (dB)
Front node (SISO)	-109.5	4.8
Back node (SISO)	-112.1	4.9
SC diversity	-108.4	4.9
MRC diversity	-107.5	5.0

Table 7.5: Average signal levels and corresponding standard deviations. ($v_{RX} = 31.1 \text{ km/h}$)

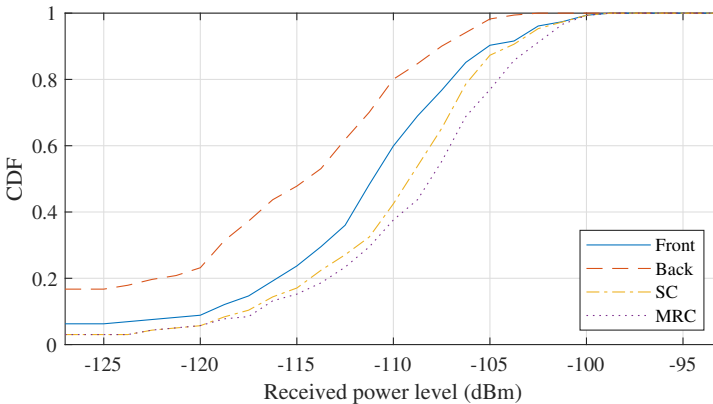


Figure 7.8: CDFs of the different links. ($v_{RX} = 31.1 \text{ km/h}$)

7.4 Conclusion

A low-power LoRa link was established between a fixed base station and a mobile user, equipped with a wearable LoRa transceiver node integrated on a substrate-integrated-waveguide antenna, on both the front and back of the body. This setup was calibrated in an anechoic chamber and exploited to perform different measurement campaigns in an omnifarious urban environment, featuring a combination of different line-of-sight (LoS) and non-line-of-sight (NLoS) passages.

By combining the signals received by both receiver nodes, the performance gained by using front-to-back (F/B) diversity techniques such as selection combining (SC) and maximum ratio combining (MRC) were investigated. SC diversity most no-

tably increased the reliability of the link by significantly increasing the packet reception ratio (PRR) in NLoS areas. This is especially true for packets that were sent at a very low transmit power (-5 dBm), for which increases of 18.7% and 31.2% in PRR were observed. MRC was found to provide a marginal additional improvement (< 1 dB) to the system's performance, which does not justify the additional complexity and cost of such a system. However, the comparison of this best-case diversity scenario to single-receiver performance reveals considerable average signal level enhancements up to 5.5 dB.

The trajectory followed when performing the channel sounding experiment was completed once at a steady walking pace of 6.2 km/h and a second time moving considerably faster, using a motorized longboard at an average speed of 31.1 km/h. No statistically significant differences were found between the average signal levels received during both of these runs. However, the data do suggest a slight reduction in PRR and received signal power in certain parts of the trajectory, confirming previous research on the matter. Overall, both measurements do share a great deal of similarity, exhibiting a large number of identical features.

In general, the wireless LoRa link is found to be adequately robust, both in terms of range and speed of the user. Given the superior propagation characteristics at sub-GHz frequencies it is proven to be a very valuable choice for low data rate body-centric applications that require a large range and good reliability, especially when combined with F/B diversity.

References

- [1] S. Agneessens, “Coupled Eighth-Mode Substrate Integrated Waveguide Antenna: Small and Wideband with High Body-Antenna Isolation”, *IEEE Access*, vol. 6, pp. 1595–1602, 2018.
- [2] T. Castel, P. Van Torre, L. Vallozzi, M. Marinova, S. Lemey, W. Joseph, C. Oestges, and H. Rogier, “Capacity of Broadband Body-to-Body Channels Between Firefighters Wearing Textile SIW Antennas”, *IEEE Transactions on Antennas and Propagation*, vol. 64, no. 5, pp. 1918–1931, 2016.
- [3] S. Lemey and H. Rogier, “SIW Textile Antennas as a Novel Technology for UWB RFID Tags”, in *2014 IEEE RFID Technology and Applications Conference (RFID-TA)*, 2014, pp. 256–260.
- [4] LoRa Alliance, *LoRa*, <https://www.lora-alliance.org/>.
- [5] J. Gaelens, P. Van Torre, J. Verhaever, and H. Rogier, “LoRa Mobile-To-Base-Station Channel Characterization in the Antarctic”, *Sensors*, vol. 17, no. 8, 2017.
- [6] N. Jovalekic, V. Drndarevic, E. Pietrosemoli, I. Darby, and M. Zennaro, “Experimental Study of LoRa Transmission over Seawater”, *Sensors*, vol. 18, no. 9, 2018.
- [7] T. Ameloot, P. Van Torre, and H. Rogier, “A Compact Low-Power LoRa IoT Sensor Node with Extended Dynamic Range for Channel Measurements”, *MDPI Sensors*, vol. 18, no. 7, p. 2137, 2018.
- [8] P. Van Torre, T. Ameloot, and H. Rogier, “Long-Range Body-to-Body LoRa Link at 868 MHz”, in *Proceedings of the 13th European Conference on Antennas and Propagation (EuCAP)*, Krakow; Poland, 2019.
- [9] M. Shahidul Islam, M. T. Islam, A. F. Almutairi, G. K. Beng, N. Misran, and N. Amin, “Monitoring of the Human Body Signal through the Internet of Things (IoT) Based LoRa Wireless Network System”, *Applied Sciences*, vol. 9, no. 9, p. 1884, 2019.
- [10] F. Wu, J. Redout, and M. R. Yuce, “WE-Safe: A Self-Powered Wearable IoT Sensor Network for Safety Applications Based on LoRa”, *IEEE Access*, vol. 6, pp. 40 846–40 853, 2018.
- [11] F. Wu, T. Wu, and M. Yuce, “An Internet-of-Things (IoT) Network System for Connected Safety and Health Monitoring Applications”, *Sensors*, vol. 19, no. 1, p. 21, 2018.

- [12] J. Petäjäjärvi, K. Mikhaylov, M. Hmlinen, and J. Iinatti, “Evaluation of LoRa LPWAN Technology for Remote Health and Wellbeing Monitoring”, in *2016 10th International Symposium on Medical Information and Communication Technology (ISMICT)*, 2016.
- [13] J. Petäjäjärvi, K. Mikhaylov, R. Yasmin, M. Hämäläinen, and J. Iinatti, “Evaluation of LoRa LPWAN Technology for Indoor Remote Health and Wellbeing Monitoring”, *International Journal of Wireless Information Networks*, vol. 24, no. 2, pp. 153–165, 2017.
- [14] P. A. Catherwood, S. McComb, M. Little, and J. A. D. McLaughlin, “Channel Characterisation for Wearable LoRaWAN Monitors”, in *Loughborough Antennas Propagation Conference (LAPC 2017)*, 2017, pp. 1–4.
- [15] K. Turbic, L. M. Correia, and M. Beko, “A Channel Model for Polarized Off-Body Communications With Dynamic Users”, *IEEE Transactions on Antennas and Propagation*, vol. 67, no. 11, pp. 7001–7013, 2019.
- [16] K. Turbic, S. J. Ambroziak, and L. M. Correia, “A Body-Shadowing Model for Off-Body and Body-to-Body Communications”, in *2018 Baltic URSI Symposium (URSI)*, 2018, pp. 53–54.
- [17] S. L. Cotton, “A Statistical Model for Shadowed Body-Centric Communications Channels: Theory and Validation”, *IEEE Transactions on Antennas and Propagation*, vol. 62, no. 3, pp. 1416–1424, 2014.
- [18] A. Michalopoulou, A. A. Alexandridis, K. Peppas, T. Zervos, F. Lazarakis, K. Dangakis, and D. I. Kaklamani, “Statistical Analysis for On-Body Spatial Diversity Communications at 2.45 GHz”, *IEEE Transactions on Antennas and Propagation*, vol. 60, no. 8, pp. 4014–4019, 2012.
- [19] S. L. Cotton and W. G. Scanlon, “Characterization and Modeling of On-Body Spatial Diversity within Indoor Environments at 868 MHz”, *IEEE Transactions on Wireless Communications*, vol. 8, no. 1, pp. 176–185, 2009.
- [20] M. Hirvonen, C. Bhme, D. Severac, and M. Maman, “On-Body Propagation Performance With Textile Antennas at 867 MHz”, *IEEE Transactions on Antennas and Propagation*, vol. 61, no. 4, pp. 2195–2199, 2013.
- [21] P. Van Torre, L. Vallozzi, L. Jacobs, H. Rogier, M. Moeneclaey, and J. Verhaevert, “Characterization of Measured Indoor Off-Body MIMO Channels with Correlated Fading, Correlated Shadowing and Constant Path Loss”, *IEEE Transactions on Wireless Communications*, vol. 11, no. 2, pp. 712–721, 2012.
- [22] I. Khan, Y. I. Nechayev, and P. S. Hall, “On-Body Diversity Channel Characterization”, *IEEE Transactions on Antennas and Propagation*, vol. 58, no. 2, pp. 573–580, 2010.
- [23] S. Wiszniewski and S. J. Ambroziak, “Characterization of Slow and Fast Fading in Off-Body Communication at 2.45 GHz with Space Diversity Scheme in an Indoor Environment”, *International Journal of Antennas and Propagation*, 2019.

- [24] U. Noreen, A. Bounceur, and L. Clavier, “A Study of LoRa Low Power and Wide Area Network Technology”, in *2017 International Conference on Advanced Technologies for Signal and Image Processing (ATSIP)*, 2017, pp. 1–6.
- [25] J. C. Liando, A. Gamage, A. W. Tengourtius, and M. Li, “Known and Unknown Facts of LoRa: Experiences from a Large-Scale Measurement Study”, *ACM Trans. Sen. Netw.*, vol. 15, no. 2, 16:1–16:35, 2019.
- [26] J. Petäjäjärvi, K. Mikhaylov, M. Pettissalo, J. Janhunen, and J. Iinatti, “Performance of a Low-Power Wide-Area Network Based on LoRa Technology: Doppler Robustness, Scalability, and Coverage”, *International Journal of Distributed Sensor Networks*, vol. 13, no. 3, 2017.
- [27] J. Isabona, “Urban Area Path loss Propagation Prediction and Optimisation Using Hata Model at 800MHz”, *IOSR Journal of Applied Physics*, vol. 3, pp. 8–18, Jan. 2013.

PART III

LoRa Modulation and Detection
with Software Defined Radio

8

LoRa Signal Synchronization and Detection at Extremely Low Signal-to-Noise Ratios

Based on "LoRa Signal Synchronization and Detection at Extremely Low Signal-to-Noise Ratios" by Thomas Ameloot, Hendrik Rogier, Marc Moeneclaey and Patrick van Torre, as submitted to *IEEE Internet of Things*.

★ ★ ★

In recent years, LoRa has been deployed in countless Internet of Things (IoT) applications across the globe. However, as LoRa is a proprietary technology, research into its physical-layer performance has been challenging. Implementing LoRa on software defined radio (SDR) platforms yields valuable insight into the physical layer of the LoRa standard and paves the way for improvements in packet reception capabilities for LoRa receivers. This chapter presents an independently developed packet reception algorithm, which drastically improves the physical performance of LoRa communication links. The advanced signal presence detection, synchronization and symbol detection strategies are shown to significantly increase packet reception ratios in extremely adverse noise conditions. Multiple algorithm variations are presented and compared in terms of SNR performance and computational cost. In comparison to a theoretical system with perfect channel state information, the simulated bit error rate performance of the best performing algorithm requires only 1.6 dB more SNR than the theoretical optimum. Finally, SDR implementations of the algorithms exhibit average SNR performance gains up to 4.7 dB when compared to commercially available hardware.

8.1 Introduction

As our world becomes increasingly connected, wireless communication technologies are continuously being conceived and improved. For long-range wireless applications, low-power wide-area network (LPWAN) technologies such as SigFox [1], NB-IoT [2] and LoRa [3] lead the way in terms of global deployment and adoption. In recent years, a large number of researchers have been interested in the effectiveness of LoRa. Several papers [4]–[7] give excellent overviews of how LoRa technology works. These are supplemented by more in-depth, theoretical reviews and investigations [8], [9]. The applicability of LoRa networks has been assessed in a wide range of indoor [10]–[16] and outdoor [17]–[21] measurement campaigns. These papers show that LoRa achieves excellent wireless performance and highlight a large range of opportunities. However, in contrast, LoRa network scalability has also been scrutinized on several occasions [5], [22]–[24]. In the light of these investigations, the limited available spectrum in industrial, scientific and medical (ISM) radio bands is an aggravating factor. Additionally, the influence of temperature and atmospheric effects on the quality of outdoor LoRa links are still under study [25]–[27].

Seeing this level of research interest in such a heavily commercialized branch of wireless technology, it is no surprise that multiple efforts have been made to implement LoRa modulation on software defined radio (SDR) platforms. From online, cooperative efforts [28]–[30] to actual scientific papers [31]–[33], a multitude of solutions exist that facilitate SDR-based LoRa communication. Moreover, through the application of SDR technology, some LoRa implementations also feature different ways of improving communication performance [34]–[37]. Additionally, a number of recent publications show how unchaining LoRa modulation from its traditional host of proprietary transceivers is a valuable way of exploring its capabilities in a diverse set of specific application environments [38]–[42]. Finally, using SDR technology also enables the user to employ other communication technologies and modulation techniques to diversify link options and serve multiple types of wireless networks [43]–[45].

8.1.1 Related Work

Recently, a number of papers have been published that present SDR implementations of LoRa modulation. In [31], conventional LoRa modulation and detection architectures are described in detail. Data manipulation steps such as channel coding, whitening and interleaving are presented along with signal-to-noise ratio (SNR) performance assessments for different LoRa spreading factors. In [32], a concise overview of SDR implementation aspects of LoRa is given. The authors analyze the impact of carrier frequency offset (CFO) and sampling frequency offset errors on communication performance and demonstrate a number of methods for correcting these offsets. Next, [33] presents an open-source LoRa physical layer prototype for the SDR ecosystem GNU Radio.

Whereas [31]–[33] present SDR-based LoRa implementations that are compatible to actual LoRa hardware, other implementations exist that also make an effort of improving wireless performance [34]–[37]. For example, in [34], a more advanced software-based detector is presented in moderate detail and all steps that need to be performed to access the raw data encapsulated in the packet are considered. An interesting clock drift correction technique is presented and robustness against frequency errors is achieved. However, compared to commercial hardware, the packet error performance from [34] is observed to be considerably more sensitive to noise. In [35], improved signal-to-interference (SIR) performance is presented for different variations of an improved preamble detection algorithm. This algorithm relaxes a number of requirements for detecting LoRa packets, which results in better signal presence detection performance. Similarly, the authors of [36] also consider signal presence detection in high LoRa interference conditions. Packets are detected based on an energy detection approach, which leads to correct signal presence detection at an SIR of -6 dB. However, in [36], no de-chirping is performed. Hence, at lower SNRs, performance is expected to be impacted heavily. More LoRa performance improvement methods are theoretically described in [37]. This chapter first presents an alternative mathematical representation of LoRa signals which ensures inter-symbol phase continuity across different LoRa symbols. As stated, this enables coherent detection of LoRa signals. Relevant expressions for the bit error rate (BER) are composed, describing a moderate SNR performance improvement of 0.7 dB. Additionally, a method is proposed to enhance network capacity by constructing additional orthogonal dimensions for LoRa signaling. Unfortunately, the methods presented in [37] have not yet been tested in practical deployments.

Yet, even when receiver performance is not altered, SDR-based LoRa implementations are still very valuable as they enable much more thorough analyses of the wireless performance of LoRa technology. For example, in [38], the authors present a low-cost, configurable and portable SDR-based system for characterizing interference in the context of IoT applications. A demonstration of this system is presented using LoRa signals. Another example is found in [39]. In this chapter, LoRa orthogonality is empirically analyzed using an SDR platform. More diverse applications also exist, for example, in [40] and [41], LoRa for satellite-to-earth communication is mimicked using SDR setups. Furthermore, in [42], SDR technology is used to add an additional encryption layer to the LoRaWAN communication stack. However, it should be mentioned that this encryption layer is added onto the physical layer. Hence, LoRa modulation and detection are performed by conventional LoRa transceivers.

Finally, LoRa implementations on SDR are also very useful for multi-service IoT applications. For example, [43] presents a re-configurable IoT gateway based on an SDR platform, which also facilitates communication using WiFi, Bluetooth Low Energy and ZigBee. Similarly, in [44], a multi-service emergency aid platform is implemented that facilitates communication using GSM, WiFi and LoRa.

8.1.2 Contributions

This chapter presents an independently developed LoRa packet reception algorithm for application on SDR. The presented algorithm intends to further improve the physical-layer performance of SDR-based LoRa receivers through a number of advanced synchronization and detection procedures. In contrast to existing research, there is a strong emphasis on the impact of accurate time and frequency synchronization on the bit error rate and packet reception ratio (PRR) performance of the LoRa links. As a consequence, the observed SNR performance gains are much larger than those presented in other papers that describe enhanced LoRa receivers. In fact, through exhaustive synchronization efforts, BERs are observed that nearly approach the performance of a link with perfect channel state information (CSI). As a result of the aforementioned synchronization efforts, the system is also highly tolerant to carrier frequency offsets, e.g., resulting from static Doppler shifts or a hardware-related frequency mismatch. This chapter also features an in-depth comparison of the preamble detection performance for different detection settings at very low SNRs and provides a number of illustrations of LoRa waveforms throughout the synchronization procedure. Compared to commercial hardware, an SDR implementation of the presented algorithm could be used to enhance either the range or reliability of existing LoRa networks, given the excellent SNR improvements featured here. Lastly, in contrast to related literature, the LoRa receiving algorithm presented in this work is described in such detail that it can be directly simulated or implemented on any SDR platform.

8.1.3 Contents

The chapter is structured as follows. First, LoRa modulation and symbol detection is discussed from a signal processing perspective in Section 8.2. Descriptions of LoRa chirps and symbols are presented in Section 8.2.1. The procedure to detect these symbols is presented in Section 8.2.2. For reference purposes, BER results are presented for a channel with additive white Gaussian noise in Section 8.2.3. In Section 8.3, the basic structure of LoRa packets is briefly summarized. Section 8.4 describes the LoRa receiving algorithm in its entirety, introducing signal presence detection, several synchronization steps and an advanced symbol detection procedure. Throughout Section 8.4, a number of key algorithm design choices are investigated in detail and compared to alternatives in order to achieve the best possible performance. Section 8.5 illustrates the simulated performance of the proposed LoRa receiving algorithm. A number of algorithm variations are compared to show the trade-offs that can be made concerning BER performance and computational cost. In the penultimate section of this chapter, an actual SDR implementation of the LoRa receiving algorithm presented in Section 8.4 is compared to commercial LoRa hardware through the packet reception rates observed in both systems. Finally, a conclusion completes the chapter in Section 8.7.

8.2 Modulation and Detection

Basic mathematical descriptions of LoRa modulation can be found in [8], [9], [37] and [46]. This chapter mostly adheres to the notation used in [9]. Additionally, oversampling is applied, and modifications are made to the original detection procedure for detecting LoRa symbols without oversampling to accommodate for these oversampled LoRa signals.

8.2.1 Data Modulation

LoRa modulation is based on linear frequency chirps. A LoRa symbol is defined in the continuous time interval $[0, T_s[$, where it is described by an instantaneous frequency in the range $[0, B]$. The duration T_s and frequency swing B of the signal are related through the spreading factor (SF), which itself is related to the size M of the symbol alphabet through $M = 2^{\text{SF}} = BT_s$. For a symbol $a \in \{0, 1, \dots, M-1\}$, the instantaneous baseband frequency f is given by

$$f(t, a) = \frac{a}{M}B + \frac{t}{T_s}B \pmod{B}. \quad (8.1)$$

As shown in the above equation, the initial frequency of the waveform is related to the symbol value through $f(0, a) = (a/M)B$. The modulo operation can be substituted by introducing the time instant τ_a , which is related to the symbol value through $\tau_a = (1 - a/M)T_s$. This represents the time at which the instantaneous frequency reaches B . At this point, f undergoes a reset to zero. The instantaneous frequency of the LoRa signal can be rewritten as

$$f(t, a) = \begin{cases} \frac{a}{T_s} + \frac{M}{T_s^2}t & 0 < t < \tau_a \\ \frac{a-M}{T_s} + \frac{M}{T_s^2}t & \tau_a < t < T_s \end{cases}. \quad (8.2)$$

The LoRa signal, with symbol energy E_s , is described by

$$s(t, a) = \sqrt{\frac{E_s}{T_s}} \exp[j\phi(t, a)]. \quad (8.3)$$

The instantaneous phase of this signal is given by

$$\begin{aligned} \phi(t, a) &= 2\pi \int_0^t f(\tau, a) d\tau \\ &= \begin{cases} 2\pi \left(a \frac{t}{T_s} + \frac{M}{2} \frac{t^2}{T_s^2} \right) & 0 < t < \tau_a \\ 2\pi \left(\left(1 - \frac{t}{T_s}\right)(M-a) + \frac{M}{2} \frac{t^2}{T_s^2} \right) & \tau_a < t < T_s \end{cases}. \end{aligned} \quad (8.4)$$

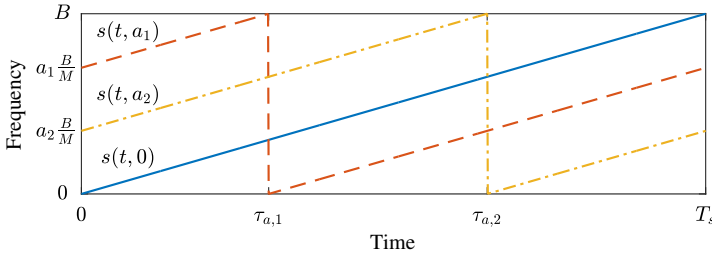


Figure 8.1: Instantaneous frequency of a pure up-chirp $s(t, 0)$ and two LoRa waveforms for arbitrary symbols $s(t, a_1)$ and $s(t, a_2)$.

8.2.2 Data Detection

Consider the received symbol $r(t)$, obtained through RF-to-baseband demodulation by an SDR receiver. In the SDR, this signal is filtered by an analog anti-aliasing filter and sampled by an analog-to-digital converter (ADC) at a sample rate of N/T_s with $N = KM$ for $K \in \mathbb{Z}_+$. In this expression, K denotes the oversampling factor applied w.r.t. the minimum sampling rate of M/T_s . This sampling operation produces a sequence of N received samples, denoted by $r[n']$ for $n' = \{0, 1, \dots, N-1\}$. A prime is added to the sample index n to indicate that oversampling was applied. As demonstrated in Fig. 8.2, which shows the block diagram for the SDR receiver and LoRa symbol detector, several operations are performed to manipulate the received samples before actual symbol detection is attempted. For example, by applying oversampling, a possible frequency shift, which is unknown when the LoRa signal, can be corrected in post-processing by the detector. Additionally, oversampling allows us to digitally filter the received signal with a more brickwall-like transfer function than provided by the analog filters in the front-end of the SDR receiver. After this operation, the signal is decimated to a sample rate of M/T_s to facilitate detection with M instead of N samples.

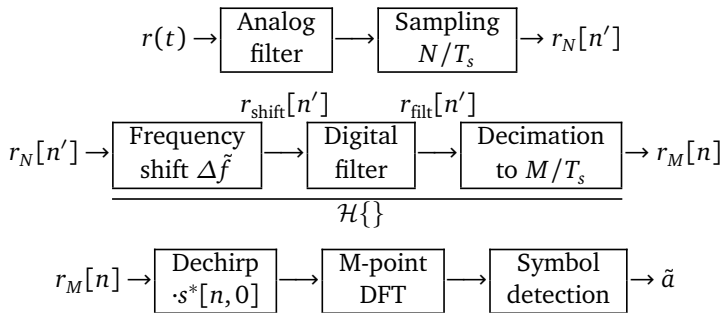


Figure 8.2: Block diagram of the proposed LoRa receiver and symbol detector.

The full data detection procedure visualized in Fig. 8.2 is now described in more detail. As mentioned earlier, a frequency error Δf can be corrected when processing the oversampled LoRa signal $r_N[n']$. While this error is unknown when first receiving the signal, estimates for Δf can be calculated when synchronization is performed (see Section 8.4). Such an estimate is denoted by $\Delta \tilde{f}$. The frequency-shifted samples $r_{\text{shift}}[n]$ are calculated by applying

$$r_{\text{shift}}[n'] = r_N[n'] \cdot \exp \left[-j2\pi \Delta \tilde{f} \frac{n' T_s}{N} \right]. \quad (8.5)$$

If no estimate is available for Δf , e.g. when still performing signal presence detection (see Section 8.4.2), its value is chosen at 0. Next, to perform decimation without losing information, an anti-aliasing filter is applied to suppress frequency components from noise or interference outside of $[0, B]$. This filter operation is performed in the frequency domain by multiplying the N -point discrete Fourier transform (DFT), represented by the operator \mathcal{F}_N , of $r_{\text{shift}}[n]$ with \mathbf{H}_i , given by

$$\mathbf{H}_i = \begin{cases} 1 & i \in [0, M-1] \\ 0 & i \in [M, N-1] \end{cases}, \quad (8.6)$$

which is the N -point ($i \in [0, N-1]$) discrete implementation of the filter window described by $H(f)$:

$$H(f) = \begin{cases} 1 & f \in [0, B] \\ 0 & \text{otherwise} \end{cases}. \quad (8.7)$$

The filtered signal is obtained by applying the inverse N -point DFT. Hence, the filtered signal $r_{\text{filt}}[n']$ is given by

$$r_{\text{filt}}[n'] = \mathcal{F}_N^{-1} \{ \mathcal{F}_N \{ r_{\text{shift}}[n'] \} \cdot \mathbf{H}_i \}. \quad (8.8)$$

After applying the anti-aliasing filter, decimation is performed to reduce the amount of samples used to describe the symbol from N to M . The decimated samples $r_M[n]$ are obtained by applying

$$r_M[n] = r_{\text{filt}}[nK], \quad (8.9)$$

where $n \in [0, M-1]$. For future reference, the frequency shift, filtering and decimation operations are described by the single operator \mathcal{H} . Hence the decimated samples can also be described as

$$r_M[n] = \mathcal{H}\{r_N[n']\}. \quad (8.10)$$

The new sampling rate of M/T_s yields $t = nT_s/M$. Hence, the complex LoRa envelope of the received symbol a is described by

$$r_M[n] = s[n, a] = \sqrt{\frac{E_s}{M}} \exp \left[j2\pi \left(\frac{an}{M} + \frac{n^2}{2M} \right) \right]. \quad (8.11)$$

Now, data detection can be performed on the decimated samples. This is realized by multiplying these samples with the complex conjugate (as indicated by the asterisk) of a pure up-chirp described by $s[n, 0]$ and applying the M -point DFT, represented by \mathcal{F}_M , to the result. If no noise is considered, the result X_m of this operation is given by

$$X_m = \mathcal{F}_M\{r_M[n] \cdot s^*[n, 0]\} = \begin{cases} E_s & m = a \\ 0 & m \neq a \end{cases}, \quad (8.12)$$

where $m \in \{0, 1, \dots, M-1\}$ denotes the output bin number of the M -point DFT. The detected symbol \tilde{a} is given by

$$\tilde{a} = \arg_m \max(|X_m|) \quad \text{for } m \in [0, M-1]. \quad (8.13)$$

The signals employed in this detection procedure are visualized in Fig. 8.3, where $r_M[n]$ is described by an arbitrary symbol $s[n, a]$ and, because of the sampling frequency $M/T_s = B$, baseband frequencies are represented in the interval $[0, B]$.

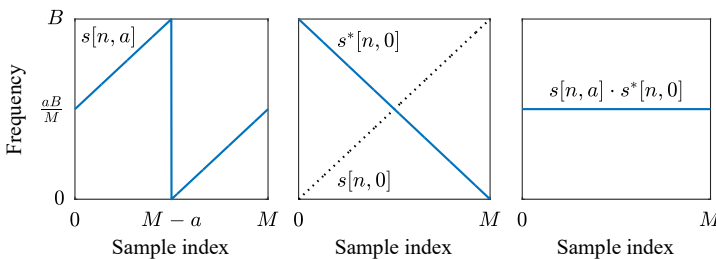


Figure 8.3: Instantaneous frequency of the received signal $r_M[n] = s[n, a]$, the complex conjugate up-chirp $s^*[n, 0]$ and the product of both in absence of noise, with no oversampling applied.

8.2.3 Bit Error Rate

As detecting a LoRa signal with oversampling required modifications to the data detection procedure, it is interesting to examine the performance of the resulting method. Hence, bit error rate (BER) simulations were performed for different SNR values for an additive white Gaussian noise (AWGN) channel. The SNR is defined as $E_s/(N_0M)$, where N_0 is the spectral density of the noise. In Fig. 8.4, the results of these simulations are compared to the approximate analytical results for LoRa BER performance presented in [46]. The calculated BERs and those predicted through the closed-form expressions in [46] agree very well. For $SF = 7$, there is a small performance penalty for lower BER values. However, in general, it can be concluded that the modifications made to the detection procedure to enable oversampling do not have a strong influence on the performance of the system.

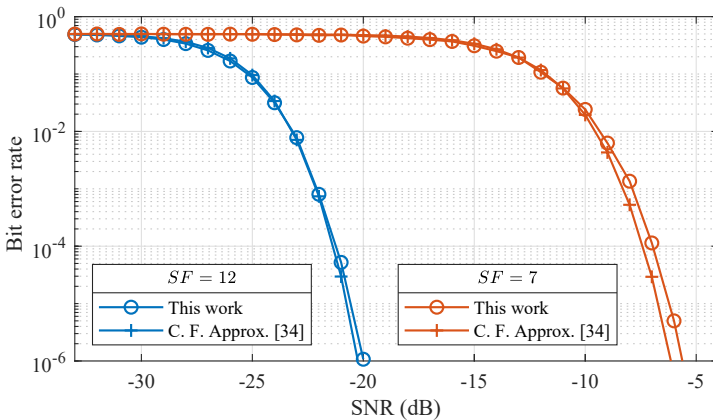


Figure 8.4: Bit error rates for $SF = 12$ and $SF = 7$ compared to closed-form approximations for the BER presented in literature [46].

8.3 Packet Structure

As the structure of LoRa packets will be referenced on multiple occasions in Section 8.4, it is briefly summarized here. Based on the definition of LoRa symbols presented in Section 8.2, LoRa packets can be constructed. In general, these take the form shown in Fig. 8.5. The preamble starts with a fixed amount of up-chirps ($s[n, 0]$), which are used to detect the presence of LoRa packets. This pilot sequence is followed by a short sync word and a so-called start-of-frame delimiter (SFD). The sync word consists of two regular LoRa symbols with known, non-zero values and aims to separate different LoRa networks using the same frequency band in the same geographical area. The start-of-frame delimiter consists of 2.25 down-chirps and is used by LoRa receivers to achieve proper synchronization when capturing a packet.

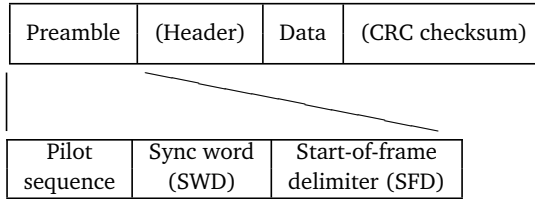


Figure 8.5: LoRa packet structure

As indicated above, the preamble is followed by a number of symbols which may consist of a header, the actual data symbols and a cyclic redundancy check (CRC), the former and latter of which are optional. Since certain LoRa settings also feature forward error correction (FEC), data are encoded according to a predefined code rate $CR \in \{4/5, 4/6, 4/7, 4/8\}$ [4]. As this chapter focuses on the uncoded physical layer of LoRa modulation, the remainder of this work assumes the optional packet header and CRC checksum to be part of the data payload. A pilot sequence of 8 up-chirps is considered, which yields a preamble length of 12.25 symbols. The interleaving and decoding steps that need to be performed to access the data encapsulated in the payload have been documented in [34] and are considered to be part of the data link layer. Consequently, these are not discussed in this chapter.

8.4 Receiving Algorithm

When receiving LoRa packets, signal presence detection and synchronization need to be performed before the raw data can be detected. In the following subsections, the implementation and optimization of both processes are discussed in detail. Subsequently, a more sophisticated strategy for detecting over-sampled LoRa packets is presented.

8.4.1 Signal Presence Detection

Assume that the received signal contains a packet that starts at the time instant $t = t_1 > 0$. This signal is represented by a sequence of samples $r_N[n']$, taken at the rate N/T_s , with $N = KM$, for which the sample with index $n' = 0$ corresponds to the time instant $t = 0$. The first sample of the packet is described by $n_1 = \lceil t_1 \cdot N/T_s \rceil$. The actual start of the LoRa packet is denoted by $\eta_1 = t_1 \cdot N/T_s$. Note that η_1 is a fractional number, with its fractional part describing the amount of sub-sample synchronization (see Section 8.4.2) that would need to be applied to achieve this point of perfect time synchronization. Additionally, a possible carrier frequency offset must be taken into account. This offset is described by Δf , such that the received LoRa signal has its instantaneous frequencies in the range $[\Delta f, \Delta f + B]$. The detection of oversampled LoRa packets is realized using a stepped delay al-

gorithm that isolates N samples from the sequence of received samples for each delay step. The index of the first sample of this interval is given by qN , such that the N received samples for a given delay step q are represented by

$$r_{N,q}[n'] = r_N[qN + n'] \quad (8.14)$$

where $n' \in \{0, 1, \dots, N-1\}$ and $q \in \mathbb{Z}$. For each delay step, the sequence of corresponding samples $r_{N,q}[n']$ is processed using the symbol detection procedure presented in Section 8.2.2. As no estimate is available for the frequency offset, $\Delta\tilde{f}$ is still zero. To avoid that the digital anti-aliasing filter causes significant signal distortion during the synchronization process when no frequency correction is yet applied, we limit our attention to the case where $-\Delta f_{\max} < \Delta f < \Delta f_{\max}$, with Δf_{\max} limited to a few percent of B . By default, a LoRa packet is considered successfully received when 4 equal LoRa symbols are detected in a row [47]. These symbols are assumed to be part of the pilot sequence of up-chirps that form the start of the preamble. When a signal is detected, a very rough estimate for the first sample of the packet is given by $\tilde{q}N$, where \tilde{q} indicates the delay step that provoked detection.

In [35], it is shown that LoRa receivers can be made more sensitive by lowering the amount of equal symbols required for packet detection and relaxing the need for them to be consecutive. Yet, in [35], the authors only present LoRa packet detection performance for limited variations on these constraints. In Fig. 8.6, the preamble detection rate is considered for a wider range of detection settings. By doing so, the algorithm can be optimized to achieve the highest detection rate. The presented variations are labeled as the amount of equal symbols required for

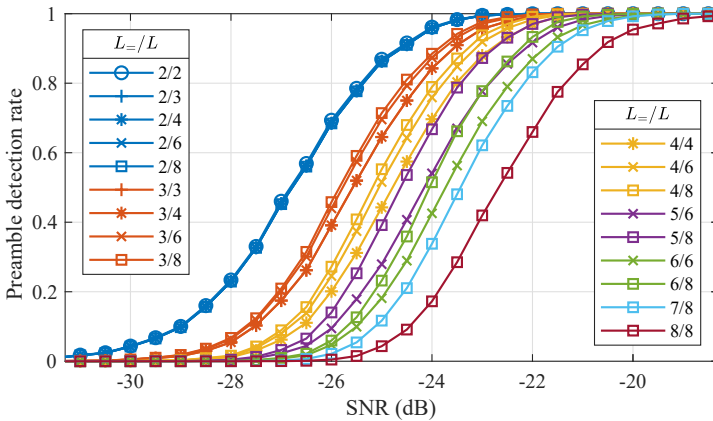


Figure 8.6: Preamble detection rates for different detection settings ($L=/L$) at $SF = 12$ and $K = 4$.

detection, indicated as $L_=$, over the total amount of symbols considered in each step of the delay algorithm, indicated as L . Hence, when $L_=$ and L are equal, L consecutive equal symbols are required for packet detection. When $L_< L$, only $L_=$ symbols need to be the same in L consecutive symbol intervals to trigger the detector. For each data point in Fig. 8.6, 10^4 attempts were made to detect a LoRa packet embedded in AWGN noise and preceded by a random number ($\in \mathbb{Z} \cap [15N, 25N]$) of noise samples to simulate a random reception delay.

Fig. 8.6 clearly illustrates how better packet detection at lower SNR values is facilitated by relaxing the requirements for packet detection through decreasing $L_=$ or increasing L . For example, the 90% packet detection threshold is lowered from -23 dB to -25 dB when using a 2/2 setting instead of the default 4/4. Fig. 8.6 also shows that packet detection performance improves very little when increasing L for $L_< 2$. Note that due to LoRa's excellent performance for very low SNR values, no signal threshold should be met when detecting packets. This does increase the odds of misinterpreting a random noise sequence as a LoRa packet. However, effective packet reception is not expected to be jeopardized as these false positives will be identified when assessing the value of the sync word described in Section 8.3, and when applying the (optional) cyclic redundancy check. Based on these considerations, the detection setting of 2/2 is used from now on.

8.4.2 Synchronization

The synchronization procedure applied in this work utilizes both the up-chirps in the pilot sequence of the LoRa packet and the down-chirps in the start-of-frame delimiter. When detecting the symbol values for these chirps, timing and frequency errors will result in non-zero symbol values for both. The current estimation for the first sample of the packet is denoted by \tilde{n}_1 and the estimation for the frequency offset is described by $\Delta\tilde{f}$. We define the relative timing and frequency errors as

$$\epsilon_n = \frac{\tilde{n}_1 - \eta_1}{N} \quad \text{and} \quad \epsilon_f = \frac{\Delta\tilde{f} - \Delta f}{B}. \quad (8.15)$$

An illustration of the up-chirps in the pilot sequence and the down-chirps in the SFD, with indication of these errors, is shown in Figure 8.7.

The symbol level found when processing an up-chirp from the pilot sequence in the absence of noise is given by

$$\tilde{a}_{\text{pilot}} = \lfloor (\epsilon_n - \epsilon_f)M \rfloor \pmod{M} \quad (8.16)$$

where $\lfloor \cdot \rfloor$ indicates rounding to the nearest integer. The down-chirps in the SFD can be processed in a similar way. In theory, their symbol values should be detected by using complex conjugate down-chirps. However, when a sample rate of M/T_s is adopted, a regular down-chirp $\bar{s}[n, 0]$ can be constructed relatively easily by

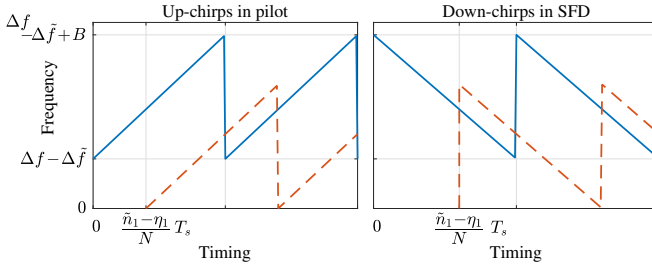


Figure 8.7: Instantaneous frequencies of the actual preamble chirps (solid line) and the estimated preamble chirps (dashed line).

applying $\bar{s}[n, 0] = s^*[n, 0]$. Hence, a complex conjugate down-chirp is actually equivalent to a normal up-chirp $s[n, 0]$. As a result, the symbol values for the down-chirps in the SFD can be detected by substituting the complex conjugate up-chirp in (8.12) by a regular up-chirp. In the absence of noise, this yields

$$\tilde{a}_{\text{sfd}} = \left[(-\epsilon_n - \epsilon_f)M \right] \pmod{M} \quad (8.17)$$

When plotting the detected symbol values for \tilde{a}_{pilot} and \tilde{a}_{sfd} as a function of different time and frequency synchronization errors, (8.16) and (8.17) yield a diamond pattern of rhombuses, as shown in Fig. 8.8.

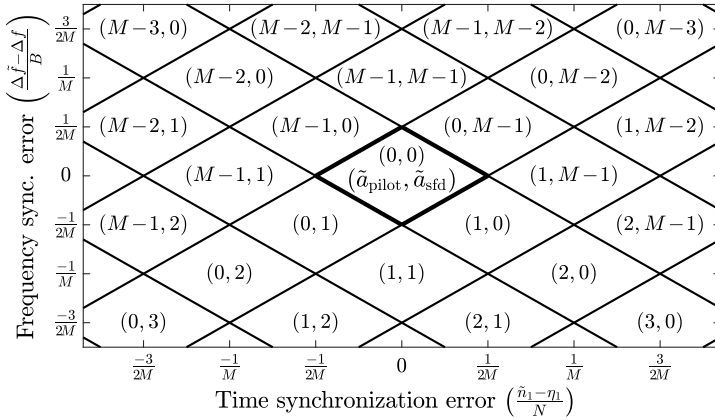


Figure 8.8: \tilde{a}_{pilot} and \tilde{a}_{sfd} for different time and frequency synchronization errors.

In this implementation of LoRa, packet synchronization is achieved in four steps. (1) First, a coarse symbol synchronization step is performed to align \tilde{n}_1 with the start of the first of the L_- symbols that triggered the packet detector. (2) Next, the first symbol of the preamble is identified by analyzing the amount of up- and down-chirps that are present before and after the detected symbol. (3) Subsequently, an

additional synchronization step is performed to correct a potential constant frequency mismatch between the detector and the received packet based on the symbol levels of the up-chirps in the pilot sequence and the down-chirps that form the SFD. (4) Finally, by employing sub-sample synchronization methods (see Section 8.4.2), synchronization can be improved further, which involves timing corrections smaller than $T_s/(KM)$. These corrections ensure that energy is not divided between two adjacent frequency bins when performing data detection. Below, all synchronization steps are described in detail based on the step-wise refinement of the first preamble sample estimation \tilde{n}_1 and the estimation for the frequency offset $\Delta\tilde{f}$. This means that the value for \tilde{n}_1 is updated after each subsequent synchronization step, each time reducing the distance between \tilde{n}_1 and η_1 . At the end of each subsection, an update for \tilde{n}_1 and $\Delta\tilde{f}$ is indicated by one or more added primes. The instantaneous frequencies of the actual preamble and the estimation for the preamble are also visualized in Figs. 8.9 to 8.12. These illustrate how each step contributes to achieving full synchronization.

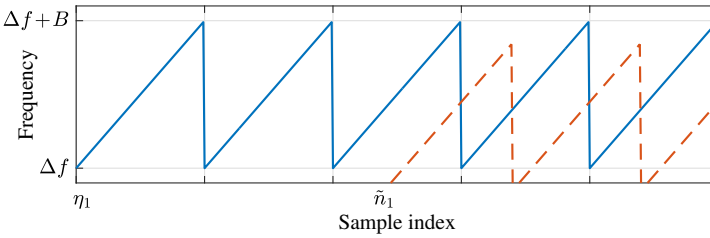


Figure 8.9: Instantaneous frequencies of the actual preamble chirps (solid line) and the estimated preamble chirps (dashed line), prior to synchronization.

Coarse symbol synchronization

In this first synchronization step, the index of the first sample of the up-chirp that triggered the detector is estimated. No frequency correction is applied yet, i.e., $\Delta f' = 0$. This operation is fairly straightforward as this update for \tilde{n}_1 , denoted as \tilde{n}'_1 , can be calculated based on the symbol level \tilde{a}_{pilot} found when processing this pilot chirp. When $\tilde{a}_{\text{pilot}} = m$, we set

$$\tilde{n}'_1 = \tilde{n}_1 - m \frac{N}{M}. \quad (8.18)$$

This operation corresponds to a horizontal shift in Fig. 8.8, from a rhombus with $\tilde{a}_{\text{pilot}} = m$ to a rhombus with $\tilde{a}_{\text{pilot}} = 0$.

$$\frac{1}{N} \left| (\tilde{n}'_1 - \eta_1) \pmod{N} + \Delta f \frac{N}{B} \right| < \frac{1}{2M}. \quad (8.19)$$

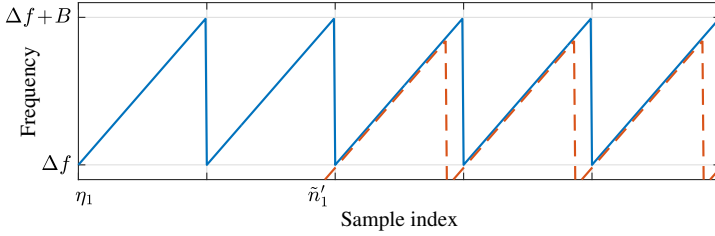


Figure 8.10: Instantaneous frequencies of the actual preamble chirps (solid line) and the estimated preamble chirps (dashed line), after coarse symbol synchronization.

Frame synchronization

As the pilot sequence at the start of the preamble is eight up-chirps long (see Section 8.3), there could be up to seven symbols preceding or up to seven symbols trailing the symbol that triggered the detector. In order to find the first symbol of the pilot sequence, trial detections are performed on the full preamble for a range of delay steps k , selecting the delay which results in the best detection. Still no frequency correction is applied, i.e., $\Delta f'' = 0$. For each trial detection $q \in \mathbb{Z}$, M samples are selected according to

$$r_{M,q}[n] = \mathcal{H}\{r_N[\tilde{n}'_1 + qN + n']\} \quad (8.20)$$

By iterating over $k \in \{-7, -6, \dots, 0\}$, the aforementioned symbol strengths are calculated for the pilot sequence (pilot) as

$$\mathbf{F}_{k,\text{pilot}} = \sum_{q=k}^{k+7} \max(|\mathcal{F}_M \{r_{M,q}[n] \cdot s^*[n, 0]\}|) \quad (8.21)$$

In a similar manner, the strength of the sync word (swd) candidates can be calculated as

$$\mathbf{F}_{k,\text{swd}} = \sum_{q=k+8}^{k+9} \max(|\mathcal{F}_M \{r_{M,q}[n'] \cdot s^*[n, 0]\}|) \quad (8.22)$$

Finally, the two full down-chirps in the start-of-frame delimiter (sfd) can be detected. In theory, these should be detected by using complex conjugate down-chirps. However, when a sample rate of M/T_s is adopted, a normal down-chirp $\bar{s}[n, 0]$ can be constructed relatively easily by applying $\bar{s}[n, 0] = s^*[n, 0]$. Hence, a complex conjugate down-chirp is actually equivalent to a normal up-chirp $s[n, 0]$.

Employing this relation yields the symbol strength for all SFD candidates:

$$F_{k,\text{sfd}} = \sum_{q=k+10}^{k+11} \max(|\mathcal{F}_M \{r_{M,q}[n] \cdot s[n,0]\}|) \quad (8.23)$$

Now, the combined strength of the pilot sequence, the sync word and the start-of-frame delimiter can be evaluated for each delay step k . This measure will reach its maximum value when the complex conjugate chirps in equations (8.21), (8.22) and the regular up-chirp in (8.23) are correctly aligned with the up- and down-chirps in the preamble. This leads to the corresponding value for k , indicated as

$$k_{\max} = \arg_k \max(F_{k,\text{pilot}} + F_{k,\text{swd}} + F_{k,\text{sfd}}). \quad (8.24)$$

Based on the result of the above equation, the new value for \tilde{n}_1 is found as

$$\tilde{n}_1'' = \tilde{n}_1' + k_{\max} \cdot N. \quad (8.25)$$

In Fig. 8.8, this synchronization step corresponds to a horizontal shift to the left, from a rhombus with $\tilde{a}_{\text{pilot}} = 0$ to another rhombus with $\tilde{a}_{\text{pilot}} = 0$, the latter being located on the diagonal characterized by

$$|\epsilon_n - \epsilon_f| < \frac{1}{2M}. \quad (8.26)$$

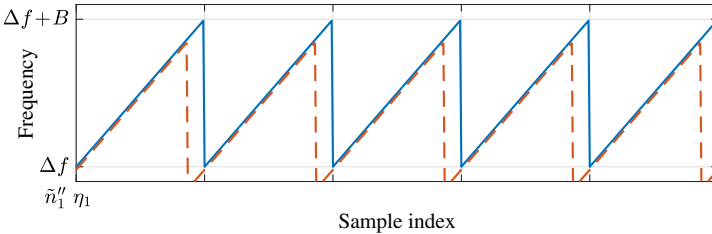


Figure 8.11: Instantaneous frequencies of the actual preamble chirps (solid line) and the estimated preamble chirps (dashed line), after frame synchronization.

Joint symbol and carrier frequency synchronization

To avoid signal distortion by the digital anti-aliasing filter during data detection, the frequency mismatch Δf needs to be compensated. An estimate of the frequency mismatch can be obtained by performing detection on the down-chirps of the start-of-frame delimiter. Performing this detection with $\Delta \tilde{f}'' = 0$ and the timing estimate \tilde{n}_1'' resulting from the frame synchronization, a symbol value $\tilde{a}_{\text{sfd}} = m$

is obtained, while the detection of the pilot symbol yields $\tilde{a}_{\text{pilot}} = 0$. This corresponds to the rhombus in Fig. 8.8, with $(\tilde{a}_{\text{pilot}}, \tilde{a}_{\text{sfd}}) = (0, m)$ characterized by (8.26). Joint symbol and carrier frequency synchronization involves the computation of the frequency estimate $\Delta\tilde{f} = 0$ and the timing correction term $\Delta\tilde{n} = 0$, according to

$$\begin{cases} \Delta\tilde{n} = \frac{1}{2} m \frac{N}{M} \\ \Delta\tilde{f} = \frac{1}{2} m \frac{B}{M} \end{cases} \quad \text{for } m \leq \frac{M}{2} \quad (8.27)$$

or

$$\begin{cases} \Delta\tilde{n} = -\frac{1}{2} (M - m) \frac{N}{M} \\ \Delta\tilde{f} = -\frac{1}{2} (M - m) \frac{B}{M} \end{cases} \quad \text{for } m > \frac{M}{2}. \quad (8.28)$$

In Fig. 8.8, application of this timing and frequency correction corresponds to a shift from the rhombus with $(\tilde{a}_{\text{pilot}}, \tilde{a}_{\text{sfd}}) = (0, m)$ to the rhombus with $(\tilde{a}_{\text{pilot}}, \tilde{a}_{\text{sfd}}) = (0, 0)$. The latter rhombus is characterized by (8.26) and

$$|\epsilon_n + \epsilon_f| < \frac{1}{2M}. \quad (8.29)$$

Note that (8.27) and (8.28) yield an integer multiple of $K/2$ for $\Delta\tilde{n}$. Hence, when K is odd, a fractional number can be obtained for $\Delta\tilde{n}$. This must be taken into consideration when calculating the new approximation for the start of the packet:

$$\tilde{n}_1''' = \tilde{n}_1'' + \lfloor \Delta\tilde{n} \rfloor + \delta\tilde{n}. \quad (8.30)$$

The remainder from $\lfloor \Delta\tilde{n} \rfloor$ can be taken into account by applying sub-sample synchronization. Sub-sample synchronization is realized by subtracting a small constant time shift $\delta\tilde{n}/K \in \mathbb{R}$, smaller than T_s/N , from n in the up-chirp $s[n, 0]$ used in the detection process. Hence, equation (8.12) is replaced by

$$X'_i = \mathcal{F}\{r_M[n] \cdot s^*[n - \delta\tilde{n}/K, 0]\}. \quad (8.31)$$

This effectively adds a small shift to the timing of the detector. In this synchronization step, the size of this time shift (expressed in sampling intervals) is given by

$$\delta\tilde{n} = \Delta\tilde{n} - \lfloor \Delta\tilde{n} \rfloor. \quad (8.32)$$

Here, $\delta\tilde{n}$ will either be zero or half a sample interval, referred to the rate N/T_s . However, in the next subsection, this value may be replaced by any fractional number. The frequency offset is corrected in the detection procedure itself, as described in Section 8.2.2. To conform to the previously introduced notation, three primes are added to $\Delta\tilde{f}$, yielding $\Delta\tilde{f}''' = \Delta\tilde{f}$. When now considering the accuracy of \tilde{n}_1''' and $\Delta\tilde{f}'''$, we note that the time and frequency errors have been reduced to a random point inside the center rhombus.

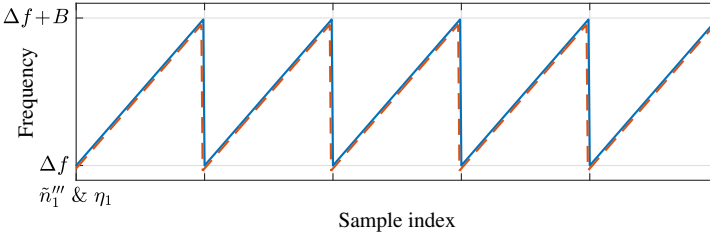


Figure 8.12: Instantaneous frequencies of the actual preamble chirps (solid line) and the estimated preamble chirps (dashed line), after joint symbol and carrier frequency synchronization. Small timing and frequency errors may still be present.

Advanced sub-symbol-level synchronization

Despite the synchronization steps taken in the previous subsections, there is still one mechanism that can noticeably degrade bit error performance, given the current accuracy of \tilde{n}_1''' and $\Delta\tilde{f}$. When the actual synchronization errors lead to a point that is close to the edges of the center rhombus in Fig. 8.8, a significant portion of the symbol energy will appear in the wrong DFT frequency bin after detection. If the received packet has a low SNR, this leads to a significant number of symbol errors as random noise often causes the detector to return $a-1$ or $a+1$ instead of the original symbol a , as illustrated in Fig. 8.13.

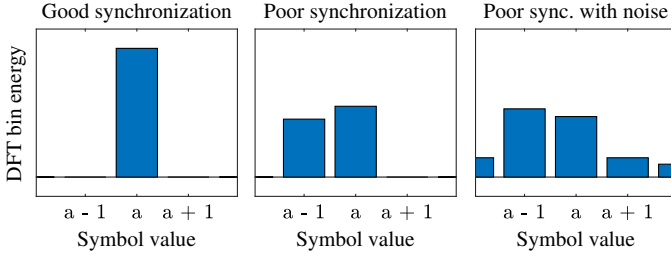


Figure 8.13: DFT bin energies for an arbitrary symbol a with good synchronization, poor synchronization and poor synchronization in combination with a low SNR. In the latter, a symbol error is observed.

To overcome these issues, more advanced synchronization strategies can be employed to better approximate η_1 and Δf . These strategies can further elaborate on sub-sample time and frequency synchronization by adding an additional time offset to $s[n, 0]$, as introduced in Section 8.4.2, and by further modifying $\Delta \tilde{f}$. This means that the symbol levels that would be detected when the signal is processed would not change when locally shifting the timing of the detector and the frequency correction applied to $r_N[n]$ if no noise were present. Yet, in case of a low SNR, this final improvement in synchronization accuracy is in fact found to positively impact the BER, as demonstrated in Section 8.5.2.

To realize this more advanced time and frequency synchronization step, a well-chosen performance indicator should be optimized as a function of the very small time ($\delta \tilde{n}/K$) and frequency ($\delta \tilde{f}$) offsets subtracted from n in $s[n, 0]$ and added to $\Delta \tilde{f}$ respectively. The corresponding time and frequency synchronization estimates are described by

$$\tilde{n}_1 = \tilde{n}_1''' + \delta \tilde{n} \quad \text{and} \quad \Delta \tilde{f} = \Delta \tilde{f}''' + \delta \tilde{f}. \quad (8.33)$$

The boundaries of the optimization space for $\delta \tilde{n}$ and $\delta \tilde{f}$ are governed by the values of \tilde{a}_{pilot} and \tilde{a}_{sfid} , which have to be zero for all test points. As illustrated in Fig. 8.14, this optimization space corresponds to the center rhombus in Fig. 8.8. A good choice for the performance indicator is the energy in the strongest frequency bin when detecting the symbol values in the preamble, as this measure will reach a maximum for $\tilde{n}_1''' + \delta \tilde{n} = \eta_1$ and $\Delta \tilde{f} + \delta \tilde{f} = \Delta f$, which corresponds to the center of the optimization space shown in Fig. 8.14. This optimization space is mapped out by detecting the symbol values for \tilde{a}_{pilot} and \tilde{a}_{sfid} as a function of different $\delta \tilde{n}$ and $\delta \tilde{f}$. As introduced in Section 8.4.2, the errors associated with the estimates $\Delta \tilde{n}_1'''$ and $\Delta \tilde{f}'''$ correspond to a random point inside this rhombus. Hence, the range for $\delta \tilde{n}$ and $\delta \tilde{f}$ should cover an area around this point four times the area of this rhombus, as the worst case scenarios for $\Delta \tilde{n}_1'''$ and $\Delta \tilde{f}'''$ correspond to the vertices of the rhombus. The resolution of $\delta \tilde{n}$ and $\delta \tilde{f}$ can be chosen freely.

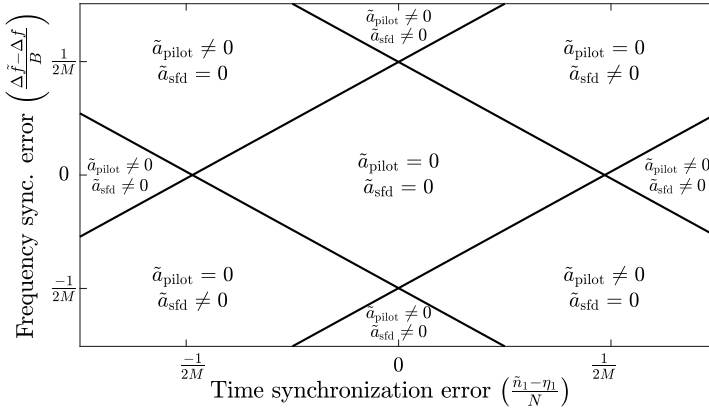


Figure 8.14: Illustration of the optimization space boundaries for $\delta\tilde{n}$ and $\delta\tilde{f}$, governed by $(\tilde{a}_{\text{pilot}}, \tilde{a}_{\text{sfd}}) = (0, 0)$.

As introduced for timing corrections of $1/2$ times the sample interval in Section 8.4.2, sub-sample synchronization is again achieved by altering the timing of the detector through subtracting $\delta\tilde{n}/K$ from n in the up-chirp $s[n, 0]$ used in the detection process, as demonstrated in equation (8.31). Optimization algorithms such as gradient descent [48] can be applied to reduce the (possibly significant) computational cost of this synchronization step if there are any relevant timing or power consumption restrictions. When the optimal values for $\delta\tilde{n}$ and $\delta\tilde{f}$ are determined (based on the chosen performance indicator), the symbols in the payload can be detected using these optimized synchronization settings.

Values near the center of the optimization space shown in Fig. 8.14 are more likely to yield a correct symbol decision than values near the edge, as these values are closer to the perfect synchronization point $(\epsilon_n, \epsilon_f) = (0, 0)$. Hence, when symbol detection is performed for a given combination of $\delta\tilde{n}$ and $\delta\tilde{f}$, symbol energy will be concentrated more in a single DFT bin. As an alternative to maximizing a performance indicator, the optimization space of $\delta\tilde{n}$ and $\delta\tilde{f}$ can also be explored without performing this calculation. In this case, the average values for all $\delta\tilde{n}$ and $\delta\tilde{f}$ that lead to $(\tilde{a}_{\text{pilot}}, \tilde{a}_{\text{sfd}}) = (0, 0)$ in this space can be used to get close to $(\epsilon_n, \epsilon_f) = (0, 0)$, which again leads to an optimized configuration of $s[n - \delta\tilde{n}/K, 0]$ and $\Delta\tilde{f} + \delta\tilde{f}$ for detecting the actual data symbols.

8.4.3 Advanced Detection

The advanced synchronization step presented above can also be extended to the detection procedure. Instead of processing the data in the packet once, with fixed values for $\delta\tilde{n}$ and $\delta\tilde{f}$, one can also perform symbol detection on each symbol in the packet for every combination of $\delta\tilde{n}$ and $\delta\tilde{f}$ that leads to synchronization points in the optimization space governed by $\tilde{a}_{\text{pilot}} = \tilde{a}_{\text{sfd}} = 0$ and shown in Fig. 8.14. For packets with a very low SNR, random symbol errors that occur for very specific combinations of $\delta\tilde{n}$ and $\delta\tilde{f}$ could then be mitigated by selecting the candidate value that occurs most frequently for a given symbol. Suppose we construct a matrix \mathbf{A} , which contains the detected symbol value when applying a certain combination of $\delta\tilde{n}$ (row element) and $\delta\tilde{f}$ (column element): $\mathbf{A}_{\delta\tilde{n},\delta\tilde{f}} = \tilde{a}$. Elements are only added to this matrix if the combination of $\delta\tilde{n}$ and $\delta\tilde{f}$ satisfies $\tilde{a}_{\text{pilot}} = \tilde{a}_{\text{sfd}} = 0$. The size of the matrix depends on the resolution of $\delta\tilde{n}$ and $\delta\tilde{f}$, which, as mentioned earlier can be chosen freely. The actual symbol value can be selected as the modal value of \mathbf{A} . The contents of this matrix are illustrated for an arbitrary symbol level of 7 in Fig. 8.15. For every LoRa symbol in the payload, this procedure can be repeated. Note that selecting the modal value of \mathbf{A} as the detected symbol actually allows for the omission of the performance indicator optimization part of the synchronization step presented in Section 8.4.2, as eventually no decision is taken for $\delta\tilde{n}$ and $\delta\tilde{f}$.

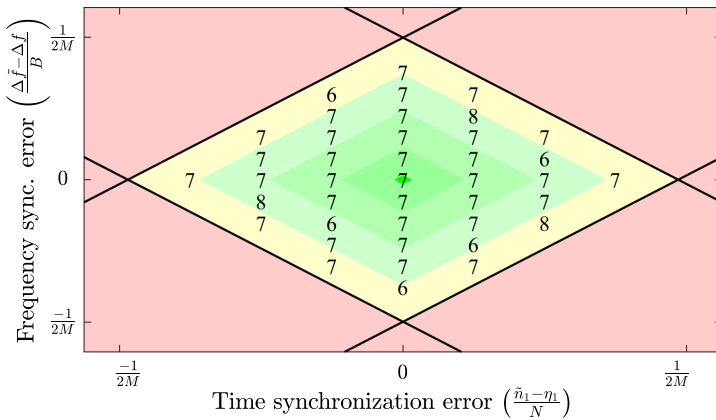


Figure 8.15: Example of detected symbol values in \mathbf{A} for an arbitrary symbol value of 7 in low SNR conditions. Red areas indicate incorrect synchronization. In the yellow area, synchronization is poor and leads to symbol errors through the mechanism demonstrated in Fig. 8.13. In greener areas, less symbol errors occur at low SNRs.

8.5 Simulated SDR Performance

When evaluating the performance of the LoRa receiving algorithm introduced in Section 8.4, it is important to keep in mind the computational cost (and hence, power consumption) of the algorithm. To this end, four variations, consisting of different combinations of the synchronization and detection strategies presented in Sections 8.4.2 and 8.4.3, are compared to the performance of LoRa signal detection under perfect CSI conditions (perfect time and frequency synchronization point is known).

8.5.1 Algorithm Variations

For the first variation of the receiving algorithm, the advanced synchronization and detection steps introduced to counteract the DFT bin mismatch mechanism described in Section 8.4.2 and illustrated in Fig. 8.13 are fully omitted. As a result, this variation, which is labeled as Direct Synchronization (DS), is expected to have a very low computational cost. The second algorithm variation uses the advanced synchronization procedure proposed in Section 8.4.2, without calculating a performance indicator (hence, the optimal values for $\delta\tilde{n}$ and $\delta\tilde{f}$ are estimated as the mean values of all combinations of $\delta\tilde{n}$ and $\delta\tilde{f}$ that lead to points in the optimization space illustrated in Fig. 8.14) and omits the advanced detection procedure presented in Section 8.4.3. This variation is labeled as Advanced Synchronization with Estimated Optimum (AS-EO). The third variation is very similar, however, now the energy in the strongest frequency bin when demodulating and processing the chirps in the preamble is chosen as a performance indicator in the last synchronization step and optimal values for $\delta\tilde{n}$ and $\delta\tilde{f}$ are determined based on this metric. Consequently, this variation is labeled as Advanced Synchronization with Computed Optimum (AS-CO). Finally, the fourth variation is fully based on the procedure presented in Section 8.4.3. As previously mentioned, no estimates for $\delta\tilde{n}$ and $\delta\tilde{f}$ are calculated, but symbol values are determined by taking the mode of all candidate symbol values. Therefore, this variation is labeled as Mode of Successive Detection (MSD). While the MSD variation is expected to be the most accurate way of detecting any given packet, it is also expected to be the most computationally expensive.

8.5.2 Bit Error Rate

To analyze the bit error performance of the algorithm variations under study, a communication channel was simulated by adding white Gaussian noise to synthesized LoRa packets (payload = 100 random symbols, $B = 125$ kHz, $SF = 12$). Each packet sequence was preceded by a random number ($\in \mathbb{Z} \cap [15N, 25N]$) of noise samples, shifted by a random frequency offset ($\in \mathbb{R} \cap [-5, 5]$ kHz) and fed into one of the receiving algorithms. Shifting the frequency of the packets simulates a realistic carrier frequency offset (CFO). The BERs obtained through this procedure are shown in Fig. 8.16. For each data point in Fig. 8.16, at least 100 packet errors were simulated. The results are also compared to the BER that would be achieved by a system with perfect CSI.

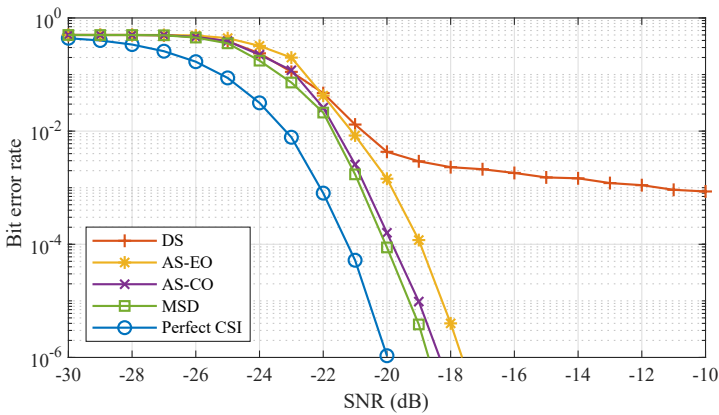


Figure 8.16: Bit error rates for all algorithm variations presented in Section 8.5.1, compared to the BER under perfect CSI conditions, as shown in Fig. 8.4.

The DS curve in Fig. 8.16 clearly illustrates how the absence of an advanced time and frequency synchronization step has a detrimental impact on the BER through the DFT bin mismatch mechanism described in Section 8.4.2 and illustrated in Fig. 8.13. However, despite this deficiency caused by the accuracy of the synchronization procedure, the DS version of the algorithm could still be very useful when an adequate error-correcting code is applied. A significant improvement w.r.t. DS is observed for AS-EO. Yet, the best performing algorithm versions are AS-CO and MSD, which exhibit very similar performance. For AS-CO, this shows that even for the lowest SNR values, the optimization space of $\delta\tilde{n}$ and $\delta\tilde{f}$ can be sufficiently explored to determine the best time and frequency correction. Applying the MSD procedure yields further improvements, which are, however, limited. In average SNR performance, the theoretical system with perfect CSI outperforms the simulated MSD algorithm by only 1.6 dB. The bit error rates presented in Fig. 8.16 also show that the CFO applied to the packets is successfully mitigated by the synchronization efforts applied in the best performing algorithms.

8.5.3 Computational Cost

To evaluate the computational cost of the algorithm variations under study, a LoRa link with sufficiently high SNR to allow the system to operate without significant packet loss was simulated on a 2.1 GHz Intel Core i7 8650U processor with 16 G of memory. In practice, each version of the algorithm was presented with 100 randomized LoRa packets, consisting of N_s symbols, the packets were once again preceded by a random number ($\in \mathbb{Z} \cap [15N, 25N]$) of noise samples. AWGN noise was added to each of the packets to achieve SNR levels uniformly distributed between -20 dB and 0 dB. With the exception of impacting the amount of signal presence detection attempts that are made to detect the packet, the exact SNR of a received packet has no significant influence on its processing time. Fig. 8.17 shows the average computation times needed to find, synchronize to and process a single LoRa packet with a given packet length. It clearly shows the computational impact of the synchronization steps taken in the MSD variation of the algorithm and also indicates why using Direct Synchronization could still be a desirable option when employing the receiving algorithm in real-world LoRa applications, especially when an appropriate coding strategy would be used. AS-EO and AS-CO clearly strike a sound balance between excellent BER performance and a manageable computational cost, with AS-CO emerging as the better choice because of its superior error performance, if either the computational cost or power consumption of the receiver is an issue.

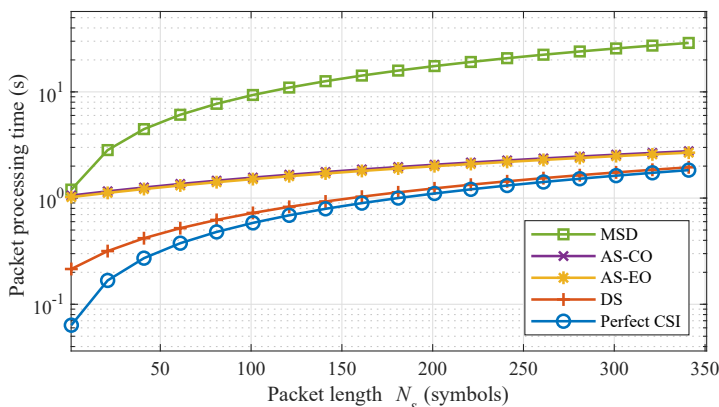


Figure 8.17: Processing time needed to find, synchronize to and detect a single LoRa packet with a given length N_s for all algorithm variations presented in Section 8.5.1.

8.6 Comparison to Commercial Hardware

To be able to demonstrate the practical improvements achieved by the LoRa receiving algorithm variations presented in this work, these were implemented on a bladeRF 2.0 micro XA4 SDR unit [49]. In this section, the performance of these solutions is compared to that of a commercial Semtech SX1276 LoRa transceiver [50]. The SX1276 chip is integrated on a compact LoRa sensor node with extended dynamic range, which was specifically developed and calibrated for performing channel measurements [15].

8.6.1 Measurement Setup

To compare the performance of both systems, a second SX1276-based LoRa sensor node was used to generate LoRa packets (carrier frequency $f_c = 868$ MHz, payload $N_a = 13$ symbols, $B = 125$ kHz, $SF = 12$, $CR = 4/5$), which contain a unique 16-bit packet number as payload. One hundred of these packets were sent to either system through a switched attenuator for each 1 dB attenuation step, and with a transmission power of 0 dBm. A Rohde and Schwarz FSV40 Spectrum Analyzer was used to verify the signal levels after cable loss. As the encrypting and coding scheme of the commercial transceiver is proprietary, the packets received by the SDR were error checked by remodulating these packets and presenting the result to another SX1276-receiver in a repeater configuration. Hence, for each packet received by the SDR, symbols are detected using one of the algorithm variations presented earlier. Next, based on the received symbol values, packets are reconstructed and transmitted to a second SX1276 at the SDR's maximum power level. At this power level, additional symbol errors are extremely rare. Hence, the PRR experienced by the second SX1276 is essentially the same as the PRR that would result from the SDR receiver. Identical to the calibration procedure presented in [15], the transmitting LoRa sensor node was placed in an anechoic chamber, while the receivers were located in a shielded control room to provide sufficient isolation between both systems. Both receivers logged the SNR of received packets, either based on the I and Q samples in the SDR, or by extracting this information from the SX1276 transceiver in the commercial receiver. The accuracy of the SNR measurements made by the SX1276 is not publicly available. However, it is known that for fixed noise levels, one dB of signal strength increase does not exactly correspond to one dB of SNR improvement as reported by this LoRa module [15], [51]. This is corrected by applying the calibration presented in [15].

8.6.2 Results

The results of this experiment are shown in Fig. 8.18. This figure shows lognormal cumulative density functions fitted to the packet reception ratio (PRR) data points as a function of the measured SNR. Lognormal distributions are found to agree relatively well with the data.

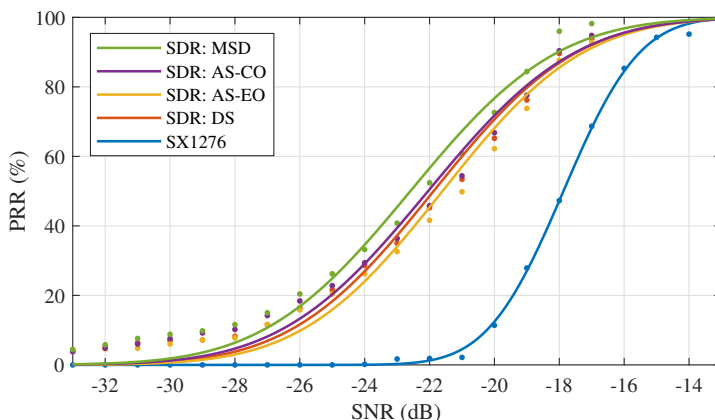


Figure 8.18: Packet reception ratios measured when increasing the attenuation between a LoRa transmitter node and the two devices under test.

Fig. 8.18 clearly illustrates the significant performance gain achieved by the SDR system and the packet reception algorithm variations presented in this work when compared to the SX1276 transceiver. On average, an SNR performance improvement of 4.7 dB is measured for the SDR system, with the 10% outage probability occurring at an SNR level of -18.0 dB. This is a significant gain when compared to the -15.5 dB measured for the commercial LoRa system. When higher outage probabilities are considered, this difference is even larger. The average 4.7 dB performance gain corresponds to a sizable 172% range improvement in free space for receivers with the same noise floor. Less obvious performance differences are observed between the different algorithm variations running on the SDR. However, these do agree with the relative BER levels presented in Fig. 8.16.

8.7 Conclusion

An advanced LoRa packet reception algorithm was developed and implemented on SDR. LoRa chirp and symbol formulations were presented and extended to include frequency offset and oversampling capabilities. Additionally, a symbol detection procedure for detecting oversampled LoRa symbols was constructed and tested. A unique LoRa receive algorithm was conceived, applying a state-of-the-art signal presence detection strategy, rigorous packet synchronization methods and an advanced data detection procedure to yield the best possible link quality. Every part of the algorithm was described in detail, keeping in mind various mechanisms that could significantly degrade bit error performance. Different algorithm variations were presented and explored by examining the bit error rates obtained from AWGN channel simulations. Those algorithm variations that actively correct small timing and frequency synchronization errors were shown to perform particularly well, at best leaving only 1.6 dB of SNR performance to be gained when compared to bit error rates obtained by a theoretical system with perfect CSI. Moreover, the proposed algorithm variations have been shown to accurately correct a possible carrier frequency offset. The comparison between all presented algorithm variations also clearly illustrated the pertinent trade-off between link performance and computational cost. When considering the best performing algorithm version's implementation on SDR, average SNR performance improvements up to 4.7 dB were observed when compared to industry standard LoRa hardware.

In future work, FPGA technology or advanced ARM architectures could be employed to parallelize certain parts of the synchronization and data detection procedures applied in this work, limiting the time needed to process packets while fully taking advantage from the excellent performance demonstrated in this chapter. The presented LoRa receiving algorithm could in theory be implemented on any SDR platform. Consequently, this implementation of LoRa enables more in depth research on the physical performance of LoRa modulation as it makes the physical layer fully available to researchers. When integrated in existing LoRa networks, the proposed algorithm could yield significant improvements in range and/or reliability for network nodes with sufficient computational power.

References

- [1] SigFox Foundation, *SigFox*, <https://www.sigfox.com/en>.
- [2] GSM Association, *NarrowBand - Internet of Things (NB-IoT)*, <https://www.gsma.com/iot/narrow-band-internet-of-things-nb-iot/>.
- [3] LoRa Alliance, *LoRa*, <https://www.lora-alliance.org/>.
- [4] A. Augustin, J. Yi, T. Clausen, and W. M. Townsley, "A Study of LoRa: Long Range & Low Power Networks for the Internet of Things", *Sensors*, vol. 16, no. 9, 2016.
- [5] M. C. Bor, U. Roedig, T. Voigt, and J. M. Alonso, "Do LoRa Low-Power Wide-Area Networks Scale?", in *Proceedings of the 19th ACM International Conference on Modeling, Analysis and Simulation of Wireless and Mobile Systems*, Malta, Malta, 2016, pp. 59–67.
- [6] U. Noreen, A. Bounceur, and L. Clavier, "A Study of LoRa Low Power and Wide Area Network Technology", in *2017 International Conference on Advanced Technologies for Signal and Image Processing (ATSIP)*, 2017, pp. 1–6.
- [7] M. Centenaro, L. Vangelista, A. Zanella, and M. Zorzi, "Long-Range Communications in Unlicensed Bands: the Rising Stars in the IoT and Smart City Scenarios", *IEEE Wireless Communications*, vol. 23, no. 5, pp. 60–67, 2016.
- [8] L. Vangelista, "Frequency Shift Chirp Modulation: The LoRa Modulation", *IEEE Signal Processing Letters*, vol. 24, no. 12, pp. 1818–1821, 2017.
- [9] M. Chiani and A. Elzanaty, "On the LoRa Modulation for IoT: Waveform Properties and Spectral Analysis", *IEEE Internet of Things Journal*, vol. 6, no. 5, pp. 8463–8470, 2019.
- [10] L. Gregora, L. Vojtech, and M. Neruda, "Indoor Signal Propagation of LoRa Technology", in *2016 17th International Conference on Mechatronics - Mechatronika (ME)*, 2016, pp. 1–4.
- [11] P. Neumann, J. Montavont, and T. Nol, "Indoor Deployment of Low-Power Wide Area Networks (LPWAN): A LoRaWAN Case Study", in *2016 IEEE 12th International Conference on Wireless and Mobile Computing, Networking and Communications (WiMob)*, 2016, pp. 1–8.
- [12] L. H. Trinh, V. X. Bui, F. Ferrero, T. Q. K. Nguyen, and M. H. Le, "Signal Propagation of LoRa Technology Using for Smart Building Applications", in *2017 IEEE Conference on Antenna Measurements Applications (CAMA)*, 2017, pp. 381–384.

- [13] J. Haxhibeqiri, A. Karağaç, F. Van den Abeele, W. Joseph, I. Moerman, and J. Hoebeke, “LoRa Indoor Coverage and Performance in an Industrial Environment: Case Study”, Limassol, Cyprus, 2017, pp. 1–8.
- [14] J. Petäjäjärvi, K. Mikhaylov, R. Yasmin, M. Hämäläinen, and J. Iinatti, “Evaluation of LoRa LPWAN Technology for Indoor Remote Health and Wellbeing Monitoring”, *International Journal of Wireless Information Networks*, vol. 24, no. 2, pp. 153–165, 2017.
- [15] T. Ameloot, P. Van Torre, and H. Rogier, “A Compact Low-Power LoRa IoT Sensor Node with Extended Dynamic Range for Channel Measurements”, *MDPI Sensors*, vol. 18, no. 7, p. 2137, 2018.
- [16] T. Ameloot, P. Van Torre, and H. Rogier, “Indoor Body-to-Body LoRa Link Characterization”, in *2019 9th IEEE-APS Topical Conference on Antennas and Propagation in Wireless Communications*, Granada, Spain, 2019.
- [17] J. Petäjäjärvi, K. Mikhaylov, A. Roivainen, T. Hanninen, and M. Pettissalo, “On the Coverage of LPWANs: Range Evaluation and Channel Attenuation Model for LoRa Technology”, in *2015 14th International Conference on ITS Telecommunications (ITST)*, 2015, pp. 55–59.
- [18] J. Petäjäjärvi, K. Mikhaylov, M. Pettissalo, J. Janhunen, and J. Iinatti, “Performance of a Low-Power Wide-Area Network Based on LoRa Technology: Doppler Robustness, Scalability, and Coverage”, *International Journal of Distributed Sensor Networks*, vol. 13, no. 3, 2017.
- [19] O. Iova, A. L. Murphy, G. P. Picco, L. Ghio, D. Molteni, F. Ossi, and F. Cagnacci, “LoRa from the City to the Mountains: Exploration of Hardware and Environmental Factors”, in *Proceedings of the 2017 International Conference on Embedded Wireless Systems and Networks*, Uppsala, Sweden: Junction Publishing, 2017, pp. 317–322.
- [20] T. Ameloot, P. Van Torre, and H. Rogier, “LoRa Base-Station-to-Body Communication With SIMO Front-to-Back Diversity”, *IEEE Transactions on Antennas and Propagation*, vol. 69, no. 1, pp. 397–405, 2021.
- [21] —, “Experimental Parameter Optimization for Adaptive LoRa Modulation in Body-Centric Applications”, in *2020 14th European Conference on Antennas and Propagation (EuCAP)*, Copenhagen, Denmark, 2020.
- [22] O. Georgiou and U. Raza, “Low Power Wide Area Network Analysis: Can LoRa Scale?”, *IEEE Wireless Communications Letters*, vol. 6, no. 2, pp. 162–165, 2017.
- [23] K. Mikhaylov, J. Petäjäjärvi, and T. Haenninen, “Analysis of Capacity and Scalability of the LoRa Low Power Wide Area Network Technology”, in *22th European Wireless Conference*, 2016, pp. 1–6.
- [24] B. Reynders, W. Meert, and S. Pollin, “Range and Coexistence Analysis of Long Range Unlicensed Communication”, in *2016 23rd International Conference on Telecommunications (ICT)*, 2016, pp. 1–6.

- [25] M. Cattani, C. A. Boano, and K. Römer, “An Experimental Evaluation of the Reliability of LoRa Long-Range Low-Power Wireless Communication”, *Journal of Sensor and Actuator Networks*, vol. 6, no. 2, 2017.
- [26] C. A. Boano, M. Cattani, and K. Römer, “Impact of Temperature Variations on the Reliability of LoRa - An Experimental Evaluation”, in *Proceedings of the 7th International Conference on Sensor Networks - Volume 1*, SciTePress, 2018, pp. 39–50.
- [27] T. Ameloot, P. Van Torre, and H. Rogier, “Periodic LoRa Signal Fluctuations in Urban and Suburban Environments”, in *2019 13th European Conference on Antennas and Propagation (EuCAP)*, Krakow, Poland, 2019.
- [28] B. Sikken, *Decoding LoRa*, <https://revspace.nl/DecodingLora>.
- [29] J. Blum, *LoRa SDR Project*, <https://github.com/myriadrf/LoRa-SDR>.
- [30] RTL-SDRangelove, *Github Project Page*, <https://github.com/hexameron/rtl-sdrangelove>.
- [31] A. Marquet, N. Montavont, and G. Z. Papadopoulos, “Towards an SDR Implementation of LoRa: Reverse-Engineering, Demodulation Strategies and Assessment over Rayleigh Channel”, *Computer Communications*, vol. 153, pp. 595–605, 2020.
- [32] R. Ghanaatian, O. Afisiadis, M. Cotting, and A. Burg, “Lora Digital Receiver Analysis and Implementation”, in *ICASSP 2019 - 2019 IEEE International Conference on Acoustics, Speech and Signal Processing (ICASSP)*, 2019, pp. 1498–1502.
- [33] J. Tapparel, O. Afisiadis, P. Mayoraz, A. Balatsoukas-Stimming, and A. Burg, “An Open-Source LoRa Physical Layer Prototype on GNU Radio”, in *2020 IEEE 21st International Workshop on Signal Processing Advances in Wireless Communications (SPAWC)*, 2020, pp. 1–5.
- [34] P. Robyns., P. Quax., W. Lamotte., and W. Thenaers., “A Multi-Channel Software Decoder for the LoRa Modulation Scheme”, in *Proceedings of the 3rd International Conference on Internet of Things, Big Data and Security - Volume 1*, SciTePress, 2018, pp. 41–51.
- [35] P. Edward, A. Muhammad, S. Elzeiny, M. Ashour, T. Elshabrawy, and J. Robert, “Enhancing the Capture Capabilities of LoRa Receivers”, in *2019 International Conference on Smart Applications, Communications and Networking (SmartNets)*, 2019, pp. 1–6.
- [36] A. A. Kherani and K. M. P. Maurya, “Improved Packet Detection in LoRa-Like Chirp Spread Spectrum Systems”, in *2019 IEEE International Conference on Advanced Networks and Telecommunications Systems (ANTS)*, 2019, pp. 1–4.
- [37] T. Elshabrawy, P. Edward, M. Ashour, and J. Robert, “On the Different Mathematical Realizations for the Digital Synthesis of LoRa-Based Modulation”, in *European Wireless 2019; 25th European Wireless Conference*, 2019, pp. 1–6.

- [38] H. Poveda, K. Navarro, F. Merchan, E. Ramos, and D. Gonzalez Gonzalez, “A Software Defined Radio-Based Prototype for Wireless Metrics Studies in IoT Applications”, *Wireless Personal Communications*, 2021.
- [39] A. Lavric, A. I. Petrariu, E. Coca, and V. Popa, “LoRa Traffic Generator Based on Software Defined Radio Technology for LoRa Modulation Orthogonality Analysis: Empirical and Experimental Evaluation”, *Sensors*, vol. 20, no. 15, 2020.
- [40] A. A. Doroshkin, A. M. Zadorozhny, O. N. Kus, V. Y. Prokopyev, and Y. M. Prokopyev, “Experimental Study of LoRa Modulation Immunity to Doppler Effect in CubeSat Radio Communications”, *IEEE Access*, vol. 7, pp. 75 721–75 731, 2019.
- [41] Fernandez, Lara and Ruiz de Azua Ortega, Joan and Calveras, Anna and Camps, Adriano, “Assessing LoRa for Satellite-to-Earth Communications Considering the Impact of Ionospheric Scintillation”, *IEEE Access*, vol. 8, pp. 165 570–165 582, Jan. 2020.
- [42] S. Hassayoun, S. Lahouar, and K. Besbes, “SDR Bridge for a Secure Wireless Sensor Network (WSN)”, Jun. 2020, pp. 1–5.
- [43] C. Gavrilă, C. Kertesz, M. Alexandru, and V. Popescu, “Reconfigurable IoT Gateway Based on a SDR Platform”, in *2018 International Conference on Communications (COMM)*, 2018, pp. 345–348.
- [44] D. M. Molla, H. Badis, A. A. Desta, L. George, and M. Berbineau, “SDR-Based Reliable and Resilient Wireless Network for Disaster Rescue Operations”, in *2019 International Conference on Information and Communication Technologies for Disaster Management (ICT-DM)*, 2019, pp. 1–7.
- [45] R. Narayanan and S. Kumar, “Revisiting Software Defined Radios in the IoT Era”, in *Proceedings of the 17th ACM Workshop on Hot Topics in Networks*, Redmond, WA, USA: Association for Computing Machinery, 2018, 4349.
- [46] T. Elshabrawy and J. Robert, “Closed-Form Approximation of LoRa Modulation BER Performance”, *IEEE Communications Letters*, vol. 22, no. 9, pp. 1778–1781, 2018.
- [47] A. Rahmadhani and F. Kuipers, “When LoRaWAN Frames Collide”, in *Proceedings of the 12th International Workshop on Wireless Network Testbeds, Experimental Evaluation and Characterization*, New Delhi, India: Association for Computing Machinery, 2018, pp. 89–97.
- [48] S. Ruder, “An overview of gradient descent optimization algorithms”, *arXiv preprint arXiv:1609.04747*, 2016.
- [49] Nuand, *BladeRF 2.0 micro xA4*, <https://www.nuand.com/product/bladerf-xa4/>.
- [50] *137 MHz to 1020 MHz Low Power Long Range Transceiver*, SX1276/77/78/79, Rev. 5, Semtech Corporation, Aug. 2016.

-
- [51] J. Gaelens, P. Van Torre, J. Verhaevert, and H. Rogier, “LoRa Mobile-To-Base-Station Channel Characterization in the Antarctic”, *Sensors*, vol. 17, no. 8, 2017.

9

Characterizing the Impact of Doppler Effects on Body-Centric LoRa Links with SDR

Based on "Characterizing the Impact of Doppler Effects on Body-Centric LoRa Links with SDR" by Thomas Ameloot, Marc Moeneclaey, Patrick van Torre and Hendrik Rogier, as accepted by *MDPI Sensors*.

★ ★ ★

Long-range, low-power wireless technologies such as LoRa have been shown to exhibit excellent performance when applied in body-centric wireless applications. However, the robustness of LoRa technology to Doppler spread has recently been called into question by a number of researchers. This chapter evaluates the impact of static and dynamic Doppler shifts on a simulated LoRa symbol detector and two types of simulated LoRa receivers. The results are interpreted specifically for body-centric applications and confirm that, in most application environments, pure Doppler effects are unlikely to severely disrupt wireless communication, confirming previous research, which stated that the link deteriorations observed in a number of practical LoRa measurement campaigns would mainly be caused by multipath fading effects. Yet, dynamic Doppler shifts, which occur as a result of the relative acceleration between communicating nodes, are also shown to contribute to link degradation. This is especially so for higher LoRa spreading factors and larger packet sizes.

9.1 Introduction

In recent years, sub-GHz low-power wide-area network (LPWAN) technologies such as SigFox [1], NB-IoT [2] and LoRa [3] have played key roles in the development of the rapidly evolving Internet of Things (IoT). Following the widespread adoption of these technologies in a wide range of application environments, several research efforts have been devoted to assessing the viability of using LoRa modulation for body-centric wireless communication [4]–[6]. LoRa employs wide-band frequency-modulated pulses called chirps to achieve spreading gain, which results in the successful reception of packets at extremely low signal-to-noise ratio (SNR) levels [7]. Compared to its competitors, LoRa is especially suitable for body-centric applications as its data rate can be adapted, which has been shown to benefit the coverage of body-centric LoRa networks [8]. LoRa modulation is most often deployed in the 868 MHz industrial, scientific and medical (ISM) radio band. For body-centric wireless communication, this band is very interesting as it both enables applications to benefit from the excellent propagation characteristics observed at sub-GHz frequencies, while still allowing compact wearable antennas to be designed, given the wavelength of 35 cm.

To properly assess the viability of using LoRa modulation in body-centric networks, it is important to thoroughly evaluate its physical-layer performance. Unfortunately, as LoRa is a proprietary technology, research into its wireless performance has been challenging. Up till now, it has mostly relied on either theoretical reviews [9]–[12] or channel measurements gathered by commercial transceivers [4]–[7]. Recently, efforts have been carried out to implement LoRa modulation in signal processing code, either for simulation purposes or for implementation on software defined radio (SDR) platforms [13]–[18]. Having access to individual I and Q samples enables much more accurate channel estimation than possible with commercial transceivers. Furthermore, using these implementations, different propagation mechanisms can be simulated, and their influence on LoRa modulation can be analyzed.

One mechanism that can impact body-centric wireless links is the Doppler effect. As people move around, their relative velocities change continuously. Several sources declare that LoRa shows good immunity against the Doppler effect [19], [20]. Some practical studies confirm this, however, others do not. In [21], LoRa link degradations are demonstrated for relative velocities around 40 km/h. In [22], the Doppler effect is blamed for severe link degradations. In [23], the authors presented two body-to-base-station measurement campaigns at different velocities (6.2 km/h and 31.1 km/h), which show no significant difference. These contradictions were also examined in [24], which presents lab measurements and outdoor experiments investigating the Doppler effect in LoRa satellite communication. In [24], it is demonstrated that LoRa is indeed reasonably Doppler-resistant, and it is stated that the link degradations observed in [21] are expected to be the result of Doppler spread. However, most of these conclusions are based on fully experimental examinations.

This chapter assesses the impact of Doppler effects on a recently developed SDR-implementation of LoRa [25]. General conclusions are drawn based on computer simulations of static and dynamic Doppler effects, assuming a worst-case angle of incidence. For both cases, a comparison is made between two packet synchronization strategies. Results are also interpreted specifically for body-centric LoRa networks. Finally, guidelines are provided on how static and dynamic Doppler effects can be mitigated in LoRa networks, e.g. by modifying the packet structure. The chapter is structured as follows. In Section 9.2, LoRa modulation is described in general. Additionally, key points on the SDR implementation applied in this work are presented. Section 9.3 elaborates on relevant considerations published in other research and describes the software-based simulation of Doppler effects on LoRa modulation. A discussion of the results in perspective of previous research is presented in Section 9.4. General conclusions are drawn in Section 9.5.

9.2 SDR-based LoRa Modulation

9.2.1 LoRa Modulation Basics

LoRa is based on chirp spread spectrum (CSS) modulation [26], which uses wide-band frequency modulated pulses to encode information. The most important modulation parameters are the spreading factor $SF \in \{7, 8, 9, 10, 11, 12\}$, bandwidth $BW \in \{125, 250, 500\}$ kHz and code rate $CR \in \{4/5, 4/6, 4/7, 4/8\}$. In most LoRa research, the bandwidth is actually used to describe the frequency swing B of the signals, since very little energy is present for frequencies outside of the range described by B . The spreading factor determines the slope of the chirp w.r.t. the frequency swing. For a given B , a higher spreading factor spreads any given LoRa symbol over a longer symbol interval. A detailed description of LoRa packet air times and data rates for different SF values is provided in [8]. Increasing the spreading factor or the frequency swing also impacts the sensitivity of LoRa receivers, as presented in [27]. On the packet level, a default preamble length of 12.25 symbols is considered. This preamble consists of eight up-chirps that constitute the pilot sequence, two so-called sync word symbols, which enable the user to distinguish packets from different LoRa networks, and 2.25 down-chirps, which make up the start-of-frame delimiter (SFD), used for packet synchronization. The optional header and/or cyclic redundancy check that can be added to LoRa packets are considered to be part of the data payload. The interleaving and decoding steps that are applied to data when encapsulated in a LoRa packet have been documented in [13] and are considered to be part of the data link layer. Consequently, these are not discussed in this chapter. Additional details and considerations on high-level aspects of LoRa and LoRaWAN can be found in [27] and [28].

9.2.2 Software Implementation

As mentioned earlier, this chapter employs a software implementation of LoRa to investigate the impact of Doppler shifts on the physical layer of LoRa modulation. In this implementation, which is based on LoRa waveform expressions presented in [12] and [25], a discrete LoRa up-chirp with symbol energy E_s and symbol duration T_s is described by the waveform

$$s_{\text{up}}[n] = \sqrt{\frac{E_s}{N}} \exp \left\{ j 2\pi \left[\frac{\alpha T_s^2 n^2}{2 N^2} \right] \right\}, \quad (9.1)$$

where $n \in \{0, 1, 2, \dots, N-1\}$ signifies the sample index and N equals the amount of samples used to describe the up-chirp. N is related to the spreading factor through $N = K \cdot M$, with $M = 2^{\text{SF}}$ and $K \in \mathbb{Z}_+$ the oversampling factor. The slope α (in Hz/s) of the up-chirp is related to the symbol duration and the frequency swing B through $\alpha = B/T_s$. A LoRa symbol $a \in \{0, 1, 2, \dots, M-1\}$ is encoded by changing the starting frequency of the chirp to aB/M and resetting the instantaneous frequency of the chirp to zero when it reaches B . According to the slope of the chirp, this occurs at the time instant when $n = (1 - a/M)N$. After the reset, the chirp frequency again increases linearly according to α . Hence, the encoded LoRa symbol $s[n, a]$ is described by

$$s[n, a] = \sqrt{\frac{E_s}{N}} \exp \left\{ j 2\pi \left[\frac{\alpha T_s^2 n^2}{2 N^2} + F_a[n, a] \frac{T_s n}{N} \right] \right\}, \quad (9.2)$$

$$\text{where } F_a[n, a] = \begin{cases} \frac{aB}{M} & n < (1 - \frac{a}{M})N \\ \frac{aB}{M} - B & n > (1 - \frac{a}{M})N \end{cases}. \quad (9.3)$$

When no oversampling is applied ($K = 1$, $N/T_s = B$ and $N = M$), this symbol can be detected by first multiplying $s[n, a]$ by the complex conjugate (as indicated by the asterisk) of the up-chirp $s_{\text{up}}[n]$ and then applying the discrete Fourier transform (DFT), indicated by the operator \mathcal{F} , yielding

$$X_i = \mathcal{F} \left\{ s[n, a] \cdot s_{\text{up}}^*[n] \right\}. \quad (9.4)$$

As the signal s_{up}^* corresponds to a chirp with a frequency that linearly decreases, it will be referred to as the down-chirp s_{down} from now on. The frequency bins X_i resulting from equation (9.4) describe the possible symbol levels that can be obtained when detecting the LoRa symbol. An estimate \tilde{a} for the encoded symbol a is found by determining

$$\tilde{a} = \arg_i \max(|X_i|). \quad (9.5)$$

In Fig. 9.1, spectrograms are shown for the chirps described by $s_{\text{up}}[n]$, $s_{\text{up}}^*[n]$ ($= s_{\text{down}}[n]$) and the modulated symbol $s[n, a]$, with a an arbitrary symbol value. Additionally, the result of the element-wise multiplication of $s[n, a]$ and $s_{\text{up}}^*[n]$ is shown, which illustrates how all symbol energy is concentrated in a single DFT bin when applying (9.4).

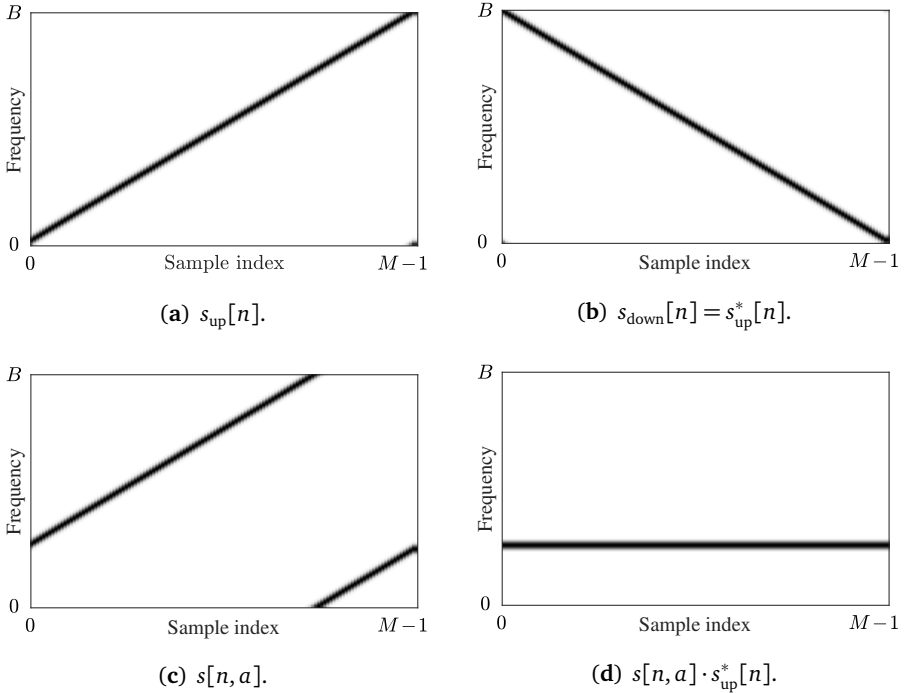


Figure 9.1: Spectrograms of the waveforms for an up-chirp $s_{\text{up}}[n]$, a down-chirp $s_{\text{down}}[n] = s_{\text{up}}^*[n]$, an arbitrary LoRa symbol $s[n, a]$ and the product $s[n, a] \cdot s_{\text{up}}^*[n]$ as applied in (9.4), for $K = 1$ and $N = M$.

When oversampling is applied ($K > 1$, $N/T_s = KB$ and $N = KM$), frequency shifts can be simulated without suffering from aliasing. However, as thoroughly described in [25], when detecting the symbol, the signal must first be filtered using an anti-aliasing filter and decimated such that $N = M$ in order to apply the detection procedure presented above. Additionally, a frequency error Δf can be corrected by applying a frequency shift before filtering and decimating the signal. When $\tilde{\Delta f}$ denotes an estimate of Δf , this shift is applied by multiplying each sample by the following complex exponential:

$$\exp \left\{ -j2\pi \tilde{\Delta f} \frac{nT_s}{N} \right\}. \quad (9.6)$$

9.3 Doppler Effects Simulation and Analysis

In current literature on LoRa Doppler effects, contradictory conclusions are presented. The most thorough examinations of this topic are found in [21] and [24]. In [21], the impact of Doppler spread is first analyzed by comparing the coherence time of the channel to LoRa symbol durations for different modulation settings. Then, a LoRa receiver node is attached to a lathe, rotating it at high speeds to determine the impact of different angular velocities on the link quality. Finally, a long-range outdoor measurement campaign is presented. In [24], Doppler effects are analyzed in the context of satellite radio applications. Lab measurements are presented based on SDR-synthesized LoRa packets, received by an SX1276 LoRa transceiver. Additionally, an outdoor measurement campaign is performed as well. Whereas the authors of both papers consider the impact of Doppler effects on the full LoRa modulation protocol based on experimental data gathered with commercial transceiver modules, the present work also focuses on the fundamental performance impact of the Doppler effects on the symbol detector itself. This standalone symbol detector is implemented in software and assumes perfect packet detection and synchronization. Additionally, physical-layer performance is estimated using fully simulated LoRa receivers, described in detail in [25]. As a result, the impact of LoRa implementation details - e.g. specific parameters that can be enabled or disabled in the Semtech SX1276 LoRa transceiver used in [21] and [24] - is ignored. Doppler shifts are considered as static and dynamic contributions in Sections 9.3.1 and 9.3.2, respectively.

9.3.1 Static Doppler Shift

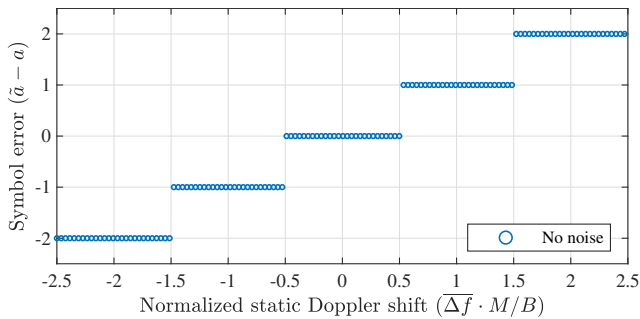
A static Doppler shift occurs when the transmitter and receiver are moving at a constant relative velocity with respect to one another. When the frequency swing B is assumed to be much smaller than the RF carrier frequency F , static Doppler shifts can be simulated by adding a frequency offset Δf to the $F_a[n, a]$ term in (9.2). Assuming a worst-case angle of incidence, the offset Δf can be calculated based on the value for F and the relative velocity Δv of the receiver w.r.t. the transmitter as

$$\Delta f = \frac{\Delta v}{c} \cdot F, \quad (9.7)$$

where c denotes the speed of light.

When a frequency shift occurs as a result of the Doppler effect, the LoRa receiver's frequency settings will no longer be matched to the one of the incoming LoRa signal. As LoRa uses linear chirps, this causes symbol energy to shift to other frequency bins. If the down-chirp of the receiver is perfectly time-aligned with the LoRa symbol and the absolute value of Δf is larger than $0.5 \cdot B/M$, this will cause a symbol error. Moreover, when a significant amount of noise is present, symbol errors may occur even $|\Delta f| < 0.5 \cdot B/M$. This is demonstrated in Fig. 9.2,

which shows the symbol errors recorded when adding different Doppler shifts to a synthesized LoRa symbol ($SF = 12$, $B = 125$ kHz), transmitted over a noise-free channel and an additive white Gaussian noise (AWGN) channel with very adverse noise conditions ($SNR = -24$ dB). As the same exercise can be performed for other spreading factors, the average frequency offsets are normalized w.r.t. M and B through $\Delta f \cdot M/B$. However, it should be kept in mind that the SNR values at which this performance is observed will vary when changing either of these parameters. For each SF decrement by one, or each frequency swing multiplication by two, this approximately corresponds to a 3 dB SNR performance penalty [11], [25].



(a) No noise.

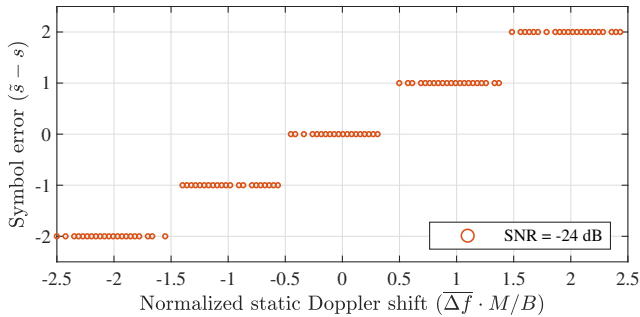
(b) $SNR = -24$ dB.

Figure 9.2: Symbol errors observed when detecting a synthesized LoRa symbol subject to different amounts of static Doppler shift. When no dot is present, the symbol error is outside $[-2, 2]$. ($SF = 12$, $B = 125$ kHz)

To provide some reference with regard to the normalized Doppler shift, Table 9.1 shows the denormalized frequency errors for each SF value, assuming a fixed frequency swing of 125 kHz, which is default for LoRa modulation. Table 9.1 also shows the corresponding relative velocities that would cause this Doppler shift for an operating frequency of $F = 868$ MHz. The values in Table 9.1 confirm that, for the LoRa symbol detector, the effects of Doppler shift are significantly worse for higher spreading factors. This was first shown in [21], where the coherence time

SF	Δf for * (Hz)	Δv (m/s)	Δv (km/h)
7	488.28	168.64	607.12
8	244.14	84.32	303.56
9	122.07	42.16	151.78
10	61.04	21.08	75.90
11	30.52	10.54	37.95
12	15.26	5.27	18.97

* $\Delta f \cdot M/B = 0.5$

Table 9.1: Reference values for Δf and Δv for a normalized Doppler shift of 0.5. ($B = 125$ kHz and $F = 868$ MHz).

of a channel impacted by Doppler shifts is expressed as a function of the relative velocity between both communicating nodes. These coherence times are compared to the duration of LoRa symbols at each spreading factor. For higher SF values, these symbol durations are significantly larger.

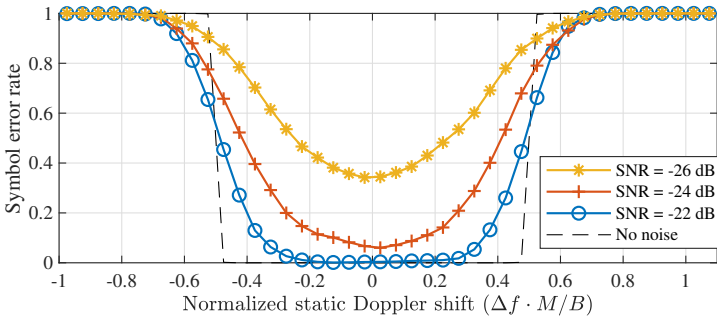
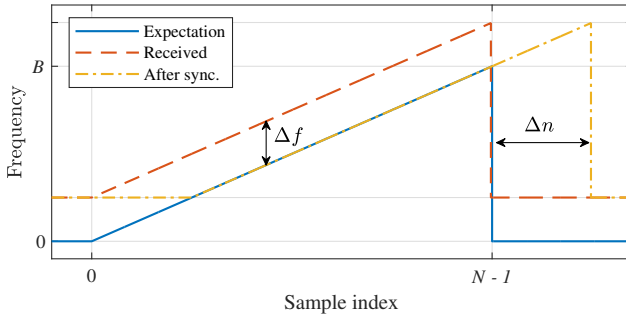


Figure 9.3: Symbol detection performance for static Doppler shifts with a perfectly time-aligned down-chirp. (SF = 12, $B = 125$ kHz)

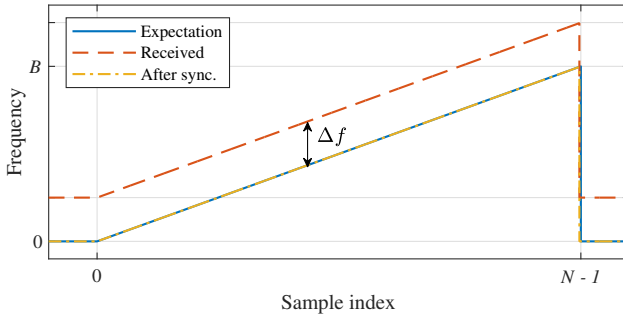
The range of normalized Doppler shifts that remains error-free in the absence of noise in Fig. 9.2, is explored in more detail in Fig. 9.3. This figure shows the symbol error rate (SER) as a function of the normalized Doppler shift, defined earlier as $\Delta f \cdot M/B$. Based on Figs. 9.2 and 9.3, one might be tempted to conclude that static Doppler shifts have a strong impact on the entire physical layer of LoRa modulation, even for relatively low velocities, as even a slight frequency offset might easily cause symbol errors in the detector.

However, it should be noted that the discrete symbol errors shown in Fig. 9.2 will only occur when the down-chirp is perfectly time-aligned. If the receiver performs any form of synchronization based on the timing of the pilot sequence in the packet’s preamble, this frequency mismatch will at least be reduced to the interval $[-0.5, 0.5] \cdot M/B$, mitigating the discrete symbol errors shown in Fig. 9.2 if no noise is present. In practice, this very rudimentary form of synchronization

introduces a relative time shift $\Delta n/N$, equal to $\Delta f/B$, as illustrated in Fig.9.4a. Unfortunately, countering the frequency shift solely with a time shift results in the loss of some symbol energy as the received chirp is not aligned with the frequency range $(0, B)$ expected by the receiver. Moreover, the detection is performed in the presence of a timing error Δn , causing some intersymbol interference. Therefore, frequency errors larger than about $B/2$ cannot be handled when using this synchronization strategy.



(a) Pure time synchronization through Δn .

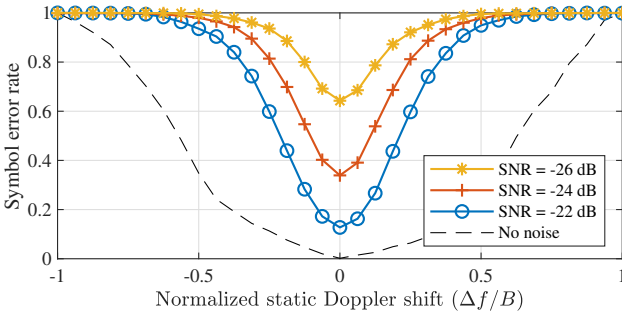


(b) Frequency offset synchronization by Δf .

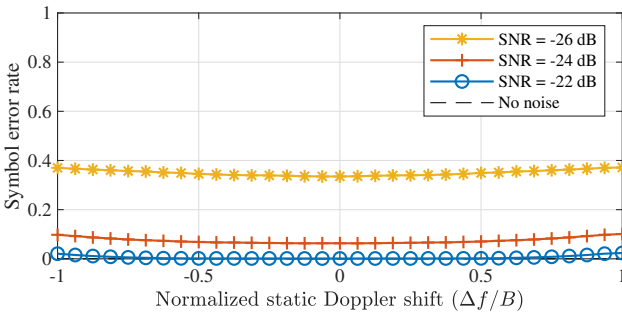
Figure 9.4: Up-chirps for time and frequency synchronization strategies that mitigate static Doppler shifts.

Alternatively, the frequency shift can be corrected by the receiver, based on the frequency contents of the preamble, as is introduced in [25] and illustrated in Fig. 9.4b. Naturally, as presented in [25], estimating this frequency offset does come at a slightly higher computational cost. Either way, the receiver should be able to correctly process the packet as the detected symbol values shift equally across the packet w.r.t. the pilot symbols in the preamble. Yet, if no frequency correction is performed, the error performance is improved by performing time synchronization. This is confirmed in Fig. 9.5, which shows the LoRa symbol detection performance for both strategies at different noise levels and $SF = 12$. Both these strategies are presented with the value for the frequency shift that was ap-

plied to the synthesized symbol. Hence, in the time synchronization case, Δn is calculated based on this known value. Static Doppler shifts are again normalized. However, as it is no longer appropriate to normalize the frequency offset w.r.t. B/M , it is now expressed as a fraction of B . All simulations assume $B = 125$ kHz.



(a) Pure time synchronization.



(b) Frequency offset synchronization.

Figure 9.5: LoRa symbol detection performance when using the different synchronization strategies illustrated in Figure 9.4. Both strategies are presented with the value for the frequency shift applied to the synthesized symbol. Δn is calculated based on this metric. ($SF = 12$, $B = 125$ kHz)

A few interesting points are demonstrated in Fig. 9.5. First, it is shown that symbol detection performance is significantly better when applying an appropriate frequency offset instead of purely relying on time synchronization. In fact, in the latter case, symbol errors are observed for all non-zero static Doppler shifts when no noise is present. However, it should be mentioned that applying an appropriate coding strategy is expected to relieve part of this problem. When applying a correct receiver frequency offset, the same symbol error rate is observed for all applied Doppler shifts.

When considering the performance of LoRa modulation under static Doppler shifts, a distinction is made between the symbol error performance of the detector presented in Fig. 9.5, which assumes perfect signal detection and synchronization performance to isolate the impact of the Doppler effect on the symbol detector, and the bit error rate (BER) performance of a simulated receiver, which performs packet detection and synchronization based on the received signal, as presented in [25]. Using simulated receivers allows us to more accurately assess the performance of actual LoRa hardware. Whereas [25] also presents advanced methods for improving the synchronization, beyond frequency offset correction, these are omitted here. The bit error rates observed for both synchronization strategies presented earlier are presented for $SF = 7$ and $SF = 12$ in Fig. 9.6.

Fig. 9.5 illustrated that applying frequency offset synchronization results in better SER performance than employing pure time synchronization. The disparity in performance between both strategies is also apparent in the results for the simulated receivers. In Figs. 9.6a and 9.6c, bit errors are again observed for all non-zero Doppler shifts, even when no noise is present. In contrast, the BER is very low for normalized Doppler shifts in the range $[-0.1, 0.1]$ presented in Figs. 9.6b and 9.6d. The limits of this range correspond to relative velocities around 4320 m/s. Hence, static Doppler immunity is observed to be very high. Additionally, when no noise is present, Doppler immunity is slightly better for $SF = 12$ than for $SF = 7$. At very low SNRs, the comparison between spreading factors is less straightforward, mainly due to the differences in SNR performance.

In general, it can be concluded that, when the right synchronization and/or coding strategy is applied, LoRa modulation is practically immune to purely static Doppler shifts as long as these do not exceed about 10% of B . For body-centric LoRa networks, this means that a constant Doppler shift is expected to have very little influence on link performance for the overwhelming majority of applications due to the sheer magnitude of the relative velocities presented above. However, these results could be relevant for satellite-to-body communication or other space-related applications, where relative velocities are much higher [29]. Yet, in space applications, relative velocities are also known to a certain degree. Consequently, the operating frequencies of LoRa receivers could be adapted to correct for static Doppler shifts.

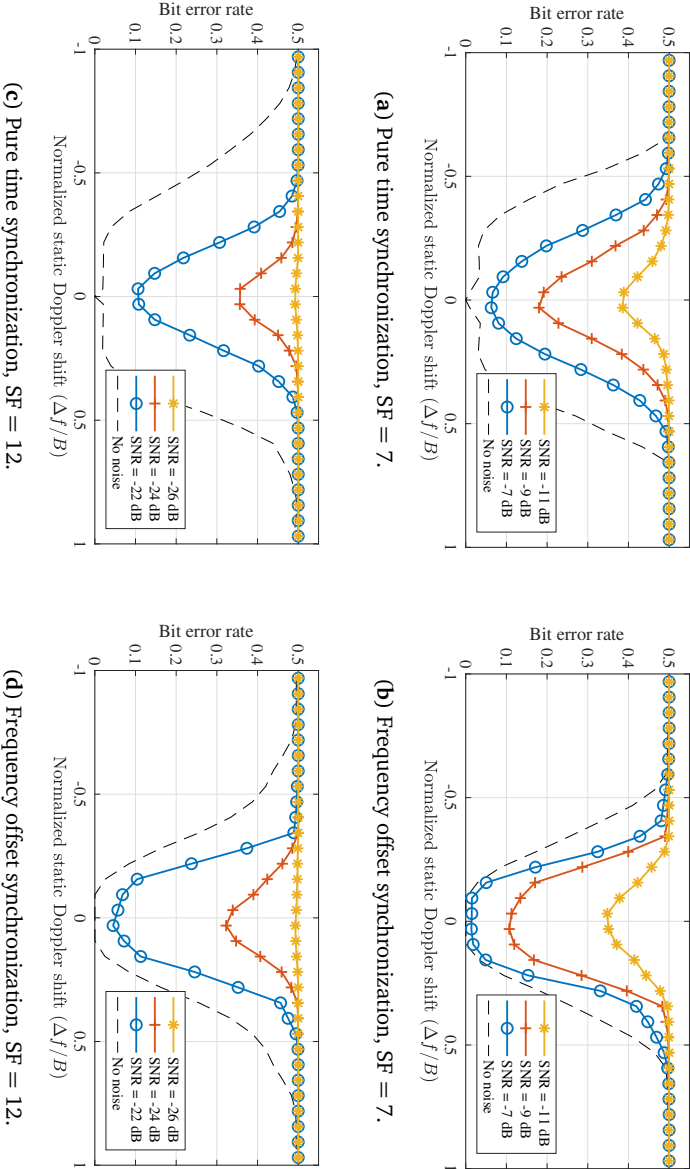


Figure 9.6: Bit error performance when using the different synchronization strategies illustrated in Figure 9.4 for different spreading factors. Based on synthesized LoRa packets with 100 data symbols, received by simulated LoRa receivers. ($B = 125$ kHz)

9.3.2 Dynamic Doppler Shift

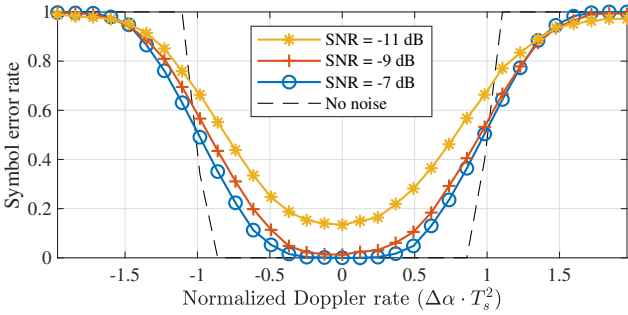
As the relative velocity between two communicating nodes is rarely constant in body-centric networks, dynamic Doppler effects should also be considered. Considering a constant relative acceleration Δa of the receiver w.r.t. the transmitter during a LoRa packet, a constant Doppler rate $\Delta\alpha$ (in Hz/s) is introduced, which manifests itself as an offset $\Delta\alpha$ to be added to the slope α of the chirps described by (2). Once again assuming a worst-case angle of incidence, the Doppler rate is given by

$$\Delta\alpha = \frac{\Delta a}{c} \cdot F, \quad (9.8)$$

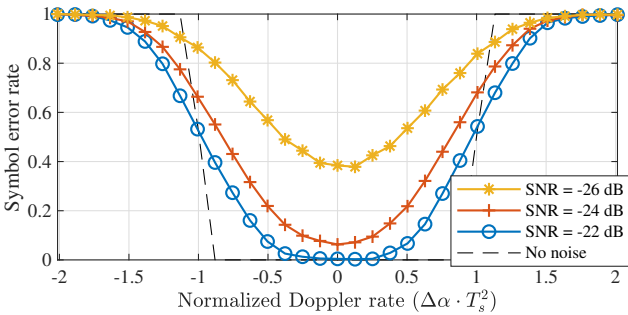
where F again indicates the RF frequency of the chirp.

For a single LoRa symbol transmitted and received in realistic acceleration conditions, this Doppler rate is expected to have almost no influence on the performance of the symbol detector. After all, using this kind of slope offset is equivalent to communicating with a receiver utilizing a slightly different chirp rate. The symbol error rates observed for $SF = 7$ and $SF = 12$ are shown in Fig. 9.7. These were acquired by synthesizing LoRa packets with a slope $\alpha + \Delta\alpha$ and applying these packets to a symbol detector with a perfectly time-aligned down-chirp and no chirp rate offset. In this figure, the Doppler rate is normalized through $\Delta\alpha \cdot T_s^2$.

Fig. 9.7 confirms that the symbol detector is very robust against constant Doppler rates. In fact, when no noise is considered, errors are only observed for normalized Doppler rates outside $[-1, 1]$. These rates correspond to acceleration values of 285 km/s^2 and 285 m/s^2 . While the Doppler rate immunity for $SF = 12$ is three orders of magnitude worse than the one for $SF = 7$, both of these acceleration values are quite unrealistic in practice. However, despite the minimal impact on symbol detection performance, it can be expected that the introduction of $\Delta\alpha$ will have a much larger effect at the packet level. As the frequency offset between the received packet and the one expected or estimated by the receiver changes over time, the impact of a constant Doppler rate will depend on the duration of the packet, which is determined by the spreading factor, the frequency swing, and the length of the data payload. As shown in Section 9.3.1, the static Doppler shift is mostly eliminated through packet synchronization, which is based on the contents of the preamble. Consequently, when a constant acceleration is assumed, the resulting Doppler rate will have a larger impact on symbols at the end of the data payload, while those directly following the preamble may be relatively unimpacted. To quantify this, the impact of the constant Doppler rate caused by a constant acceleration on the BER is determined for packets with different packet lengths (in number of data payload symbols). LoRa packets were synthesized with a modified chirp rate $\alpha + \Delta\alpha$. The receiver decoded these packets using perfectly aligned down-chirps with chirp rate α , after applying a constant frequency correction to the packet, equal to the average of the true frequency mismatch observed in the



(a) SF = 7.

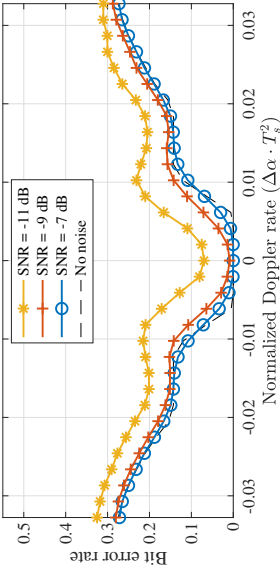


(b) SF = 12.

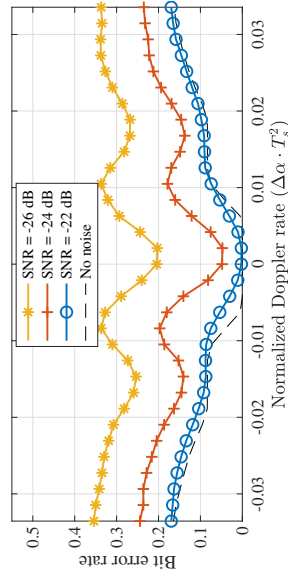
Figure 9.7: Symbol detection performance for constant Doppler rates when the down-chirp is perfectly time-aligned. ($B = 125$ kHz)

preamble of the packet. The results of these simulations are shown for SF = 7 and SF = 12 in Fig. 9.8.

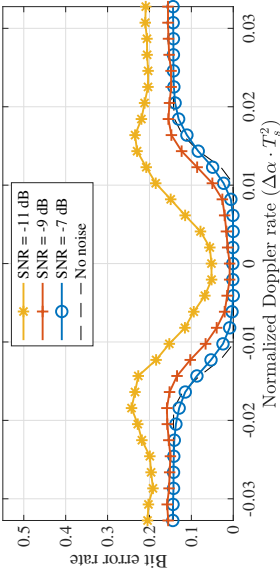
When no noise is considered, a range of acceleration values that do not lead to bit errors can be observed for each subfigure of Fig. 9.8. For both spreading factors, the normalized Doppler rates that lead to points inside this error-free range is given by $[-0.01, 0.01]$ and $[-0.006, 0.006]$ for 16 and 32 symbol payloads, respectively. We denote the denormalized absolute values for the limits of these ranges as $\Delta\alpha_{\max}$. Reference values for $\Delta\alpha_{\max}$ and the corresponding relative acceleration values Δa are shown for all spreading factors in Table 9.2. These were determined by repeating the simulations presented in Fig. 9.8 for each SF value.



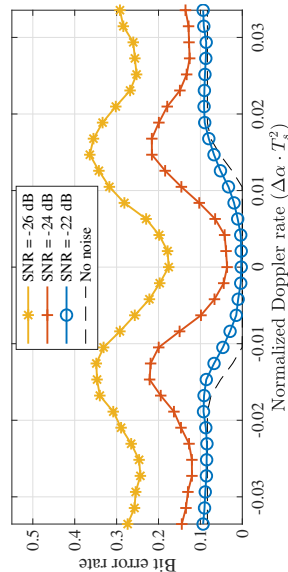
(b) Data payload = 32 symbols, SF = 7.



(d) Data payload = 32 symbols, SF = 12.



(a) Data payload = 16 symbols, SF = 7.



(c) Data payload = 16 symbols, SF = 12.

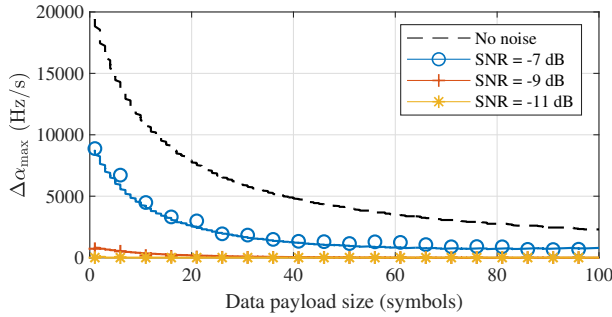
Figure 9.8: Bit error performance impact of constant Doppler rates for different data payload sizes and spreading factors. ($B = 125$ kHz)

Data payload = 16 symbols		
SF	$\Delta\alpha_{\max}$ (Hz/s)	Δa (m/s ²)
7	9125	3152
8	2735	944.6
9	586.3	202.5
10	175.8	60.72
11	39.13	13.51
12	9.50	3.28

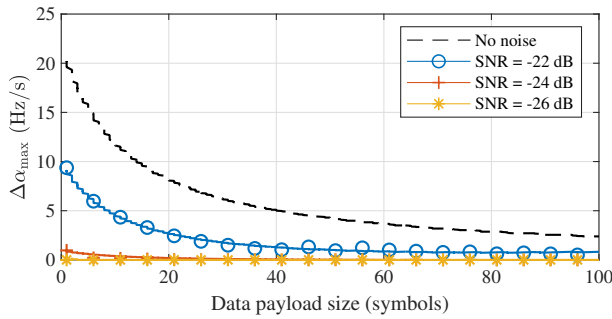
Data payload = 32 symbols		
SF	$\Delta\alpha_{\max}$ (Hz/s)	Δa (m/s ²)
7	5625	1943
8	1563	539.8
9	391.3	135.1
10	97.63	33.72
11	23.05	7.96
12	5.75	1.98

Table 9.2: Reference values for $\Delta\alpha_{\max}$ and Δa . ($B = 125$ kHz and $F = 868$ MHz).

Table 9.2 clearly shows that constant Doppler rates have a much larger impact on the BER when LoRa packets are considered. For higher spreading factors (11 and 12), errors are observed as a result of relative acceleration values that are relatively high, but not altogether unrealistic in certain body-centric wireless applications. For SF = 7, the relative accelerations that lead to bit errors are much higher, even for a hypothetical satellite-to-body communication system. The relation between the size of the data payload and the denormalized limit of the error-free range $\Delta\alpha_{\max}$, is shown for both spreading factors under study in Fig. 9.9, where the same time synchronization and frequency correction as in Fig. 9.8 are assumed.



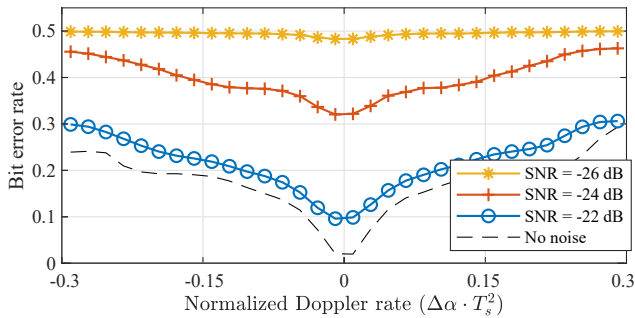
(a) SF = 7.



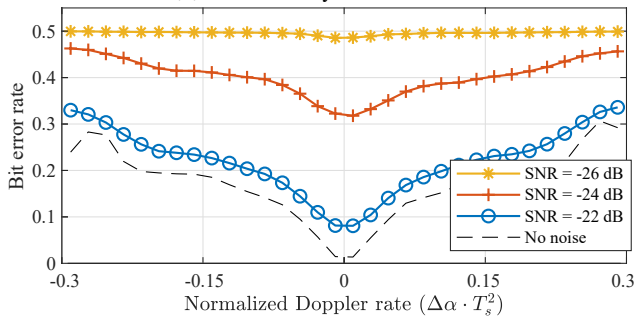
(b) SF = 12.

Figure 9.9: Lowest constant Doppler rate for which bit errors were observed ($\Delta\alpha_{\max}$) for different data payload sizes. ($B = 125$ kHz)

Finally, the impact of constant Doppler rates on LoRa receivers can be illustrated by also considering the simulated detectors presented earlier. This is realized by simulating the transmission and reception of LoRa packets (SF = 12, $B = 125$ kHz), synthesized with a certain chirp rate offset $\Delta\alpha$. The synthesized 32 symbol payload of these packets contains a random data sequence, to which the detected symbol sequence is compared. The BER that results from this operation, shown in Fig. 9.10, demonstrates that the full detection algorithm is similarly impacted by constant Doppler rates as the symbol detector (see Fig. 9.8). Hence, packet detection and synchronization are impacted less than or as much as symbol detection. In general, both receive strategies presented in Fig. 9.4 show very similar performance. This is fully in line with expectations, as a constant Doppler rate cannot be mitigated by the type of synchronization applied in these simulated receivers. A transmit strategy that would enable LoRa receivers to alleviate constant Doppler rates caused by a constant relative acceleration could solve this by repeating a number of known pilot symbols after the data payload, effectively adding an end-of-frame delimiter. Based on the frequency offset observed for these symbols, the estimated frequency offset could be adapted dynamically to mitigate the chirp rate mismatch.



(a) Pure time synchronization.



(b) Frequency offset synchronization.

Figure 9.10: BER performance for different dynamic Doppler shifts, using the different synchronization strategies illustrated in Figure 9.4. (SF = 12, B = 125 kHz)

In summary, constant Doppler rates may have a larger impact on the performance of LoRa receivers than purely static Doppler shifts. In body-centric wireless applications, packet loss may occur when higher spreading factors (11 or 12) are used. For these SF values, a significant amount of bit errors are to be expected when using large packets in an environment where acceleration values are high. This occurs, for example, when using LoRa to monitor athletes in professional sports applications (skiing, cycling, skydiving...) or when tracking wild animals.

9.4 Discussion

In this section, the results presented in Section 9.3 are compared to those of previous studies. Literature stating that LoRa modulation is very resistant to Doppler shifts possibly draws this conclusion based on indicators related to the excellent static Doppler immunity demonstrated in Section 9.3.1 of this chapter. In experiments that led to the conclusion that LoRa is a lot more vulnerable to the Doppler effect, a multitude of factors may have impacted link performance. First of all, in addition to the relative acceleration between the communicating nodes (see Section 9.3), rapid changes in antenna orientation will definitely impact the link budget available for communication. Furthermore, the type of antenna that is used may also have an impact on the severity of Doppler effects, as the directivity impacts the SNR of the incoming signal. For body-centric applications, this is especially relevant as there are a lot of constraints on antenna design, the most obvious of which is its size. As already mentioned in [24], fading caused by multipath effects may also play a significant role. For example, in [21], the measurements gathered on the lathe must have been greatly impacted by multipath propagation effects, as the transmitter was placed on a radio mast outdoors. This interpretation also agrees with most other research results presented in literature. The experiments presented in [23] were indeed performed in a relatively open environment, employing a base-station placed on a high office building. These factors might have alleviated multipath effects to a certain degree. In [30], results indicated that packets were lost in a LoRa body-to-body range test when the test persons were moving towards each other, while several packets were received at considerable distances while the test persons were standing still. This range test was also performed in a relatively open environment, however, both test persons were walking on the same ground level. Hence, when more distance separated the test persons, more scatterers may have had a larger impact on the link as the direct link path got weaker. When considering multipath propagation contributions, it is again important to address the fact that also the reception and transmission of certain multipath components may be influenced by the radiation characteristics of the antennas under consideration. For example, different antenna topologies exist that actively resist multipath effects [31], [32].

9.5 Conclusion

An assessment of static and dynamic Doppler effects on LoRa symbol detection performance was presented based on experiments with a simulated LoRa symbol detector that can be implemented on SDR. Additionally, two types of LoRa receivers were simulated, comparing two different synchronization strategies. For static Doppler effects, it has been shown that, while the symbol detector itself is highly vulnerable to frequency shifts, Doppler effects are largely mitigated by either of these synchronization strategies. For simulated receivers, immunity with respect to constant frequency shifts up to 10 % of the frequency swing of the LoRa signal is demonstrated, assuming a worst-case angle of incidence, the Doppler rate is given by. As expected, the best performance is observed for a receiver that applies frequency correction. Dynamic Doppler shifts, modeled as constant Doppler rates, mainly impact LoRa communication on the packet level, as opposed to the symbol detection level, which is highly robust against constant Doppler rates. As expected, packets with a larger payload are impacted proportional to their length. When considering the impact on the performance of the symbol detector, a range of Doppler rates that do not lead bit errors is observed. For payload lengths of 16 and 32 symbols, respectively, this range corresponds to 1 % and 0.6 % of the inverse of the squared symbol duration. Both static and dynamic Doppler effects can be mitigated by either applying time and/or frequency synchronization, or by modifying the structure of LoRa packets by e.g. including an end-of-frame delimiter that contains another sequence of pilot symbols, respectively.

When applying these results to body-centric LoRa applications, static Doppler shifts are expected to have very little impact on link performance, especially for lower spreading factors. Yet, large dynamic Doppler shifts may significantly reduce the quality of the wireless link for higher spreading factors when the SNR is very low. Overall, however, LoRa is still regarded as an excellent modulation technology for application in body-centric wireless networks, given the extremely low power use and high sensitivity of LoRa hardware.

References

- [1] SigFox Foundation, *SigFox*, <https://www.sigfox.com/en>.
- [2] GSM Association, *NarrowBand - Internet of Things (NB-IoT)*, <https://www.gsm.com/iot/narrow-band-internet-of-things-nb-iot/>.
- [3] LoRa Alliance, *LoRa*, <https://www.lora-alliance.org/>.
- [4] J. Petäjäjärvi, K. Mikhaylov, M. Hmlinen, and J. Iinatti, “Evaluation of LoRa LPWAN Technology for Remote Health and Wellbeing Monitoring”, in *2016 10th International Symposium on Medical Information and Communication Technology (ISMICT)*, 2016.
- [5] J. Petäjäjärvi, K. Mikhaylov, R. Yasmin, M. Hämäläinen, and J. Iinatti, “Evaluation of LoRa LPWAN Technology for Indoor Remote Health and Wellbeing Monitoring”, *International Journal of Wireless Information Networks*, vol. 24, no. 2, pp. 153–165, 2017.
- [6] P. A. Catherwood, S. McComb, M. Little, and J. A. D. McLaughlin, “Channel Characterisation for Wearable LoRaWAN Monitors”, in *Loughborough Antennas Propagation Conference (LAPC 2017)*, 2017, pp. 1–4.
- [7] T. Ameloot, P. Van Torre, and H. Rogier, “A Compact Low-Power LoRa IoT Sensor Node with Extended Dynamic Range for Channel Measurements”, *MDPI Sensors*, vol. 18, no. 7, p. 2137, 2018.
- [8] T. Ameloot, P. Van Torre, and H. Rogier, “Experimental Parameter Optimization for Adaptive LoRa Modulation in Body-Centric Applications”, in *2020 14th European Conference on Antennas and Propagation (EuCAP)*, Copenhagen, Denmark, 2020.
- [9] L. Vangelista, “Frequency Shift Chirp Modulation: The LoRa Modulation”, *IEEE Signal Processing Letters*, vol. 24, no. 12, pp. 1818–1821, 2017.
- [10] C. Ferreira Dias, E. Rodrigues de Lima, and G. Fraidenraich, “Bit Error Rate Closed-Form Expressions for LoRa Systems under Nakagami and Rice Fading Channels”, *Sensors*, vol. 19, no. 20, p. 4412, 2019.
- [11] T. Elshabrawy and J. Robert, “Closed-Form Approximation of LoRa Modulation BER Performance”, *IEEE Communications Letters*, vol. 22, no. 9, pp. 1778–1781, 2018.
- [12] M. Chiani and A. Elzanaty, “On the LoRa Modulation for IoT: Waveform Properties and Spectral Analysis”, *IEEE Internet of Things Journal*, vol. 6, no. 5, pp. 8463–8470, 2019.

- [13] P Robyns., P Quax., W. Lamotte., and W. Thenaers., “A Multi-Channel Software Decoder for the LoRa Modulation Scheme”, in *Proceedings of the 3rd International Conference on Internet of Things, Big Data and Security - Volume 1*, SciTePress, 2018, pp. 41–51.
- [14] P Edward, A. Muhammad, S. Elzeiny, M. Ashour, T. Elshabrawy, and J. Robert, “Enhancing the Capture Capabilities of LoRa Receivers”, in *2019 International Conference on Smart Applications, Communications and Networking (SmartNets)*, 2019, pp. 1–6.
- [15] T. Elshabrawy, P. Edward, M. Ashour, and J. Robert, “On the Different Mathematical Realizations for the Digital Synthesis of LoRa-Based Modulation”, in *European Wireless 2019; 25th European Wireless Conference*, 2019, pp. 1–6.
- [16] B. Sikken, *Decoding LoRa*, <https://revspace.nl/DecodingLora>.
- [17] J. Blum, *LoRa SDR Project*, <https://github.com/myriadrf/LoRa-SDR>.
- [18] RTL-SDRangelove, *Github Project Page*, <https://github.com/hexameron/rtl-sdrangelove>.
- [19] U. Noreen, A. Bounceur, and L. Clavier, “A Study of LoRa Low Power and Wide Area Network Technology”, in *2017 International Conference on Advanced Technologies for Signal and Image Processing (ATSIP)*, 2017, pp. 1–6.
- [20] J. C. Liando, A. Gamage, A. W. Tengourtius, and M. Li, “Known and Unknown Facts of LoRa: Experiences from a Large-Scale Measurement Study”, *ACM Trans. Sen. Netw.*, vol. 15, no. 2, 16:1–16:35, 2019.
- [21] J. Petäjäjärvi, K. Mikhaylov, M. Pettissalo, J. Janhunen, and J. Iinatti, “Performance of a Low-Power Wide-Area Network Based on LoRa Technology: Doppler Robustness, Scalability, and Coverage”, *International Journal of Distributed Sensor Networks*, vol. 13, no. 3, 2017.
- [22] D. Patel and M. Won, “Experimental Study on Low Power Wide Area Networks (LPWAN) for Mobile Internet of Things”, in *2017 IEEE 85th Vehicular Technology Conference (VTC Spring)*, 2017, pp. 1–5.
- [23] T. Ameloot, P. Van Torre, and H. Rogier, “LoRa Base-Station-to-Body Communication With SIMO Front-to-Back Diversity”, *IEEE Transactions on Antennas and Propagation*, vol. 69, no. 1, pp. 397–405, 2021.
- [24] A. A. Doroshkin, A. M. Zadorozhny, O. N. Kus, V. Y. Prokopyev, and Y. M. Prokopyev, “Experimental Study of LoRa Modulation Immunity to Doppler Effect in CubeSat Radio Communications”, *IEEE Access*, vol. 7, pp. 75 721–75 731, 2019.
- [25] T. Ameloot, H. Rogier, M. Moeneclaey, and P. Van Torre, “LoRa Signal Synchronization and Detection at Extremely Low Signal-to-Noise Ratios”, *submitted to IEEE Internet of Things Journal*, 2021.

- [26] A. Springer, W. Gugler, M. Huemer, L. Reindl, C. C. W. Ruppel, and R. Weigel, "Spread Spectrum Communications using Chirp Signals", in *IEEE/AFCEA EUROCOMM 2000. Information Systems for Enhanced Public Safety and Security*, 2000, pp. 166–170.
- [27] *137 MHz to 1020 MHz Low Power Long Range Transceiver*, SX1276/77/78/79, Rev. 5, Semtech Corporation, Aug. 2016.
- [28] A. Augustin, J. Yi, T. Clausen, and W. M. Townsley, "A Study of LoRa: Long Range & Low Power Networks for the Internet of Things", *Sensors*, vol. 16, no. 9, 2016.
- [29] Fernandez, Lara and Ruiz de Azua Ortega, Joan and Calveras, Anna and Camps, Adriano, "Assessing LoRa for Satellite-to-Earth Communications Considering the Impact of Ionospheric Scintillation", *IEEE Access*, vol. 8, pp. 165 570–165 582, Jan. 2020.
- [30] P. Van Torre, T. Ameloot, and H. Rogier, "Long-Range Body-to-Body LoRa Link at 868 MHz", in *Proceedings of the 13th European Conference on Antennas and Propagation (EuCAP)*, Krakow; Poland, 2019.
- [31] L. Vallozzi, W. Vandendriessche, H. Rogier, C. Hertleer, and M. L. Scarpello, "Wearable Textile GPS Antenna for Integration in Protective Garments", eng, in *Proceedings of the fourth European Conference on Antennas and Propagation*, Barcelona, Spain: IEEE, 2010, p. 4.
- [32] Y. Zhang, X. meng Yu, L. yu Kong, L. peng Zhang, and H. lei Qin, "Anti-Multipath Dual-Band GNSS Antenna Design with Peano Fractal EBG Structure", in *2016 Asia-Pacific International Symposium on Electromagnetic Compatibility (AP EMC)*, vol. 1, 2016, pp. 523–525.

10

Conclusions

10.1 Overview

In this dissertation, a diverse set of techniques was presented to characterize and enhance the performance of wireless sensor network (WSN) communication technologies. By focusing efforts on LoRa modulation, one of the most popular technologies on the market, industry-relevant performance assessments were documented. Additionally, advanced methods for increasing the link budget were proposed and/or demonstrated for a number of real-world WSN application environments.

In the second chapter of this work, custom LoRa channel characterization hardware was presented, which features an extended dynamic range for signal-to-noise ratio (SNR) measurements. Hardware verification experiments demonstrated the correct operation of this system and unveiled a number of unique link characteristics. In the outdoor measurement setup, reduced antenna performance was observed after rainfall occurred, while in the indoor link monitoring experiment, the influence of people inside the building was clearly visible in the received power levels.

In the next chapter, this hardware was deployed in a research-oriented sensor network. Variable link performance was observed for two long-distance (> 10 km) links. The recorded fluctuations were monitored over a period of one year and analyzed thoroughly. When compared to seasonal weather variations, a strong correlation was found between the intensity of temperature and humidity fluctuations, and the received power levels. It was concluded that the variable link performance recorded on these links are likely the result of daily tropospheric refractivity variations, which may in turn influence the fading process caused by diffraction around obstacles. Additionally, mechanisms such as multipath propagation, troposcatter, and weather-related antenna losses were also indicated as possible contributors.

This shows that when deploying long-range WSNs, potential weather-induced link deteriorations must be taken into account in order to increase their quality and reliability.

In Chapter 4, the channel characterization hardware from Chapter 2 was integrated onto a textile substrate-integrated-waveguide (SIW) antenna. Radiation patterns of the standalone SIW antenna and the integrated node were compared. Additionally, body-to-body directivity was examined. An outdoor range test between two walking test persons demonstrated a communication range of several hundreds of meters in an open environment.

Body-to-body link characterization efforts were also performed in an indoor environment, as described in Chapter 5. In a modern office building, the influence of body shadowing was examined. Additionally, Chapter 5 also documented the impact of large obstructions (such as the heavy concrete core of the building and its floor structure) on the quality of the communication link.

In Chapter 6, the pertinent trade-off between range and data rate was investigated for LoRa devices in a body-to-base-station context. For a proposed system that dynamically adapts the LoRa spreading factor (SF) through repeated negotiation with the base-station, it was shown that the optimal number of active SF values depends on the speed of the user. For running or slow cycling speeds, it is best not to use more than two or three SF options, mainly to reduce the overhead of switching communication parameters. When a strict duty cycle is imposed, this overhead may become very impactful and switching spreading factors may actually be less efficient altogether.

The research presented in Chapter 7 demonstrated that significant link quality improvements are possible when applying front-to-back diversity in a similar body-to-base-station situation. Measurements showed that up to 5.5 dB of additional link budget was obtained by applying diversity. Furthermore, packet reception ratios (PRR) also clearly illustrated the achieved performance gains. Additionally, Chapter 7 compared received signal strengths for different user speeds to assess the impact of Doppler spread. Interestingly, comparing the power levels received when riding a motorized longboard at an average 31.1 km/h to those measured at a steady walking pace of 6.2 km/h revealed no significant link deteriorations. The range of the body-to-base-station setup easily reached 1.5 km in line-of-sight conditions.

Chapter 8 documented another leap forward in enhancing the performance of LoRa receivers. In this Chapter, a novel receive algorithm was presented which facilitates the successful reception of LoRa packets at extremely low SNR values. By applying rigorous time and frequency synchronization, SNR performance was achieved just 1.6 dB shy of a theoretical system with perfect channel state information. Different algorithm variations were compared, which clearly illustrated a trade-off between bit error rate (BER) performance and computational cost. When implemented on a software defined radio (SDR) platform, the best performing algorithm exhibited an

average SNR performance gain of 4.7 dB in comparison to commercially available LoRa hardware.

Finally, in Chapter 9, the influence of Doppler shifts on LoRa communication was determined, based on the SDR implementation presented in Chapter 8. It was shown that despite their large impact on the symbol detector, the effects of static Doppler shifts are mostly mitigated by applying synchronization. However, for very large relative velocities, BER performance deterioration is observed for higher spreading factors. This could primarily be an issue for the most demanding application environments, such as satellite-to-body communication. Dynamic Doppler shifts principally affect packets with a large payload. To alleviate these effects, more pilot symbols could be introduced, e.g. at the end of the payload. However, as the resulting frame structure would no longer conform to conventional LoRa specifications, this is only possible when leaving the realm of standardization.

10.2 General Conclusions

By reliably facilitating long-range wireless communication at very low power levels, LoRa modulation justifiably maintains a leadership position in the LPWAN technology landscape. The outstanding link performance demonstrated in this work in a variety of application environments is a testament to this claim. Furthermore, for body-centric wireless networks, LoRa features several advantages when compared to alternative solutions for sharing sensor information. However, notwithstanding these considerations, this dissertation also demonstrated that physical-layer performance can be improved further. From the application of diversity methods to unleashing the full power of SDR, significant range and link quality improvements have been illustrated. In fact, many LoRa advantages could be carried over to potential alternative CSS-based modulation techniques. The most inhibiting factors for LoRa itself are the heavy occupation of sub-GHz industrial, scientific and medical (ISM) bands and the related legal restrictions for channel access in these bands. By applying this modulation technique in even more challenging environments or implementing an alternative CSS modulation technique with a modified frame structure, more innovation is undoubtedly possible. These ideas form the cornerstone for future work, which is discussed next.

10.3 Future Work

In close relation to the topics presented in this dissertation, a number of improvements can be conceived. For example, it would be very interesting to implement multiple-input multiple-output (MIMO) LoRa systems on SDR. Furthermore, the receive algorithm presented in Chapter 8 of this dissertation can also be refined further in order to better handle LoRa communication in even more challenging environments, e.g. in those where a lot of Doppler spread is produced or those featuring same spreading factor LoRa interference. In relation to Doppler spread, this

dissertation also demonstrated how body-centric wireless communication strongly benefits from key advantages provided by LoRa modulation. However, LoRa offers valuable opportunities for many more applications as it takes in a unique trade-off position between power consumption, range and data rate. For example, when communicating flight telemetry in small unmanned areal vehicles (e.g. very low-power drones or micro-satellites), the Doppler robustness, range and low power consumption of LoRa are very interesting indeed.

Today, advanced modulation techniques are steadily being adopted for diverse applications. For example, in Belgium, analog terrestrial television broadcasting is no longer operational, and frequency modulation (FM) radio stations are planned to transition to digital audio broadcasting (DAB). However, large portions of the radio frequency spectrum are still used very inefficiently. In a number of applications, for example in aviation, analogue channels are still allocated to a single user, who only uses this channel for very limited amounts of time overall. For LoRa modulation, this is not the case, as this technique is very robust in the presence of noise and applies a number of channel sharing strategies (e.g. by varying the spreading factor and applying time diversity through obeying to a maximum duty cycle). Similar to chirp spread spectrum (CSS), and therefore LoRa, other modulation techniques such as direct-sequence spread spectrum (DSSS) also allow communication channels to be used by multiple users at the same time. However, LoRa features a few advantages when compared to DSSS. For example, LoRa is easily bandwidth scalable and features a constant power envelope, which means that low-cost, high-efficiency hardware can be employed for power amplification.

Lessons learned from LoRa technology could be applied in alternative CSS-based sub-GHz communication standards in order to tailor this type of modulation to different applications. For example, transmission power and duty cycle regulations might be waived in certain radio bands, enabling entirely new types of LoRa/CSS deployments. Furthermore, the current frame structure of LoRa could be adapted or multiple spreading factors might be used at the same time to further facilitate new functionality. Similarly, even longer links could be set up than those featured in this dissertation by stacking LoRa modulation with other coding techniques. For example, by using LoRa packets with predefined payloads, status information data could be spread out even more over time. To facilitate detection, an SDR receiver could correlate the data to the known possible payloads, further increasing noise tolerance. Moreover, techniques similar to DSSS and CDMA could be integrated with CSS in various ways, pushing the limits of long-range low-power communication technologies even further.



Wireless sensor networks share information on an unprecedented scale.